Technical Physics, Vol. 46, No. 1, 2001, pp. 1–6. Translated from Zhurnal Tekhnicheskoĭ Fiziki, Vol. 71, No. 1, 2001, pp. 3–8.

A Method of Tomographic Reconstruction of the Three-Dimensional Velocity Distribution Function of Electrons

A. N. Cheburkin[1] and S. A. Kharchenko[2]

[1] *General Physics Institute, Russian Academy of Sciences, Moscow, 117942 Russia*
[2] *Computing Centre, Russian Academy of Sciences, Moscow, 117967 Russia*

Received December 8, 1999

Abstract—An experimental method is proposed for the determination of an arbitrary three-dimensional distribution function for initial energies of electrons emitted by a point source with resolution for two exit direction angles. In a computer experiment, two model distribution functions have been reconstructed using the proposed method. © *2001 MAIK "Nauka/Interperiodica".*

INTRODUCTION

The distribution function for initial energies and exit directions of electrons emitted by some source is of interest in various fields of modern science. The distribution function for the initial energies and exit directions of electrons from a point source (briefly called below the distribution function) will be understood as the probability density of electrons found at particular points in the initial velocity space. In the general case, the distribution function depends on three independent variables.

Information on the distribution function is of particular value in studies of some physical phenomena, for example, of the photoeffect and ionization of gases. Besides, a beam of electrons can be used as an investigative tool in electron spectroscopy, diffraction, and in electron microscope studies. Comparison of the distribution functions of an electron beam before and after its interaction with an object under study provides information on the object's structure. However, in most contemporary scientific investigations, either one-dimensional [1–4] or two-dimensional [4–6] distribution functions are obtained. One-dimensional functions usually describe distributions of the initial electron energy or one of the two exit angles. Two-dimensional functions mostly provide distributions over energy and either of the two exit angles. A three-dimensional distribution function over energy and two exit angles in a limited spatial angle has been measured in [7]. In this experiment, the electron detector incorporating an energy analyzer was moved over a spherical surface.

METHODS

In the present paper, a method for the experimental determination of the three-dimensional distribution function is proposed. This method has many advantages over existing approaches to the distribution function measurement. The distribution function is determined for all directions of the exit of electrons from a point source. All electrons exiting the source are registered. No perturbations are introduced in this method because there are no grids, slits, or orifices between the electron source and the detector. The method is not intended to register variations of the distribution function with time. An essential feature of the method is the necessity of carrying out several experimental runs to register several images of the electrons exiting the source.

Tomographic Method for Reconstruction of the Three-Dimensional Distribution Function

1. The essence of the method. Suppose a distribution of electrons instantaneously emitted by a point source over their initial energies and directions of exit (called below the distribution function) is being studied. Let us position at some distance from the source a flat registration unit (screen) for registering the spatial distribution of the emitted electrons. Between the source and the registration unit, electromagnetic fields of various configurations can be applied. The basic problem in reconstructing the distribution function in such an experimental setup is as follows. In the general case, the distribution function contains three independent variables. These could be, for example, Cartesian coordinates in the space of initial velocities. On the screen, we have information on the distribution of the electron image intensity, which is a function of only two independent spatial variables. Each point of the image on the screen corresponds to a curve in the space of initial velocities, namely, all electrons corresponding to the velocity space points on this curve hit a certain screen point. Two different screen points correspond to two noncrossing curves in the velocity space. Let us

1063-7842/01/4601-0001$21.00

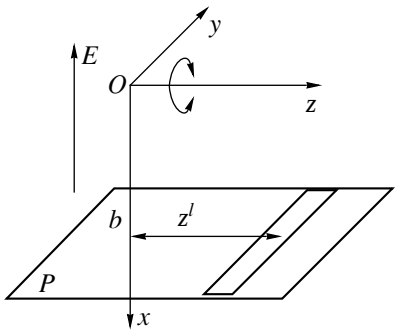

Fig. 1.

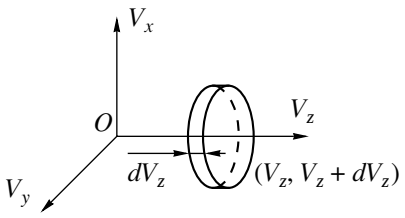

Fig. 2.

call the curve in the space of velocities corresponding to a point on the registration screen an isoline.

The knowledge of the electron image intensity at a screen point is not sufficient for the unambiguous reconstruction of the probability density distribution over the isoline corresponding to this point. Therefore, on the basis of one image on the registration screen it is generally impossible to unambiguously reconstruct a three-dimensional distribution function. To obtain an unambiguous solution of the inverse problem of the distribution function reconstruction, a third independent variable parameter is needed to characterize each distribution of electron intensity obtained on the flat screen. These independent variable parameters include the electromagnetic field in the space between the electron source and the screen, the distance between the source and the screen, the angle between the normal to the screen and the vector characterizing the emission pattern of the source, or the instant and the time of exposure of the screen.

The reconstruction problem is simplified if the distribution function has symmetry properties. In many cases, for physical reasons or due to the experimental symmetry, the distribution function possesses axial symmetry and, with a proper choice of the coordinate system, can be considered two-dimensional. Then for certain relative positions of the source and the screen, one image will be enough for the reconstruction of a two-dimensional distribution function.

In the present paper, the general case of the reconstruction of a three-dimensional distribution function is considered. Computational experiments on the reconstruction of two model distribution functions are carried out. As the initial data for the reconstruction, we used the electron distributions on the screen calculated analytically for various relative positions of the emission pattern of the source and the electromagnetic field–registration screen system.

2. The experiment schematic. Let there be a point electron source *O* placed in a uniform electric field *E* (Fig. 1). At a distance *b* from the source, a flat registration screen *P* is arranged perpendicular to the electric field *E*. Electrons emitted by the source *O* are accelerated by the field and hit the screen. Let us set up a Cartesian coordinate system whose origin coincides with the source *O* and axis *OX* is directed from the source to the screen opposite to the electric field direction. Plane *OYZ* is parallel to the screen plane. The distribution function is considered to be a bounded body of variable density in the space of velocities. The body density corresponds to the probability density of the distribution function. Let us introduce orthogonal coordinates in the space of velocities with the axes directed in such a way that the projections of the electron velocities V_x, V_y, and V_z coincide with their projections on axes OV_x, OV_y, and OV_z (Fig. 2).

Consider a plane section of the distribution function which is at a normal to the OV_z axis. If the maximum initial energy of the electrons is assumed to be much less than that acquired by the electrons in the accelerating field, then such a section through the velocity space is mapped with a sufficient accuracy as a segment parallel to the *OY* axis on the screen *P*.

A layer of the distribution function enclosed between two close plane sections at a normal to the OV_z axis and having a thickness dV_z will be registered on the screen as a slit bounded by two segments parallel to the *OY* axis and corresponding to sections

$$V = V_z^l \quad \text{and} \quad V = V_z^l + dV_z. \tag{1}$$

The slit center is at a distance z^l from the origin of the coordinates along the *OZ* axis:

$$z^l = V_z^l \sqrt{\frac{2mb}{eE}}, \tag{2}$$

where *m* and *e* are the electron mass and charge; this slit will be called the registration slit below.

Let us divide the whole distribution function in the space of velocities into a set of plane layers normal to the OV_z axis. Reconstruction of the distribution function within every layer will be equivalent to reconstructing the distribution function as a whole. Each layer of the distribution function is imaged on the screen *P* as a corresponding slit. Thus, under this assumption, the problem of distribution function reconstruction can be reduced to reconstructing two-dimensional distribution functions within thin layers normal to the OV_z axis using one-dimensional images at the corresponding registration slits.

3. The isoline equation. Consider the problem of the reconstruction of the electron distribution in a thin layer normal to the OV_z axis. Let us introduce polar coordinates (V, φ) in the OV_xV_y plane. Here, V is the radius vector of a point and φ is the angle measured from the positive direction of the OV_x axis. The equation of motion of an electron with parameters (V, φ) in a uniform electric field E directed along the OX axis has the form

$$y = V\sin\varphi^*\tau, \tag{3}$$

$$b = V\cos\varphi^*\tau + a\tau^2/2, \tag{4}$$

where τ is the time of electron flight from the source to the screen and $a = eE/m$ is the electron acceleration in a uniform electric field.

Let us introduce a nondimensional parameter

$$r = \frac{V}{V_0}, \tag{5}$$

where V_0 is the maximum velocity in a chosen section.

From definition (5), it follows that the distribution function of electrons in the space of velocities may be nonzero only within a circle of $r = 1$. Let us eliminate time from Eqs. (3) and (4). Elementary transformations give

$$r = \frac{y}{V_0\sin\varphi}\sqrt{\frac{a}{2(b - y\cot\varphi)}}. \tag{6}$$

It follows from Eq. (6) that if the points in the space of velocities specifying the velocity vectors of emitted electrons are in the plane of the considered section on curve (6), then the corresponding electrons hit one and the same point of the registration screen with coordinate y (Fig. 3). This point lies within a slit parallel to the OY axis and corresponds to the section considered. Thus, the isoline equation corresponding to the registration slit point with coordinate y has been derived.

In the considered case of a one-dimensional electric field, we have succeeded in obtaining an explicit form of the isoline equation. In cases of more complicated electromagnetic fields, elimination of time from the electron motion equations may turn out to be hard to implement. However, obtaining an explicit form of the isoline equation is not necessary. In this method, it is important to be able to solve the direct problem of mapping the electrons with given initial parameters onto the screen. The corresponding numerical methods have been developed and are successfully applied in practice [8].

4. Mathematical formulation of the problem. The isoline concept helps to illustrate the reconstruction method proposed. Let us choose two points with coordinates y_1 and y_2 in the registration slit (Fig. 3). These points belong to two isolines $r_1 = r(\varphi, y_1)$ and $r_2 = r(\varphi, y_2)$ lying in the considered section through the space of velocities. The segment of the registration slit

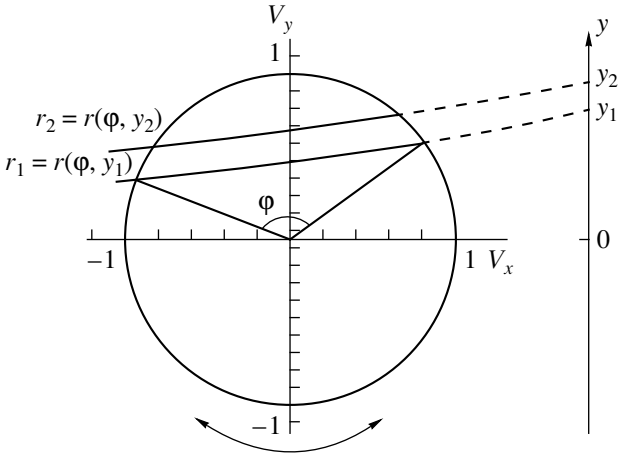

Fig. 3.

bounded by points y_1 and y_2 registers only those electrons which are found between isolines $r_1 = r(\varphi, y_1)$ and $r_2 = r(\varphi, y_2)$. The number of such electrons is

$$\Delta N = \iint_S \rho(r, \varphi)\,ds, \tag{7}$$

where $\rho(r, \varphi)$ is the distribution function in question and $ds = r^*dr^*d\varphi$ is the area element in polar coordinates. The integration range S denotes the region in the considered section of the distribution function between isolines r_1 and r_2.

Quantity ΔN, which is the number of electrons registered by a screen cell bounded by y_1 and y_2, can be experimentally measured. For this purpose, the registration slit has to be a system capable of registering the electrons with spatial resolution. Such systems are, for example, CCD matrices or conventional systems for recording electron images in electron-optical cameras.

Relation (7) can be written for all spatial cells within the registration slit. As a result, a set of integral equations with the sought for function under the integral signs will be obtained.

In the case considered, when the isoline equation (6) is known, it is convenient to use the intensity of the electron number at a screen point instead of the number of electrons in a screen cell. Let us bring points y_1 and y_2 of the screen closer. Ultimately, we will obtain a limit of the number ΔN of electrons in a small vicinity Δy of screen point y. The ratio $\Delta N/\Delta y$ in the vicinity of screen point y can be treated as the intensity of the number of incident electrons at screen point y. An intensity curve along the registration slit can be obtained by processing the experimental data on the number of electrons in the slit cells.

By dividing both sides of equation (7) by length dy of the cell and proceeding to the limit $dy = y_2 - y_1 \longrightarrow 0$,

we obtain

$$I(y) = \frac{dN}{dy} = \iint_{\Phi} \rho(r, \varphi) r \frac{dr}{dy} d\varphi, \qquad (8)$$

where $r = r(\varphi, y)$ is the isoline equation in the explicit form; and Φ is an interval between angles corresponding to intersection points of the isoline with the boundaries of the section being reconstructed.

Thus, the problem of reconstructing the distribution function in a plane section through the space of velocities is reduced to the problem of reconstructing the function $\rho(r, \varphi)$ using the known values of integral (8) for different isolines.

In the computational experiment $I(y)$, we use the results of analytical or numerical calculations of the intensity distribution of the number of electrons on the screen for a given model distribution function of electrons over initial energies and exit directions as the experimental data. Equation (8) is the Fredholm equation of the first kind. It has been shown [9] that its solution with respect to the function under the integral sign may be unstable relative to small variations of initial data $I(y)$. Therefore, the reconstruction of the distribution function density is an ill-posed problem and calls for special methods of solving.

The formulation of the reconstruction problem of the electron distribution function in the space of initial velocities and its subsequent reduction to a set of integral equations are very similar to the problem statement and mathematics in computational reconstructive tomography [10, 11]. To reconstruct the distribution function, let us proceed from analogy with the computational reconstructive tomography method. Let us measure the electron number intensity distribution over the registration slit corresponding to the section under consideration. Then, let us rotate the section by some angle about the OV_z axis. This can be achieved by turning the source around the OZ axis. The field–screen system will remain in the same place in the chosen spatial coordinates and so will the velocity isolines for the registration slit corresponding to the section.

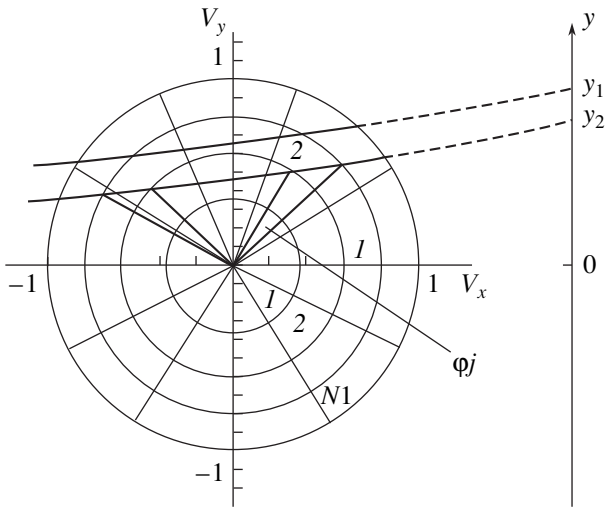

Fig. 4.

Therefore, in the space of velocities or, more precisely, in the V_xV_y plane, a turn of the section considered and of the set of isolines for the registration slit corresponding to this section will occur. In this way, a new projection of the considered section onto the registration slit will be obtained. Having recorded the profiles of the electron number intensity over the registering slit at various turn angles, we obtain values of integral (8) along isolines of different directions passing through the section under reconstruction. The turn directions of the source and its distribution function are shown by arrows in Figs. 1 and 3, respectively. In the present study, modeling of the turn of the source and corresponding distribution function was performed with a fixed electric field and screen. Inasmuch as only the relative turn of the isolines and the distribution function is of importance, another way of carrying out the experiment is possible with a fixed electron source and a rotating field–screen system around the OZ axis.

5. The reconstruction algorithm. For reconstruction of the distribution function, an algebraic reconstruction algorithm was used [10, 11]. The image to be reconstructed has to be discretized prior to reconstruction. The distribution function in the section considered may be nonzero only within a circle of radius $r = 1$ with its center on the OV_z axis. Let us superimpose an elementary grid in polar coordinates on the circle of radius $r = 1$ by dividing the circle into N_1 concentric rings and N_2 sectors (Fig. 4). The resulting elementary cells will be called discretization elements.

The sought-for distribution function is assumed to be continuous and will be reconstructed in the form of a piecewise-constant function, assuming that within a discretization element the distribution function is constant. The smaller the discretization elements, the closer the piecewise-constant function is to the real distribution function.

The contribution of a discretization element to the total intensity at a point of the registration slit is equal to integral (8) taken over the corresponding isoline within the considered discretization element. The total intensity at point y of the registration slit is also described by integral (8). In a discrete model, this integral transforms into a finite sum. The intensity at a point y of the registration slit is equal to the sum of contributions from discretization elements of the distribution function through which the corresponding isoline passes.

Let us choose M points on the registration slit at which the electron image intensity is to be measured. For each of these points, Eq. (8) can be written in the form of a finite sum. Thus, the considered model leads

to an inhomogeneous system of linear algebraic equations

$$\sum_{j=1}^{N} A_{ij}^{*}\rho_j = I(y_i), \quad i = 1, 2, \ldots, M. \tag{9}$$

Here, $I(y_i)$ is the intensity at point y_i of the registration slit obtained in a physical or computational experiment; ρ_j are the sought for unknown quantities forming a set $\rho = \{\rho_j\}$, $j = 1, 2, \ldots, N1*N2$ representing the distribution function being reconstructed in the section; and $A_{ij}^{*}\rho_j$ is the contribution of the jth discretization element to the total intensity at an ith point of the screen. The expression for A_{ij} is derived from (8) by removing from the integrand the density term $\rho(r, \varphi) = \rho_j$, which is constant inside the jth ring,

$$A_{ij}\int\int_{\Phi_j} r(dr/dy)d\varphi, \tag{10}$$

where Φ_j is an interval between the angular coordinates φ of the end points of the portion of the isoline within the jth discretization element.

The set of Eq. (9) can be written for each of the turn angles α_k, $k = 1, 2, \ldots, K$ of the source relative to the field–screen system. As a result, we obtain the combined set for all projections of the distribution function

$$\sum_{j=1}^{N} A_{pj}^{*}\rho_j = I(y_p), \quad p = 1, 2, \ldots, M, M+1, \ldots, M*K. \tag{11}$$

All coefficients of the matrix $A = \{A_{ij}\}$ are nonnegative, because they are the contributions to the intensity of the number of electrons incident on the screen. The solution to (11) must be a set of nonnegative numbers due to the physical sense of the probability density of the distribution of electrons. Some other constraints may be imposed on the solution according to the physical sense of the problem. The set of Eqs. (11) includes the rectangular matrix A. This set may have no solution in the classical sense; that is, the vector ρ satisfying equation $A\rho = I(y)$ may be nonexistent. The way to solve such a set is to seek the vector ρ that would best satisfy set (11) according to the appropriate criteria of optimality.

In the present study, we used a reconstruction algorithm based on quadratic optimization for solving set (11). In solving the set we sought a singular expansion of matrix A and a least squares problem was solved by minimizing the differences between the left and right sides of the equations in the sense of the 2-norm. Analysis of the singular numbers and singular vectors of matrix A provided estimates of the independence and fullness of the information obtained from the modeling.

Computational Simulation and Discussion

The computational simulation of the experiment and subsequent reconstruction of the distribution function were carried out for two distributions: $\rho = 1$ in a circle of radius $r = 1$ and $\rho = r^2(1 - r^2)\sin^2\varphi$ in the same circle. The distribution $\rho = r^2(1 - r^2)\sin^2\varphi$ is shown in Fig. 5. Outside the unit circle the distribution function was assumed to be zero in both cases. It was also assumed that the region of the nonzero function values was exactly known.

In the course of the computational simulations, the parameters of the numerical experiments were varied in the following ranges: (a) the number of screen points for registering the intensity of the number of electrons ranged from 50 to 800; (b) the coordinates of the registration slit boundaries were usually symmetric relative to the origin of coordinates, and the registration slit length varied from 5 to 10 mm; (c) the distance between the source and the screen plane varied from 1 to 15 cm; (d) the voltage between the screen and the source was from 200 to 3000 V; (e) and the maximum initial energy of the electrons in the section being reconstructed was from 1.0 to 3.0 eV, and the number of equations in set (11) always exceeded the number of discretization rings (that is, the number of unknowns). To obtain different projections, the distribution function was turned in both directions by angles in a range $(-\alpha, \alpha)$, and the angle α was varied from 50 to 90°. The reconstructed distribution functions were in good agreement with the given ones if the turn angle exceeded (–70, +70). For the $\rho = 1$ distribution, in those experiments where all the electrons emitted in the section considered hit the screen within the registration slit length, the reconstruction of the distribution function was accurate to within the computational error. The relative error of the reconstruction of function $\rho = 1$ was not worse than 10^{-7}. The

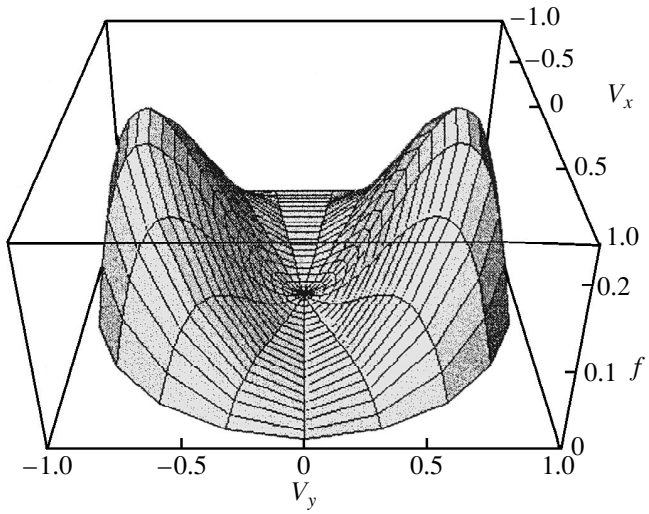

Fig. 5.

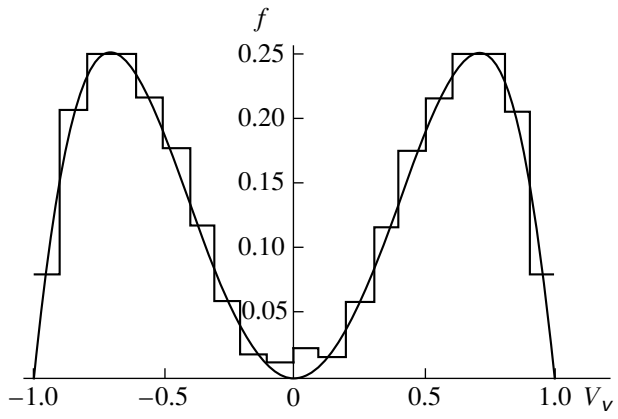

Fig. 6.

distribution $\rho = r^2(1 - r^2)\sin^2\varphi$ is not piecewise-constant. The vector in the right side of the set of equations was obtained by the exact calculation of the intensity of the number of electrons at the screen for function $\rho = r^2(1 - r^2)\sin^2\varphi$. At the same time, this intensity was approximated using a piecewise-constant function. Therefore, an approximation error and discrepancy between the left and right sides of the equations of the set was inevitable.

In those experiments where the entire section fitted within the registration slit length and with the turn angles of the distribution function, the number of different turn positions and the number of points on the screen as specified above, a good reconstruction was obtained. The relative error of the reconstruction in comparison with the true solution vector depended on the size of the distribution function discretization elements and did not exceed 5%, with the exception of the discretization elements of the innermost and outermost rings, where the given distribution function is close to zero and has an appreciable gradient. The true solution vector was calculated using formula

$$\rho_{av} = \frac{1}{S}\iint_{\sigma}\sigma_{tr}ds, \quad j = 1, 2, \ldots, N1*N2, \qquad (12)$$

where ρ is the model density function specified, with the integration over the entire area σ of the jth discretization element considered $S = \iint_{\sigma} ds$ is the area of the jth division element.

An example of the reconstruction results for the distribution function $\rho = r^2(1 - r^2)\sin^2\varphi$ in section $\varphi = \pi/2$ is shown in Fig. 6. The smooth curve in this figure is a section of the true distribution function and the piecewise-constant function is the section of the reconstructed distribution function.

CONCLUSION

In this work, a method is proposed for the reconstruction of the three-dimensional distribution function from known initial energies and exit directions of electrons emitted by a point source. The method is based on registering the spatial distribution of the intensity of the electron numbers on a registration screen at different turn angles of the source relative to the screen. The reconstruction is implemented on the basis of a conformity between the screen points and the corresponding curves in the space of the initial velocities of the emitted electrons. The proposed method is similar to the reconstructive computational tomography. The inverse problem arising is solved with the use of the algebraic reconstruction algorithm. In the conducted computational experiments, successful reconstruction of two model distribution functions for electrons has been fulfilled.

REFERENCES

1. N. A. Soboleva and A. E. Melamid, *Photoemissive Devices* (Vysshaya Shkola, Moscow, 1974).
2. D. Charalambidis, H. Hontzopoulos, C. Fotakis, *et al.*, J. Appl. Phys. **65** (7), 2843 (1989).
3. A. Yu. Elizarov, Laser Phys. **7** (2), 292 (1997).
4. M. V. Gomoyunova, Usp. Fiz. Nauk **136**, 105 (1982) [Sov. Phys. Usp. **25**, 58 (1982)].
5. H. Helm, N. Bjerre, M. J. Dyer, *et al.*, Phys. Rev. Lett. **70** (21), 3221 (1993).
6. W. Becker, M. Kleber, *et al.*, Laser Phys. **8** (1), 56 (1998).
7. S. J. McNaught, J. P. Knauer, and D. D. Meyerhofer, Laser Phys. **7** (3), 712 (1997).
8. S. V. Andreev, M. A. Monastirski, and V. A. Tarasov, in *Proceedings of the 22nd International Congress on High-Speed Photography and Photonics, Santa Fe, 1996*; Proc. SPIE **2869**, 92 (1997).
9. A. N. Tikhonov and V. Ya. Arsenin, *Solutions of Ill-Posed Problems* (Nauka, Moscow, 1986; Halsted, New York, 1977).
10. G. T. Herman, *Image Reconstruction from Projection: The Fundamentals of Computerized Tomography* (Academic, New York, 1980; Mir, Moscow, 1983).
11. Proc. IEEE **71** (3) (1983).

Translated by N. Mende

Technical Physics, Vol. 46, No. 1, 2001, pp. 101–106. Translated from Zhurnal Tekhnicheskoĭ Fiziki, Vol. 71, No. 1, 2001, pp. 106–111.

The Conductivity of a 2D System with a Doubly Periodic Arrangement of Circular Inclusions

B. Ya. Balagurov and V. A. Kashin

Émanuél' Institute of Biochemical Physics, Russian Academy of Sciences, ul. Kosygina 4, Moscow, 117997 Russia

Received April 10, 2000

Abstract—We present a scheme for the evaluation of the conductivity and other effective properties of a model composite with a regular anisotropic structure, namely, a 2D system with circular inclusions forming a rectangular array. Exact expressions for the electric potential and the effective conductivity tensor $\hat{\sigma}_e$ were obtained in the form of infinite series. For small inclusion densities, a virial expansion for $\hat{\sigma}_e$ was derived from the general formulas and its applicability conditions were found. The first terms of this expansion yield the well-known Rayleigh result for the isotropic model (square array). © *2001 MAIK "Nauka/Interperiodica".*

(1) The study of electrophysical properties of inhomogeneous disordered media (in particular, composite materials) runs into certain mathematical problems. Composites with a regular structure (especially 2D systems) are much easier to examine. The problem is essentially simplified, since it is sufficient to find the potential within one unit cell in this case. The conductivity and other properties of such systems are of considerable interest from the standpoints of both general physics (e.g., the problem on phase transitions) and applications (microelectronics).

The conductivity of two-component 2D systems with a periodic arrangement of inclusions (dielectric or perfectly conducting) was considered in [1–3]. In the case of prime interest, when both components have a finite (nonzero) conductivity, a closed solution was obtained only for the stagger model [1]. A more realistic model, i.e., a 2D system with a regular arrangement of circular inclusions, was considered even by Rayleigh [4]. However, despite the relative simplicity of this model, only the first several terms of the virial expansion for the effective conductivity of the system were found because of the cumbersome computational scheme used in [4].

In this paper, we propose a sequential method for solving the conductivity problem as applied to a doubly periodic arrangement of circular inclusions of radius R that form a 2D rectangular array. The complex potential outside the inclusions is expressed in terms of the Weierstrass zeta function [5, 6] and its derivatives. An infinite set of equations was obtained for unknown coefficients involved in the general expression for the potential. For small R's, this system is solved by iteration. This makes it possible to find virial expansions for conductivity and other effective parameters in an analytic form. For large R's, the set of equations can be solved numerically, so that it becomes possible to study various effective properties of the model throughout the whole range of parameters involved in the problem.

(2) The model under consideration is a 2D isotropic matrix of conductivity σ_1 with circular inclusions of radius R and conductivity σ_2. The inclusions form a regular structure, i.e., a rectangular array with spacings $2a$ along the x axis and $2b$ along the y axis. We consider the case when the potential difference is applied in the x direction. In this case, the electric field strength $\mathbf{E} = \mathbf{E}(x, y)$, along with the evident periodicity $\mathbf{E}(x + 2a, y) = \mathbf{E}(x, y + 2b) = \mathbf{E}(x, y)$, has the symmetry

$$\begin{aligned} E_x(-x, y) &= E_x(x, -y) = E_x(x, y), \\ E_y(-x, y) &= E_y(x, -y) = -E_y(x, y). \end{aligned} \quad (1)$$

In particular, the vertical boundaries of a unit cell and the straight line $x = 0$ are equipotential lines where $E_y = 0$, whereas the horizontal boundaries and the line $y = 0$ are lines of current where $E_y = 0$ as well.

In view of symmetry (1) of the electric field, the complex potential $\Phi(z)$ inside an inclusion has the form (the origin is at the center of the circle)

$$|z| \le R\colon\ \Phi^{(i)}(z) = \sum_{n=0} A_{2n+1} z^{2n+1} (z = x + iy), \quad (2)$$

where the coefficients A_{2n+1} are real. The derivative of the function $\Phi(z)$ is related to the components of the electric field strength $\mathbf{E}$ as $\Phi'(z) = -E_x + iE_y$. The electric potential $\varphi(\mathbf{r})$ is given by the real part of $\Phi(z)$: $\varphi(\mathbf{r}) = \mathrm{Re}\Phi(z)$.

Outside the circle, solutions with both positive and negative powers of z are possible. The complex potential that explicitly allows for the array structure of the

model and symmetry (1) of the electric field may be represented in the form

$$|z| > R\colon \Phi^{(e)}(z) = \beta z + \sum_{n=0}^{\infty} B_{2n}\zeta^{(2n)}(z), \tag{3}$$

$$\zeta(z) = \frac{1}{z} + \sum_{l,m}{}'\left[\frac{1}{z - z_{lm}} + \frac{1}{z_{lm}} + \frac{z}{(z_{lm})^2}\right]; \tag{4}$$

$$z_{lm} = 2al + i2bm.$$

Here, $\zeta(z)$ is the Weierstrass zeta function [5, 6] and $\zeta^{(2n)}(z)$ is the $2n$th derivative of $\zeta(z)$. The prime in (4) means that summation is over integer l's and m's except $l = m = 0$. In (3), the term linear in z is due to the external uniform field; the term with $n = 0$ corresponds to the field of induced dipole moments; and the terms with $n \geq 1$, of higher multipoles. The coefficients β and B_{2n} in (3) are real. Using well-known properties of Weierstrass elliptic functions [5, 6], one can easily check that potential (3) satisfies the aforementioned conditions at the boundaries and the axes of symmetry of the unit cell.

(3) We cite some information about the function $\zeta(z)$ that will be used later. According to [5, 6], the zeta function is quasi-periodic:

$$\begin{aligned}\zeta(z + 2\omega) &= \zeta(z) + 2\eta, \quad \eta = \zeta(\omega),\\ \zeta(z + 2\omega') &= \zeta(z) + 2\eta', \quad \eta' = \zeta(\omega'),\end{aligned} \tag{5}$$

where $\omega = a$ and $\omega' = ib$.

The quantities η and η' are related by the Legendre relation [5, 6], which, in this case, has the form

$$ib\eta - a\eta' = i\frac{\pi}{2}. \tag{6}$$

The function $\zeta(z)$ can be expanded in the following power series in z [6]:

$$\zeta(z) = \frac{1}{z} - \sum_{k=2}^{\infty}\frac{c_k}{2k-1}z^{2k-1}, \tag{7}$$

where

$$\begin{aligned}c_2 &= \frac{g_2}{20}, \quad c_3 = \frac{g_3}{28}, \quad c_4 = \frac{1}{3}c_2^2,\\ c_5 &= \frac{3}{11}c_2c_3, \quad c_6 = \frac{1}{39}(2c_2^3 + 3c_3^2), \ldots.\end{aligned} \tag{8}$$

In (8), g_2 and g_3 are the invariants of the Weierstrass function [5, 6]:

$$g_2 = 60\sum_{l,m}{}'\frac{1}{(z_{lm})^4}, \quad g_3 = 140\sum_{l,m}{}'\frac{1}{(z_{lm})^6} \tag{9}$$

with z_{lm} from (4). The quantities c_k satisfy the recurrence relation [6]

$$c_k = \frac{3}{(2k+1)(k-3)}\sum_{m=2}^{k-2} c_m c_{k-m} (k \geq 4), \tag{10}$$

which makes it possible to find the coefficients c_k sequentially in increasing order of subscript k.

The definitions for η, η', g_2, and g_3 imply the following symmetry relations:

$$\begin{aligned}\eta(b, a) &= i\eta'(a, b), \quad g_2(b, a) = g_2(a, b),\\ g_3(b, a) &= -g_3(a, b).\end{aligned} \tag{11}$$

Correspondingly, for the coefficients c_k, we have

$$c_k(b, a) = (-1)^k c_k(a, b), \tag{12}$$

so that all c_k's with odd subscripts are equal to zero in the case of a square array ($a = b$) [6]. In this case, we can find the explicit expressions for η, η', g_2, and g_3 [5, 6]:

$$\begin{aligned}a = b\colon \eta &= \frac{\pi}{4a}, \quad \eta' = -i\frac{\pi}{4a},\\ g_2 &= \frac{1}{a^4}\left[K\left(\frac{1}{\sqrt{2}}\right)\right]^4, \quad g_3 = 0,\end{aligned} \tag{13}$$

where $K(1\sqrt{2}) = 1.85407\ldots$ is the complete elliptic integral of the first kind with the modulus $k = 1\sqrt{2}$.

For $a \neq b$, the quantities η, η', g_2, and g_3 are determined by numerical procedures; associated tables are presented, e.g., in [6]. Explicitly, they can be found in the limiting cases

$$\begin{aligned}\frac{b}{a} \ll 1\colon \eta(a, b) &\simeq -\frac{a}{b^2}\frac{\pi^2}{12},\\ g_2(a, b) \simeq \frac{1}{b^4}\frac{\pi^4}{12}, &\quad g_3(a, b) \simeq -\frac{1}{b^6}\frac{\pi^6}{216};\end{aligned} \tag{14}$$

$$\begin{aligned}\frac{b}{a} \gg 1\colon \eta(a, b) &\simeq \frac{1}{a}\frac{\pi^2}{12},\\ g_2(a, b) \simeq \frac{1}{b^4}\frac{\pi^4}{12}, &\quad g_3(a, b) \simeq \frac{1}{a^6}\frac{\pi^6}{216}.\end{aligned} \tag{15}$$

The limiting values of η' follow from relations (6) and (11). The coefficients c_k are given by the expressions

$$\begin{aligned}\frac{b}{a} \ll 1\colon c_k &\simeq (-1)^k 2\frac{2k-1}{(2b)^{2k}}\sum_{m=1}^{\infty}\frac{1}{m^{2k}},\\ \frac{b}{a} \gg 1\colon c_k &\simeq 2\frac{2k-1}{(2a)^{2k}}\sum_{m=1}^{\infty}\frac{1}{m^{2k}},\end{aligned} \tag{16}$$

which are related by (12).

(4) The electrical potentials $\varphi^{(e)}(\mathbf{r}) = \mathrm{Re}\Phi^{(e)}(z)$ and $\varphi^{(i)}(\mathbf{r}) = \mathrm{Re}\Phi^{(i)}(z)$ at the inclusion edge ($r = R$) must satisfy the conventional conditions

$$r = R: \begin{cases} \varphi^{(e)} = \varphi^{(i)}, \\ \dfrac{\partial\varphi^{(e)}}{\partial r} = h\dfrac{\partial\varphi^{(i)}}{\partial r}, \quad h = \dfrac{\sigma_2}{\sigma_1}. \end{cases} \tag{17}$$

Differentiating expansion (7) $2n$ times yields

$$\zeta^{(2n)}(z) = \frac{(2n)!}{z^{2n+1}} - \sum_{m=0}^{\infty} \frac{(2n+2m)!}{(2m+1)!} c_{n+m+1} z^{2m+1}. \tag{18}$$

Substituting (18) into (3), setting $z = r\exp\{i\Theta\}$, and separating out the real part, we come to

$$\varphi^{(e)}(\mathbf{r}) = \beta r\cos\Theta + \sum_{n=0}^{\infty}\left\{ B_{2n}\frac{(2n)!}{r^{2n+1}} - \sum_{m=0}^{\infty} B_{2m}\frac{(2n+2m)!}{(2n+1)!} c_{n+m+1} r^{2n+1}\right\}\cos(2n+1)\Theta. \tag{19}$$

In a similar way, we find from (2)

$$\varphi^{(i)}(\mathbf{r}) = \sum_{n=0}^{\infty} A_{2n+1} r^{2n+1}\cos(2n+1)\Theta. \tag{20}$$

Substituting (19) and (20) into (17) results in the set of equations

$$\begin{gathered} \beta\delta_{n0} + B_{2n}\frac{(2n)!}{R^{4n+2}} - \sum_{m=0}^{\infty} B_{2m}\frac{(2n+2m)!}{(2n+1)!} c_{n+m+1} = A_{2n+1}, \\ \beta\delta_{n0} - B_{2n}\frac{(2n)!}{R^{4n+2}} - \sum_{m=0}^{\infty} B_{2m}\frac{(2n+2m)!}{(2n+1)!} c_{n+m+1} = hA_{2n+1}. \end{gathered} \tag{21}$$

Here, δ_{n0} is Kronecker's symbol. Subtracting the second equation in (21) from the first one, we obtain

$$A_{2n+1} = \frac{2}{1-h}\frac{(2n)!}{R^{4n+2}} B_{2n}. \tag{22}$$

Having eliminated the coefficient A_{2n+1} in (21), we get

$$B_{2n} + \frac{1-h}{1+h}\sum_{m=0}^{\infty} B_{2m}\frac{(2n+2m)!}{(2n)!(2n+1)!} R^{4n+2} c_{n+m+1} = \frac{1-h}{1+h}\beta R^2\delta_{n0}. \tag{23}$$

Having introduced the variables x_n instead of B_{2n},

$$B_{2n} = \frac{R^{2n+2}\delta}{\sqrt{(2n)!(2n+1)!}} x_n, \quad \delta = \frac{1-h}{1+h}, \tag{24}$$

we recast (23) as

$$x_n + \sum_{m=0}^{\infty} S_{nm} x_n = \beta\delta_{n0}, \tag{25}$$

where

$$S_{nm} = \frac{(2n+2m)!R^{2(n+m+1)}c_{n+m+1}}{\sqrt{(2n)!(2n+1)!(2m)!(2m+1)!}}\delta. \tag{26}$$

Here, the coefficients c_{n+m+1} are defined in (7)–(10) and δ, in (24). The matrix $\hat{S}$ is symmetric; the quantity $S_{00} = 0$, since $c_1 \equiv 0$.

Basically, Eqs. (23), (25), and (26) and relations (22) and (24) make it possible to express all the coefficients B_{2n} and A_{2n+1} in terms of β. In its turn, β is related to the potential difference U_x [see (28)], which is assumed to be fixed. Thus, expressions (22)–(26) represent a formal exact solution of the basic problem, i.e., finding the potential $\varphi(\mathbf{r})$.

(5) The voltage drop U_x across a unit cell and the total current I_x through it along the x axis are expressed in terms of the complex potential $\Phi(z)$ as follows:

$$\begin{aligned} U_x &= -\mathrm{Re}[\Phi(a+iy) - \Phi(-a+iy)], \\ I_x &= -\sigma_1\mathrm{Im}[\Phi(x+ib) - \Phi(x-ib)]. \end{aligned} \tag{27}$$

Substituting $\Phi(z)$ from (3) into (27), in view of (5), yields

$$\begin{aligned} U_x &= -2a\left(\beta + \frac{1}{a}B_0\eta\right), \\ I_x &= -2b\sigma_1\left[\beta - \frac{B_0}{ab}\left(\frac{\pi}{2} - b\eta\right)\right]. \end{aligned} \tag{28}$$

In the expression for I_x, the quantity $\mathrm{Im}\eta'$ is expressed in terms of η by relation (6). From (28), the conductivity in the x-axis direction (the principal value of the effective conductivity tensor $\hat{\sigma}_e$) $\sigma_{xe} = (aI_x)/(bU_x)$ is given by ($B_0 = x_0R^2\delta$)

$$\begin{gathered} \sigma_{xe} = \sigma_1\left[\alpha - \frac{R^2}{ab}\left(\frac{\pi}{2} - b\eta\right)\delta\right]\left(\alpha + \frac{R^2}{a}\eta\delta\right)^{-1}, \\ \alpha = \frac{\beta}{x_0}. \end{gathered} \tag{29}$$

Thus, knowing x_0 (i.e., B_0) suffices to determine σ_{xe}.

For small R's, the set of Eqs. (25) may be solved by iteration, i.e., by expanding it in terms of powers of the matrix $\hat{S}$. The corresponding expansion for α is found

from (29). According to (25), for $n = 0$, we have (taking into account that $S_{00} = 0$)

$$\beta = x_0 + \sum_{m \neq o} S_{0m} x_m, \tag{30}$$

whereas, for $n \neq 0$, (25) gives

$$n \neq 0\colon\ x_n = -x_0 S_{n0} - \sum_{m \neq 0} S_{nm} x_m. \tag{31}$$

Solving equation (31) by iteration, we find

$$n \neq 0\colon\ x_n = x_0 \Bigg\{ -S_{n0} + \sum_m{}' S_{nm} S_{m0} - \sum_l{}' \sum_m{}' S_{nl} S_{lm} S_{m0} + \ldots \Bigg\}. \tag{32}$$

Inserting (32) into (30) yields

$$\alpha = 1 - \sum_m{}' S_{0m} S_{m0} + \sum_l{}' \sum_m{}' S_{0e} S_{lm} S_{m0} - \sum_k{}' \sum_l{}' \sum_m{}' S_{0k} S_{kl} S_{lm} S_{m0} + \ldots. \tag{33}$$

In (32) and (33), the prime at the summation symbol means that the summation is carried out from 1 to ∞. Note that, with the matrix $\hat{T}$ defined as

$$T_{nm} = \begin{cases} 0, & m = 0, \\ S_{nm}, & m \neq 0, \end{cases} \tag{34}$$

expressions (32) and (33) may be represented in the compact form

$$n \neq 0\colon\ x_n = -x_0 ((1 + \hat{T})^{-1} \hat{S})_{n0}, \tag{35}$$

$$\alpha = 1 - (\hat{S}(1 + \hat{T})^{-1} \hat{S})_{00}. \tag{36}$$

With the explicit expression for the matrix $\hat{S}$ [see (26)], the expansion of α in terms of powers of R can be found from (33). Up to terms $\sim R^{24}$ inclusive, we get

$$\alpha = 1 - \frac{1}{3} R^8 c_2^2 \delta^2 - \frac{1}{5} R^{12} c_3^2 \delta^2 + \frac{2}{3} R^{14} c_2^2 c_3 \delta^3 - \frac{1}{7} R^{16} c_4^2 \delta^2 + 2 R^{18} c_2 c_3 c_4 \delta^3 - \frac{1}{3} R^{20} \left(\frac{1}{3} c_5^2 + 4 c_2^2 c_3^2 \delta^2 \right) \delta^2 + 2 R^{22} \left(\frac{4}{3} c_2 c_4 c_5 + \frac{7}{5} c_3^2 c_5 \right) \delta^3 - R^{24} \left(\frac{1}{11} c_6^2 + 4 c_2 c_3^2 c_4 \delta^2 + 5 c_2^2 c_4^2 \delta^2 \right) \delta^2 + \ldots. \tag{37}$$

Here, c_2, c_3, c_4, δ are defined in (8) and δ, in (24). In the case of a square array ($a = b$), when all the odd-subscript coefficients c_k are equal to zero, the expression for α is simplified. In this case, we have, up to terms $\sim R^{40}$ inclusive,

$$\alpha = 1 - \frac{1}{3} R^8 c_2^2 \delta^2 - \frac{1}{7} R^{16} c_4^2 \delta^2 - R^{24} \left(\frac{1}{11} c_6^2 + 5 c_2^2 c_4^2 \delta^2 \right) \delta^2 - R^{32} \left[\frac{1}{15} c_8^2 + 5 (12 c_2 c_4^2 c_6 + 5 c_2^2 c_6^2) \delta^2 \right] \delta^2 - R^{40} \left[\frac{1}{19} c_{10}^2 + 13 \left(124 c_2 c_4 c_6 c_8 + \frac{49}{9} c_2^2 c_8^2 \right) \delta^2 + 180 c_4^2 c_6^2 \delta^2 + 75 c_2^2 c_4^4 \delta^4 \right] \delta^2 - \ldots. \tag{38}$$

For a square array, the effective conductivity σ_e of the system is isotropic and is given by

$$\frac{\sigma_e}{\sigma_1} = \frac{\alpha - c\delta}{\alpha + c\delta} = 1 - \frac{2c\delta}{\alpha + c\delta} \tag{39}$$

with α from (38) and $c = \pi R^2/(2a)^2$. The Rayleigh expression for σ_e [4] follows from (39) if one retains the first three terms (up to terms $\sim R^{16}$ inclusive) in expansion (38).

Expressions (37) and (38) are virial expansions in which the inclusion concentration $c = \pi R^2/(4ab)$ is a formal small parameter. For $a \sim b$, the condition $c \sim (R/a)^2 \ll 1$ (or $R \ll a$) provides rapid convergence of series (37). For $a = b$, the applicability domain of the virial expansion is even wider, since, in this case, the concentration to the fourth power is an expansion parameter [see (38)]. Indeed, the correction $\sim R^8$ in (38) does not exceed 1% in the range $0 \le R \le 0.7a$ at $|\delta| = 1$ (i.e., at $h = 0$ and $h = \infty$). At the same time, the condition $c \ll 1$ is insufficient in the case of strong anisotropy ($a \gg b$ or $a \ll b$). For example, from the expression for g_2 in (14), we find, for $b/a \ll 1$, that the correction $\sim R^8$ in (37) is small for $c \ll b/a$ or $R \ll b$. Correspondingly, for $b/a \gg 1$, this correction is small for $c \ll a/b$ or $R \ll a$ (in both estimations, we assumed that $|\delta| \sim 1$). Thus, $R \ll \min\{a, b\}$ is the condition for fast convergence of expansion (37).

According to (12), the odd-subscript coefficients c_k change the sign on the permutation $a \rightleftarrows b$. This permutation also changes the sign of some terms in expansion (33) for α. Equation (37) shows that these terms contain δ to odd powers; therefore, the double replacement $a \rightleftarrows b$ and $\delta \longrightarrow -\delta$ does not change $\alpha = \alpha(a, b; \delta)$:

$$\alpha(b, a; -\delta) = \alpha(a, b; \delta). \tag{40}$$

The same conclusion follows from the general expression (33) for α. Similarly, for $\xi_n = x_n/\beta$, we obtain

$$\xi_n(b, a; -\delta) = (-1)^n \xi_n(a, b; \delta); \tag{41}$$

thus, equality (40) for $\alpha = 1/\xi_0$ is a special case of (41).

(6) The case when the potential difference is applied along the y axis is considered by the same method as above. In particular, the complex potentials inside and outside an inclusion have the form

$$\Phi^{(i)}(z) = -i\sum_{n=0}^{\infty} C_{2n+1} z^{2n+1}, \tag{42}$$

$$\Phi^{(e)}(z) = -i\left\{\gamma z - \sum_{n=0}^{\infty} D_{2n}\xi^{(2n)}(z)\right\} \tag{43}$$

with the real coefficients γ, C_{2n+1}, and D_{2n}. Further calculations almost completely repeat the foregoing ones. As a result, we find

$$\begin{aligned} D_{2n} &= \frac{R^{2n+2}\delta}{\sqrt{(2n)!(2n+1)!}} y_n, \\ C_{2n+1} &= \frac{2}{1+h}\frac{1}{R^{2n}}\frac{1}{\sqrt{2n+1}} y_n, \end{aligned} \tag{44}$$

where the values of y_n satisfy the set of equations

$$y_n - \sum_{m=0}^{\infty} S_{nm} y_m = \gamma\delta_{n0} \tag{45}$$

with the matrix $\hat{S}$ from (26).

The voltage drop U_y and the total current I_y are expressed through the complex potential $\Phi(z)$ as

$$\begin{aligned} U_y &= -\mathrm{Re}[\Phi(x+ib) - \Phi(x-ib)], \\ I_y &= \sigma_1 \mathrm{Im}[\Phi(a+iy) - \Phi(-a+iy)]. \end{aligned} \tag{46}$$

Substituting (43) into (46), in view of (5) and (6), yields

$$\begin{aligned} U_y &= -2b\left[\gamma + \frac{D_0}{ab}\left(\frac{\pi}{2} - b\eta\right)\right], \\ I_y &= -2a\sigma_1\left(\gamma - \frac{1}{a}D_0\eta\right). \end{aligned} \tag{47}$$

The conductivity in the direction of the y axis, i.e., $\sigma_{ye} = (bI_y)/(aU_y)$, is ($D_0 = y_0 R^2\delta$)

$$\begin{aligned} \sigma_{ye} &= \sigma_1\left(\bar{\alpha} - \frac{R^2}{a}\eta\delta\right)\left[\bar{\alpha} + \frac{R^2}{ab}\left(\frac{\pi}{2} - b\eta\right)\delta\right]^{-1}, \\ \bar{\alpha} &= \frac{\gamma}{y_0}. \end{aligned} \tag{48}$$

The expression for $\bar{\alpha}$ is derived from those for α [see (33) and (36)–(38)] after the substitution $\delta \longrightarrow -\delta$ or, according to (40), $a \rightleftharpoons b$. It is clear that, in the latter case, σ_{xe} is expected to change to σ_{ye}: $\sigma_{xe}(b, a) = \sigma_{ye}(a, b)$. Indeed, it is easy to check [in view of relations (11) and (6)] that the permutation $a \rightleftharpoons b$ yields (48) from (29).

With the permutation $\sigma_1 \rightleftharpoons \sigma_2$ (i.e., $h \longrightarrow 1/h$ and $\delta \longrightarrow -\delta$), the initial system turns into a so-called reciprocal system (the corresponding quantities will be denoted by a tilde). Going to the reciprocal system in (48) ($\bar{\alpha} \longrightarrow \tilde{\bar{\alpha}} = \alpha$) and comparing the result with (29), we infer that the reciprocity relation for structurally anisotropic 2D systems [7] (see, also, [8])

$$\sigma_{xe} = \tilde{\sigma}_{ye} = \sigma_1\sigma_2 \tag{49}$$

is automatically satisfied in this case.

(7) A knowledge of the potentials when the mean electric field strength $\langle\mathbf{E}\rangle$ is directed along the x and y axes makes it possible to find (in a linear approximation with respect to a magnetic field $\mathbf{H}$) the Hall component σ_{ae} of the effective conductivity tensor $\hat{\sigma}_e$. According to [9], it is given by

$$\sigma_{ae} = \sigma_{a2} + (\sigma_{a1} - \sigma_{a2})\varphi(p, h), \tag{50}$$

where σ_{ai} is the Hall component of the conductivity tensor for the ith component ($i = 1, 2$).

The function φ can be expressed in terms of the electric field strength $\mathbf{E}^{(\nu)}(\mathbf{r})$ at $\mathbf{H} = 0$ [9]:

$$\varphi = 1 - \frac{\langle E_x^{(x)}E_y^{(y)} - E_y^{(x)}E_x^{(y)}\rangle^{(2)}}{\langle E_x^{(x)}\rangle\langle E_y^{(y)}\rangle}. \tag{51}$$

Here, $\langle\ldots\rangle^{(2)}$ is the integral over the inclusion surface area divided by the unit cell area; the superscript ν means that $\mathbf{E}^{(\nu)}$ is directed along the $\langle\mathbf{E}^{(\nu)}\rangle$ axis. By determining $\mathbf{E}^{(x)}$ and $\mathbf{E}^{(y)}$ from (2) and (42), respectively, and evaluating the integral appearing in (51), we obtain

$$\langle E_x^{(x)}E_y^{(y)} - E_y^{(x)}E_x^{(y)}\rangle^{(2)} = \frac{1}{(1+h)^2}\frac{\pi R^2}{ab}\sum_{n=0}^{\infty} x_n y_y. \tag{52}$$

Then, we multiply equations (25) and (45) by y_n and x_n, respectively; add them together; and carry out the sum over all n. Eventually, taking into account the symmetry of the matrix $\hat{S}$ and the definitions of α and $\bar{\alpha}$, we get

$$\frac{1}{x_0 y_0}\sum_{n=0}^{\infty} x_n y_n = \frac{1}{2}(\alpha + \bar{\alpha}). \tag{53}$$

Finally, by inserting (52), (53), $\langle E_x^{(x)} \rangle = U_x/(2a)$ with U_x from (28), and $\langle E_y^{(y)} \rangle = U_y/(2b)$ with U_y from (46) into (51), we obtain

$$\varphi = \frac{\sigma_{xe}\sigma_{ye} - \sigma_2^2}{\sigma_1^2 - \sigma_2^2} \tag{54}$$

with σ_{xe} from (29) and σ_{ye} from (48). Note that the expression for φ in the form of (54) is valid for any structurally anisotropic 2D system and may be derived, in the general case, by the method proposed in [9].

(8) Partial square-law characteristics of the electric field strength are closely related to the effective conductivity of a composite. Just as in the isotropic case [9], we have

$$\psi_i^{(\alpha)}(p, h) \equiv \langle (\mathbf{e}^{(\alpha)})^2 \rangle^{(i)} = \frac{\partial \sigma_{\alpha e}}{\partial \sigma_i}; \qquad \mathbf{e}^{(\alpha)}(\mathbf{r}) = \mathbf{E}^{(\alpha)}(\mathbf{r})(|\langle \mathbf{E}^{(\alpha)} \rangle|)^{-1}. \tag{55}$$

Here, $\sigma_{\alpha e}$ are the principal values of the effective conductivity tensor ($\alpha = x, y, z$), $\langle \ldots \rangle^{(i)}$ is the integral over the volume (or area in a 2D case) of the ith component divided by the sample volume V, and $\mathbf{E}^{\alpha}(\mathbf{r})$ is the same as in the previous section.

For our model, $\langle E_x^{(x)} \rangle = U_x/(2a)$ with U_x from (28) and $\mathbf{E}^2 = |\Phi'(z)|^2$. By using, for example, (2), we find for the quantity $\psi_2^{(x)}$

$$\psi_2^{(x)} = \frac{1}{(1+h)^2}\frac{\pi R^2}{ab}\left(\alpha + \frac{R^2}{a}\eta\delta\right)^{-2} J, \tag{56}$$

$$J = 1 + \sum_{n=1}^{\infty}\left(\frac{x_n}{x_0}\right)^2. \tag{57}$$

The differentiation of σ_{xe} from (29) with respect to σ_2 yields

$$\frac{\partial \sigma_{xe}}{\partial \sigma_2} = \frac{1}{(1+h)^2}\frac{\pi R^2}{ab}\left(\alpha + \frac{R^2}{a}\eta\delta\right)^{-2}\left(\alpha - \frac{\partial \alpha}{\partial \delta}\delta\right). \tag{58}$$

By evaluating (57) [using expansion (32) for x_n] and the last factor in (58) [with α from (37)] up to terms $\sim R^{24}$ inclusive, it is easy to check that the relation $\psi_2^{(x)} = \partial\sigma_{xe}/\partial\sigma_2$ is satisfied in this approximation. However, the satisfiability of this relation for our model can be proved by straightforward calculation for an arbitrary R.

Taking into account the linear dependence of the matrices $\hat{S}$ and $\hat{T}$ on δ and using general expression (36) for α, we arrive at

$$\alpha - \frac{\partial \alpha}{\partial \delta}\delta = 1 + (\hat{S}(1+\hat{T})^{-1}(1+\hat{T})^{-1}\hat{S})_{00}. \tag{59}$$

On the other hand, substituting (35) into (57) yields

$$J = 1 + \sum_{n=1}^{\infty}(\hat{S}(1+\hat{T})^{-1})_{0n}((1+\hat{T})^{-1}\hat{S})_{n0}, \tag{60}$$

where we used the equality

$$n \neq 0\colon ((1+\hat{T})^{-1}\hat{S})_{n0} = (\hat{S}(1+\hat{T})^{-1})_{0n},$$

which is easy to check.

From the definition (34) of the matrix $\hat{T}$, it follows that

$$(\hat{S}(1+\hat{T})^{-1})_{00} = 0.$$

Therefore, summation in (60) can be extended to all $n \geq 0$, so that J eventually takes the form

$$J = 1 + (\hat{S}(1+\hat{T})^{-1}(1+\hat{T})^{-1}\hat{S})_{00}. \tag{61}$$

A comparison of (58) and (59) with (56) and (61) leads us to relation (55) with $\alpha = x$ and $i = 2$. The other equalities of (55) are proved in a similar way.

REFERENCES

1. Yu. P. Emets, *Electrical Properties of Composites with Regular Structure* (Naukova Dumka, Kiev, 1986).
2. B. Ya. Balagurov, Zh. Éksp. Teor. Fiz. **79**, 1561 (1980) [Sov. Phys. JETP **52**, 787 (1980)].
3. B. Ya. Balagurov, Zh. Tekh. Fiz. **51**, 1146 (1981) [Sov. Phys. Tech. Phys. **26**, 651 (1981)].
4. Lord Rayleigh, Philos. Mag. **34**, 481 (1892).
5. *Higher Transcendental Functions (Bateman Manuscript Project)*, Ed. by A. Erdelyi (McGraw-Hill, New York, 1955; Nauka, Moscow, 1967), Vol. 3.
6. *Handbook of Mathematical Functions*, Ed. by M. Abramowitz and I. A. Stegun (Dover, New York, 1971; Nauka, Moscow, 1979).
7. J. B. Keller, J. Math. Phys. **5**, 548 (1964).
8. B. Ya. Balagurov, Zh. Éksp. Teor. Fiz. **81**, 665 (1981) [Sov. Phys. JETP **54**, 355 (1981)].
9. B. Ya. Balagurov, Zh. Éksp. Teor. Fiz. **93**, 1888 (1987) [Sov. Phys. JETP **66**, 1079 (1987)].

Translated by M. Fofanov

Technical Physics, Vol. 46, No. 1, 2001, pp. 107–111. Translated from Zhurnal Tekhnicheskoĭ Fiziki, Vol. 71, No. 1, 2001, pp. 112–116.

EXPERIMENTAL INSTRUMENTS AND TECHNIQUES

Ion Formation and the Conductivity of an Active Film MIM Structure during Through Penetration of Cosmic Particles

S. V. Rotov, N. D. Semkin, and K. E. Voronov

Korolev State Aerospace University, Moskovskoe sh. 34, Samara, 443086 Russia

Received March 13, 2000

Abstract—The formation of a multicomponent plasma and the conductivity of a film MIM structure area short-circuited by a particle due to a high-velocity impact are considered. A model for calculating the conductivity of a shock-compressed metal–insulator–metal (MIM) structure is suggested. The model was constructed by solving the problem on inertial expansion of an impact-produced plasma and is based on the volume ionization model. With this model, the effect of an external electric field on the parameters of a plasma produced by particle–MIM structure interaction was clarified. The model can be used in designing particle detectors, measuring physicochemical properties of micrometeoroid and technogenic particles, and processing ion spectra. © *2001 MAIK "Nauka/Interperiodica".*

Interaction between an energetic particle and an active thin MIM structure ($U_{MDM} > 0$) is associated with the problem of detecting micrometeoroids and cosmic waste particles [1–4]. The use of active MIM structures in particle parameter transducers is dictated by the need for improving the sensitivity in the lower ranges of particle velocities and weights ($W < 10$ km/s, $m < 10^{-8}$ kg). This is of special importance for determining the elemental composition of micrometeoroids. Space-borne data processing equipment runs into obstacles when tackling this problem [2, 5, 6]. The conductivity of a shock-compressed film MIM structure was studied in [6].

In this work, we consider, on a qualitative basis, ion formation in a multicomponent plasma and the conductivity of an active film MIM structure area short-circuited by a particle upon a high-velocity shock. Our model is valid for particle velocities between 10 and 15 km/s [7]. The model for calculating the conductivity of a shock-compressed MIM structure is based on solution of the problem on inertial expansion of an impact-produced plasma and also on the volume ionization model [7, 8]. Within the model elaborated in this work, the effect of an external electric field on the parameters of a plasma produced by interaction between an energetic particle and a thin obstacle (an MIM structure) was elucidated.

Using relationships well known from the theory of shock waves [8], for particle (striker) velocities in the range W = 15–50 km/s, one can obtain the following expressions.

(1) The temperature at the shock front is given by

$$T_1 = G\frac{W}{1+\sqrt{\rho_2/\rho_3}}, \qquad (1)$$

where W is the striker velocity; ρ_2 and ρ_3 are the densities of the striker and target, respectively; $G = 1/\beta^{1/2}x^{1/4}$ is a proportionality coefficient; β is the electronic specific heat; and x is the dimensionless specific volume.

As the target density, we take the density of the MIM insulator, since its thickness (10–20 μm) far exceeds that of the metal coating (0.1 μm).

(2) The initial temperature of a resulting plasmoid is

$$T_i = T_0\left(\frac{n_0}{n_1}\right)^{\gamma-1}, \qquad (2)$$

where $n_0 \le 10^{20}$ cm^{-3} is the concentration of heavy particles in the plasma, $n_1 \le 10^{23}$ cm^{-3} is the concentration of atoms of the shock-compressed matter, $\gamma = 4/3$ is the effective adiabatic exponent, and

$$T_0 = 0.1\frac{W}{1+\sqrt{\rho_2/\rho_3}}. \qquad (3)$$

(3) The plasmoid formation time is $t_0 = R_0/u$, where $u = \dfrac{W}{1+\sqrt{\rho_2/\rho_3}}$ is the expansion rate of the plasmoid boundary and $R_0 = 10R_2$ (R_2 is the characteristic size of the striker).

Consider the process of expansion of a plasma cloud. In the x and y directions, it expands much more slowly than in the z direction (Fig. 1). This is because one part of the plasmoid remains inside the capacitor, while the other is displaced outside and is free to expand under the action of gas-dynamic forces. Inside the capacitor, expansion conditions differ: the plasma cloud has an obstacle on its way, i.e., the capacitor plates. This part of the cloud can expand if the capacitor plates and the insulator evaporate when subjected to high temperatures.

1063-7842/01/4601-0107$21.00

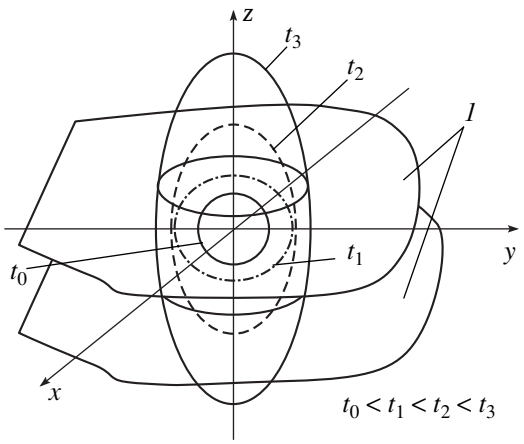

Fig. 1. Expansion of plasma cloud (*1*, capacitor plates).

The expansion rate of the plasma cloud depends on the velocity of a particle interacting with the cloud, the work of the external electric field, and the effect of high temperatures (random motion of particles). The ionic composition of the plasma is determined from the Saha equations. For dust particles of size $R_2 = 10^{-5}$–10^{-3} cm and $W = 20$–50 km/s, the parameters of plasmoids lie in the ranges $10^{-4} \le R_0 \le 10^{-2}$ cm, $n_0 \le 10^{20}$ cm^{-3}, and $1 \le T \le 3$ eV. If the plasma temperature is low, we can take into consideration only single ionization. Then, residual charges can be calculated without applying numeric techniques.

In our case, the problem is stated as follows. At a time instant $t = t_0$ let us have an equilibrium multicomponent (in general) plasma of density $n_0 = \sum_{k=1}^{k_{\max}} n_{0_k}$, radius R_0, and temperature T_0. Let also expansion and cooling obey the laws adopted in [8]. A set of equations that describes the ionization kinetics in an expanding plasmoid has the form [8]

$$\frac{dx_k}{dt} = (1-x_k)x_e\frac{ACt_0n(t)}{T^3(t)}\exp\left(-\frac{J_k}{T_0}\right) - \frac{x_kx_e^2n^2(t)At_0}{T^{9/2}(t)}, \tag{4}$$

$$n(t) = \frac{n_0}{t^3}, \quad T(t) = \frac{T_0}{t}, \quad x_e = \sum_{k=1}^{k_{\max}} C_kx_k, \quad (5)\text{–}(7)$$

where t is dimensionless time normalized by t_0; x_e and x_k are the ionizations of electrons and ions of the kth element, respectively; and C_k is the content of heavy particles of the kth sort:

$$C_k = \frac{n_k}{n_0} = \frac{n_{k0}}{n_0} = \text{const}, \quad \sum_{k=1}^{k_{\max}} C_k = 1.$$

The initial conditions are defined by the Saha equations. If, initially, $x_k \ll 1$, the solution to the Saha equations is given by [1]

$$x_{e0} = \left(\sum_{k=1}^{k_{\max}} C_k\mu_k\right)^{1/2}, \tag{8}$$

where

$$\mu = \frac{CT^{3/2}}{n_0}\exp\left(-\frac{J_k}{T_0}\right), \quad x_{k_0} = \frac{\mu_k}{x_{e0}}. \tag{9}$$

If ionization equilibrium breaks down at a time instant t_1 ($t_1 > t_0$), set (8)–(9) can be solved as follows. At $t_0 \le t \le t_1$, approximate values of the ionizations are determined from the Saha equations for $n = n(t)$ and $T = T(t)$. At $t > t_1$, the ionization rate is much smaller than the recombination rate (because of the strong exponential dependence) and can be neglected; hence, Eq. (4) can be written as

$$\frac{dx}{dt} = \frac{x_kx_e^2n^2(t)At_0}{T^{9/2}(t)}. \tag{10}$$

Multiplying the right and the left of (10) by C_k and taking the sum over subscript k in view of (7), we come to

$$\frac{dx_e}{dt} = -\frac{x_e^2At_0}{T^{9/2}}. \tag{11}$$

Integrating (11) yields the solution to the set of Eqs. (4)–(8) in the form

$$x_e(t) = r\left[1 + \left(\frac{r}{x_{e1}}\right)^2 - \sqrt{\frac{t_1}{t}}\right]^{-\frac{1}{2}}, \tag{12}$$

$$x(t) = r\frac{x_{k1}}{x_{e1}}\left[1 + \left(\frac{r}{x_{e1}}\right)^2 - \sqrt{\frac{t_1}{t}}\right]^{-\frac{1}{2}}, \tag{13}$$

where

$$r = \left(\frac{T_0^{9/2}t_1^{1/2}}{2At_0^{3/2}n_0^2}\right)^{1/2}.$$

The parameters x_{e1} and x_{k1} are the respective ionizations at $t = t_1$, which are determined from the Saha equations for $n_1 = n(t_1)$ and $T_1 = T(t_1)$.

To estimate t_1, we will take advantage of the expression

$$\frac{An_1^2x_e^2t_0}{T_1^{9/2}} = \frac{3}{2}(\gamma-1)\frac{J}{T_1}, \tag{14}$$

which is valid for a single-component plasma.

As follows from the Saha equation, for a single-component plasma, we have

$$x_{e1}^2 = \frac{CT_0^{9/2}}{n_0}\exp\left(-\frac{J}{T_0}\right). \quad (15)$$

If the form of Eq. (14) is retained for a multicomponent plasma, the potential J will be determined from the equality of the electron ionizations for both plasmas:

$$x_{e1}^2(J_k) = x_{e1}^2(J). \quad (16)$$

Substituting (8) and (14) into (16) yields the equation for the effective potential J:

$$\sum_{k=1}^{k_{\max}} C_k \exp\left(-\frac{J_k}{T_1}\right) = \exp\left(-\frac{J}{T_1}\right). \quad (17)$$

The dependences $t_1 = t_1(n_0, T_0, t_0, C_k, J_k)$ and $J = J(n_0, T_0, t_0, C_k, J_k)$ are found by jointly solving (14), (15), and (17). The asymptotic values of the ionizations can be determined from (12) and (13) at $t \longrightarrow \infty$:

$$x_{e\infty} = \frac{r}{[1 + (r/x_{el})^2]^{1/2}}, \quad (18)$$

$$x_{k\infty} = \frac{x_{k1}}{x_{e1}} x_{e\infty}. \quad (19)$$

Here, we put $x_{e\infty} \approx r$, since $(r/x_{el})^2 \ll 1$. With regard for (18) and (19), the formulas for residual charges are written as

$$Q_e = \frac{4}{3}\pi R_0^3 n_0 x_{e\infty}, \quad (20)$$

$$Q_k = \frac{4}{3}\pi R_0^3 n_0 C_k x_{k\infty}; \quad Q_e = \sum_{k=1}^{k_{\max}} Q_k. \quad (21)$$

These expressions describe the approximate model for inertial expansion of a plasmoid subjected to gasdynamic forces.

In terms of this model, one can also solve the problem of plasma heating by current. An increase in the plasma temperature due to current (Joule) heating must be taken into account in tackling the problem of kinetic expansion of a plasma cloud.

The plasma conductivity is known to be the sum of the electronic and ionic components [9]:

$$\sigma - \sigma_e + \sigma_i = e(n_e\mu_e + n_i\mu_i), \quad (22)$$

where σ_e and σ_i are the electronic and ionic conductivities, respectively, and μ_e and μ_i are the mobilities of electrons and ions, respectively.

The electronic component of the conductivity is responsible for current heating of a plasma. The electric field raises the kinetic energy of charged particles (electrons and ions); in this case, ions of weight $m_i > m_e$ can be considered immobile. A plasma can be considered as a mixture of electronic and ionic liquids. The friction force between these liquids increases the plasma temperature. The rate of heating of electrons due to the friction force is determined from the expression [9]

$$\frac{3}{2}n_e\frac{dT}{dt} = \sigma_e E. \quad (23)$$

The temperature of the ionic liquid increases $\sqrt{m_i/m_e}$ times more slowly because of the difference between the heat conductivities of the electronic and ionic liquids.

The total plasma temperature is the sum of the two components:

$$T_\Sigma = T + \tilde{T}, \quad (24)$$

where T is the temperature of an expanding plasmoid [expression (6)] and $\tilde{T}$ is the temperature increment due to Joule heating [this increment is found from Eq. (23)].

Since the plasma conductivity is initially relatively high, the external electric field penetrates into the plasma to a small depth. The penetration depth can be estimated from the formula [10]

$$E(y) = E_0\exp\left(-\frac{y}{r_D}\right), \quad (25)$$

where E_0 is the external electric field strength; $E(y)$ is the field strength inside the plasma at a depth y;

$$r_D = \sqrt{\frac{T_i + T_e}{8\pi n e^2}}$$

is the Debye screening radius; T_e and T_i are the temperatures of the electronic and ionic liquids, respectively; and n is the equilibrium concentration of particles.

The model can be simplified if we assume that the electric field does not affect ionization and recombination processes at the initial time instant. Only after a lapse of time, when the plasma conductivity drops, does the external field penetrate into the plasma to a noticeable depth, accelerate charged particles, and heat up the plasma.

To derive an expression for charge variation in time, it is first necessary to find the current passing through the broken-down capacitor. According to [6], the equation for current variation in MIM structures has the form

$$I(t) = \frac{U(t)}{d^2}\int_V \sigma dV, \quad (26)$$

where $U(t)$ is the external field voltage, d is the insulator thickness, σ is the MIM conductivity, and V is the volume of the conductive channel in the broken-down capacitor.

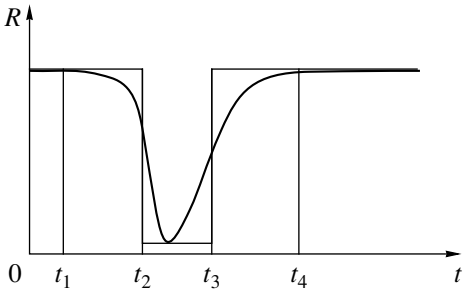

Fig. 2. Approximation of MIM channel resistance variation.

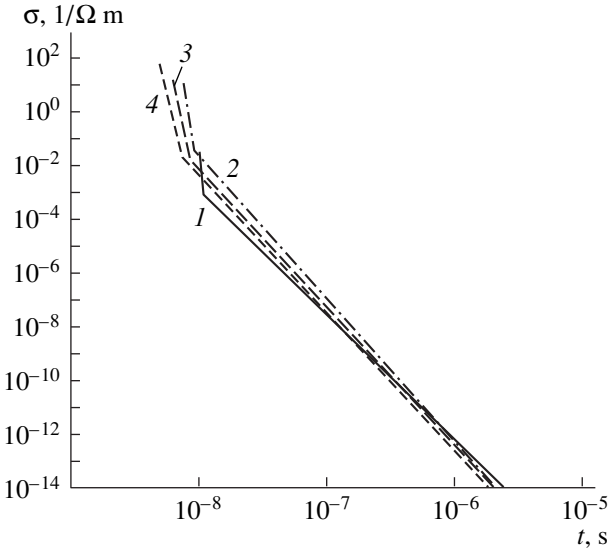

Fig. 3. Conductivity vs. time at particle velocities of (*1*) 10, (*2*) 15, (*3*) 20, and (*4*) 30 km/s. U_0 = 200 V.

Now we will find the variation of the voltage across the MIM structure when the capacitor discharges through the resulting high-conductivity channel (plasma). The differential equation for capacitor discharge has the form

$$U_C + \frac{dU_C}{dt} R_p C = 0, \tag{27}$$

where U_C is the voltage across the capacitor, R_p is the plasma resistance, and C is the capacitance of the capacitor (we put $C \approx 1$).

The plasma resistance is given by

$$R_p = \frac{1}{\sigma}\frac{d}{S}, \tag{28}$$

where $\sigma = en(t)\mu(t)$ is the plasma conductivity; $n(t)$ and $\mu(t)$ are the concentration and mobility of charged particles, respectively (these parameters vary according to the above kinetic laws for plasma expansion); d is the insulator thickness; and S is the cross-section area of the conductive channel ($S \approx 4\pi R_0^2$, where R_0 is the radius of the channel produced by a particle).

To simplify the calculations, we approximate the variation of the plasma conductivity by a step function (Fig. 2). The solution to differential equation (27) is then straightforward. The voltage drop across the capacitor short-circuited by the plasma is given by

$$\ln\left[\frac{U_C(t)}{U_0}\right] = \int_{t_1}^{t_2} \frac{-1}{R_1 C} dt + \int_{t_2}^{t_3} \frac{-1}{R_2 C} dt + \int_{t_3}^{t_4} \frac{-1}{R_1 C} dt, \tag{29}$$

where U_0 is the dc voltage applied to the capacitor, U_0 = 50–100 V; C is the MIM capacitance; R_i are the plasma resistances after the approximation; t_1 is the time instant thermal equilibrium breaks down; t_4 is the time of plasma "quenching;" and t_3–t_2 is the mean step width (Fig. 2).

Thus, in calculating the temperature increment (due to Joule heating), current, and charge of the plasma, one should take into account the process of capacitor (MIM structure) discharge. In view of (29), the discharge volt-

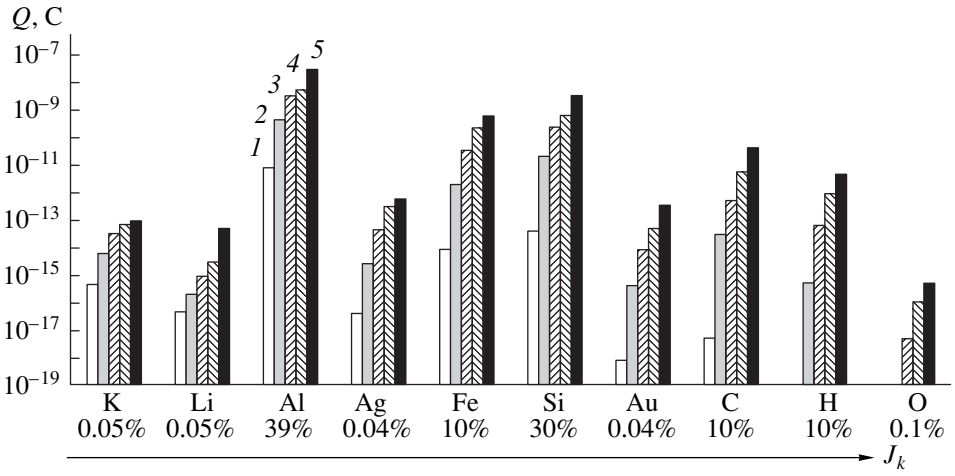

Fig. 4. Charge spectra of various elements for particle velocities of (1) 10, (*2*) 15, (*3*) 20, (*4*) 25, and (*5*) 30 km/s. U_0 = 200 V.

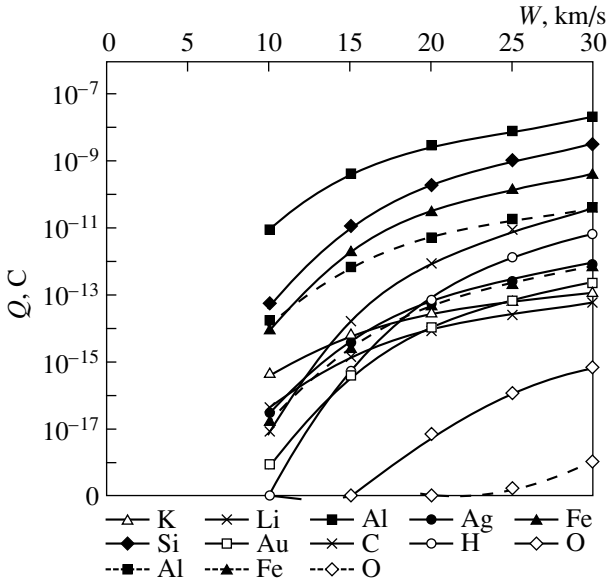

Fig. 5. Integral charges vs. particle velocity at $0 < U_0 < 1$ V.

age of the capacitor during plasma expansion is expressed as

$$\Delta U = U_0 - U(t). \tag{30}$$

It is evident from (29) that the process of capacitor discharge is controlled by the parameters of a plasma produced by the interaction of an energetic particle with the target. For voltages between 10 and 50 V, the capacitor field affects the parameters of an impact-produced plasma only slightly. The MIM structure may even break down near the conductive channel.

As the capacitance decreases, the discharge duration becomes comparable to that of plasma expansion between the capacitor plates and the effect of the discharge on the plasma characteristics grows.

The charge accumulated in the capacitor is found from the well-known formula [9]

$$Q = \int_{t_0}^{t_3} I(t)dt, \tag{31}$$

where $I(t)$ is determined from (26).

The charge of either component of the plasma is determined in a similar way. The integral charge of the plasma differs from that given by (31) by 50–70% for particle velocities between 10 and 15 km/s and 20–30% for velocities between 20 and 30 km/s, because the ionization potentials of the elements J_k are replaced by the effective potential J.

Qualitatively, the obtained results agree with available experimental data [6, 11, 12]. For practical purposes, we developed a simple model that describes processes initiated in an MIM structure by a high-velocity impact. The model data are shown in Figs. 3–5. Figure 3 depicts the time dependence of the MIM conductivity, Fig. 4 represents the charge spectra for particle velocities in the range of 10–30 km/s, and Fig. 5 shows the integral charge vs. velocity throughout the process (from the beginning to quenching).

Thus, we showed that detection of the MIM integral charge from the beginning of the interaction up to plasma quenching may improve the sensitivity of the ionization method by more than one order of magnitude and thereby find the physical parameters and elemental composition of low-energy micrometeoroids.

This model is useful in designing particle detectors, measuring physicochemical parameters of micrometeoroid and technogenic particles, and processing ion spectra.

REFERENCES

1. *Dust in the Atmosphere and Near-Earth Space: Proceedings of Scientific Congresses and Conferences* (Nauka, Moscow, 1973).
2. V. B. Leonas and Yu. G. Malama, Preprint No. Pr-885, IKI AN SSSR (Institute for Space Research, Academy of Sciences of USSR, Moscow, 1984).
3. R. Z. Sagdeev, J. Kissel, J.-L. Bertaux, *et al.*, Pis'ma Astron. Zh. **12** (8), 605 (1986) [Sov. Astron. Lett. **12**, 254 (1986)].
4. N. D. Semkin, K. E. Voronov, and S. V. Rotov, Izmer. Tekh., No. 8, 3 (1999).
5. G. I. Kanel', S. V. Razorenov, A. V. Utkin, and V. E. Fortov, *Impact–Wave Phenomena in Condensed Media* (Yanus-K, Moscow, 1996).
6. N. D. Semkin and K. E. Voronkov, Zh. Tekh. Fiz. **68** (8), 63 (1998) [Tech. Phys. **43**, 934 (1998)].
7. V. K. Grishin, N. D. Semkin, and G. Ya. Yusupov, in *Processing and Mapping Information Methods in Wireless Devices* (Kuĭbyshevsk. Aérokosm. Inst., Kuĭbyshev, 1985).
8. Ya. B. Zel'dovich and Yu. P. Raizer, *Physics of Shock Waves and High-Temperature Hydrodynamic Phenomena* (Fizmatgiz, Moscow, 1966, 2nd ed.; Academic, New York, 1966).
9. R. V. Telesnin and V. F. Yakovlev, *Course of Physics* (Prosveshchenie, Moscow, 1970).
10. V. N. Oraevskiĭ, *Plasma on the Earth and in Space* (Naukova Dumka, Kiev, 1974).
11. N. D. Semkin, K. E. Voronov, and V. N. Kondrashov, Preprint No. 0040-A, TRINITI (TsNIIAtomInform, Moscow, 1998).
12. L. S. Novikov, N. D. Semkin, and V. A. Kulikauskas, Fiz. Khim. Obrab. Mater., No. 6, 49 (1989).

Translated by V. Isaakyan

Technical Physics, Vol. 46, No. 1, 2001, pp. 112–116. Translated from Zhurnal Tekhnicheskoĭ Fiziki, Vol. 71, No. 1, 2001, pp. 117–121.

Simulation of a Multilayer Planar Capacitor

O. G. Vendik and M. A. Nikol'skiĭ

St. Petersburg State University of Electrical Engineering, St. Petersburg, 197376 Russia

Received April 27, 2000

Abstract—A model of a ferroelectric planar capacitor containing a thin linear insulator under the electrodes is developed. This structure is shown to reduce microwave losses in the capacitor without significantly decreasing the controllability of its properties. In the framework of the model, the size of the charge spreading region on the electrodes is estimated. *© 2001 MAIK "Nauka/Interperiodica".*

INTRODUCTION

Strong interest has recently arisen in ferroelectrics as promising materials for controllable microwave devices [1–4]. The use of ferroelectrics in this field relies on planar technology, the basic design components being a planar capacitor and a coplanar or a slot transmission line [5]. A planar capacitor, whose capacitance varies with an external electric field, is of particular interest. The use of these components necessitates the development of mathematical models that can be employed as the basis for computer-aided design (CAD) of ferroelectric microwave devices.

A conventional planar capacitor consists of an insulating substrate, a ferroelectric layer, and planar electrodes (metallic or superconducting). Its capacitance can be calculated by the well-established methods of conformal mapping and partial capacitances [6–11]. This paper addresses a planar capacitor containing an additional insulating layer under the electrodes.

The advantages of the planar structure with the additional underelectrode layer are the following.

(1) This layer provides better protection of the ferroelectric film from electric breakdown.

(2) This layer separates the ferroelectric film from the conducting electrodes, which prevents the injection of charge carriers from the electrodes to the ferroelectric and provides a more uniform electric field distribution in the ferroelectric film. The uniform electric field minimizes microwave losses due to electrostriction conversion of the microwave field into acoustic vibration, which occurs in the presence of a nonuniform field [12, 13].

(3) In the presence of the underelectrode layer, the evaporation of the conducting electrodes and their subsequent etching in order to form the capacitor gap do not proceed directly on the ferroelectric surface.

(4) An underelectrode layer made from a linear insulator similar to the substrate material lowers the mechanical stress in the ferroelectric film and, as a consequence, reduces microwave losses in the multilayer planar capacitor.

On the other hand, the presence of this layer makes calculation of the capacitance of such a capacitor more difficult. It becomes necessary to invoke cumbersome numerical methods, which can hardly be used in CAD. The goal of this paper is to derive an analytical expression for the capacitance of a planar structure containing an underelectrode insulator. It will be shown that the low-permittivity underelectrode layer does not significantly decrease the capacitance of the planar capacitor.

APPLICATION OF THE CONFORMAL MAPPING METHOD TO THE STANDARD PLANAR CAPACITOR

The electric field distribution in a planar capacitor is nonuniform. The capacitance is usually calculated by the conformal mapping method, which transforms the field in a planar structure into the field in a usual plane capacitor.

Consider the planar capacitor illustrated in Fig. 1. Let $h_d = 0$ (i.e., there is no underelectrode insulator) and

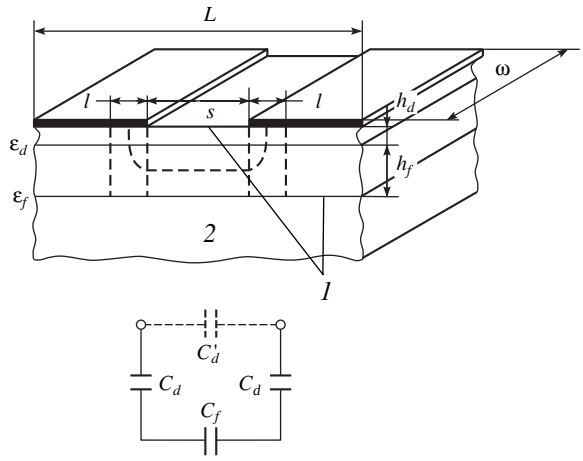

Fig. 1. Planar ferroelectric capacitor with a thin linear dielectric underelectrode layer and its equivalent circuit: (*1*) magnetic wall and (*2*) substrate.

1063-7842/01/4601-0112$21.00

the ferroelectric–substrate and ferroelectric–air interfaces act as "magnetic walls." The capacitance of such a capacitor (a ferroelectric film with the electrodes on its surface) can be represented as [8–11]

$$C_f = \frac{\varepsilon_0 \varepsilon_f w}{s/h_f + (4/\pi)\ln 2}. \quad (1)$$

A MODEL OF A CAPACITOR WITH AN ANISOTROPIC INSULATOR

We will use the formula for capacitance of a planar capacitor with an anisotropic dielectric layer [9, 11]. Then, expression (1) is recast as

$$C_f = \varepsilon_0 \frac{w\varepsilon_s}{s/(h_f + h_d) + (4/\pi)\ln 2\sqrt{\varepsilon_s/\varepsilon_h}}. \quad (2)$$

Refer to Fig. 1 (at $h_d = 0$). Let ε_s and ε_h be the effective permittivities of a film composed of two layers with the parameters h_d, ε_d and h_f, ε_f for the field components parallel and perpendicular to the interfaces, respectively. We assume that

$$\varepsilon_d \ll \varepsilon_f, \quad h_d \ll h_f. \quad (3)$$

Then, for the field components parallel to the interfaces (film), the layers can be considered as capacitors connected in parallel:

$$\begin{aligned} \varepsilon_s(h_d + h_f) &= \varepsilon_f h_f + \varepsilon_d h_d, \\ \varepsilon_s &= \varepsilon_f \frac{h_f}{h_d + h_f} + \varepsilon_d \frac{h_d}{h_d + h_f}. \end{aligned} \quad (4)$$

In view of inequalities (3), one can write

$$\varepsilon_s = \varepsilon_f. \quad (5)$$

For the field components perpendicular to the interfaces (across the film), the layers can be considered as capacitors connected in series:

$$\begin{aligned} \frac{h_f + h_d}{\varepsilon_h} &= \frac{h_d}{\varepsilon_d} + \frac{h_f}{\varepsilon_f}, \\ \frac{1}{\varepsilon_h} &= \frac{h_d}{h_d + h_f}\frac{1}{\varepsilon_d} + \frac{h_f}{h_d + h_f}\frac{1}{\varepsilon_f}. \end{aligned} \quad (6)$$

From (4) and (5), we obtain

$$\frac{\varepsilon_s}{\varepsilon_h} = 1 + \frac{h_f h_d}{(h_f + h_d)^2}\left(\frac{\varepsilon_f}{\varepsilon_d} + \frac{\varepsilon_d}{\varepsilon_f} - 2\right). \quad (7)$$

With (3), we come to the simplified formula

$$\frac{\varepsilon_s}{\varepsilon_h} = 1 + \frac{h_d \varepsilon_f}{h_f \varepsilon_d}. \quad (8)$$

MODEL DESCRIPTION OF THE MULTILAYER PLANAR CAPACITOR

Refer to Fig. 1 again. Assume that the ferroelectric–substrate and air–insulator interfaces act as magnetic walls; i.e., the normal electric field components vanish at these interfaces. Then, we can consider our capacitor as consisting of the underelectrode dielectric layer and the ferroelectric layer. The equivalent circuit of the capacitor represents series-connected capacitances due to the dielectric layer, C_d, and the capacitance due to the ferroelectric layer, C_f (Fig. 1). The interelectrode capacitance

$$C_d \approx \frac{\varepsilon_0 \varepsilon_d w h_d}{s}$$

(Fig. 1) can be neglected, because it is much smaller than C_f (no more than 2% of the total capacitance of the capacitor). The relationship between C_d and C_f in Fig. 1 becomes clear from the Christoffel–Schwartz transform (Fig. 2). The substrate shown in Fig. 1 is but an element of the structure.

If $\varepsilon_d \ll \varepsilon_f$, the capacitance of a two-layer capacitor cannot be found by the partial capacitance method. It can be calculated by the numerical method developed in [14]; however, this method requires much machine time.

Now the above relationships will be used to derive an approximate formula for the capacitance of the two-layer capacitor. In this case, the adjustment coefficient can be found by contrasting this approximate formula

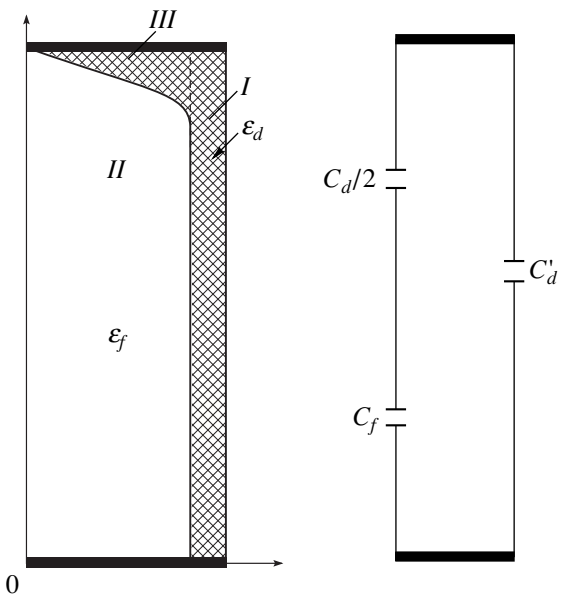

Fig. 2. Representation of the two-layer planar capacitor in the form of a plane capacitor through the Christoffel–Schwartz transform: region *I* is represented by capacitor C'_d; region *II*, by C_f; and region *III*, by $C_d/2$. In Fig. 1, the last region is shown as series-connected capacitors C_d formed by the ferroelectric layer and the electrodes.

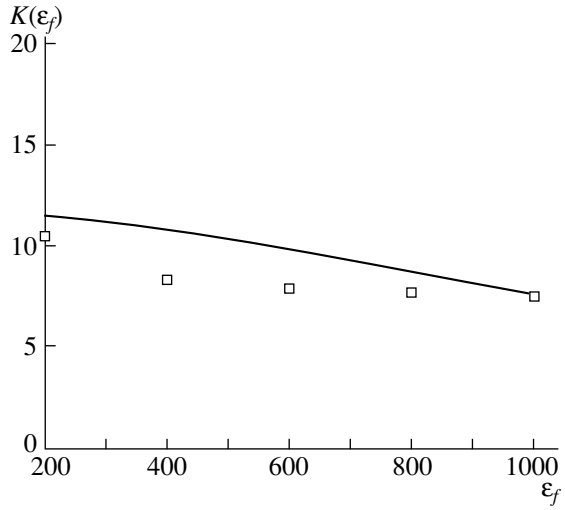

Fig. 3. Fitting coefficient K versus the permittivity of the ferroelectric layer. Squares, formula (10); solid line, formula (14) for a capacitor with $s = 4$ μm, $h_d = 0.05$ μm, $h_f = 0.7$ μm, $w = 0.29$ mm, $L = 1150$ μm, and $H_s = 500$ μm.

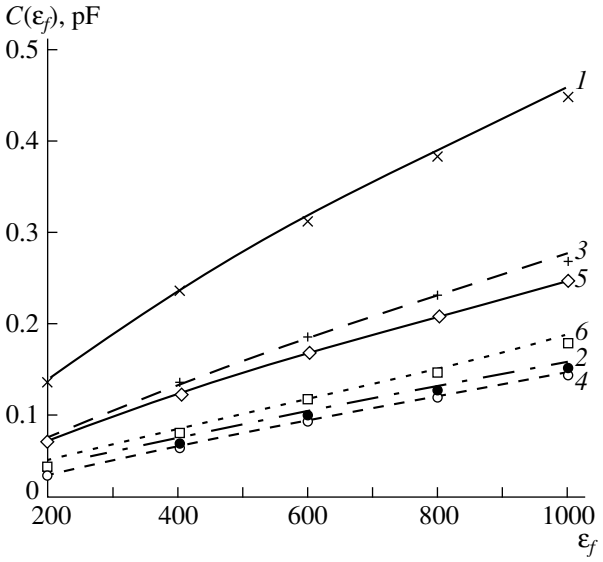

Fig. 4. $C(\varepsilon_f)$ curves showing agreement between the numerical simulation [formula (10)] and analytical expression (14) for the capacitor geometries listed in Table 2.

with exact calculations [14]. Substituting (5) and (8) into (2) yields the expression for the total capacitance of the ferroelectric and dielectric layers:

$$C_{fd} = \varepsilon_0\varepsilon_f w\left(\frac{s}{h_f} + \frac{4}{\pi}\ln 2\sqrt{1 + K\frac{\varepsilon_f}{\varepsilon_d}\frac{h_d}{h_f}}\right)^{-1}, \qquad (9)$$

where K is the adjustment coefficient, which accounts for the fact that the film anisotropy is due to only one pair (and not many pairs) of layers.

In other words, the field does not penetrate the layer throughout its thickness h_f; therefore, in this case, the effective thickness of the layer $h_{f\text{eff}} < h_f$ and $K > 1$.

DETERMINING THE ADJUSTMENT COEFFICIENT K

From (9), the coefficient K can be expressed as

$$K(\varepsilon_f, s, h_f, h_d) = \frac{h_f}{h_d}\frac{\varepsilon_d}{\varepsilon_f} \times\left[\left(\frac{\varepsilon_0 w\varepsilon_f}{C(\varepsilon_f)} - \frac{s}{h_f}\right)^2\left(\frac{\pi}{4\ln 2}\right)^2 - 1\right]. \qquad (10)$$

Thus, the adjustment coefficient of the model depends on the dimensions of the planar capacitor and the permittivities of the ferroelectric and underelectrode dielectric layers. In expression (10), $C(\varepsilon_f)$ is the total capacitance of the ferroelectric and underelectrode dielectric layers that was calculated by the numerical method [14]. Introduce the notation

$$S = \frac{s}{h_f}, \quad H = \frac{h_d}{h_f}. \qquad (11)$$

An analytical expression that relates the adjustment coefficient K to the dimensions of the capacitor and the permittivities of the ferroelectric and underelectrode dielectric layers can be written as follows:

$$K(S, H, \varepsilon_f) = A(\varepsilon_f) + B(\varepsilon_f)S + C(\varepsilon_f)H + D(\varepsilon_f)SH. \qquad (12)$$

Write the coefficient A in (12) in the form

$$A(\varepsilon_f) = A_1\frac{\varepsilon_d}{\varepsilon_f} + A_2 + A_3\frac{\varepsilon_f}{\varepsilon_d}. \qquad (13)$$

Using similar representations for $B(\varepsilon_f)$, $C(\varepsilon_f)$, and $D(\varepsilon_f)$, we obtain

$$K(S, H, \varepsilon_f) = (A_1 + B_1S + C_1H + D_1SH)\frac{\varepsilon_d}{\varepsilon_f} + A_2 + B_2S + C_2H + D_2SH + (A_3 + B_3S + C_3H + D_3SH)\frac{\varepsilon_f}{\varepsilon_d}. \qquad (14)$$

The coefficients A_i, B_i, C_i, and D_i (Table 1) in expression (14) were calculated by minimizing the discrepancy between the values of K obtained from (10) and from (14) for various geometries of the planar capacitor and various permittivities of the ferroelectric. Figure 3 shows K calculated from formulas (10) and (14) for a capacitor with a specified geometry. The values of K obtained numerically and analytically are in good agreement. The analytical expression can be used when $0 < H < 0.1$, $1 < S < 10$, and $\varepsilon_f/\varepsilon_d < 100$, as follows from in-depth examination.

Figure 4 shows the capacitance of the two-layer capacitor versus the ferroelectric permittivity dependences obtained numerically (symbols) and analytically (curves). The rms deviation between the analytical and numerical data is 2 to 4.5% for various geometries of the planar capacitor (Table 2).

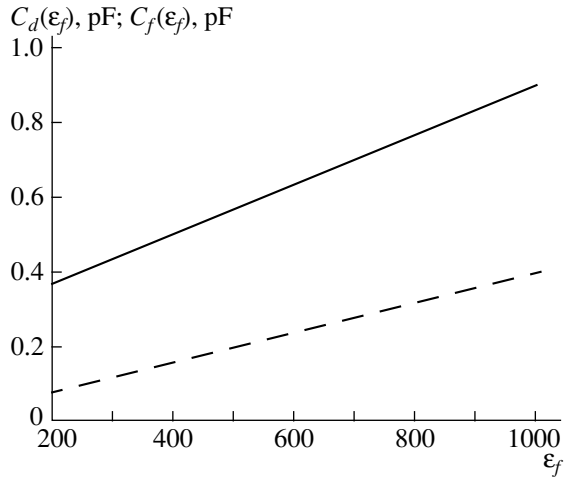

Fig. 5. Capacitances of the underelectrode dielectric layer C_d (17) and ferroelectric layer C_f (1) versus ferroelectric permittivity at s = 4 μm, h_d = 0.05 μm, h_f = 0.7 μm, w = 0.29 mm, L = 1150 μm, and H_s = 500 μm.

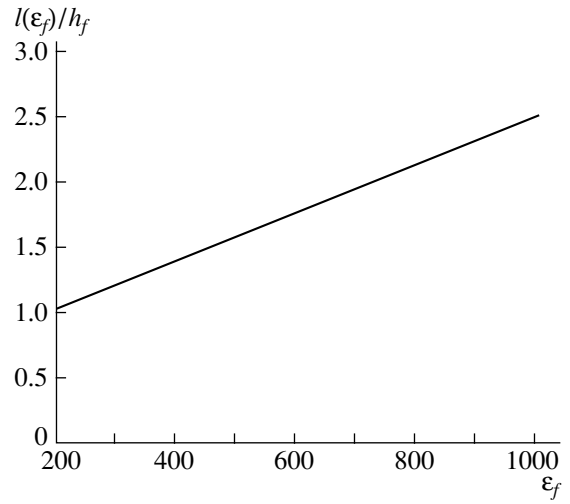

Fig. 6. Relative extension of the charge spreading region l (Fig. 1) on the capacitor electrodes [formula (18)] versus ferroelectric permittivity at s = 4 μm, h_d = 0.05 μm, h_f = 0.7 μm, w = 0.29 mm, L = 1150 μm, and H_s = 500 μm.

EFFECTIVE CAPACITANCE OF THE UNDERELECTRODE DIELECTRIC LAYER. DIMENSION OF THE CHARGE SPREADING REGION

Estimates given below may help to illuminate the performance of the planar capacitor and its controllability. Let C_f (Fig. 1, equivalent circuit) be determined by formula (1). Then, (9) can be used to obtain an expression for the capacitance C_d. From the geometry in Fig. 1,

$$C_d = \frac{\varepsilon_0 \varepsilon_d w l}{h_d}, \tag{15}$$

where l is the dimension of the charge spreading region.

From the equivalent circuit in Fig. 1, we have

$$\frac{1}{C_{fd}} = \frac{1}{C_f} + \frac{2}{C_d}, \tag{16}$$

where C_{fd} is defined by expression (9) and C_f, by (1).

Then, C_d can be found from the formula

$$C_d = \frac{\pi}{2\ln 2} \frac{\varepsilon_0 \varepsilon_f w}{\sqrt{1 + K(S, H, \varepsilon_f)\dfrac{h_d \varepsilon_f}{h_f \varepsilon_d}} - 1}. \tag{17}$$

As can be seen from Fig. 5, $C_d > C_f$ and grows with increasing permittivity of the ferroelectric layer. Hence, the additional underelectrode linear insulator cannot significantly deteriorate the controllability of the planar capacitor. From (15) and (17), the size of the charge spreading region l is given by

$$l(S, H, \varepsilon_f) = h_f \frac{\dfrac{\pi}{2\ln 2}}{\dfrac{\varepsilon_d h_f}{\varepsilon_f h_d}\left[\sqrt{1 + K(S, H, \varepsilon_f)\dfrac{h_d \varepsilon_f}{h_f \varepsilon_d}} - 1\right]}. \tag{18}$$

As follows from Fig. 6, the charge spreading region l of the two-layer capacitor (Fig. 1) can not only exceed the thickness of the ferroelectric layer, but can also, under certain conditions, be comparable to the gap of the capacitor. Hence, the length of the capacitor must satisfy the condition $L > s + 2l$.

Table 1. Coefficients of analytical expression (14)

i	A_i	B_i	C_i	D_i
1	−6.679	−2.193	0.024	0.143
2	6.64	2.216	−0.02	−0.144
3	0.039	−0.023	-3.645×10^{-3}	1.548×10^{-3}

Table 2

Curve no. in Fig. 4	ε_d	s, μm	h_d, μm	h_f, μm
1	10	2	0.02	1.1
2	10	11	0.11	1.1
3	10	2	0.02	0.5
4	10	5	0.05	0.5
5	10	4	0.06	0.9
6	10	6	0.04	0.7

CONCLUSION

Analytical expressions for the capacitance of a planar structure containing a layer of underelectrode insulator are obtained. These formulas can be used in CAD of a two-layer planar capacitor. The analytical method suggested can be used not only for estimating the contribution of the additional underelectrode layer to the capacitance of the planar capacitor, but also for numerically determining the size of the charge spreading region on its electrodes.

REFERENCES

1. O. G. Vendik, L. T. Ter-Martirosyan, A. I. Dedyk, *et al.*, Ferroelectrics **144** (1–4), 33 (1993).
2. O. G. Vendik, I. G. Mironenko, and L. T. Ter-Martirosyan, Microwaves & RF **33** (7), 67 (1994).
3. S. S. Gevorgian, D. I. Kaparkov, and O. G. Vendik, Proc. IEE (London) **30**, 1236 (1994).
4. A. T. Findikoglu, Q. X. Jia, I. H. Campbell, *et al.*, Appl. Phys. Lett. **66**, 3674 (1995).
5. *Ferroelectrics in Microwave Technology*, Ed. by O. G. Vendik (Sov. Radio, Moscow, 1979).
6. É. S. Kochanov, Radiotekhnika **22** (7), 82 (1967).
7. É. S. Kochanov, Radiotekhnika **30** (1), 92 (1975).
8. K. C. Gupta, R. Gardj, and R. Chadha, *Computer-Aided Design of Microwave Circuits* (Artech House, Dedham, 1981; Radio i Svyaz', Moscow, 1987).
9. V. I. Lavrik and V. N. Savel'ev, *Conformal Mapping: A Handbook* (Naukova Dumka, Kiev, 1970).
10. K. R. Hoffman, *Handbook of Microwave Integrated Circuits* (Artech House, Norwood, 1987).
11. O. G. Vendik, S. P. Zubko, and M. A. Nikol'skiĭ, Zh. Tekh. Fiz. **69** (4), 1 (1999) [Tech. Phys. **44**, 349 (1999)].
12. O. G. Vendik and L. T. Ter-Martirosyan, Zh. Tekh. Fiz. **69** (8), 93 (1999) [Tech. Phys. **44**, 954 (1999)].
13. O. G. Vendik and A. N. Rogachev, Pis'ma Zh. Tekh. Fiz. **25** (17), 62 (1999) [Tech. Phys. Lett. **25**, 702 (1999)].
14. A. N. Deleniv, Zh. Tekh. Fiz. **69** (4), 8 (1999) [Tech. Phys. **44**, 356 (1999)].

Translated by A. Khzmalyan

Technical Physics, Vol. 46, No. 1, 2001, pp. 117–118. Translated from Zhurnal Tekhnicheskoĭ Fiziki, Vol. 71, No. 1, 2001, pp. 122–124.

BRIEF COMMUNICATIONS

Motion Invariants for a Charge in a Linearly Polarized Wave Field

V. N. Komarov

Saratov State University, ul. Universitetskaya 42, Saratov, 410601 Russia

Received December 8, 1998; in final form, March 22, 2000

Abstract—Six motion integrals for a relativistic charge in the field of a transverse linearly polarized electromagnetic wave propagating with an arbitrary phase velocity $u > c$ were obtained by solving the canonical equations of motion. On the basis of these integrals, the charge trajectory as a function of the wave phase is analyzed in a fixed coordinate system. The coordinates, time, and phase are related by elliptic functions. © *2001 MAIK "Nauka/Interperiodica".*

The charge motion in the field of a linearly polarized wave propagating with the phase velocity $u = c$ is well studied for a reference frame where the charge is, on average, at rest [1, 2]. This motion can be described by the motion invariants, which are known for this case [3]. In a collisionless plasma, $u > c$ and the generalization of the invariants to this case is of considerable interest. We assume that a linearly polarized wave is described by a vector potential directed along the X axis:

$$A_x = -\frac{cE}{\omega}\sin\xi, \quad \xi = \omega t - kz. \tag{1}$$

The Hamiltonian for a relativistic charge in an electromagnetic field has the form [4]

$$\varepsilon = \sqrt{m^2c^4 + c^2\left(\bar{P} - \frac{e}{c}\bar{A}(\xi)\right)^2}, \quad \bar{P} = \bar{p} + \frac{e}{c}\bar{A}, \tag{2}$$

hence, the following system of canonical equations:

$$\frac{dx}{dt} = \frac{c^2 p_x}{\varepsilon}, \quad \frac{dy}{dt} = \frac{c^2 p_y}{\varepsilon}, \quad \frac{dz}{dt} = \frac{c^2 p_z}{\varepsilon}, \tag{3}$$

$$\frac{dp_x}{dt} = eE\left(1 - V_z\frac{k}{\omega}\right)\cos\xi,$$
$$\frac{dp_y}{dt} = 0, \quad \frac{dp_z}{dt} = eE\frac{k}{\omega}V_x\cos\xi. \tag{4}$$

(1) Integrating the first and second equations in (4), we get

$$p_x - \frac{eE}{\omega}\sin\xi = \Psi_1, \quad p_y = \Psi_2. \tag{5}$$

We multiply the first equation in (4) by the velocity $V_x = dx/dt$ from (3) and, after invoking the other equations in (4) and integrating, obtain

$$\varepsilon - up_z = \Psi_3. \tag{6}$$

These integrals are well known [5, 6].

(2) We express the longitudinal momentum from the integral Ψ_3:

$$p_z = \frac{-u\Psi_3 + \sqrt{c^2\Psi_3^2 + (u^2 - c^2)(m^2c^4 + c^2 p_\perp^2(\xi))}}{u^2 - c^2}, \tag{7}$$
$$p_\perp^2 = p_x^2 + p_y^2.$$

The plus sign before the root is chosen to provide the correct value for $u \longrightarrow c$. Substitute the derivative dp_z/dt, with $p_\perp^2(\xi)$ expressed in terms of the integrals Ψ_1 and Ψ_2, into the third equation of (4). After integration,

$$\int_0^\xi \frac{c^2(\Psi_1 + (eE/\omega)\sin\xi)d\xi}{\sqrt{c^3\Psi_3^2 + (u^2 - c^2)[m^2c^4 + c^2\Psi_2^2 + c^2(\Psi_1 + (eE/\omega)\sin\xi)^2]}} = kx + \Psi_4. \tag{8}$$

The integral Ψ_3 and the energy ε are related as $\varepsilon = \Psi_3/(1 - uV_z/c^2)$. From the second equation in (3), it follows that $\varepsilon = p_y c^2/V_y$. Equating the energies and integrating, we come to

$$y\Psi_3 = \Psi_2 c^2\left(t - u\frac{z}{c^2}\right) + \Psi_5. \tag{9}$$

1063-7842/01/4601-0117$21.00

From the definition of phase, $d\xi/\omega dt = 1 - p_z c^2/u\varepsilon$ or $d\xi/\omega(1 - p_z c^2/u\varepsilon) = dt$. Insert the energy $\varepsilon = \Psi_3 = up_z$ into the left-hand side and express, as before, p_z through the transverse momentum $p_\perp(\xi)$; then,

$$\int_0^\xi \frac{u}{\omega(u^2 - c^2)}\left(u - \frac{c^2\Psi_2}{\sqrt{c^2\Psi_3^2 + (u^2 - c^2)[m^2c^4 + c^2\Psi_2^2 + c^2(\Psi_1 + (eE/\omega)\sin\xi)^2]}}\right)d\xi = t + \Psi_6. \quad (10)$$

(3) The invariants Ψ_4 and Ψ_6 involve elliptic integrals. With certain substitutions [7], the left-hand side of (8) can be expressed in terms of arcsines and elliptic integrals of the first and third kinds. The form of the integral Ψ_4 implies that the X component of the charge momentum is the sum of the constant component due to the invariant Ψ_1 and oscillations induced by the variable field. Note that an increase in the oscillation amplitude slows down with increasing wave field strength. The more the phase velocity differs from the velocity of light in a vacuum, the less the change in both the oscillation amplitude and the X coordinate.

In the limit $u = c$, Ψ_5 involves the quantity ξ/ω, which is proportional to the wave phase [3]. In this expression, the term with the longitudinal coordinate z specifies the delay. For $u \neq c$, this term cannot be considered as delay, since this parameter should be inversely proportional to the phase velocity u of the wave. The invariant Ψ_6 involves the elliptic integral of the first kind and makes it possible to relate the phase and time. Expression (7) shows that the longitudinal momentum has, in general, a constant component and oscillations with the frequencies ω and 2ω. Which of them prevails depends on the ratio between the initial momentum Ψ_1 and the quantity eE/ω. For large momenta Ψ_1, the influence of the electric component of the field on the velocity V_x is small, the variable magnetic field alone contributes to the variable component of p_z, and the frequency ω prevails. For small momenta Ψ_1, an additional effect is exerted by the electric component, changing the velocity involved in the Lorentz force, and the amplitude of the component with the frequency 2ω increases in the spectrum.

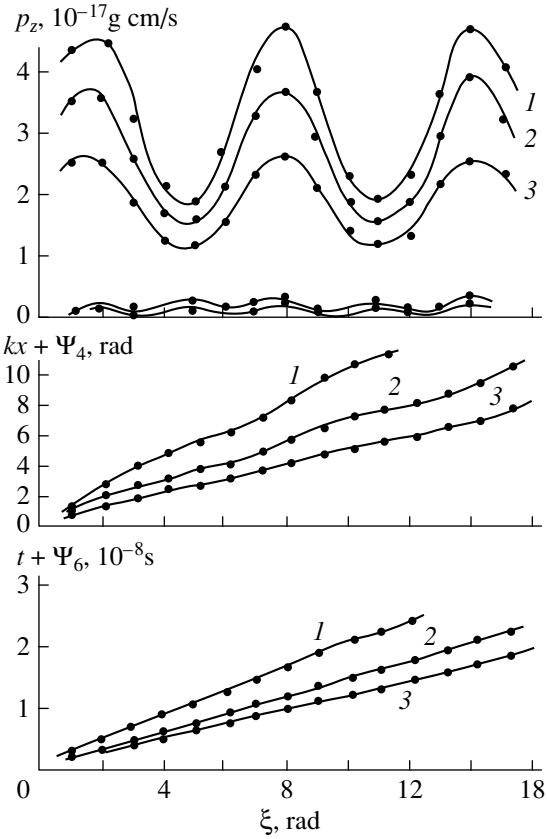

Phase dependences of the longitudinal momentum, coordinate, and time: *1–3*, $\Psi_1 = \Psi_2 = mc$.

In the figure, the dependences of p_z, $kx + \Psi_4$, and $t + \Psi_6$ on the phase ξ are presented for $\Psi_3 = mc^2$, $eE/\omega = mc/2$, $k \approx 0.02$ rad/cm, and $\omega = 10^9$ rad/s. The phase velocity for curves *1* and *4* is $u = 1.05$ s; for curve *2*, $u = 1.2$ s; and for curves *3* and *5*, $u = 1.5$ s; m and e are the mass and charge of an electron, respectively. These curves may be applied in analyzing Langmuir waves excited by pulsed transverse electromagnetic waves. Until now, such analysis has been carried out in terms of relativistic hydrodynamics, mainly in the one-dimensional case [8].

REFERENCES

1. L. D. Landau and E. M. Lifshitz, *The Classical Theory of Fields* (Nauka, Moscow, 1973; Pergamon, Oxford, 1975).
2. P. C. Clemmow and J. P. Dougherty, *Electrodynamics of Particles and Plasmas* (Addison-Wesley, Reading, 1990; Mir, Moscow, 1996).
3. R. Kh. Amirov, V. N. Komarov, A. V. Prozorkevich, and S. A. Smolyanskiĭ, *Problems of Theoretical and Nuclear Physics* (Saratovsk. Gos. Univ., Saratov, 1986), pp. 34–39.
4. M. M. Bredov, V. V. Rumyantsev, and I. N. Toptygin, *Classical Electrodynamics* (Nauka, Moscow, 1985).
5. A. I. Morozov and L. S. Solov'ev, in *Reviews of Plasma Physics*, Ed. by M. A. Leontovich (Gosatomizdat, Moscow, 1963; Consultants Bureau, New York, 1963, 1966), Vol. 2, pp. 177–261.
6. V. Ya. Davydovskiĭ, Zh. Éksp. Teor. Fiz. **77**, 519 (1979) [Sov. Phys. JETP **50**, 263 (1979)].
7. *Higher Transcendental Functions (Bateman Manuscript Project)*, Ed. by A. Erdelyi (McGraw-Hill, New York, 1955; Nauka, Moscow, 1967).
8. L. M. Gorbunov and V. I. Kirsanov, *Plasma Wave Excitation by Electromagnetic Pulses* (Nauka, Moscow, 1992); Tr. Fiz. Inst. Akad. Nauk **219**, 3 (1992).

Translated by M. Fofanov

Technical Physics, Vol. 46, No. 1, 2001, pp. 119–121. Translated from Zhurnal Tekhnicheskoĭ Fiziki, Vol. 71, No. 1, 2001, pp. 125–127.

BRIEF COMMUNICATIONS

The Limiting Electron Activity of Cesium in Potassium-Based Alloys

B. B. Alchagirov

Kabardino-Balkar State University, ul. Chernyshevskogo 173, Nalchik, 360004 Russia

e-mail: alch@kbsu.ru

Received May 25, 2000

Abstract—Temperature and concentration dependences of the electron work function in cesium–potassium alloys were studied by the Fowler photoelectric method for the first time. Our results indicate that the limiting electron activity of cesium in potassium–cesium alloys is six times larger than that obtained by extrapolating the work function isotherm to pure potassium. © *2001 MAIK "Nauka/Interperiodica".*

The study of the electron work function and its temperature coefficient in alkaline metals and their alloys is of considerable importance in developing the theory of photoemission, effective sources of charged particles, new high-power chemical sources of electrical energy, etc. [1, 2]. Temperature and concentration dependences of the electron work function for these materials have not been adequately studied [3–6]. In particular, the emission properties of the K–Cs system were investigated only in [7], where the work function isotherm was first constructed using photoemission current measurements for 11 alloys at +25 and –90°C (Fig. 1).

Figure 1 shows the work function isotherm constructed from data in [7] (open circles). It is seen that the emission properties in the most interesting composition ranges (close to the pure components in the K–Cs system) remained virtually unstudied. In particular, from 0% Cs (pure K) to 26 at. % Cs, only a single alloy was examined. Thus, the isotherm in this composition range was obtained by extrapolation. However, it is in this composition range that the most significant variation in the run of the isotherm might be expected, as follows from available data for the surface activity of components in alloys [8]. In this paper, we performed a detailed study of temperature and concentration dependences of the work function for potassium–cesium alloys. As in [7], we used the photoelectric method of Fowler isotherms, whereby the work function is measured with an accuracy of no worse than 1% [4]. The alloys under investigation were prepared from pure metals in which the content of the base element was no less than 99.99% (for K, the main impurity was Na, 0.008%; for Cs, the main impurities were Na, 0.002%; K, 0.003%; and Rb, 0.002%).

Experiments were performed under an ultrahigh vacuum (10^{-7} Pa) in a soldered measuring cell [9] designed to study the work function in liquid solutions of alkaline metals. The preparation of the alloys and work function measurements were described in [10].

Unlike [7], where measurements were made at two fixed temperatures, we measured the work function in 2–3 degree intervals between 20 and 100°C. Moreover, in the temperature range where the alloys are two-phase, the work function was determined in one-degree intervals and the time of keeping the alloys at a given temperature was increased severalfold to make sure that possible structure transformations were completed and thermodynamic equilibrium was established.

The temperature dependences of the work function for pure potassium and its nine alloys with cesium demonstrate that the work function polytherms are linear throughout the temperature interval studied (Fig. 2). For pure potassium, the temperature coefficient of the work function is negative, $d\varphi/dT < 0$, whereas for the alloys, it is positive. The $d\varphi/dT$ vs. cesium content curve (Fig. 3) first sharply rises by nearly one order of magnitude and then gradually decreases almost to zero. Note that the negative value of the temperature coefficient for pure potassium, $d\varphi/dT = -3.50 \times 10^{-4}$ eV/K, obtained in this work is in agreement with theoretical values [11, 12] and is close to that obtained in [13].

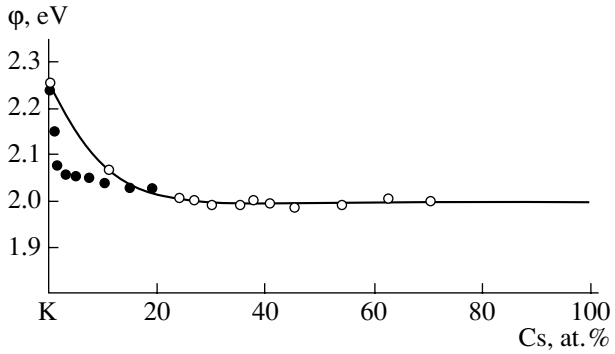

Fig. 1. Work function isotherm for alloys in the potassium–cesium system at 25°C. ○, data from [7]; ●, our data.

1063-7842/01/4601-0119$21.00

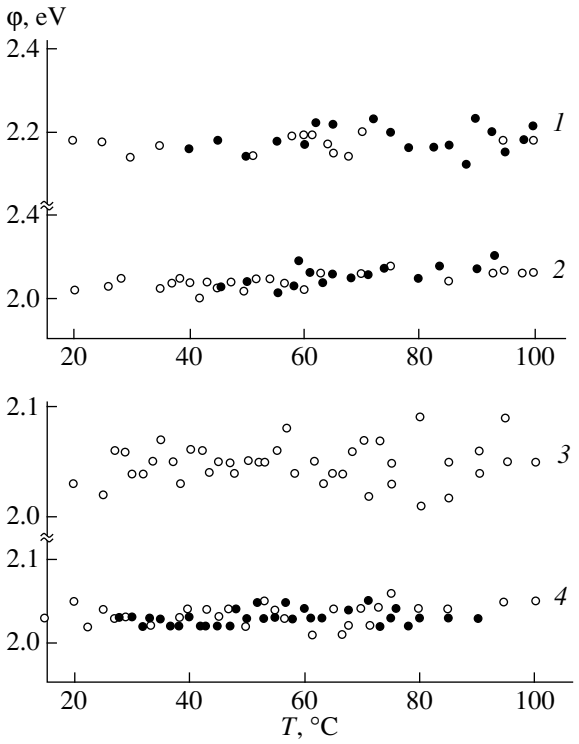

Fig. 2. Temperature dependence of the wave function for several alloys from the potassium–cesium system: (*1*) 0.66, (*2*) 2.37, (*3*) 9.77, and (*4*) 17.56 at. % of cesium. Open and filled circles correspond to increase and decrease in temperature, respectively.

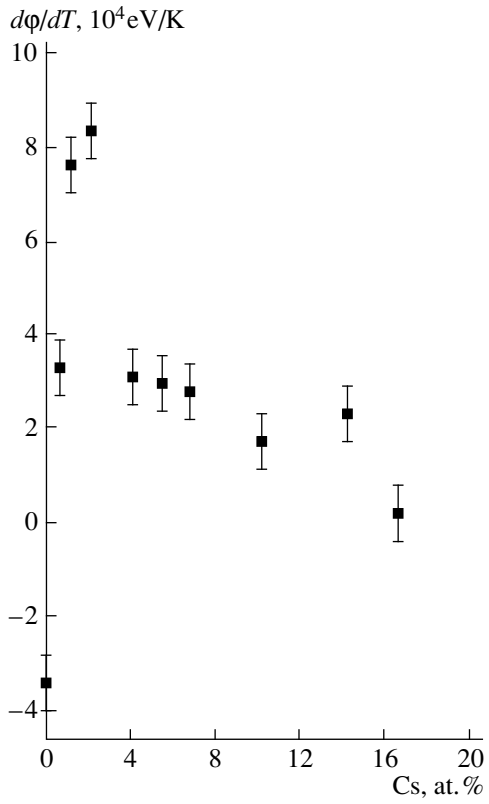

Fig. 3. Concentration dependence of the temperature coefficient of the work function for the potassium–cesium alloys.

Theoretically, the temperature coefficient of the work function in pure metals is governed by various factors, such as thermal expansion, accompanied by loosening interatomic bonds; a change in the dipole electrical moment of the double layer at the surface; etc. Calculated and estimated contributions from each of these factors to $d\varphi/dT$ differ by one order of magnitude and even have opposite signs. We can merely conclude that the absolute values of the temperature coefficients of the work function for pure metals are relatively small: $d\varphi/dT \approx 10^{-4}$–$10^{-5}$ eV/K [11, 12, 14].

The positive values of the temperature coefficients for the alloys with small cesium concentrations seem to be associated mainly with vigorous surface adsorption and can be explained as follows. As the temperature rises, two basic tendencies govern the behavior of the electron work function in the potassium–cesium alloys. On the one hand, the work function decreases because of loosening interatomic bonds, as in the pure components. On the other hand, it gradually increases owing to the desorption of the surface-active component (cesium) from the alloy surface (the work function of cesium is smaller than that for potassium). Cesium segregation in the surface layers of K–Cs alloys has been clearly demonstrated in [15] (Fig. 4). Depending on the temperature and the concentration of the alloy components, either of the two tendencies prevails and specifies the values of the temperature coefficients observed experimentally. Note that such effects are also typical of temperature dependences of the surface energy and surface tension in metal alloys containing surface-active components in small amounts [16].

Using the temperature dependences of the work function, we constructed work function isotherms for the K–Cs alloys. Data points obtained at 25°C are shown in Fig. 1. Even for small amounts of cesium (1.5–2 at. %), the work function of the solvent rapidly decreases and then (at least to 20 at. % of Cs) remains practically unchanged. Therein lies the difference between our results and those obtained in [7], where the concentration interval in which the work function drops extends to 20–25 at. % Cs.

It is worth noting that the concentration dependence of the work function calculated for the K–Cs system by the method of electron density functional also indicates the high surface activity of cesium in K–Cs alloys, especially at small Cs concentrations [15].

The limiting electron activity χ^0 of cesium is estimated as

$$\chi^0 = \lim_{x \to 0}\left(-\frac{\partial \varphi}{\partial x}\right)$$

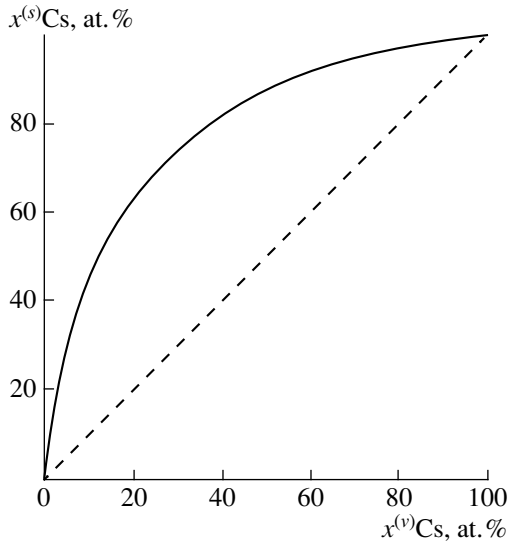

Fig. 4. Cesium segregation in the potassium–cesium binary solution: the cesium concentration in the surface layer of the solution (solid curve) as a function of the cesium content in the bulk (dashed curve).

(χ^0 characterizes the variation of the work function φ of an alloy with the concentration x of a surface-active component as x tends to zero). The value of χ^0 obtained from our data for $\varphi(x)$ exceeds that calculated from the work function isotherm obtained in [7] by a factor of 6.

Thus, the existing opinion that cesium decreases the work function of the alloys to the value of pure cesium only at concentrations of 20–25 at. % seems to be incorrect. Our detailed measurements in the concentration range close to pure potassium showed that the concentration interval where φ drops is actually one order of magnitude narrower. Moreover, the surface activity of cesium was found to be nearly six times that obtained in [7].

REFERENCES

1. M. E. Drits and L. L. Zusman, *Alkali and Alkali-Earth Metal Alloys: A Handbook* (Metallurgiya, Moscow, 1986).
2. B. K. Petrin, Itogi Nauki Tekh., Ser.: Gener. Pryamogo Preobraz. Tepl. Khim. Énerg. Élektr. **8** (1986).
3. H. Riviera, in *Solid State Surface Science*, Ed. by M. Green (Marcel Dekker, New York, 1970; Mir, Moscow, 1972).
4. B. B. Alchagirov, V. B. Lazarev, and Kh. B. Khokonov, Obz. Teplofiz. Svoĭstvam Veshchestv **79**, 76 (1989).
5. J. Hölzl and F. K. Schulte, in *Work Function of Metals*, Ed. by G. Höhler and E. A. Nickish (Springer-Verlag, Berlin, 1979).
6. V. S. Fomenko, *Emission Properties of Materials: A Handbook* (Naukova Dumka, Kiev, 1981).
7. I. Malov, M. D. Shebzuhov, and V. B. Lazarev, Surf. Sci. **44**, 21 (1974).
8. A. A. Shebzukhov, Poverkhnost, No. 8, 13 (1983).
9. B. B. Alchagirov, RF Inventor's Certificate No. 20086659, Byull. Izobret., No. 4 (1994).
10. B. B. Alchagirov, R. Kh. Arkhestov, and Kh. B. Khokonov, Zh. Fiz. Khim. **67**, 1892 (1993).
11. A. Kiejna, Surf. Sci. **178**, 349 (1986).
12. V. V. Pogosov and A. G. Khrapak, Teplofiz. Vys. Temp. **25**, 1231 (1987).
13. B. B. Alchagirov, R. Kh. Arkhestov, and Kh. B. Khokonov, Dokl. Ross. Akad. Nauk **326** (1), 121 (1992).
14. C. Herring and M. Nichols, Rev. Mod. Phys. **21**, 185 (1949).
15. H. Bogdanov and F. K. Wojciechowski, J. Phys. D **29**, 1310 (1996).
16. B. B. Alchagirov, Obz. Teplofiz. Svoĭstvam Veshchestv **89–90** (1991).

Translated by Yu. Vishnyakov

Technical Physics, Vol. 46, No. 1, 2001, pp. 122–124. Translated from Zhurnal Tekhnicheskoĭ Fiziki, Vol. 71, No. 1, 2001, pp. 128–130.

BRIEF COMMUNICATIONS

On the Conditions of Convective Instability in the Upper Layer of Liquid Solutions

L. Kh. Ingel'

Typhoon SPA, Federal Service of Russia for Hydrometeorology and Monitoring of the Environment, Obninsk, Kaluzhskaya oblast, 294038 Russia

e-mail: lingel@obninsk.com

Received May 25, 2000

Abstract—A linear problem of convective instability near the surface of a two-component liquid medium is considered. The specificity of the problem is in the necessity of the simultaneous allowance for the background stratification and the difference in the exchange coefficients for each component, as well for the thermocapillary effect. The allowance for the latter is shown to suggest the existence of a previously unknown region of monotonic instability. The corresponding dimensionless criterion was found, and neutral curves were calculated. © *2001 MAIK "Nauka/Interperiodica"*.

INTRODUCTION

Convective instability related to the thermocapillary effect (Marangoni convection) is usually considered only in sufficiently thin liquid layers (in water, in layers a few millimeters thick). It is usually assumed that in thicker layers this instability is unobservable against the background of the Rayleigh–Taylor convective instability [1]. However, in a two-component medium (e.g., in salt water) situations are possible when, in the presence of an unstable temperature-induced stratification (heating from below), the density-related stratification turns out to be stable owing to the stable stratification related to the saltiness. The Rayleigh–Taylor instability in this case turns out to be suppressed, and the thermocapillary instability is possible and is "free from competition." In this case, it is expedient to study such a mechanism of instability in arbitrarily thick layers of liquids.

RESULTS AND DISCUSSION

As an example, we investigate the stability, in the quiescent state, of a semibounded water layer stratified in temperature and salinity with allowance for the thermocapillary effect. We will use the Boussinesq approximation (also known as the free-convection approximation), whose applicability to liquids has been well investigated and substantiated [1–3]. According to this approximation, the liquid is considered to be incompressible, except for the allowance for its thermal expansion. The linearized set of equations in this case is written as follows [1, 3]:

$$(\partial_t - \nu\nabla^2)\mathbf{v} = -\frac{1}{\rho_0}\nabla p + g(\alpha T - \beta s)\mathbf{e}_z, \quad \nabla\mathbf{v} = 0, \tag{1}$$

$$(\partial_t - \kappa\nabla^2)T + \gamma_T \mathbf{v}\mathbf{e}_z = 0, \quad (\partial_t - \chi\nabla^2)s + \gamma_s \mathbf{v}\mathbf{e}_z = 0.$$

Here, the z axis is directed vertically upward; T, and s are the disturbances of the temperature and salinity, respectively; γ_T and γ_s are the background vertical gradients of these quantities; $\mathbf{v}$ is the three-dimensional vector of the velocity-field disturbance; α is the thermal expansion coefficient of the liquid; β is the coefficient of solutal (salinity-related) compression that characterizes the density dependence on the solution concentration; ρ_0 is the average unperturbed density of water; ν, κ, and χ are the exchange coefficients; and g is the acceleration of gravity.

The problem of the stability of an infinite layer of salt water has already been studied (see, e.g., [3, 4]). Assuming the values of the parameters γ_T and γ_s corresponding to the stable state of an infinite layer [4], we will investigate the possibility of the development of instability due to surface effects. Consequently, we consider disturbances that are damped far from the surface, at $z \longrightarrow -\infty$. The deformations of the liquid surface are neglected. This corresponds to the condition $w|_{z=0} = 0$, where w is the vertical component of the velocity. For simplicity, we restrict ourselves to homogeneous boundary conditions of second order (the absence of disturbances of fluxes) for heat and salt at $z = 0$. The thermocapillary effect is taken into account, as usual, by the boundary condition [1]

$$\rho_0\nu\partial_z\mathbf{u} = -\sigma_T\nabla_h T \quad \text{at} \quad z = 0. \tag{2}$$

Here, $\mathbf{u}$ is the vector of the horizontal velocity, ∇_h is the horizontal Hamilton operator, and σ_T is the absolute magnitude of the temperature derivative of the coefficient of surface tension σ. The thus-formulated problem of stability was investigated with respect to monotonic disturbances using the standard method of normal

modes. We seek for a solution of the form

$$w(x, y, z, t) = W(z)\exp[i(k_x x + k_y y) + \omega t] \quad (3)$$

(analogous solutions are sought for other unknowns). Eliminating all unknowns except for w from the initial set of equations, we obtain the following equation at $w = 0$ (implying the calculation of neutral curves):

$$\left(\frac{d^2}{dz^2} - k^2\right)^3 W = k^6 S W. \quad (4)$$

Here,

$$S = \frac{1}{\nu k^4}\left(\frac{N_T^2}{\kappa} + \frac{N_s^2}{\chi}\right), \quad (5)$$

$k^2 = k_x^2 + k_y^2$, and $N_T = (\alpha g \gamma_T)^{1/2}$ and $N_s = (-\beta g \gamma_s)^{1/2}$ are the "thermal" and "salinity" frequencies of the (Brunt–Väisälä) buoyancy. The parameter S is an analog and a generalization of the Rayleigh number [1–3] to the case of a two-component medium. However, instead of the thickness of the liquid layer (which is infinite in the problem under consideration), the horizontal disturbance length k^{-1} enters into it. As was mentioned above, situations are considered in which, in the absence of surface effects, the system is stable (due to the stability of the solutal stratification) but the temperature-related stratification is unstable:

$$\gamma_T < 0, \quad \gamma_s < 0, \quad N_T^2 < 0, \quad N_s^2 > 0, \quad N_s^2 + N_T^2 > 0; \quad N_T^2/\kappa + N_s^2/\chi > 0. \quad (6)$$

The last inequality in (6) represents one of the conditions of stability against the so-called effects of double (differential) diffusion that are capable of destabilizing the system even in the case of a stable density stratification [3, 4]. In accordance with condition (6), we consider only positive values of the parameter S. Note that since the transfer coefficient for salt in water is smaller by two orders of magnitude than the coefficient of thermal diffusivity κ [3], the parameter S, with other conditions being equal, depends much more strongly on the salinity-related stratification than on the temperature-related one. In particular, stable stratification of the salinity stabilizes the medium much more strongly than a similar stratification of thermal origin.

We seek a solution to Eq. (4) in the form of a sum of exponential terms. With allowance for damping, the solution for the vertical velocity at $z \longrightarrow -\infty$ represents a sum of three exponential terms:

$$W(z) = \sum_{i=1}^{3} C_i e^{q_i k z}, \quad q_1 = (1 + S^{1/3})^{1/2}, \quad q_{2,3} = \left[1 + S^{1/3}\exp\left(\pm\frac{2}{3}\pi i\right)\right]^{1/2} \quad (7)$$

($\mathrm{Re}\, q_i > 0$). In the expressions for the temperature and the salinity, there is a fourth exponent e^{kz}. From the boundary conditions, we obtain a set of equations for the coefficients C_i:

$$\sum_{i=1}^{3} C_i = 0, \quad \sum_{i=1}^{3} \frac{q_i}{q_i^2 - 1} C_i = 0, \quad \sum_{i=1}^{3}\left[q_i^2 - \frac{M}{q_i^2 - 1}\right] C_i = 0, \quad (8)$$

where M is the analog of the Marangoni number:

$$M = -\frac{\sigma_T \gamma_T}{\rho_0 \kappa \nu k^2}. \quad (9)$$

The determinant D of the set of equations (8) can be reduced to the form

$$D = \frac{\sqrt{3}i}{S^{1/3}}\left\{-\frac{M}{S^{1/3}}\left[2q\cos\left(\phi - \frac{\pi}{3}\right) - q_1\right] + S^{1/3} q_1 + q[(q_1^2 - q^2)\cos\phi + (q_1^2 + q^2)\sin\phi/\sqrt{3}]\right\}. \quad (10)$$

Here, q and φ are the modulus and the phase of the quantity q_2:

$$q_{2,3} = q e^{\pm i\varphi}; \quad q = (1 - S^{1/3} + S^{2/3})^{1/4},$$

$$\varphi = \frac{1}{2}\begin{cases} \arctan\{[(\sqrt{3}/2)S^{1/3}]/[1 - (1/2)S^{1/3}]\} \\ \text{at} \quad 0 \le S < 8, \\ \pi + \arctan\{[(\sqrt{3}/2)S^{1/3}]/[1 - (1/2)S^{1/3}]\} \\ \text{at} \quad S > 8. \end{cases}$$

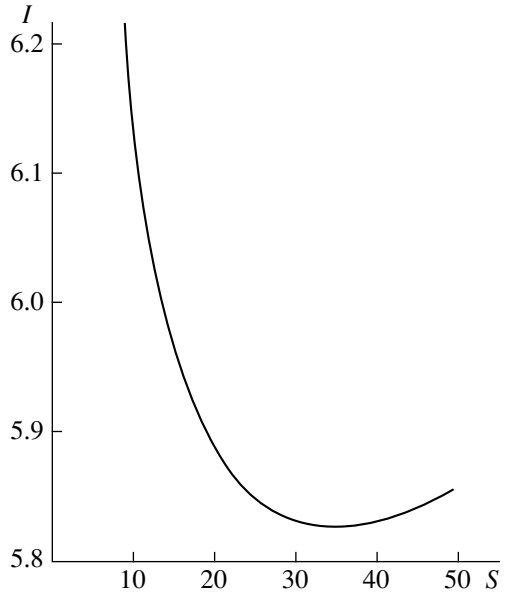

Fig. 1. Neutral curve on the plane (S, I).

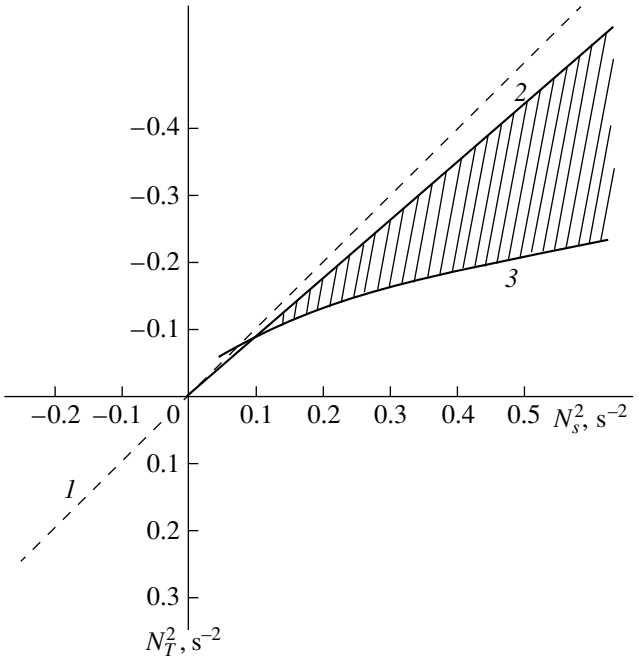

Fig. 2. Neutral curves on the "frequency" plane (N_s^2, N_T^2): (*1*) neutral density-related stratification and (*2*) the lower boundary of the region of vibrational instability [3, 4]. The hatched region represents a region of instability (found in this work), whose lower boundary (*3*) is determined by criterion (12).

The neutral stability curve $M(S)$ corresponds to a zero right-hand side of Eq. (10). An analysis of the obtained characteristic equation shows that, as a dimensionless criterion of instability, we can consider the parameter

$$I = -(\chi/\nu)^{1/2}\sigma_T\gamma_T/\rho_0\kappa N_s. \quad (11)$$

The condition of instability has the form

$$I > S^{1/6}[(2q/q_1) \times \cos\varphi + 1]/\left[(2q/q_1)\cos\left(\varphi - \frac{\pi}{3}\right) - 1\right]. \quad (12)$$

The neutral curve on the plane (S, l) is shown in Fig. 1; the region of instability lies above this curve. To the most "dangerous" mode, there correspond parameters $S = S_* \approx 34$, $I = I_* \approx 5.828$, and $k = k_* \approx (N_s^2/S_*\nu\chi)^{\frac{1}{4}} \approx 0.41(N_s^2/S_*\nu\chi)^{\frac{1}{4}}$. Figure 2 shows the neutral curves on the plane (N_s^2, N_T^2) that refer to the following values of the parameters: $\rho_0 = 10^3$ kg m^{-3}, $\sigma_T = 1.4 \times 10^{-4}$ N m^{-1} K^{-1}, $\nu = 10^{-6}$ m^2 s^{-1}, $\kappa = 1.4 \times 10^{-7}$ m^2 s^{-1}, and $\chi = 1.5 \times 10^{-9}$ m^2 s^{-1}. It is seen that allowance for the thermocapillary effect leads to the appearance (for stable density-related stratification) of a region of instability above curve *3*. If $\gamma_s = 0.33$‰ cm^{-1} and $\beta = 0.76 \times 10^{-3}$(‰)$^{-1}$, then $N_s \approx 0.5$ s^{-1}, $k_* = 1.5 \times 10^3$ m^{-1}; at $\alpha = 2 \times 10^{-4}$ K^{-1}, an unstable background vertical temperature gradient on the order of 10^2 K m^{-1} is required for the instability to appear. The effective depth of penetration of neutral disturbances into the medium for the most dangerous mode is somewhat smaller than its wavelength.

CONCLUSION

Thus, the main results of the work are as follows. We showed that, with allowance for surface effects, a significant part of the region of physical parameters of the upper layer of a two-component medium that is traditionally considered stable is, strictly speaking, a region of instability. We found the corresponding dimensionless criterion and calculated neutral curves.

REFERENCES

1. G. Z. Gershuni and E. M. Zhukhovitskiĭ, *Convective Stability of Incompressible Fluids* (Nauka, Moscow, 1972).
2. L. D. Landau and E. M. Lifshitz, *Course of Theoretical Physics*, Vol. 6: *Fluid Mechanics* (Nauka, Moscow, 1986; Pergamon, New York, 1987).
3. J. Turner, *Buoyancy Effects in Fluids* (Cambridge Univ. Press, Cambridge, 1973; Mir, Moscow, 1977).
4. G. Walin, Tellus **16**, 389 (1964).

Translated by S. Gorin

Technical Physics, Vol. 46, No. 1, 2001, pp. 125–126. Translated from Zhurnal Tekhnicheskoĭ Fiziki, Vol. 71, No. 1, 2001, pp. 131–133.

BRIEF COMMUNICATIONS

The Effect of Prestressing on the Fracture Toughness of ZrO_2–(3, 4) mol % Y_2O_3 Ceramics

G. Ya. Akimov and V. M. Timchenko

Donetsk Physicotechnical Institute, National Academy of Sciences of Ukraine, Donetsk, 83114 Ukraine

e-mail: akimov@host.dipt.donetsk.ua

Received May 25, 2000

Abstract—It is shown that the fracture toughness of prestressed ZrO_2–(3, 4) mol % Y_2O_3 ceramics monotonically increases, the growth being as high as ~50% of the initial value. It is believed that prestressing causes slow isothermal martensite transformation of some grains in the material. During mechanical tests, the degree of transformation rises, which shows up as increased fracture roughness. © *2001 MAIK "Nauka/Interperiodica".*

Ceramic materials based on ZrO_2 or its solid solutions are known to offer high fracture roughness K_{Ic} [1]. High mechanical properties of these materials are the result of tetragonal-to-monoclinic phase martensite transformation initiated by the elastic field of an incipient and/or propagating crack. Therefore, part of the elastic energy is spent on the phase transformation, not on fracture. In addition, the tetragonal-to-monoclinic transformation is accompanied by an increase in the volume; the resulting field of compressive strains also plagues crack propagation. Such a transformation-induced increase in the mechanical properties has been called transformation hardening.

Several equations for the fracture toughness of ceramics have been derived where the effect of transformation hardening is involved. One is given in [2]:

$$K_{Ic} = K_{Ic}^m + \frac{\eta V_f \Delta V E h^{1/2}}{1-\nu}, \qquad (1)$$

where K_{Ic} is the actual fracture roughness, K_{Ic}^m is the fracture roughness of the matrix in the absence of transformation hardening (~1.1 MPa $m^{1/2}$ for ZrO_2–Y_2O_3 ceramics [3]), η is a constant, V_f is the volumetric fraction of the tetragonal phase that underwent the transformation, ΔV is a transformation-induced increase in the volume, E is Young's modulus, h is the half-width of the transformation zone, and ν is Poisson's ratio.

Lange [4] gives another relationship between the fracture roughness and transformation hardening parameters:

$$K_{Ic} = \left[K_0^2 + \frac{2RE_cV_i(|\Delta G^c| - \Delta U_{se} f)}{(1-\nu_c^2)}\right]^{1/2}, \qquad (2)$$

where K_0 is the fracture roughness in the absence of transformation hardening, R is the size of the transformation zone, E_c is the modulus of elasticity, V_i is the volumetric fraction of the tetragonal phase that underwent the transformation, ΔG^c is the change in the free chemical energy during the ZrO_2(tetr.)-to-ZrO_2(monocl.) transformation, ΔU_{se} is the transformation-induced change in the elastic energy, $(1 - f)$ is the elastic energy loss due to crack propagation, and ν_c is Poisson's ratio. The factor $(|\Delta G^c| - \Delta U_{se} f)$ has the meaning of the work spent by the strain field to initiate the transformation per unit volume.

In Eqs. (1) and (2), the variable, i.e., K_{Ic}-controlling, parameters are the size of the transformation zone and the degree of transformation inside this zone (the volumetric fraction of the transformed material). Hence, within the formalism used to derive both equations, a change in K_{Ic} should be treated as the result of a change in the transformation zone size and/or degree of transformation.

Tetragonal-to monoclinic transformation is initiated by the stress field; this field need not be that of a crack. Then, a mechanical stress that does not cause fracture may result in the phase transformation, showing up as a change in K_{Ic}. In this work, we studied the effect of prestressing on the fracture roughness.

Starting materials were ceramic samples measuring $3 \times 4 \times 20$ mm of composition ZrO_2–3 mol % Y_2O_3 (series I) and ZrO_2–4 mol % Y_2O_3 (series II). The density of the samples measured by hydrostatic weighing was 5.90 g/cm^3 (for series I) and 5.99 g/cm^3 (series II). The fracture roughness was determined with notched 3-point bend tests. The gage length was 14.5 mm. The tests were carried out in a UME-10TM testing machine. It was calibrated by loading a DOSM 3-0.2 reference dynamometer. The samples were notched by a circular diamond saw with a cutting edge thickness of 0.4 mm. Prestressing was accomplished as follows. The test sample was loaded to the value of K_I not exceeding K_{Ic}

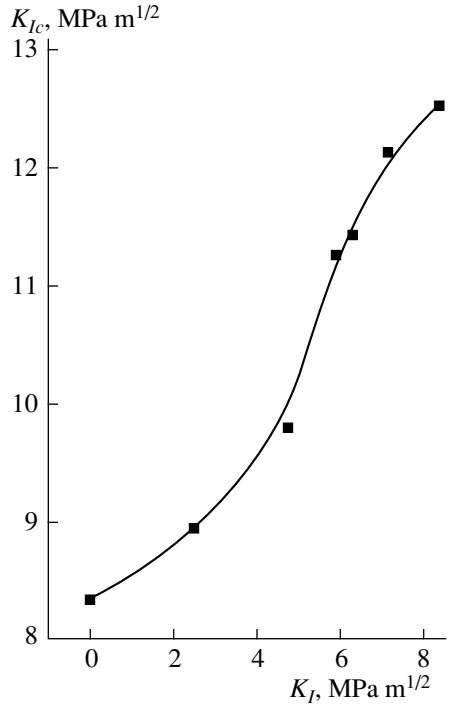

Fig. 1. K_{Ic} vs. prestressing parameter K_I (series I).

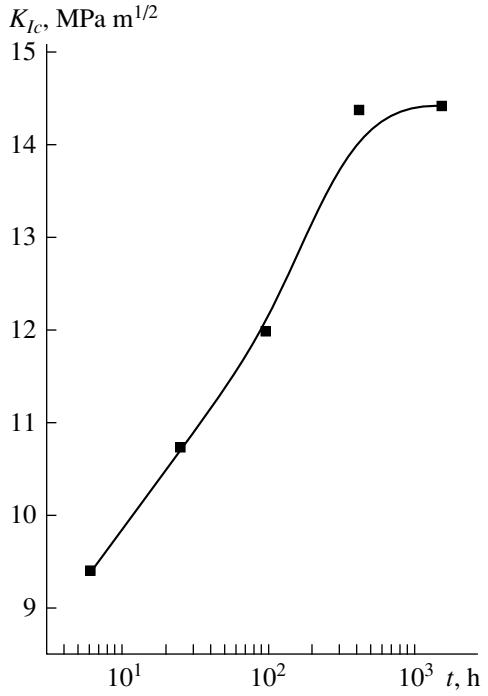

Fig. 2. K_{Ic} vs. prestressing time (series II).

with a rate of 0.005 mm/min (the speed of the traverse of the testing machine), kept in the stressed state for a certain time, unloaded, and tested to determine K_{Ic} under standard conditions (at a traverse velocity of 0.5 mm/min). Two types of experiments were employed: the samples were kept for a certain (constant) time at different K_I's (series I) and for different times at the same K_I (series II). For series-I samples, the prestressing time was 6 h and K_I was varied from zero (K_{Ic} was measured without prestressing) to 8 MPa m$^{1/2}$ (the value of K_{Ic} attained in the sample that was not prestressed). In series-II samples, K_I was within the range 5.5–6.2 MPa m$^{1/2}$ and the prestressing time was varied from 6 to 1461 h, increasing four times in each subsequent run.

Figures 1 and 2 plot the fracture roughness against the prestressing parameters for series I and II, respectively. In both cases, prestressing raises K_{Ic}. The increase in K_{Ic} may attain 50% of its initial value. On further increasing K_I or prestressing time, K_{Ic} changes insignificantly.

Earlier [5], the term martensite transformation was used in reference to transformations having athermic kinetics. Later, this term was applied to transformations where the crystal structure is modified by shear. It was assumed [5] and then experimentally demonstrated (with ZrO_2 crystals) [6] that martensite transformation may have isothermal kinetics under certain conditions. Therefore, there is reason to think that tetragonal-to-monoclinic transformation in ZrO_2–(3, 4) mol % Y_2O_3 ceramics may have both athermic and isothermal kinetics. Under conventional test conditions, only grains where the phase transition proceeds athermically experience transformation hardening. Prestressing may favor the slow stage of the phase transition in those grains transformed isothermally. By the slow stage, we mean the nucleation of the monoclinic phase or crossing crystal defects. Eventually, the degree of transformation and, hence, the value of K_{Ic}, will rise in subsequent mechanical tests.

REFERENCES

1. M. Rühle and A. G. Evans, Prog. Mater. Sci. **33**, 85 (1989).
2. G. S. A. M. Theunissen, J. S. Bouma, A. J. A. Winnubst, and A. J. Burggraaf, J. Mater. Sci. **27**, 4429 (1992).
3. T. K. Gupta, F. F. Lange, and J. H. Bechtold, J. Mater. Sci. **13**, 1464 (1978).
4. F. F. Lange, J. Mater. Sci. **17**, 235 (1982).
5. J. W. Christian, *Theory of Transformations in Metals and Alloys* (Pergamon, Oxford, 1975; Mir, Moscow, 1978), Part 1.
6. B. Ya. Sukharevskiĭ, A. M. Gavrish, and B. G. Alapin, Sb. Tr., Ukr. Nauchno-Issled. Inst. Ogneuporov **9**, 5 (1968).

Translated by V. Isaakyan

Technical Physics, Vol. 46, No. 1, 2001, pp. 127–128. Translated from Zhurnal Tekhnicheskoĭ Fiziki, Vol. 71, No. 1, 2001, pp. 134–135.

BRIEF COMMUNICATIONS

On the Theory of Laser Heating of Water Drops

V. I. Trigub and P. B. Boldyrevskiĭ

Nizhni Novgorod State Technical University, Nizhni Novgorod, 603600 Russia

Received May 25, 2000

Abstract—It is shown that pressure caused by the law of momentum conservation and a nonuniform distribution of energy sources over a drop volume should be taken into account when describing the evaporation of large water drops subjected to high-intensity optical radiation. *© 2001 MAIK "Nauka/Interperiodica".*

Systems composed of liquid drops dispersed in gas are widely used to produce media with specific properties. The problems of effective heating and evaporation of drops dispersed in gas are of primary importance for many technological processes. The use of a laser as a source of high-intensity electromagnetic radiation for the heating and evaporation of drops is more effective than the use of other sources of optical radiation [1].

It has been shown theoretically and experimentally [1] that a change in the radius of a water drop R as a function of time t during laser heating can be approximately represented as

$$R(t) = R_0 - k(\omega)t, \tag{1}$$

where $k(\omega) = \lambda\omega q/4\rho^2 cLa$; a is the thermal diffusivity of water; λ, c, and p are its thermal conductivity, heat capacity, and density; L is the specific heat of vaporization; $q = \exp[-0.2(|m| - 1)]$; m is the complex refractive index; ω is the flux density of electromagnetic radiation; R_0 is the initial drop radius; and t is time.

Equation (1) can be easily rewritten as

$$\frac{dm}{dt} = -3\frac{mk(\omega)}{R}, \tag{2}$$

where $m = (4/3)\pi\rho R^3$ is the drop mass.

Integrating Eq. (2), we obtain

$$\ln\frac{m_0}{m} = -3k(\omega)\int\frac{dt}{R}, \tag{3}$$

where m_0 is the drop mass before irradiation.

Since a change in the drop mass is caused by its evaporation (drop fission is not taken into account in this approximation), the law of momentum conservation should be taken into account [2]. Then, (3) may be written as

$$\frac{V}{U} = 3k(\omega)\int\frac{dt}{R}, \tag{4}$$

where U is the velocity of water molecules leaving the drop surface, and V is the rate of drop compression.

Relationship (4) allows one to estimate the pressure compressing a drop on its evaporation. For $U \cong 10^3$ m/s, $t \cong 0.55$ s, $\omega \cong 10^5$ W/m^2 and $R_0 \cong 5 \times 10^{-4}$ m, we have $p \cong 10^6$ Pa. If the results obtained are compared with the surface density of the forces of normal atmospheric pressure equal to 1.013×10^5 Pa [3], one can see that the pressure compressing a drop during its evaporation is an order of magnitude higher than atmospheric pressure. Drop compression results in a decrease in its surface area according to the Laplace law [4] and, consequently, in an increase in the volume density of energy stored in the drop. The latter, in turn, is conducive to an extra increase in the drop temperature and enhancement of the evaporation effect [4], which were disregarded in [1]. In fact, the law of energy conservation during evaporation of a water drop can be expressed as

$$\sigma S = \Theta\rho l S,$$

where σ is the surface tension of water, ρ is the concentration of water molecules in the drop, Θ is the bonding energy of a water molecule in the drop, S is the drop surface area, and is l is the mean distance between water molecules in the drop.

If the energy of a water molecule is higher than its bonding energy in a water drop, the molecule overcomes the surface tension forces and leaves the drop. When $l \le 2$ mm, Van der Waals repulsion forces act between the molecules and this distance is the minimum. Then, for $\sigma = 7.2 \times 10^{-2}$ J/m^2 and $\rho = 3 \times 10^{28}$ m^{-3}, we obtain $\Theta = \sigma/(lp) \cong 1.2 \times 10^{-21}$ J. A pressure value conducive to evaporation can be estimated at $p = \Theta\rho = 10^6$ Pa, which coincides with the estimate of the pressure compressing a drop during its evaporation (see above). It is therefore concluded that, as water molecules evaporate, they exert pressure on the drop surface and thus initiate its evaporation.

When deriving a theoretical dependence like (1), it was assumed initially in [1] that the energy absorbed by a drop from the electromagnetic field is spent completely on an increase in its temperature and on evaporation. To clarify the validity of this assumption, let us use the following model. A water drop of diameter of

1063-7842/01/4601-0127$21.00 © 2001 MAIK "Nauka/Interperiodica"

10^{-3} m can be regarded as a spherical optical resonator. Based on geometrical optics, it follows that some part of light always experiences a total internal reflection and remains confined inside the sphere. This part of radiation is spent on heating a drop. If the wave properties of electromagnetic radiation are considered, the following relationships are valid for the electromagnetic oscillation modes with the largest Q factor [5]:

$$Q_1 = (n^2-1)^{1/2}(2\pi R/\delta)\exp(2\tau),$$
$$Q_2 = n^{-2}(n^2-1)^{1/2}(2\pi R/\delta)\exp(2\tau). \quad (5)$$

Here, the Q factors for the magnetic and electric oscillation modes are designated by subscripts 1 and 2, respectively; n is the ratio between refractive indices of a sphere n_1 and the environment n_2; R is the radius of a spherical drop; δ is the radiation wavelength in free space; and $\tau = 2\pi R\{\operatorname{arcsinh}(n) - [(n^2-1)/n]^{1/2}\}\delta^{-1}$. For $n_1 = 1.33$, $n_2 = 1$, $R = 10^{-3}$ m and $\delta = 10.6$ μm, $\tau \cong 4.2 \times 10^2$. Hence, for oscillations with the highest Q factor, the probability of degenerating whispering modes is high. We note that ring oscillation modes are conducive to the more efficient conversion of optical energy stored in the resonator to thermal energy [6]. Since the field of ring oscillation modes is concentrated inside a drop (near its surface) [5, 6], the energy of these oscillations is spent on heating the surface region. Thus, the assumption that energy sources are uniformly distributed throughout the drop volume as suggested in [1] is incorrect. On the other hand, it is well known that light propagating inside a sphere along a polygonal path roughly close to a circle will penetrate outside the sphere [5, 7]. Let us introduce a coefficient that accounts for such losses. To introduce it, we use the known analogy between optics and mechanics [8]. Then, based on concepts of quantum mechanics, a plane light wave propagating along a polygonal path must tunnel through a drop surface according to the following law [7] for some minimum value of a polygon leg:

$$\frac{|S_3|^2}{|S_1|^2} \cong \exp\left(-2\frac{d}{\lambda}\right). \quad (6)$$

Here, S_3 is the amplitude of the electromagnetic wave passing through a drop surface, S_1 is the amplitude of the electromagnetic wave incident on the inner drop surface, d is the geometric dimension of a polygon leg, and λ is the light wavelength inside a drop.

Taking into account (6), we can determine the value of a minimum polygon leg for which tunneling is possible:

$$\gamma \cong d\tan\alpha\exp\left(-2\frac{d}{\lambda}\right), \quad (7)$$

where α is the angle of wave incidence on the inner surface of a sphere relative to a line tangent to its surface.

For $\alpha = 45°$, $d \cong \lambda/4$ and $\lambda = 10.6$ μm, $\gamma \cong 4.37$ μm. In formula (7), it was taken into account that radiation goes out tangentially to the drop surface in two mutually opposite directions [9]. Thus, the amplitude of a plane wave propagating along a circular path decreases by a factor of $\exp(-4\pi R/\gamma)$ per cycle. For $R = 5 \times 10^{-4}$ m and $\gamma \cong 4.37$ μm, $(4\pi R)/\gamma \cong 1.2 \times 10^3$. The coefficient accounting for a part of wave energy left inside a drop in one cycle can be written as

$$\Phi \cong \left[1 - \exp\left(-2\frac{2\pi R}{\gamma}\right)\right]^2. \quad (8)$$

Hence, the electromagnetic energy stored in a drop can be estimated if the total flux of electromagnetic energy penetrating into a water drop ω is multiplied by coefficient (8). The presence of exponential factors in (7) and (8) and the consideration of the aforementioned drop sizes and wavelengths suggest that $\Phi \cong 1$. Thus, only a negligible fraction of energy is lost due to the escape of light, and the majority of light accumulates inside a water drop.

REFERENCES

1. V. K. Rudash, V. P. Bisyarin, N. M. Il'in, *et al.*, Kvantovaya Élektron. (Moscow), No. 3 (17), 21 (1973).
2. L. D. Landau and E. M. Lifshitz, *Course of Theoretical Physics*, Vol. 1: *Mechanics* (Nauka, Moscow, 1965; Pergamon, New York, 1988).
3. O. A. Myazdrikov and Yu. V. Tarasov, *Electrical Meters with Liquid Sensing Elements* (Énergiya, Leningrad, 1980).
4. L. D. Landau and E. M. Lifshitz, *Statistical Physics* (Nauka, Moscow, 1976; Pergamon, Oxford, 1980), Part 1.
5. C. G. B. Garrett, W. Kaiser, and W. L. Bond, Phys. Rev. **124** (6), 1807 (1961).
6. G. M. Strakhovskiĭ and A. V. Uspenskiĭ, *Foundations of Quantum Electronics* (Vysshaya Shkola, Moscow, 1979).
7. L. D. Landau and E. M. Lifshitz, *Course of Theoretical Physics*, Vol. 3: *Quantum Mechanics: Non-Relativistic Theory* (Nauka, Moscow, 1989; Pergamon, New York, 1977).
8. E. Fermi, *Notes on Quantum Mechanics* (Univ. of Chicago Press, Chicago, 1961; Mir, Moscow, 1965).
9. G. Birnbaum, *Optical Masers* (Academic, New York, 1964; Sov. Radio, Moscow, 1967).

Translated by M. Astrov

Technical Physics, Vol. 46, No. 1, 2001, pp. 129–131. Translated from Zhurnal Tekhnicheskoĭ Fiziki, Vol. 71, No. 1, 2001, pp. 136–138.

BRIEF COMMUNICATIONS

Products of Carbon Disulfide Oxidation in Ionized Air

G. V. Denisov, Yu. N. Novoselov, A. I. Suslov, and A. M. Uster

Institute of Electrophysics, Ural Division, Russian Academy of Sciences, Komsomol'skaya ul. 34, Yekaterinburg, 620049 Russia

e-mail: nov@iep.uran.ru

Received March 7, 2000

Abstract—Products of plasmochemical reactions proceeding in gas mixtures containing toxic CS_2 impurity were studied. The mixtures were excited by 180- and 300-keV electron pulses of duration 3 ns and 48 μs, respectively. © *2001 MAIK "Nauka/Interperiodica".*

Toxic CS_2 impurity is present in waste gases, specifically, from viscose production, in large amounts. Its content in exhaust industrial gases can be decreased by electron pulse irradiation. It has been shown [1] that irradiation by microsecond pulsed electron beams is an efficient way to remove CS_2 from air. Moreover, the required energy may be lower than the bond energy in this molecule in this case. A chain mechanism for CS_2 removal due to dissociative attachment of secondary beam electrons to O_2 and CS_2 molecules has been suggested. In this work, we studied products of plasmochemical reactions proceeding in CS_2-containing gas mixtures excited by pulsed electron beams.

Experiments were performed on two setups provided with electron accelerators generating nanosecond and microsecond pulses. In the former case, a small-sized Radan accelerator that generates pulses of energy 180 keV, current density to 80 A/cm^2, half-width 3 ns, and repetition rate to 10 s^{-1} was used [2]. The irradiated volume was 10 cm^3. The energy delivered to the gas was 3×10^{-4} J/cm^3 per pulse. In the other setup, the plasma-cathode electron accelerator [3] was applied. It generated a radially divergent beam of cross section 1.44 m^2, electron energy 300 keV, current density behind the output foil 10 A, and pulse half-width 48 μs. The irradiated volume was 170 l. The energy delivered to the gas was ~10^{-4} J/cm^3 per microsecond pulse.

The percentage of the gas components in model mixtures was varied as follows: N_2 from 89 to 99%, O_2 from 0.1 to 10%, and CS_2 to 1%. The mixtures were prepared in a special forced mixer. The composition of the mixtures and reaction (CS_2 removal) products were determined from heat conductivity data with a gas chromatograph using a detector and a three-meter column filled with Silokhrom-120 sorbent.

Figure 1 shows a typical dependence of the CS_2 molecule concentration in the model system on the number of nanosecond pulses. The impurity concentration drops linearly with the number of pulses, i.e., with increasing energy delivered to the process. The initial concentration of the impurity has an insignificant effect on the process of CS_2 removal. It is noteworthy that different energies are needed to decrease the CS_2 concentration by the same amount for the nanosecond and microsecond pulses. For the CS_2 concentration to decline from 2.8×10^{17} to 2.4×10^{17} cm^{-3} in the microsecond regime, about 100 pulses (or delivered energy of ~10^{-2} J/cm^3) are required. For the nanosecond pulses, the number of pulses grows to 6×10^3 (9 J/cm^3).

In the experiments, emphasis was on the determination of CS_2 decomposition products. In both regimes (Fig. 1), the CS_2 concentration drops linearly with increasing number of pulses. It was found that, after the mixture had been irradiated by the microsecond beam,

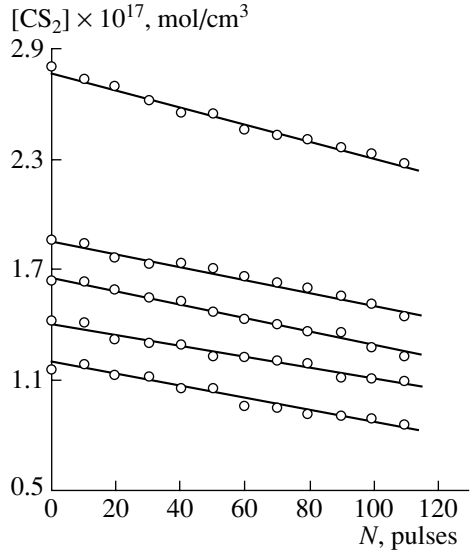

Fig. 1. CS_2 concentration vs. number of microsecond pulses N at different initial CS_2 concentrations.

1063-7842/01/4601-0129$21.00

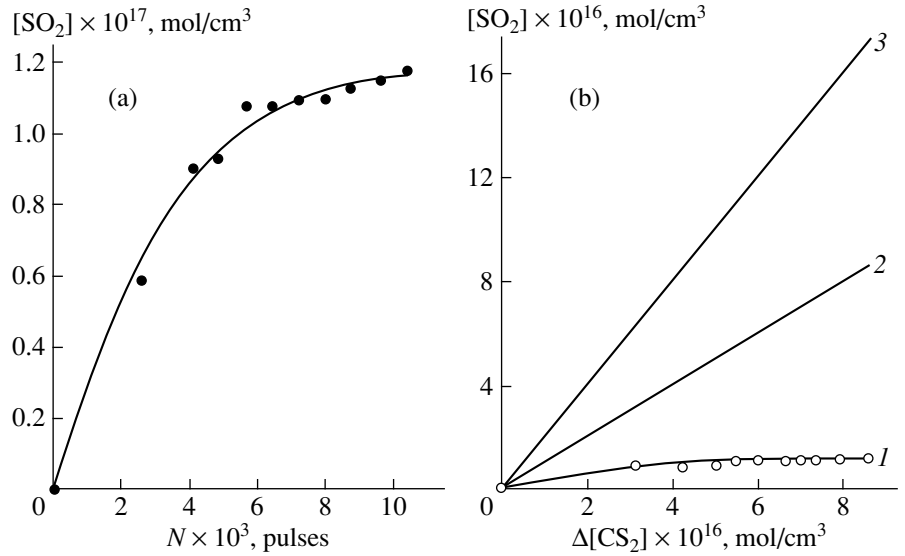

Fig. 2. SO_2 concentration vs. (a) number of nanosecond pulses and (b) concentration of removed CS_2 molecules $\Delta[CS_2]$ for the mixture $N_2 : O_2 : CS_2 = 89 : 10 : 1$.

the side surfaces and the bottom of the reactor were covered by a yellow solid phase and the top horizontal surface of the reactor, by a dark brown viscous liquid. Elemental analysis revealed that this compound has the general formula $(\text{-CS-})_n$ and its aggregative state is possibly dependent on its molecular weight: the low-molecular compound sublimates and condenses in the upper part of the reactor as a liquid, while the high-molecular phase precipitates as a powder. However, the molecular weights of the condensed phases were not determined. Note that SO_2 traces (along with the condensed phases) were found among CS_2 decomposition products in the microsecond pulse regime.

In the nanosecond regime, sulfur dioxide SO_2 was detected as the main product. Also, the yellow powder was present in small amounts on the walls of the reactor. A comparison with the microsecond pulse regime indicates that the variation of the beam parameters (current density and pulse width) does not affect the basic plasmochemical processes. Depending on these parameters, the effect of CS_2 oxidation to form SO_2 may be weak or strong. From Fig. 2a, it follows that, as the content of CS_2 drops in the nanosecond regime, that of SO_2 rises; this dependence, however, is not a linear function of the number of pulses.

With oxygen present in sufficient amounts, the reaction of complete CS_2 oxidation is given by

$$CS_2 + 3O_2 \longrightarrow CO_2 + 2SO_2. \quad (1)$$

Oxygen-deficient atmospheres lead to incomplete oxidation with the formation of a CS radical:

$$CS_2 + O_2 \longrightarrow CS + SO_2 \quad (2)$$

The CS_2-to-SO_2 stoichiometric ratio implies that reaction (1) forms twice as much of the oxidation product SO_2 as reaction (2).

Curve *1* in Fig. 2b is the experimental dependence of the SO_2 concentration on the number of CS_2 molecules $\Delta[CS_2]$ removed from the mixture under nanosecond irradiation. As $\Delta[CS_2]$ grows, the concentration of SO_2 molecules first increases and then saturates. This dependence does not obey reactions (1) and (2) (curves *3* and *2*, respectively).

A possible energy-saving mechanism of CS_2 removal in ionized air was suggested in [1]. This mechanism resembles the chain reaction of CS_2 combustion in oxygen [4, 5]. Its stages are the following:

$$CS_2 + S^- \longrightarrow CS + S_2^-, \quad (3)$$

$$CS_2 + O \longrightarrow CS + SO, \quad (4)$$

$$SO + O_2 \longrightarrow SO_2 + O, \quad (5)$$

$$CS + O_2 \longrightarrow COS + O, \quad (6)$$

$$O + S_2 \longrightarrow SO + S, \quad (7)$$

$$S + O_2 \longrightarrow SO_2 + O. \quad (8)$$

This process proceeds vigorously at an excess of atomic oxygen [4]. The oxidation of CS_2 and the production of atomic oxygen, as well as O^- and S^- ions, are initiated by dissociative attachment of electrons to oxygen and carbon disulfide [6, 7]:

$$O_2 + e \longrightarrow O + O^-, \quad (9)$$

$$CS_2 + e \longrightarrow CS + S^-. \quad (10)$$

In ionized air, these two processes proceed with a high rate.

The atomic oxygen concentration can also be increased by O_2 dissociation due to direct electron impact. One more source of atomic oxygen may be collisions of molecular oxygen with metastable nitrogen molecules $N_2(A)$.

Thus, reactions (3)–(10) produce sulfur dioxide and CS radicals. Their amounts depend on the irradiation conditions. For nanosecond irradiation with high current density, the reactions that form SO_2 proceed with a higher rate, while under microsecond irradiation with small current density, radicals are largely produced. Their polymerization leads to the appearance of the solid and liquid condensed phases.

REFERENCES

1. G. V. Denisov, D. L. Kuznetsov, and Yu. N. Novoselov, Khim. Vys. Énerg. **31** (6), 503 (1997).
2. A. S. El'chaninov, A. S. Kotov, V. G. Shpak, *et al.*, Élektron. Tekh., Ser. 4 **2**, 33 (1987).
3. A. M. Efremov, B. M. Koval'chuk, Yu. E. Kreĭndel', *et al.*, Prib. Tekh. Éksp., No. 1, 167 (1987).
4. A. V. Eletskiĭ, Khim. Plazmy **1**, 67 (1974).
5. B. Bronfin and W. Jeffers, in *Handbook of Chemical Lasers*, Ed. by R. W. F. Gross and J. F. Bott (Wiley, New York, 1976).
6. B. M. Smirnov, *Negative Ions* (Atomizdat, Moscow, 1978).
7. H. S. W. Massey, *Negative Ions* (Cambridge Univ. Press, Cambridge, 1976; Mir, Moscow, 1979).

Translated by V. Isaakyan

Technical Physics, Vol. 46, No. 1, 2001, pp. 14–19. Translated from Zhurnal Tekhnicheskoĭ Fiziki, Vol. 71, No. 1, 2001, pp. 16–21.

Concerning the Full Integrability of Hamiltonian Equations of Charged Particle Motion in a Weakly Inhomogeneous Magnetic Field

V. E. Tarasov, K. Sh. Khodzhaev, and A. G. Chirkov

St. Petersburg State Technical University, St. Petersburg, 195251 Russia

Received March 16, 2000

Abstract—The Hamiltonian of a charged particle in a weakly inhomogeneous magnetic field is calculated up to terms on the order of a small parameter. Fast phase–averaged equations of motion are derived. It is shown that these equations are intergrable in quadratures. Thus, the problem of particle motion in a weakly inhomogeneous field is solved in the first-order approximation. To calculate the Hamiltonian, the coordinates related to the field are used. Then, the canonical change of variables is done with the help of the generating function; in the case of a homogeneous field, this results in the action–angle variables. Such a procedure has been already used in [1]. However, the small parameter was not explicitly introduced and final expressions for small and large parts of the Hamiltonian were not calculated in that paper. It is shown that the small part of the Hamiltonian is a trigonometric polynomial of the fast phase (this can be important when analyzing the influence of additional perturbations). Besides, the averaged equations appear to be treatable and can be integrated in quadratures. © *2001 MAIK "Nauka/Interperiodica".*

1. MOTION IN A HOMOGENEOUS MAGNETIC FIELD, OBLIQUE COORDINATES, AND ACTION–ANGLE VARIABLES

Let us first consider the motion of a nonrelativistic particle with mass m and charge e in a homogeneous magnetic field $\mathbf{B}$ = const. We introduce the oblique coordinates x^1, x^2, and x^3 such that the coordinate x^3 is the distance along the magnetic field line starting from a certain plane inclined to the field lines, while the vectors $\mathbf{r}_\alpha = \partial\mathbf{r}/\partial x^\alpha$ (where $\alpha = 1, 2$ and $\mathbf{r}(x^1, x^2, x^3)$ is the radius vector of the point) are parallel to this plane. Then, the vector $\mathbf{r}_3 = \partial\mathbf{r}/\partial x^3 = \mathbf{B}/B$ is directed along the field line. Let the vectors $\mathbf{r}^1$, $\mathbf{r}^2$, and $\mathbf{r}^3$ be the basis mutual to the basis $\mathbf{r}^1$, $\mathbf{r}^2$, and $\mathbf{r}^3$. The coordinates x^1 and x^2 are introduced in such a way that $|\mathbf{r}^1 \times \mathbf{r}^2| = \mathbf{B}$ and the vector potential can be taken as

$$\mathbf{A} = \frac{1}{2}(x^2\mathbf{r}^2 - x^2\mathbf{r}^1). \tag{1.1}$$

We take the coordinates x^1, x^2, and x^3 with the associated generalized momenta p_1, p_2, and p_3 as the canonical variables for particle motion in the field $\mathbf{B}$. We also introduce the Cartesian coordinates x, y, and z in such a way that the z-axis is directed along the field; the y-axis is parallel to $\mathbf{r}^1$; and x, y, and z equal zero when x^1, x^2, and x^3 equal zero. The coordinates x, y, and z are related to x^1, x^2, and x^3 as follows:

$$x = \frac{g^{12}}{B\sqrt{g^{11}}}x^1 - \frac{\sqrt{g^{11}}}{B}x^2, \quad y = \frac{1}{\sqrt{g^{11}}}x^1, \tag{1.2}$$
$$z = g_{13}x^1 + g_{23}x^2 + x^3, \quad g^{\alpha\beta} = \mathbf{r}^\alpha\mathbf{r}^\beta, \quad g_{\alpha\beta} = \mathrm{r}_\alpha\mathbf{r}_\beta.$$

We will need the generating function $W(x^1, x^2, x^3, J, x_L, p_\parallel)$ of the canonical transformation from the variables x^1, x^2, x^3, p_1, p_2, and p_3 to the variables φ, y_L, z, J, x_L, and $p_\parallel$. Here, J and φ are the action–angle variables, x_L and y_L are coordinates of the Larmor circle center, and $p_\parallel$ is the projection of the mechanical momentum on the field direction. Such a function is found in [1], but it corresponds to another choice of the vector potential and is given as the function of other arguments. We will find the necessary generating function in the following way. Let us consider the known generating function $W_1(x, y, z, J, x_L, p_\parallel)$ of the transformation from the x, y, z, p_x, p_y, and p_z variables to the φ, y_L, z, J, x_L, and $p_\parallel$ variables of the form

$$W_1(x, y, z, J, x_L, p_\parallel) = -\frac{1}{2}\Big(m\omega xy - 2\sqrt{m\omega}x_L y$$
$$-(\sqrt{m\omega}x - x_L)\sqrt{2J - (\sqrt{m\omega}x - x_L)^2}\Big) \tag{1.3}$$
$$+ J\arctan\frac{\sqrt{m\omega}x - x_L}{\sqrt{2J - (\sqrt{m\omega}x - x_L)^2}} + zp_\parallel,$$

where $\omega = eB/mc$ is the Larmor frequency. The function W can be obtained from W_1 if we change x, y, and z to x^1, x^2, and x^3 according to relationships (1.2). As a result, we arrive at

$$W = (g_{13}x^1 + g_{23}x^2 + x^2)p_\parallel - \frac{e}{2c}x^1\left(\frac{g^{12}}{g^{11}}x^1 - x^2\right) + \frac{x_L\sqrt{m\omega}}{\sqrt{g^{11}}}x^1 + \frac{1}{2}\left[\sqrt{\frac{g^{11}}{m\omega}}\frac{e}{c}\left(\frac{g^{12}}{g^{11}}x^1 - x^2\right) - x_L\right] \times \sqrt{2J - \left[\frac{e}{c}\sqrt{\frac{g^{11}}{m\omega}}\left(\frac{g^{12}}{g^{11}}x^1 - x^2\right) - x_L\right]^2} + J\arctan\left(\frac{\sqrt{\frac{g^{11}}{m\omega}}\frac{e}{c}\left(\frac{g^{12}}{g^{11}}x^1 - x^2\right) - x_L}{\sqrt{2J - \left[\sqrt{\frac{g^{11}}{m\omega}}\frac{e}{c}\left(\frac{g^{12}}{g^{11}}x^1 - x^2\right) - x_L\right]^2}}\right). \quad (1.4)$$

Here, it is taken into account that $g_{33} = \mathbf{r}_3\mathbf{r}_3 = 1$.

2. COORDINATES ASSOCIATED WITH THE FIELD

We now consider a particle in an inhomogeneous magnetic field **B**. We introduce the coordinates associated with the field in the same way as in [2], but with some additions that will be used when introducing dimensionless variables and analyzing the smallness of the parameters. Let $[L]$ be the characteristic distance at which the field variations are essential and $[\mathbf{B}]$ be the characteristic value of $|\mathbf{B}|$ in the region under consideration. Then, the characteristic value of the Larmor frequency equals $[\omega_L] = e[B]/mc$. The dimensionless radius vector, magnetic induction, and time are introduced as the ratios of the corresponding dimensional quantities $[\mathbf{L}]$, $[\mathbf{B}]$, and $1/[\omega_L]$, respectively. The dimensionless vectors of the generalized momentum and vector potential are equal to the ratios of the dimensional vectors and the values of $m[\omega_L][L]$ and $[\mathbf{B}][\mathbf{L}]$, respectively. In what follows, we use the same letters to denote the dimensionless and dimensional quantities. In terms of dimensionless variables, the Hamiltonian of a particle has the form

$$H = \frac{1}{2}(\mathbf{p} - \mathbf{A}(\mathbf{r}))^2. \quad (2.1)$$

Let $[v]$ be the characteristic value of the particle velocity and $[R_L] = [v]/[\omega_L]$ be the characteristic Larmor radius. We will assume now that the magnetic field is weakly inhomogeneous, i.e., $[L] \gg [R_L]$. We introduce the main small parameter of the problem as $\varepsilon = [R_L]/[L]$. As usual, we consider such motions and time periods that the particle stays in a magnetic field tube with a diameter and length of about $[R_L]$ and $[L]$, respectively.[1] In the dimensionless space, the diameter and the length of this tube are $O(\varepsilon)$ and a length of $O(1)$, respectively. We assume that the curvilinear coordinates Q^1, Q^2, and Q^3 with the following three properties can be introduced in the vicinity of the tube: (i) each point in the region at hand is uniquely determined by these coordinates; (ii) the coordinates Q^1 and Q^2 describe the field line in the tube, and Q^3 is the length of a line starting from a certain base surface; and (iii) the vector potential can be written in the form

$$\mathbf{A} = 1/2(Q^1\mathbf{r}^2 = Q^2\mathbf{r}^1),$$

where $\mathbf{r}^i$ are the vectors of the basis mutual to $\mathbf{r}_i = \partial\mathbf{r}/\partial Q^i$ with $i = 1, 2$, and 3 (such coordinates were described, e.g., in [2]).

Then, for the Hamiltonian, we obtain

$$H = \frac{1}{2}g^{ik}(P_i - A_i)(P_k - A_k), \quad (2.2)$$

where $g^{ik}(Q^1, Q^2, Q^3) = \mathbf{r}^i\mathbf{r}^k$.

We introduce Q^1 and Q^2 in such a way that Q^1, $Q^2 = 0$ at a certain field line in the tube and Q^1, $Q^2 = O(\varepsilon)$ everywhere in the tube. The components of the vector potential are also on the order of ε. Moreover, for the motion under study, we have the following estimate for the generalized momenta:

$$[R_L] \sim [v]/[\omega_L][L] = [R_L]/[L] = \varepsilon.$$

Therefore, we can introduce the new coordinates q^1, q^2, and q^3 and generalized momenta p_1, p_2, and p_3, which satisfy the relations $Q^i = \varepsilon q^i$ and $P_i = \varepsilon p_i$. The valency of this defines the canonical transformation is $1/\varepsilon^2$. The new Hamiltonian takes the form

$$H(pq) = \frac{1}{2}g^{ik}(p_i - A_i)(p_k - A_k). \quad (2.3)$$

Here, $A_1 = -1/2q^2$ and $A_2 = 1/2q^1$ are the vector potential components, which differ from the quantities in Eq. (2.2) denoted in the same way by the factor ε, and $g^{ik} = g^{ik}(\varepsilon q^1, \varepsilon q^2, \varepsilon q^3)$ are the former components of the metric tensor, but with $Q^i = \varepsilon q^i$.

In the motion under study, all the canonical variables (except for q^3) and the components of both the vector potential and of the metric tensor are on the order of unity. The variable q^3 may have large values, on the order of $1/\varepsilon$.

3. HAMILTONIAN OF AN UNPERTURBED PROBLEM IN THE ACTION–ANGLE VARIABLES

We change from the variables q^1, q^2, q^3, p_1, p_2, and p_3 to the variables φ, y_L, z, J, x_L, and $p_\parallel$ using the gener-

[1] This corresponds to a time interval on the order of $\sim 1/\varepsilon$ (see below).

ating function (1.4) and taking into account that the coordinates q^1, q^2, and q^3 are dimensionless. The metric tensor components are now the functions of the coordinates. Then, we obtain

$$\begin{aligned} W = {} & (g_{13}q^1 + g_{23}q^2 + q^3)p_\| - \frac{1}{2}q^1\left(\frac{g^{12}}{g^{11}}q^1 - q^2\right) \\ & + \frac{x_L\sqrt{\omega}}{\sqrt{g^{11}}}q^1 + \frac{1}{2}\left[\sqrt{\frac{g^{11}}{\omega}}\left(\frac{g^{12}}{g^{11}}q^1 - q^2\right) - x_L\right] \\ & \times \sqrt{2J - \left[\sqrt{\frac{g^{11}}{\omega}}\left(\frac{g^{12}}{g^{11}}q^1 - q^2\right) - x_L\right]^2} \\ & + J\arctan\left(\frac{\sqrt{\frac{g^{11}}{\omega}}\left(\frac{g^{12}}{g^{11}}q^1 - q^2\right) - x_L}{\sqrt{2J - \left[\sqrt{\frac{g^{11}}{\omega}}\left(\frac{g^{12}}{g^{11}}q^1 - q^2\right) - x_L\right]^2}}\right). \end{aligned} \tag{3.1}$$

In the dimensionless coordinates, we have $\omega = B$. It follows from the definition of Q^3 that $\mathbf{B} = B\mathbf{r}_3$. On the other hand, due to the properties of the coordinates used, the equality $\mathbf{B} = \mathbf{r}^1 \times \mathbf{r}^2$ is valid. Since $\mathbf{r}^1 \times \mathbf{r}^2 = (1/\sqrt{g})\mathbf{r}_3$, where g_{ik} is the determinant of the matrix $\{g_{ik}\}$, we have $\omega = 1/\sqrt{g}$.

The old and the new variables are related to each other according to the following formulas:

$$\begin{aligned} \varphi &= \frac{\partial W}{\partial J} \equiv \arctan\frac{\sqrt{\frac{g^{11}}{\omega}}\left(\frac{g^{12}}{g^{11}}q^1 - q^2\right) - x_L}{\sqrt{2J - \left[\sqrt{\frac{g^{11}}{\omega}}\left(\frac{g^{12}}{g^{11}}q^1 - q^2\right) - x_L\right]^2}}, \\ y_L &= \frac{\partial W}{\partial x_L} \equiv \sqrt{\frac{\omega}{g^{11}}}q^1 \\ & - \sqrt{2J - \left[\sqrt{\frac{g^{11}}{\omega}}\left(\frac{g^{12}}{g^{11}}q^1 - q^2\right) - x_L\right]}, \\ z &= \frac{\partial W}{\partial p_\|} \equiv g_{13}q^1 + g_{23}q^2 + q^3. \end{aligned} \tag{3.2}$$

After differentiation, we obtain the second group of relationships in terms of φ and y_L from Eqs. (3.2):

$$\begin{aligned} p_k = \frac{\partial W}{\partial q^k} \equiv p_{k0} + p_{k1} = {} & p_{k0} + \frac{\partial g_{13}}{\partial q^k}p_\| q_1^1 + \frac{\partial g_{23}}{\partial q^k}p_\| q^2 \\ & - \frac{q^1}{2}\left(\frac{\partial}{\partial q^k}\frac{g^{12}}{g^{11}}\right)\sqrt{\frac{g^{11}}{\omega}}(-\sqrt{2J}\cos\varphi + y_L) \\ & - \sqrt{\frac{\omega}{g^{11}}}\left(\frac{\partial}{\partial q^k}\sqrt{\frac{g^{11}}{\omega}}\right)[x_L y_L - 2J\cos\varphi\sin\varphi]. \end{aligned} \tag{3.3}$$

Here, expressions for p_{k0} are the result of the differentiation of W without taking into account the dependence of the metric coefficients on εq^1, εq^2, and εq^3:

$$\begin{aligned} p_{10} &= \frac{1}{2}\sqrt{\frac{\omega}{g^{11}}}(-\sqrt{2J}\sin\varphi + x_L) \\ & + \frac{1}{2}\frac{g^{12}}{\sqrt{g^{11}\omega}}(\sqrt{2J}\cos\varphi - y_L) + g_{13}p_\|, \\ p_{20} &= -\frac{1}{2}\sqrt{\frac{g^{11}}{\omega}}(\sqrt{2J}\cos\varphi - y_L) + g_{23}p_\|, \\ p_{30} &= p_\|. \end{aligned} \tag{3.4}$$

To get the Hamiltonian in the new variables, it is necessary to represent the old variables in terms of the new variables. In the following, we obtain the Hamiltonian correct to terms on the order of ε. Therefore, the expressions for the old variables are derived with the same accuracy. From Eqs. (3.2), we have

$$q^3 = z - g_{13}q^1 - g_{23}q^2. \tag{3.5}$$

It follows from this formula that both the z coordinate and q^3 are large. Hence, ω can be written with the prescribed accuracy as follows:

$$\begin{aligned} & \omega(\varepsilon q^1, \varepsilon q^2, \varepsilon q^3) = \omega(0, 0, \varepsilon q^3) \\ & + \varepsilon\left(\frac{\partial\omega}{\partial(\varepsilon q^1)}\right)_0 q^1 + \varepsilon\left(\frac{\partial\omega}{\partial(\varepsilon q^2)}\right)_0 q^2 = \omega(0, 0, \varepsilon z) \\ & + \varepsilon\left(\frac{\partial\omega}{\partial(\varepsilon q^1)} - g_{13}\frac{\partial\omega}{\partial(\varepsilon q^2)}\right)_0 q^1 + \left(\frac{\partial\omega}{\partial(\varepsilon q^2)} - g_{23}\frac{\partial\omega}{\partial(\varepsilon q^3)}\right)q^2 \\ & = \omega_0 + \varepsilon((\omega)_1 q^1 + (\omega)_2 q^2). \end{aligned} \tag{3.6}$$

Here, the zero subscript means the substitutions $q^1 = q^2 = 0$ and $\varepsilon q^3 = \varepsilon z$. In addition, the following notation is used:

$$(\omega)_i = \left(\frac{\partial\omega}{\partial(\varepsilon q^i)} - g_{i3}\frac{\partial\omega}{\partial(\varepsilon q^3)}\right)_0; \quad i = 1, 2. \tag{3.7}$$

We will show below that it is sufficient to solve Eqs. (3.2) only partially with respect to q^1 and q^2, representing q^1 and q^2 by the formulas

$$q^1 = \sqrt{\frac{g^{11}}{\omega}}(\sqrt{2J}\cos\varphi + y_L),$$

$$q^2 = \frac{g^{12}}{\sqrt{g^{11}\omega}}(\sqrt{2J}\cos\varphi + y_L) - \sqrt{\frac{\omega}{g^{11}}}(\sqrt{2J}\sin\varphi + x_L). \quad (3.8)$$

For the same reason, we do not need to exclude q^1, q^2, and q^3 from the formulas for p_{i0}. The quantities p_{i1} in Eqs. (3.2) are on the order of ε, because they contain the derivatives of the metric tensor components with respect to q^i. Therefore, to calculate p_{i1}, we can substitute the equalities $q^1 = q^2 = 0$ and $\varepsilon q^3 = \varepsilon z$ into g^{ik}, g_{ik}, and their derivatives with respect to the coordinates and take q^1 and q^2 from Eqs. (3.8) to calculate g^{11} and other quantities with the same accuracy.

Now, we will derive the Hamiltonian in the first-order approximation. Let us substitute the above formulas into expression (2.3). We get

$$H = \frac{1}{2}g^{ik}(p_{i0} + p_{i1} - A_i)(p_{k0} + p_{k1} - A_k) = \frac{1}{2}g^{ik}(p_{i0} - A_i)(p_{k0} - A_k) + g^{ik}p_{i1}(p_{k0} - A_k). \quad (3.9)$$

Using $A_1 = -1/2q^2$ and $A_2 = 1/2q^1$, we insert relationships (3.8) into the first term on the right hand side of Eq. (3.9). Then, the resulting expression is transformed in the same way as for the motion in a homogeneous field. The coordinate dependence of the metric tensor components does not change the procedure. As a result, we obtain

$$\frac{1}{2}g^{ik}(p_{i0} - A_i)(p_{k0} - A_k) = \omega J + \frac{p_\parallel^2}{2}. \quad (3.10)$$

It is sufficient to use formulas (3.6) to extract the large term and the term on the order of ε in expression (3.10). When calculating the second (small) term on the right hand side of Eq. (3.9), only the large terms must be taken into account in the expressions for q^1, q^2, q^{ik}, p_{k0}, and A_k. Finally, we have

$$\begin{aligned} H &= H_0 + \varepsilon H_1 = \omega_0 J + \frac{p_\parallel^2}{2} \\ &+ \varepsilon[p_\parallel^2(x_L F_1 + y_L F_2) + p_\parallel F_3 + p_\parallel(y_L^2 - J)F_4 \\ &+ p_\parallel x_L y_L F_5 + y_L J F_6 + x_L J F_7 \\ &+ (p_\parallel^2 F_1 + p_\parallel x_L F_9 + p_\parallel y_L F_8 + y_L^2 F_{10} \\ &+ x_L y_L F_{11} + J F_{12})\sqrt{2J}\sin\varphi + (p_\parallel^2 F_2 + p_\parallel y_L F_{13} \\ &+ p_\parallel x_L F_{14} + y_L^2 F_{15} + x_L y_L F_{16} + J F_{17})\sqrt{2J}\cos\varphi \\ &+ p_\parallel J F_{18}\sin 2\varphi + p_\parallel J F_{19}\cos 2\varphi \\ &+ J\sqrt{2J}F_{20}\sin 3\varphi + J\sqrt{2J}F_{21}\cos 3\varphi]. \end{aligned} \quad (3.11)$$

Here, the following notation is used for the functions of εz:

$$F_1 = -\left(\sqrt{\frac{\omega}{g^{11}}}\frac{\partial g_{23}}{\partial(\varepsilon q^3)}\right)_0,$$

$$F_2 = \left(\sqrt{\frac{g^{11}}{\omega}}\right)_0\left(\frac{\partial g_{13}}{\partial(\varepsilon q^3)} + \frac{g^{12}\partial g_{23}}{g^{11}\partial(\varepsilon q^3)}\right)_0,$$

$$F_3 = \omega_0\left(\frac{\partial g_{23}}{\partial(\varepsilon q^1)} - \frac{\partial g_{23}}{\partial(\varepsilon q^2)} + (g_{23} - g_{13})\frac{\partial g_{13}}{\partial(\varepsilon q^3)}\right)_0,$$

$$F_4 = -\frac{1}{2}\left(\frac{g^{11}}{\omega}\right)_0\left(\frac{\partial}{\partial(\varepsilon q^3)}\frac{g^{12}}{g^{11}}\right)_0,$$

$$F_5 = -\left(\sqrt{\frac{\omega}{g^{11}}}\right)_0\left(\frac{\partial}{\partial(\varepsilon q^3)}\sqrt{\frac{g^{11}}{\omega}}\right)_0,$$

$$F_6 = (\omega)_1\left(\sqrt{\frac{g^{11}}{\omega}}\right)_0 + (\omega)_2\left(\frac{g^{12}}{\sqrt{g^{11}\omega}}\right)_0,$$

$$F_7 = -(\omega)_2\left(\sqrt{\frac{\omega}{g^{11}}}\right)_0,$$

$$F_8 = -g^{11}\left(\frac{\partial g_{13}}{\partial(\varepsilon q^1)} + \frac{g^{12}}{g^{11}}\frac{\partial g_{23}}{\partial(\varepsilon q^1)}\right) + g^{12}\left(\frac{\partial g_{13}}{\partial(\varepsilon q^2)} + \frac{g^{12}}{g^{11}}\frac{\partial g_{23}}{\partial(\varepsilon q^2)}\right) + g^{13}\left(\frac{\partial g_{13}}{\partial(\varepsilon q^3)} + \frac{g^{12}}{g^{11}}\frac{\partial g_{23}}{\partial(\varepsilon q^3)}\right)_0,$$

$$F_9 = \omega_0\left(\frac{\partial g_{23}}{\partial(\varepsilon q^1)} + \frac{g^{12}}{g^{11}}\frac{\partial g_{23}}{\partial(\varepsilon q^3)} + \frac{g^{13}}{g^{11}}\frac{\partial g_{23}}{\partial(\varepsilon q^3)}\right)_0,$$

$$F_{10} = \frac{1}{2}\left(\sqrt{\frac{g^{11}}{\omega}}\right)_0\left(g^{11}\left(\frac{\partial}{\partial(\varepsilon q^1)} + \frac{g^{12}}{g^{11}}\right) + g^{12}\left(\frac{\partial}{\partial(\varepsilon q^3)}\frac{g^{12}}{g^{11}}\right) + g^{13}\left(\frac{\partial}{\partial(\varepsilon q^3)}\frac{g^{12}}{g^{11}}\right)\right)_0,$$

$$F_{11} = \omega_0\left(\left(\frac{\partial}{\partial(\varepsilon q^1)}\sqrt{\frac{g^{11}}{\omega}}\right) + \frac{g^{12}}{g^{11}} \times \left(\frac{\partial}{\partial(\varepsilon q^2)}\sqrt{\frac{g^{11}}{\omega}}\right) + \frac{g^{13}}{g^{11}}\left(\frac{\partial}{\partial(\varepsilon q^3)}\sqrt{\frac{g^{11}}{\omega}}\right)\right)_0,$$

$$F_{13} = -\omega_0\left(\frac{\partial g_{13}}{\partial(\varepsilon q^2)} + \frac{g^{12}}{g^{11}}\frac{\partial g_{23}}{\partial(\varepsilon q^2)} - g_{23}\frac{\partial g_{13}}{\partial(\varepsilon q^3)} - \frac{g_{23}g^{12}}{g^{11}}\frac{\partial g_{23}}{\partial(\varepsilon q^3)}\right)_0,$$

$$F_{14} = \left(\frac{\omega}{g^{11}}\right)_0\left(-\frac{\partial g^{23}}{\partial(\varepsilon q^2)} + g_{23}\frac{\partial g_{23}}{\partial(\varepsilon q^3)}\right)_0,$$

$$F_{15} = \frac{1}{2}\left(\sqrt{\frac{g^{11}}{\omega}}\right)_0\left(-\left(\frac{\partial}{\partial(\varepsilon q^2)}\frac{g^{12}}{g^{11}}\right) + g_{23}\left(\frac{\partial}{\partial(\varepsilon q^3)}\frac{g^{12}}{g^{11}}\right)\right)_0,$$

$$F_{16} = \left(\frac{\omega}{g^{11}}\right)_0\left(-\left(\frac{\partial}{\partial(\varepsilon q^2)}\sqrt{\frac{g^{11}}{\omega}}\right) + g_{23}\left(\frac{\partial}{\partial(\varepsilon q^3)}\sqrt{\frac{g^{11}}{\omega}}\right)\right)_0,$$

$$F_{12} = F_7 + F_{20}, \quad F_{17} = -\frac{1}{2}(F_{11} + 3F_{15}) + F_6,$$

$$F_{18} = F_8 + F_{14} - F_5, \quad F_{19} = F_{13} - F_9 - F_4,$$

$$F_{20} = -\frac{1}{2}(F_{10} + F_{16}), \quad F_{21} = \frac{1}{2}(F_{11} - F_{15}).$$

4. APPLICATION OF THE AVERAGING METHOD AND THE INTEGRATION OF THE AVERAGED EQUATIONS

Let us consider the Hamiltonian equations corresponding to the Hamiltonian (3.11). The small part of this Hamiltonian is the following trigonometric polynomial of φ:

$$H_1 = H_{10} + \sum_{k=1}^{3}(H_{1k}\cos k\varphi + H_{1k}^*\sin k\varphi) = H_{10} + H_{11}. \tag{4.1}$$

Up to terms on the order of ε, the Hamiltonian equations take the form

$$\begin{aligned}
\dot\varphi &= \frac{\partial H}{\partial J} = \omega_0 + \varepsilon\frac{\partial(H_{10} + H_{11})}{\partial J},\\
\dot J &= -\frac{\partial H}{\partial \varphi} = -\varepsilon\frac{\partial H_{11}}{\partial \varphi},\\
\dot z &= \frac{\partial H}{\partial p_\parallel} = p_\parallel + \varepsilon\frac{\partial(H_{10} + H_{11})}{\partial p_\parallel},\\
\dot p_\parallel &= -\frac{\partial H}{\partial z} = -\varepsilon J\frac{\partial \omega_0}{\partial(\varepsilon z)},\\
\dot y_L &= \frac{\partial H}{\partial x_L} = \varepsilon\frac{\partial(H_{10} + H_{11})}{\partial x_L},\\
\dot x_L &= -\frac{\partial H}{\partial y_L} = -\varepsilon\frac{\partial(H_{10} + H_{11})}{\partial y_L}.
\end{aligned} \tag{4.2}$$

It is important that the z variable that enters the Hamiltonian only through the product εz. Therefore, in the expression for $\partial H/\partial z$, it is sufficient to keep only the term $\partial H_0/\partial z$. Moreover, one may introduce the new variable $\zeta = \varepsilon z$, which satisfies the equation $\dot\zeta = \varepsilon p_\parallel$ with the prescribed accuracy. Taking this equation instead of the third equation in set (4.2), we obtain the set of equations with one fast phase φ and thus, we can apply the averaging method. We will use the same notation for the slow variables and their evolutionary components, which is acceptable in the first-order approximation. The averaged equations are obtained by neglecting the terms depending on $\dot J$ in the last four equations in set (4.2). Then, these equations take the form

$$\begin{aligned}
\dot\zeta &= \varepsilon p_\parallel,\\
\dot p_\parallel &= -\varepsilon J\frac{\partial \omega_0}{\partial \zeta},\\
\dot y_L &= \varepsilon(p_\parallel F_5 y_L + p_\parallel^2 F_1 + JF_7),\\
\dot x_L &= -\varepsilon(p_\parallel F_5 x_L + 2p_\parallel F_4 y_L + p_\parallel^2 F_2 + JF_6).
\end{aligned} \tag{4.3}$$

The averaged equation for the variable J is $\dot J = 0$. Hence, the equality $J = J(0)$ is valid up to terms on the order of ε at times on the order of $1/\varepsilon$. This means that J is an adiabatic invariant (this fact must be proven in the case of non-Hamiltonian equations; see, for example, [3]). Thus, $J = J(0) = \text{const}$ in Eqs. (4.3).

Now, we will show that Eqs. (4.3) are integrable in quadratures. The first two equations have an integral describing the conservation law for the energy of the particle correct to the large terms

$$\frac{1}{2}p_\parallel^2 + J\omega_0 = h_0, \tag{4.4}$$

where $h_0 = \text{const}$. Using this formula, we can express $p_\parallel$ in terms of ζ:

$$p_\parallel = \sqrt{2(h_0 - J\omega_0)}. \tag{4.5}$$

Substituting expression (4.5) into the first equation in set (4.3), we obtain the quadrature

$$\int_{\zeta_0}^{\zeta}\frac{d\xi}{\sqrt{2(h - J\omega_0)}} = \tau - \tau_0, \quad \tau = \varepsilon t. \tag{4.6}$$

Inverting expression (4.6), we can find $\zeta(\tau)$ and then, $p_\parallel(\tau)$. As a result, we arrive at a first-order linear equation with known coefficients, which is obviously integrable in quadratures. After $y_L(\tau)$ is found, we can obtain $x_L(\tau)$ by solving another first-order linear equation with known coefficients. Thus, the problem of particle motion in a weakly inhomogeneous magnetic field is solved in the first-order approximation. It turns out that solving the problem does not require additional

assumptions on the existence of the longitudinal and transverse adiabatic invariants.

However, the solution of a particular problem may encounter difficulties related to introducing the use of the coordinates Q^1, Q^2, and Q^3 and calculating the above quadratures. The first difficulty is overcome if we know two integrals of the field line equations [2]. In any case, the calculation of geometric characteristics is highly simplified by considering a thin field line tube. The solution of the linear equations and the calculation of the quadratures can be simplified if we take ζ as a new variable in set (4.3), find $p_\parallel(\zeta)$ from expression (4.5), and solve the linear equations for $y_L(\zeta)$ and $x_L(\zeta)$. Then, the quadratures determining the time dependence then must be calculated only at the end of the solution procedure.

It is also of interest (see, e.g., [2, 3]) to consider the case in which, in addition to the Lorentz force, an order of magnitude weaker the Coulomb force caused by a weakly inhomogeneous electric field acts on a particle. In this case, Hamiltonian (2.3) takes the form

$$H = \frac{1}{2}g^{ik}(p_i - A_i)(p_k - A_k) - U(\varepsilon q^1, \varepsilon q^2, \varepsilon q^3), \quad (4.7)$$

where U is proportional to the scalar potential.

After the variables are changed in (3.11), the following additional term will appear in expression (3.11)

$$-U_0 - \varepsilon(U)_1\sqrt{\frac{g^{11}}{\omega_0}}(\sqrt{2J}\cos\varphi + y_L) + \varepsilon(U)_2\left[\frac{g^{12}}{\sqrt{g^{11}\omega_0}}\right. \quad (4.8)$$
$$\left.\times(\sqrt{2J}\cos\varphi + y_L) - \sqrt{\frac{\omega_0}{g^{11}}}(\sqrt{2J}\sin\varphi + x_L)\right].$$

Here,

$$U_0 = U(0, 0, \varepsilon z),$$
$$(U)_i = \left(\frac{\partial U}{\partial(\varepsilon q^i)} - g_{i3}\frac{\partial U}{\partial(\varepsilon q^3)}\right)_0, \quad (4.9)$$

and the other designation is the same as in Eqs. (3.6) and (3.7).

After averaging the Hamiltonian equations, in the first-order approximation, instead of set (4.3), we obtain:

$$\dot\zeta = \varepsilon p_\parallel, \quad \dot p_\parallel = -\varepsilon\left(J\frac{\partial\omega_0}{\partial\zeta} + \frac{\partial U_0}{\partial\zeta}\right),$$
$$\dot y_L = \varepsilon(p_\parallel F_5 y_L + p_\parallel^2 F_1 + JF_7 + G_1), \quad (4.10)$$
$$\dot x_L = -\varepsilon(p_\parallel F_5 x_L + 2p_\parallel F_4 y_L + p_\parallel^2 F_2 + JF_6 + G_2),$$

where

$$G_1 = \sqrt{\frac{\omega_0}{g^{11}}}(U)_2,$$
$$G_2 = -\sqrt{\frac{g^{11}}{\omega_0}}(U)_1 - \frac{g^{12}}{\sqrt{g^{11}\omega_0}}(U)_2. \quad (4.11)$$

The first two equations in set (4.10) have the integral

$$\frac{1}{2}p_\parallel^2 + J\omega_0 + U_0 = h_0. \quad (4.12)$$

With the help of this integral, the relation between ζ and τ can be derived in a quadratures form. The last two equations in set (4.10) differ from the corresponding equations in set (4.3) only by the terms $G_1(\zeta)$ and $G_2(\zeta)$, and can be integrated as described above.

REFERENCES

1. G. V. Stupakov, Pis'ma Zh. Éksp. Teor. Fiz. **36**, 318 (1982) [JETP Lett. **36**, 387 (1982)].
2. T. G. Nothrop, *The Adiabatic Motion of Charged Particles* (Interscience, New York, 1963; Atomizdat, Moscow, 1967).
3. V. M. Volosov and B. I. Morgunov, *Averaging Method in Theory of Nonlinear Oscillating Systems* (Mosk. Gos. Univ., Moscow, 1971).

Translated by V. Gurskiĭ

Technical Physics, Vol. 46, No. 1, 2001, pp. 20–23. Translated from Zhurnal Tekhnicheskoĭ Fiziki, Vol. 71, No. 1, 2001, pp. 22–25.

SOLIDS

Equation of State at the Adiabat of Unloading

I. K. Kokhanenko and E. M. Levchenko

Received December 20, 1999

Abstract—On the assumption that condensed matter at high pressures and temperatures behaves as an ideal gas, a functional dependence of the adiabatic exponent on the Grüneisen constant was obtained, as well as an equation of state that relates the velocity of the shock front and the mass velocity in the shock wave. The calculated estimates of the rate of unloading for cadmium, tin, aluminum, and iron are given as functions of the mass velocities. A comparison with experimental data shows that such an equation of state sufficiently well describes the behavior of the substance and can be used instead of the conventional semiempirical dependences.

INTRODUCTION

In studies of high-velocity shock effects and in the related investigations of the equation of state of substances at high-intensity loading (shock loading, explosion on a surface, effect of high-power radiation fluxes), as well as in studies of extremal states, it is important to know the exponent of the adiabat of the vapors upon subsequent expansion. The dynamical methods of the investigation of properties permit one to determine only the pressure p, density ρ, and internal energy as functions of the pressure and volume of the system. But this information is insufficient to obtain the equation of state, since it does not contain information on thermodynamic quantities such as the temperature and entropy of the shock-compressed substance. In some cases, the measurement of these quantities by optical methods is impossible. However, the entropy and the temperature can be determined from the parameters of the final state of the substance upon its isentropic expansion [1], if the adiabatic exponent is known. In this connection, the success of theoretical studies of expansion of the vapors of solids is determined to a great extent by knowledge of the adiabatic exponent γ.

In addition, there exist theoretical dependences [2, 3] that in limiting cases link the shock-front velocity D and the mass velocity u if the adiabatic exponent is known. In the model where the pressures and densities are determined from the corresponding equations of conservation, they are used as equations of state. However, theoretical dependences by no means always satisfactorily describe the real behavior of a substance; therefore, as a rule, the numerically calculated or experimentally obtained curves are approximated by this or that technique [2, 4]. In this connection, it is of interest to find and substantiate an adequate theoretical dependence for $D(u, \gamma)$. In this work, we solved the problem of determining the adiabatic exponent as a function of the Grüneisen constant and the $D(u, \gamma)$ dependence that agrees with experimental results.

FORMULATION OF PRINCIPAL DEPENDENCES

Slater, Landau, and Stanyukovich used the relationship between the Grüneisen constant and the function of cold compression [3]. Since the Grüneisen constant is known for many substances, the dependences given in [3] are constructive and can be used in numerous applications. In [2–4], when considering two-dimensional self-similar model problems of lumped and filamentary shocks, the adiabatic and self-similarity exponents were determined in combination from the results of a computational experiment. But in order to determine the adiabatic exponent of a gas cloud, unlike the problem of investigating equation of state under high-intensity dynamical loads considered in [3], one should study not only the shock adiabat, but also the expansion isentrope. Since, because of the isentropic character of the process, the entropy in the unloading waves is equal to that of the shocked (compressed) state, we are able to obtain, assuming that the adiabatic exponent remains unaltered and based on the study of the equation of motion of the polytropic gas, a functional dependence between the adiabatic exponent and the degree of compression.

The results of experiments carried out in [4–8] confirm that at terapascal pressures (greater than 100–200 Mbar) the individuality of a substance can be characterized by an electron analog of the Grüneisen constant. In the range of extreme pressures (extremal states of the substance), the pressure dependence exhibits an asymptotic behavior and the relationship between the adiabatic exponent and the Grüneisen constant has the form $\beta = \gamma - 1$ [3]. However, in the range of pressures of about several megabars, one should also know the physical quantities that primarily characterize the indi-

1063-7842/01/4601-0020$21.00

vidual properties of the substance. The adiabatic expansion after the passage of strong shock waves drives the substance into a state that is characterized by a wide spectrum of its own (intrinsic only in it) properties. The near-critical states of normal metals (the high-temperature portion of their boiling curves) have been intensely studied both experimentally and theoretically. In such investigations, the specific features of the processes of boiling and condensation upon adiabatic expansion are very informative and are of great importance.

Sometimes, the use of a certain "effective" value of the adiabatic exponent $\gamma \approx 2$ up to pressures of 2–4 Mbar upon the investigation of problems of spalling strength of structural materials under the effect of high-power radiation fluxes and dynamical factors leads to useful conclusions. However, in the region of high temperatures and pressures, in which the condensed substance behaves as an ideal gas, such an approach may be unjustified. This is related to the fact that the value of the slope of the shock adiabat, $\lambda = 3/2$, usually assumed in calculations is measured in experiments at relatively small amplitudes, i.e., under conditions where the mass velocity u is significantly smaller than the sound velocity $c_0 (u \ll c_0)$. Therefore, if the initial slope is $\lambda = 3/2$, this does not mean that at large degrees of compression and heating the adiabatic exponent will also be equal to $\gamma = 2$.

The problem of finding the dependence for a pressure range of several megabars is solved on the basis of studying the equation of motion of a polytropic gas

$$p_t + up_x + \gamma p u_x = 0, \tag{1}$$

where x and t are the coordinates and time and u is the velocity of the substance.

Its solution can easily be found in the form

$$\begin{aligned} u &= (u_1 - u_0)H(x - Dt) + u_0, \\ p &= (p_1 - p_0)k(x - Dt) + p_0, \end{aligned} \tag{2}$$

where $H \neq k$ are the Heaviside functions as they are understood in the new theory of generalized functions [9] and p_0, ρ_0, u_0, p_1, ρ_1, and u_1 are the values of the unperturbed (subscript "0") pressure, density, and velocity of the substance and those observed behind the shock-wave front (subscript "1"), respectively.

Let the pressure p change in the vicinity of the point of intersection of the wave ray, shock adiabat, and expansion isentrope in the p–u diagram in such a manner that the coefficient in front of u_x in (1) satisfies the equality

$$\gamma p = \gamma_1 p_1 = \gamma \delta^{-1} p_1 = \text{const}, \tag{3}$$

where $\delta = \rho_1/\rho_0$.

Then, after the substitution of (2) into (1), we obtain

$$\begin{aligned} &[(D - u_0) - (u_1 - u_0)H]k' \\ &= \frac{u_1 - u_0}{p_1 - p_0}\gamma\delta^{-1}p_1 H', \quad p_1 \neq p. \end{aligned}$$

However, it is known that

$$\begin{aligned} (D - u_0) &= u_1 - u_0 + \rho_0 \frac{u_1 - u_0}{\rho_1 - \rho_0} \\ &= \left(1 + \frac{\rho_0}{\rho_1 - \rho_0}\right)(u_1 - u_0), \quad \rho_1 \neq \rho_0. \end{aligned} \tag{4}$$

Therefore, we have

$$k' = \frac{-\gamma\delta^{-1}p_1}{p_1 - p_0} \frac{H'}{H - \left(1 + \dfrac{\rho_0}{\rho_1 - \rho_0}\right)}. \tag{5}$$

After integration of the left-hand and right-hand sides of equality (5), we obtain

$$k = \frac{-\gamma\delta^{-1}p_1}{p_1 - p_0} \ln\left|\frac{\rho_1}{\rho_1 - \rho_0} - H\right| + c. \tag{6}$$

Here, the integration constant c is calculated from the definition of the Heaviside function. If its representative is denoted $R(x, \varepsilon)$, where ε is an infinitely small positive quantity, then we have

$$\forall \varepsilon > 0, \quad \exists A(\varepsilon)\ R(\varepsilon, x) = 0 \quad \text{at} \quad x < -A(\varepsilon),$$

and it follows from (6) that

$$c = \frac{\gamma\delta^{-1}p_1}{p_1 - p_0} \ln\left|\frac{\rho_1}{\rho_1 - \rho_0}\right|. \tag{7}$$

Here, $A(\varepsilon)$ is a certain interval. Similarly, if $\forall \varepsilon > 0$, and $\exists A(\varepsilon)$ and $R(\varepsilon, x) = 1$ at $x > A(\varepsilon)$, then expression (6) transforms into

$$\begin{aligned} &\frac{-\gamma\delta^{-1}p_1}{p_1 - p_0} \ln\left|\frac{\rho_1}{\rho_1 - \rho_0} - 1\right| \\ &+ \frac{\gamma p_1}{p_1 - p_0} \ln\left|\frac{\rho_1}{\rho_1 - \rho_0}\right| = 1 \end{aligned} \tag{8}$$

or

$$\frac{p_1 - p_0}{\gamma p_1}\delta = \ln\left|\frac{\rho_1}{\rho_0}\right|. \tag{9}$$

It is known that the degree of compression is related to the Grüneisen constant as follows [5]:

$$\delta = 1 + \frac{2}{\beta}.$$

Since $p_1 \gg p_0$, then at $p_1 \gg 1$, with allowance for this

relation and for (9), we obtain

$$\gamma = \frac{1 + \frac{2}{\beta}}{\ln\left|1 + \frac{2}{\beta}\right|}. \quad (10)$$

If we replace restriction (3) by more rigid conditions $\gamma p = \gamma p_1 = \text{const}$ and perform transformations analogous to those considered above, we obtain a new expression for the adiabatic exponent:

$$\gamma = \frac{1}{\ln\left|1 + \frac{2}{\beta}\right|}. \quad (11)$$

The corresponding expression (9) will now differ from the written one in that in its left-hand side the degree of compression is equal to unity.

From (11), with allowance for this modified expression (9), we now can easily obtain, using the continuity equation, a functional dependence of the shock-front velocity on the mass velocity in the form

$$D = [1 - \exp(-1/\gamma)^{-1}]u. \quad (12)$$

It is known that the shock-front parameters are expressed through the shock-front velocity with the help of the limiting formulas for a strong shock wave [2]. In particular, the velocity behind the shock front is related to D by the relationship [2, 3]

$$D = \frac{\gamma + 1}{2}u. \quad (13)$$

We can show that the dependence (12) with adiabatic exponent (11) is equivalent to the well-known expression (12) with γ calculated for an ideal gas with a constant heat capacity; i.e., $\gamma = \beta + 1$.

The problem of deriving the dependence of the front velocity on the mass velocity corresponding to (3) and (10) is more complex. Designating $u/D = \alpha$, we obtain from (10)

$$\gamma = \frac{1}{(1 - \alpha)\ln\frac{1}{1 - \alpha}}.$$

Now, approximating this dependence by a parabola in the range $0.4 < \alpha < 0.5$ of practical interest, we obtain

$$D = \frac{u}{0.6 - 0.5(0.32\gamma - 0.90)^{0.5}}. \quad (14)$$

The functional dependences (10)–(12) and (14) represent a solution to the problem stated above.

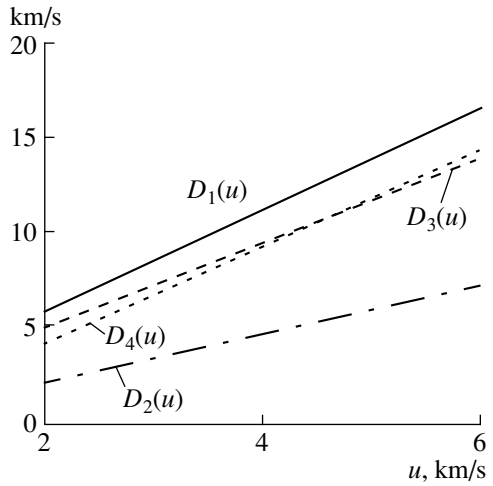

Figure.

COMPARISON WITH EXPERIMENT

In order to confirm the adequacy of these dependences, we performed a comparison with the experimental results given in [1]. From the relations obtained, we calculated the velocities upon unloading for Cd, Sn, Al, and Fe; similar calculations were also carried out for the limiting relation (13) and for the dependence

$$D = u\sqrt{\frac{2\gamma}{\gamma - 1}},$$

which is characteristic of the adiabatic expansion of a gas sphere into vacuum.

The experimental results were approximated by parabolas. Since the latter may be of independent interest, they are given below:

$$D = 1.73 + 0.12u + 0.57u^2 \text{ for Cd,}$$

$$D = 0.81 + 1.83u + 0.24u^2 \text{ for Sn, and}$$

$$D = 0.06 + 1.75u + 0.11u^2 \text{ for Al.}$$

The parabola for Fe was taken from [10]. In the figure, the $D(u)$ dependences for aluminum are given. The subscripts 1–4 at D mean the dependences for the adiabatic expansion of a gas sphere given by relations (12), (13), and (14) and by the experimental curve for the velocity of expansion [1], respectively. Analogous graphs were also constructed for the other metals that were studied (Cd, Sn, Fe); they are analogous and therefore are not given here.

It is seen from the graphs that the experimental curve $D_4(u)$ obtained in the unloading waves is close to $D_3(u)$ plotted from the theoretical relation (14) with an adiabatic exponent calculated by (10).

Numerical estimates also showed that the value $\gamma = 1.33$, which is assumed in calculations [2] with allowance for ionization, yields for Cd, Sn, Al, and Fe a significant (by a factor of about 2, see figure) difference in the velocities of isentropic expansion $D_2(u)$ as compared to the results of calculations (individually for each metal) by formulas (10) and (14). The discrepancies between the velocity of isentropic expansion in the

limiting case of $\gamma = 1.67$ [2, 7, 8] and the experiment [1] are less significant and are different for different metals. Note that these discrepancies correlate with the binding energies. The straight line $D_1(u)$ for the adiabatic expansion of the gas sphere upon the limiting value of $\gamma = 1.67$ is close to the curve obtained from (14).

Taking into account the model character of relations (10)–(12) and (14), the obtained degree of coincidence of the velocities in the unloading waves can be considered satisfactory. Therefore, the model of the polytropic gas on the assumption that the change in the product of the adiabatic exponent and pressure is proportional to the degree of compression describes the equation of state of structural materials sufficiently well in the range of pressures of up to several megabars.

REFERENCES

1. A. A. Bakanova, I. P. Dudoladov, M. V. Zhernokletov, *et al.*, Prikl. Mekh. Tekh. Fiz. **177** (2), 177 (1983).
2. Ya. B. Zel'dovich and Yu. P. Raĭzer, Zh. Tekh. Fiz. **35**, 1402 (1958).
3. Ya. B. Zel'dovich and Yu. P. Raĭzer, *Physics of Shock Waves and High-Temperature Hydrodynamic Phenomena* (Nauka, Moscow, 1966; Academic, New York, 1966).
4. Yu. P. Raĭzer, Prikl. Mekh. Tekh. Fiz. **57**, 1741 (1963).
5. *Properties of Condensed Substances at High Pressures and Temperatures*, Ed. by R. F. Trunin (VNIIÉF, Arzamas-16, 1992).
6. *Physical Quantities: Handbook*, Ed. by I. S. Grigor'ev and E. Z. Meĭlikhov (Énergoizdat, Moscow, 1991).
7. R. F. Trunin, Usp. Fiz. Nauk **164** (11), 1215 (1994) [Phys. Usp. **37**, 1123 (1994)].
8. E. N. Avrorin, B. K. Vodolaga, V. A. Simonenko, and V. E. Fortov, Usp. Fiz. Nauk **163** (5), 1 (1993) [Phys. Usp. **36**, 337 (1993)].
9. Yu. V. Egorov, Usp. Mat. Nauk **275** (5), 3 (1990).
10. J. D. O'Keefe and Th. J. Ahrens, in *Lunar Science VI: Abstracts and Papers Submitted to the Sixth Lunar Science Conference, Houston, 1975*, p. 2831.

Translated by S. Gorin

Technical Physics, Vol. 46, No. 1, 2001, pp. 24–28. Translated from Zhurnal Tekhnicheskoĭ Fiziki, Vol. 71, No. 1, 2001, pp. 26–30.

SOLIDS

Phase Diagram and Physical Properties of the Sodium Niobate–Lithium Niobate–Cadmium Niobate Three-Component System

L. A. Reznichenko, O. N. Razumovskaya, L. A. Shilkina, A. Ya. Dantsiger, S. I. Dudkina, I. V. Pozdnyakova, and V. A. Servuli

Research Institute of Physics, Rostov State University, pr. Stachki 194, Rostov-on-Don, 344090 Russia

e-mail: larisa@riphys.rnd.su

Received October 19, 1999; in final form, May 5, 2000

Abstract—The phase diagram of the $(Na,Li,Cd_{0.5})NbO_3$ ternary system is refined. The electrical properties of solid solutions over a broad range of the component concentrations were studied. The compositions promising for high-temperature transducers were obtained. © *2001 MAIK "Nauka/Interperiodica".*

INTRODUCTION

In this paper, we refine information on the phase transitions and physical properties of the $(Na,Li,Cd_{0.5})NbO_3$ system studied in [1]. The refined phase diagram of this ternary system enabled a more detailed interpretation of its properties. Similar to [1], we considered six cross sections with a content of the *z* component, $Cd_{0.5}NbO_3$, from 5 to 20 mol %. In each of the sections, we synthesized compounds corresponding to the *y* sections with 1–15 mol % of $LiNbO_3$. Synthesis and sintering conditions were presented in [1].

RESULTS AND DISCUSSION

We studied the phase diagram region adjacent to the $NaNbO_3$ vertex (Fig. 1). Thin lines depict the *y* and *z* sections, and thick lines represent interfaces between regions of different symmetry (single-, two-, and three-phase).

The phase diagram of the ternary system is consistent with those of the associated binary systems. In $(100 - z)NaNbO_3 - zCd_{0.5}NbO_3$ [2], solid solutions (SS) form up to $z = 25$. In the range of $0 < z < 15$, SS have rhombic symmetry. The unit cell parameters are related to the parameters of the perovskite monoclinic cell *a*, *b*, and β through the following expressions: $A = 2a\cos\beta/2$, $B = 4b$, and $C = 2a\sin\beta/2$ (the M_4 phase). At $z \cong 15$, the multiplicity factor for *B* changes: $B = 2b$ (the M_2 phase). In the range of $19 < z \le 25$, SS have tetragonal symmetry (the *T* phase); we failed to reveal superstructures here because of the very weak reflections from impurity phases in the X-ray diffraction patterns. The M_2 and *T* phases are separated by the broad region of their coexistence.

In the $(100 - y)NaNbO_3 - yLiNbO_3$ system [3], as *y* grows, SS of different symmetry arise in the following sequence: rhombic M_4 $(0 < y < 3.5)$ ⟶ rhombic M_2 $(4 \le y \le 10.5)$ ⟶ rhombohedral *Rh* $(12 \le y \le 12.5)$ ⟶ rhombic M_2 $(12.5 < y < 14)$. The monophase regions are separated by regions of phase coexistence. With a further increase in *y*, a broad heterogeneous region is observed where, along with the $NaNbO_3$-based SS, $LiNbO_3$ is present. Accordingly, the area adjacent to the $NaNbO_3$ vertex of the ternary phase diagram is divided into several regions of SS crystallization: broad single-phase M_2, M_4, and *T* regions; narrow single-phase *Rh* and M_2 regions; broad two-phase $M_2 + Rh$, $M_2 + T$, and $T + Rh$ regions; narrow two-phase $M_2 + M_4$ and $Rh + M_2$ regions; and a three-phase $M_2 + T + Rh$ region.

We considered the uniform deformation parameter δ [4] and the electrical parameters of the SS in the *y* and *z* sections. The electrical parameters of different ferroelectric SS containing morphotropic regions (MRs) are known [5–7] to exhibit extrema that are located in the vicinity of MRs and correlate with the structure parameters, in particular, with δ.

In this system, sections crossing the greatest number of phases and MRs have been studied most extensively. Among the *z* sections, such is the cross section $z = 5$. It goes through three phases: M_4, M_2, and *Rh*; and three MRs: the narrow two-phase MR_1 ($M_2 + M_4$), broad three-phase MR_2 ($M_2 + T + Rh$), and very narrow two-phase MR_3 ($Rh + M_2$) (Figs. 2a, 2b).

Figure 2a presents the concentration dependences of δ, the relative permittivities $\varepsilon/\varepsilon_0$ and $\varepsilon_{33}^T/\varepsilon_0$, the electro-

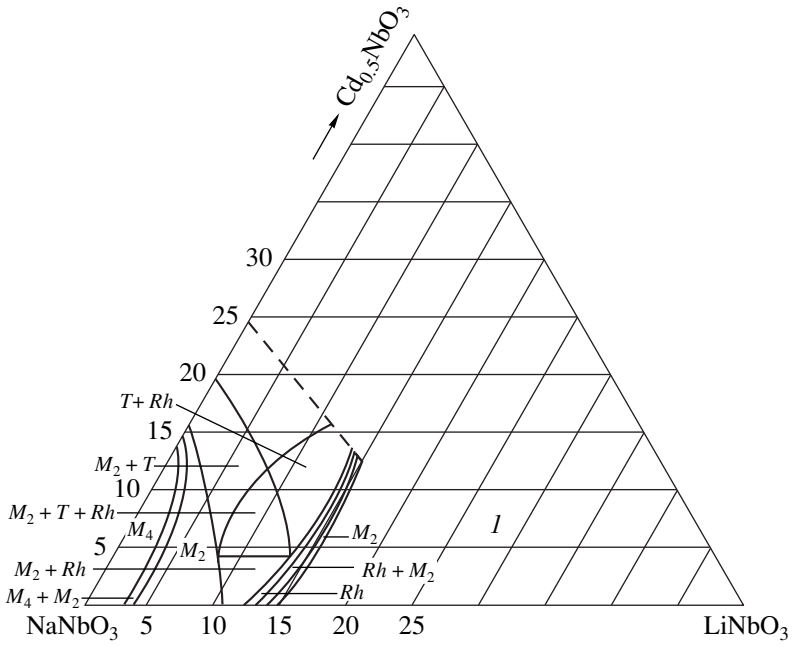

Fig. 1. Phase diagram of the ternary $(Na,Li,Cd_{0.5})NbO_3$ system (*1*, heterogeneous region).

mechanical coupling coefficient K_p, and the piezoelectric parameters d_{31} and g_{31}. Figure 2b shows these dependences for the dielectric loss tangent $\tan\delta$, the mechanical Q factor Q_M, the sound velocity V_R, and Young's modulus Y_{11}^E. It is evident from Fig. 2a that the permittivities, as well as K_p and d_{31}, exhibit two maxima: the higher maxima approach the center of the three-phase MR_2, and the lower ones are located at the right edge of the narrow MR_1. The positions of the latter maxima with respect to the MR_1 cannot be considered accurate, since the measurement step was rather large, 2 mol %, whereas the MR_1 width is about 1 mol %. Note also that all of the above-mentioned parameters have minima within the M_2 phase.

The maxima of the piezoelectric parameter g_{31}, which is known to be proportional to the residual polarization P_r, are shifted to the left of both MRs toward the M_2 and M_4 phases (in the M_4 phase, this maximum is incomplete due to a lack of appropriate samples). Such positions of the g_{31} maxima are typical of ferroelectric systems [5, 6].

The above dependences of the electrical parameters correlate with the run of δ, which has a minimum in both MRs and peaks in the M_2 phase.[1]

It is worth noting that the higher maximum of $\varepsilon_{33}^T/\varepsilon_0$ in Fig. 2a is not beyond the right edge of the broad MR_2, which is common [5, 6], but lies within it. The same situation was observed for several cross sections of the $(Na,Li,Pb_{0.5})NbO_3$ system [7]. This fact was attributed [7], in particular, to the coexistence of the *M* and *Rh* phases, resulting in a considerable increase in the number *N* of possible directions of the spontaneous polarization ($N = 8(Rh) + 12(M) = 20$) compared with that in the monophase regions. (In PZT-based systems [5, 6], this number is considerably smaller, $N = 8(Rh) + 6(T) = 14$, and virtually does not affect the position of the $\varepsilon_{33}^T/\varepsilon_0$ maximum.) In the three-phase MR_2, *N* is still greater, $N = 8(Rh) + 12(M) + 6(T) = 26$, which markedly increases the orientation part of the permittivity inside the MR and affects the position of $\varepsilon/\varepsilon_0$ and $\varepsilon_{33}^T/\varepsilon_0$ peaks. This in turn influences the maxima of K_p and d_{31}, which are much less affected by g_{31} (in addition, the g_{31} values are small in this system). The same is also observed in the narrow MR_1, where $N = 12(M_2) + 12(M_4) = 24$ and the maximum of $\varepsilon_{33}^T/\varepsilon_0$ has a greater effect on K_p and d_{31} than that of g_{31}.

The concentration dependences of $\tan\delta$, Q_M, V_R, and Y_{11}^E (Fig. 2b) can be explained in terms of SS ferroelectric elasticity, which characterizes the domain stability to external actions [5]. According to [5], with a growth of the ferroelectric elasticity, δ, Q_M, V_R, and Y_{11}^E increase, while $\varepsilon_{33}^T/\varepsilon_0$ and $\tan\delta$ decrease. That is the reason why the maxima and minima of $\varepsilon_{33}^T/\varepsilon_0$ and $\tan\delta$ are close to each other (Fig. 2b), whereas the max-

[1] The effect of the MR_3 on the concentration dependences of the parameters is hard to include, because this region is extremely narrow.

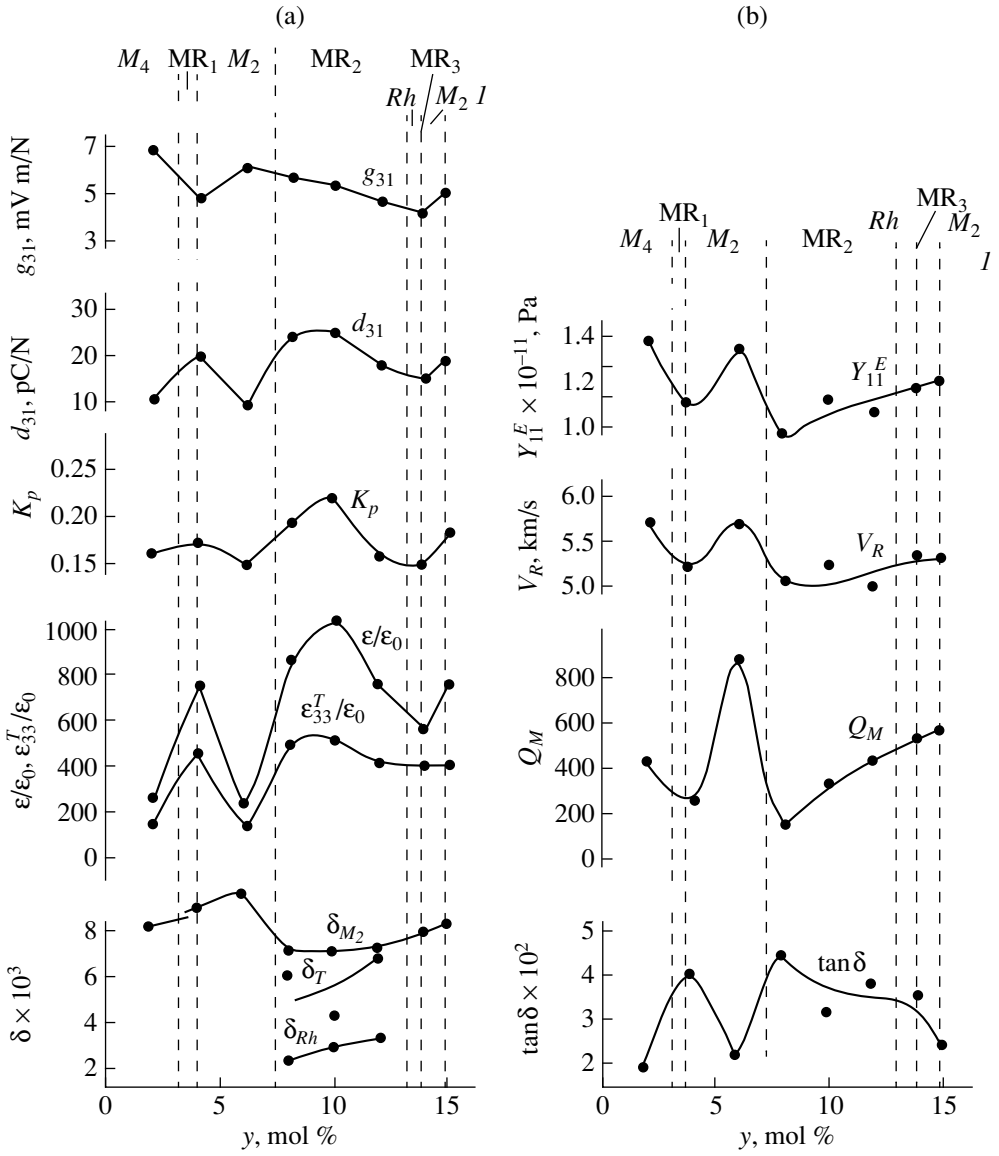

Fig. 2. Structure and electrical parameters of (Na,Li,Cd$_{0.5}$)NbO$_3$ solid solutions versus LiNbO$_3$ content in the cross section z = 5 mol % Cd$_{0.5}$NbO$_3$ (*1*, heterogeneous region).

ima of Q_M, V_R, and Y_{11}^E lie near the minimum of $\varepsilon_{33}^T/\varepsilon_0$ (and vice versa).

Among the y sections, the most distinct variations of the parameters occur for y = 4 (Figs. 3a, 3b). This section crosses two phases, M_2 and T, and two MRs, the broad MR$_1$ (T + M_2) and narrow MR$_2$ (M_4 + M_2) (Fig. 1). In Fig. 3a, the run of the curves near and inside the broad MR$_1$ is typical of ferroelectric systems [5, 6]: the incomplete peak of $\varepsilon_{33}^T/\varepsilon_0$ is shifted to the MR$_1$ right edge and the maximum of g_{31} is shifted to its left edge (beyond the MR$_1$); K_p and d_{31} peak at the center of the MR. As the edge of the narrow MR$_2$ is approached, the parameters $\varepsilon/\varepsilon_0$, $\varepsilon_{33}^T/\varepsilon_0$, K_p, and d_{31} increase. Such behavior correlates with the run of the δ curve.

Parameters of (Na,Li,Cd$_{0.5}$)NbO$_3$ compounds

Compound no.	T_k, °C	$\varepsilon_{33}^T/\varepsilon_0$	K_p	g_{31}, mV m/N	Q_M	V_R, km/s
1	365	195	0.13	5.1	670	5.8
2	395	1070	0.28	6.2	225	5.8
3	400	295	0.14	4.4	560	5.6
4	420	520	0.22	5.4	340	5.2
5	430	415	0.18	5.1	560	5.3

The parameters Q_M, V_R, and Y_{11}^E (Fig. 3b) vary in the direction opposite to $\varepsilon/\varepsilon_0$ and $\varepsilon_{33}^T/\varepsilon_0$, whereas

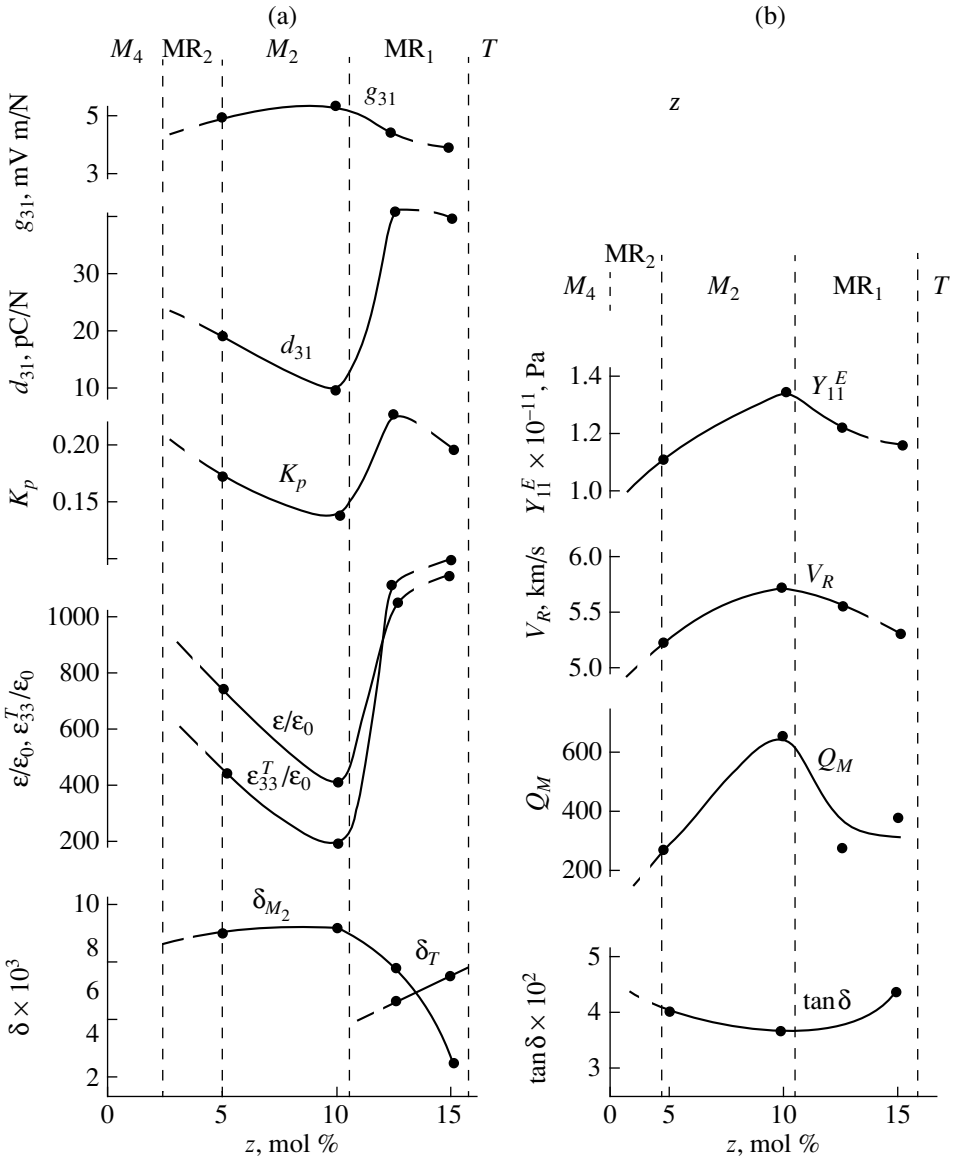

Fig. 3. Structure and electrical parameters of (Na,Li,$Cd_{0.5}$)NbO_3 solid solutions versus $Cd_{0.5}NbO_3$ content in the cross section y = 4 mol % $LiNbO_3$.

tanδ varies similarly to the permittivities. This is consistent with the variations of the SS ferroelectric elasticity.

Our system, like most niobate systems, is of low density and offers high sound velocity, which makes them promising for some applications [6]. Of practical interest also are the high Curie temperature T_C (≥400°C) and the broad range of the permittivity (from 160 to 1000–1200) coupled with good piezoelectric properties. Such a combination is favorable for their application in high-temperature transducers operating at high and medium frequencies. The properties of several compounds are listed in the table.

CONCLUSION

Precise X-ray diffraction studies of solid solutions in the (Na,Li,$Cd_{0.5}$)NbO_3 system allowed us to accurately determine the crystallizing phase symmetry, structural phase transitions, and morphotropic region morphology.

The electrical properties of the solid solutions were studied in a wide range of the component concentrations, and their relation to the structure parameters, in particular, uniform deformation parameter, was set. Compounds combining a high Curie temperature, a broad range of the permittivity, and good piezoelectric parameters were obtained. They are candidates for

high-temperature transducers operating at high and medium frequencies.

ACKNOWLEDGMENTS

This work was supported in part by the Russian Foundation for Basic Research, project no. 99-02-17575.

REFERENCES

1. E. G. Fesenko, L. A. Reznichenko, L. S. Ivanova, *et al.*, Zh. Tekh. Fiz. **55**, 601 (1985) [Sov. Phys. Tech. Phys. **30**, 354 (1985)].
2. B. Lewis and E. A. D. White, J. Electron. **1**, 646 (1956).
3. L. A. Shilkina, L. A. Reznichenko, M. F. Kupriyanov, and E. G. Fesenko, Zh. Tekh. Fiz. **47**, 2173 (1977) [Sov. Phys. Tech. Phys. **22**, 1262 (1977)].
4. E. G. Fesenko, V. S. Filip'ev, and M. F. Kupriyanov, Fiz. Tverd. Tela (Leningrad) **11**, 466 (1969) [Sov. Phys. Solid State **11**, 366 (1969)].
5. E. G. Fesenko, A. Ya. Dantsiger, and O. N. Razumovskaya, *Novel Piezoelectric Ceramic Materials* (Rostov. Gos. Univ., Rostov-on-Don, 1983).
6. A. Ya. Dantsiger, O. N. Razumovskaya, L. A. Reznichenko, and S. I. Dudkina, *High-Efficiency Piezoceramic Materials: Optimization of Search* (Paik, Rostov-on-Don, 1995).
7. L. A. Reznichenko, O. N. Razumovskaya, A. Ya. Dantsiger, *et al.*, in *Proceedings of the International Conference "P'ezotekhnika'97," Obninsk, 1997*, pp. 197–207.

Translated by A. Sidorova-Biryukova

Technical Physics, Vol. 46, No. 1, 2001, pp. 29–33. Translated from Zhurnal Tekhnicheskoĭ Fiziki, Vol. 71, No. 1, 2001, pp. 31–35.

SOLIDS

Hydrogen Evolution from Austenitic Steel Irradiated with High-Temperature Pulse Plasma

A. G. Zaluzhnyĭ, B. A. Kalin, V. P. Kopytin, M. A. Kozodaev, and A. L. Suvorov

Institute of Theoretical and Experimental Physics, ul. Bol'shaya Cheremushkinskaya 25, Moscow, 117259 Russia

Received January 26, 2000

Abstract—Evolution of hydrogen from samples of grade 12Kh18N10T austenitic steel that had been electrolytically saturated with hydrogen using the interaction with a deuterium plasma with an energy content of 40–60 kJ/pulse is examined. *© 2001 MAIK "Nauka/Interperiodica".*

INTRODUCTION

When studying samples of austenitic steel 12Kh18N10T after treatment with a deuterium plasma, anomalously large blisters (with caps to ~1 μm thick) [1, 2], containing hydrocarbons, including methane, were observed. Since methane is insoluble in steel, it behaves as an inert gas until its dissociation temperature T_{dis} is reached. Blisters were shown to be destroyed if the methane pressure at temperatures below T_{dis} exceeds the pressure necessary to break blisters. If at the dissociation temperature the methane pressure in blisters is insufficient for them to be broken, the blisters are retained upon further heating.

We suggest a mechanism of the formation of anomalously large blisters that were observed experimentally.

When choosing and designing materials that can serve as candidates for the first wall of fusion reactors, great attention is given to the problem of the interaction of hydrogen isotopes with these materials. This is explained first of all by the ecology requirements (release of tritium into the environmental atmosphere), as well as by the danger of losing expensive fuel, which in turn is determined by the accumulation of tritium in the materials of the first wall. Therefore, the investigation of the retention of hydrogen isotopes by structural materials is a topical problem.

EXPERIMENTAL

The investigation of the kinetics of hydrogen evolution was performed using a high-vacuum mass-spectroscopic device [3] and uniformly heating the samples. The measurement of hydrogen release was carried out using continuous pumping of gases with a NORD-100 pump connected to the working volume of the device through a vacuum pipeline with a throughput of 1.3 l/s for air and 5.0 l/s for hydrogen. The total pressure in the working volume was measured by a VIT-1A vacuum gauge; the partial pressures of gases were measured using an IPDO-2A mass spectrometer.

The electrolytic saturation of samples with hydrogen was performed in boiled distilled water (with an addition of sulfuric acid to increase the water conductivity) at a current density of 50 A/m^2 for 1 h. With this regime, no noticeable damage of the surface layer was observed [4]. Some samples were also saturated with hydrogen by irradiation with four pulses of deuterium plasma (40–60 kJ/pulse) [1].

EXPERIMENTAL RESULTS

When structural materials of the first wall of a fusion reactor are irradiated with fluxes of hydrogen or deuterium plasma, their surface undergoes strong erosion [5]. At large energy contents in the plasma fluxes, mainly surface remelting occurs with no blisters formed. At smaller energy contents, the austenitic steel samples reveal unbroken anomalously large blisters with caps ~1 μm thick, which exceeds by an order of magnitude the range of hydrogen ions of the given energy [1]. Heating to 870 K, i.e., to a temperature close to the critical temperature of the destruction of helium blisters [6], leads only to the development of new, smaller bubbles without destruction and changing dimensions of the previously formed ones [7]. It is only after heating to 1020 K that partial opening of the domes of the largest blisters occurs, but even at 1300 K, many blisters remain unbroken [7].

Upon uniform heating of austenitic steel samples that were electrolytically saturated with hydrogen, the hydrogen-evolution curves exhibit a single peak corresponding to hydrogen releasing from solid solution, as was shown in [8, 9]. Figure 1 displays the curves of thermal desorption of deuterium from steel 12Kh18N10T samples 0.3-mm thick irradiated with four pulses of deuterium plasma with an energy content of 40–60 kJ/pulse. The investigation was performed

1063-7842/01/4601-0029$21.00

3–5 days after irradiation. Curve *2* was obtained for a sample taken from the center of a fuel assembly, where no blisters were present because of the remelting of the sample surface. The kinetic curve of hydrogen evolution obtained for this case completely corresponds to the kinetics of hydrogen release from a sample that was uniformly saturated with hydrogen electrolytically [8, 9]. In curve *1* (obtained using samples from the periphery of the assembly, where blisters were observed), two additional peaks are present apart from the peak related to the diffusional release of deuterium from solid solution, namely a low-temperature peak at ~500 K and a high-temperature one at ~900 K. These peaks can be due to the release of hydrogen from blisters, where it can be present in the molecular form or in the form of chemical compounds, e.g., hydrocarbons.

In order to confirm the above assumptions, we consider the kinetics of the evolution of molecular hydrogen from blisters. It was shown in [10, 11] that, for objects such as blisters, upon their degassing, the hydrogen concentration in the blister caps decreases linearly when approaching the surface; i.e., a hydrogen distribution characteristic of the experiments on hydrogen permeability in the regime of a steady-state flow is established. Therefore, for a hydrogen flux from blisters per unit area of the sample surface, we can write

$$I = \bar{S}(P/h)\sqrt{p} = (\bar{S}/h)P_0\exp(-E/RT)\sqrt{p}, \quad (1)$$

where $\bar{S}$ is the fraction of the surface that is occupied by blisters, P is the permeability coefficient, E is the activation energy for the permeability, h is the blister-cap thickness, and p is the molecular-hydrogen pressure in blisters.

Neglecting the escape of hydrogen from blisters into the bulk of the sample and knowing the rate of pumping of the system, we can compute a thermodesorption curve. The computations of the thermodesorption curves for the case of linear heating at a rate of 0.3 K/s

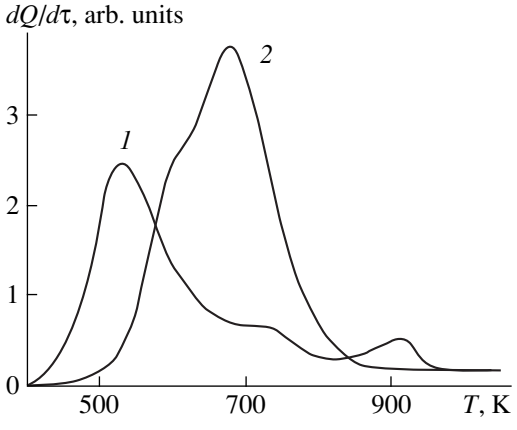

Fig. 1. Variation of the rate of deuterium thermodesorption in the process of uniform heating of the samples of steel 12Kh18N10T as a function of the heating temperature after treating with four plasma pulses.

for blisters with caps 0.1 μm thick and the pressure of gaseous hydrogen of 50 MPa (the maximum possible gas pressure in blisters [12]) gave the following results. When the calculations were performed by using the permeability parameters characteristic of austenitic steels [13], a curve with a maximum at 320 K was obtained. In this case, the redissolution of hydrogen from blisters should occur at room temperature.

Let us write Eq. (1) for the maximum temperature T_m and for any temperature T_n at the descending or ascending branches of the peak, where the gas release is lower than that in the maximum point by a factor of n:

$$I_m = (\bar{S}/h)P_0\exp(-E/RT_m)\sqrt{p_m},$$

$$I_n = I_m/n = (\bar{S}/h)P_0\exp(-E/RT_n)\sqrt{p_n}.$$

Here, p_m and p_n are the pressures of gas in blisters at the temperatures T_m and T_n, respectively. Dividing one equation by the other, we obtain the following expression for the activation energy for the permeability:

$$E = R(T_mT_n/T_m - T_n)\ln n\sqrt{p_n/p_m}.$$

Given the blister dimensions and the rate of pumping, the values of p_m and p_n can be determined from the area under the corresponding experimental desorption curves. An estimation of the activation energy made on the basis of the first peak of the desorption curve (Fig. 1) yields 0.7 eV, which is close to the values of the activation energy for the permeability of hydrogen in austenitic steels [13].

Thus, the first peak in the curve of hydrogen evolution from austenitic steel samples with blisters can be explained by the redissolution of molecular hydrogen evolved from blisters (Fig. 1). This conclusion is corroborated by the results of [14], where it was shown that in austenitic steels at a temperature of 800 K the radiation-produced pores do not retain molecular hydrogen. Therefore, the molecular hydrogen cannot cause the observed breaking of blisters upon heating [6] and the appearance of blisters of a new generation.

The high-temperature peak in the curve of hydrogen evolution from the samples of austenitic steel (Fig. 1) is possibly related to hydrogen release due to the dissociation of hydrocarbon compounds that were contained in blisters. Estimates that were performed in [15] show that the concentration of hydrogen in the solid solutions of the steels studied is sufficient for hydrocarbon compounds (of methane, in particular) to be formed in the blisters. When determining the parameters of the dissociation reaction from the parameters of the high-temperature peak by the technique that was described in [7], the energy of activation was found to be 2.5 eV, which is close to the values of the parameters of dissociation of ethylene [16].

The assumption [15, 17] on the formation of hydrocarbons, of methane in particular, upon the irradiation

of metals with hydrogen ions satisfactorily explains the destruction of blisters and the formation of new (secondary) blisters in the process of postirradiation heating. Since methane prior to its dissociation is insoluble in the metal, it should behave as an inert gas (e.g., helium) upon heating. If the methane pressure in blisters at the dissociation temperature is insufficient for them to be broken, the blisters will be retained upon further heating up to 1300 K [6].

To check this supposition, we studied the thermal desorption of gases from samples of austenitic steel 0Kh16N15M3B heated at a rate of 0.3 K/s. The surface topography was studied before and after heating [1].

To directly determine the composition of the gas, the effect of breaking of some of the blisters upon heating was used [6]. Since the occurrence of breaks depends on the plasma-flux power and, consequently, on the distance at which the sample is taken from the fuel assembly studied, it is impossible to predict in advance samples in which this effect will be maximum; therefore, a group of blister-containing samples irradiated with three pulses of hydrogen plasma was studied [6]. The choice of hydrogen plasma in this case is explained by the fact that, in general, the separation of CD_4 peaks is a more complex problem as compared to CH_4 peaks. The main interference in these experiments is the presence of water vapor on the surface of the samples [18], which give a series of peaks hindering the registration of methane peaks [19].

The corresponding curves of gas evolution are shown in Fig. 2. The first peak was observed for all samples. It is likely to be related to the degassing of the sample surface. The second peak was observed only for samples in which the blisters broke after heating. An analysis of the spectra obtained suggests that, at a temperature of ~750 K, methane and a higher temperature compound of a C_2H_x type (to which a peak with a mass equal to 26 corresponds) evolve associated with blister destruction.

From the known pumping rate and assuming the curves of gas evolution corresponding to samples with undestroyed blisters as representing a background, we estimated the amount of hydrocarbons that release from the sample when the blisters are destroyed. The volume of the blisters destroyed is known from the electron-microscopic data; based on these data, we determined the gas pressure in blisters at the instant of blister destruction and obtained a value of ~100 MPa, which, according to available estimates [20], is quite sufficient for the blisters to be broken.

MECHANISM OF ANOMALOUS BLISTERING

As was already noted, when irradiating samples of steel 12Kh18N10T with deuterium plasma, Zholnin *et al.* [1] observed the formation of anomalously large blisters with caps about 1 μm thick, which exceeds the range of hydrogen ions of given energy by more than an order of magnitude. It was shown in [1] that blister formation occurred at a certain distance from the center of a target (beam) and the size of the anomalous blisters decreased away from the center. It was determined that for a given pulse of hydrogen plasma (with an energy content of 40–60 kJ/pulse), the center of the sample was heated to temperatures close to the melting point of the sample.

It was shown above that the blisters contained hydrocarbons, in particular methane. We can assume that the cause of the formation of anomalous blisters is the appearance at a certain distance from the sample surface corresponding to the thickness of the blister cap of conditions favorable for the formation of hydrocarbons, i.e., the presence of reactive components (carbon, hydrogen), temperatures necessary for hydrocarbons to form (700–1000 K [21–23]), and the presence of porosity. The estimates show that the amount of carbon that is incorporated into the material from plasma [7] is negligible compared to the amount of carbon present in solid solution. Therefore, we can assume that the formation of hydrocarbons occurs due to uniformly distributed carbon present in solid solution, whose content in this steel is sufficient for the formation of hydrocarbons [15]. Plastic deformation that occurs in a surface layer of the sample due to thermal stresses that arise under given actions on the sample, which, possibly, is the cause of the formation of primary microcracks (microvoids) at a distance of several microns from the surface of the sample, should proceed at almost the same rate [6]. The temperature within this layer of the sample virtually does not change. Therefore, the only cause of the formation of hydrocarbons in the region located at a certain distance from the sample surface is the nonuniform distribution of hydrogen over the bulk

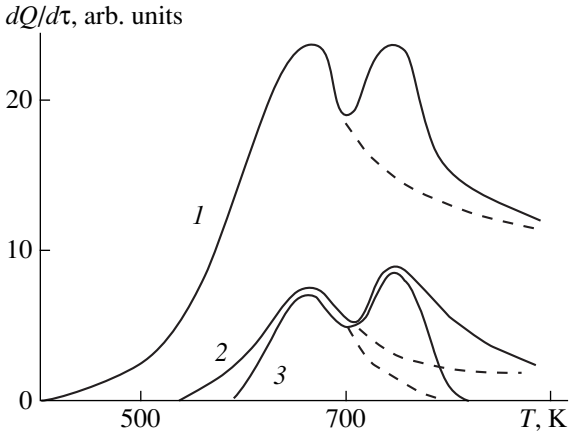

Fig. 2. Variation of the rate of deuterium thermodesorption in the process of uniform heating of the samples of steel 12Kh18N10T as a function of the heating temperature after treating by three plasma pulses. Dashed lines correspond to samples with undestroyed blisters; solid lines, to samples with destroyed blisters; lines *1–3* correspond to masses 16, 15, and 26, respectively.

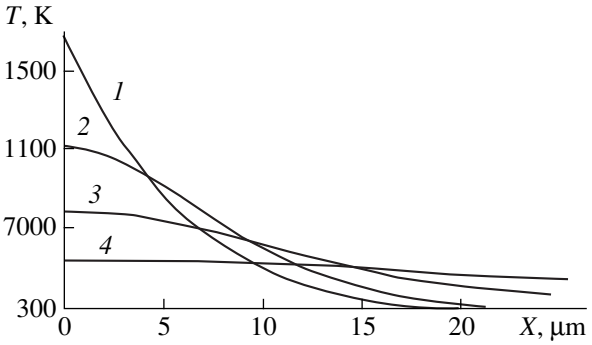

Fig. 3. Temperature distribution over the depth of the sample. Time after the pulse termination: *1*, 0; *2*, 2; *3*, 10; and *4*, 50 μs.

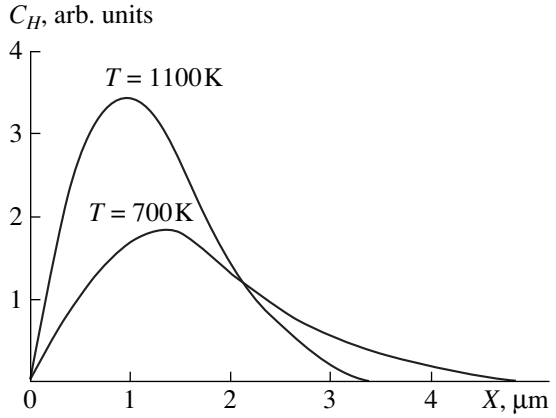

Fig. 4. Hydrogen distribution over the depth of the sample by the instant at which the surface temperature becomes favorable for the formation of hydrocarbons.

of the material. With the given action of plasma pulses on the sample, the surface of the sample may reach temperatures above the melting point of the material studied. In the process of cooling of the sample surface to temperatures necessary for hydrocarbons to form, a smearing of the initial profile of the hydrogen distribution can occur, which will lead to a shift of the zone with the maximum hydrogen concentration from the surface deeper into the sample and to the creation of conditions favorable for the formation of hydrocarbons at a certain depth exceeding the range of hydrogen ions of given energies. It is in this region that the most intense nucleation of hydrocarbons will occur and subsequent blistering will take place.

In order to confirm these assumptions, we performed corresponding estimations. Figure 3 represents dependences of temperature distribution on the surface and over the depth of the sample that were calculated using the technique suggested in [24] for the case of a semi-infinite body with a thermally isolated boundary. To simplify the calculations, we assumed that the pulse (6 μs long) has a rectangular shape and that the heat emission from the surface can be neglected. With such heat transfer, the increase in the temperature on the back side of the target is 10 K, which is much smaller than was observed experimentally. Therefore, it was supposed that some additional mechanisms are operative that ensure the absorption of half the heat energy of plasma without melting of the sample surface [25, 26]. For this case, the calculations of the profile of hydrogen distribution using the technique described in [7] showed that, by the instant at which the surface was cooled to temperatures favorable for the formation of hydrocarbons, the zone of maximum hydrogen concentration would be located at a depth of about 1 μm (Fig. 4), which corresponds to the thickness of the caps of anomalous blisters.

It is natural to expect that, with decreasing energy content in the plasma flux, which occurs with moving away from the target center, the zone with the maximum concentration of hydrogen will shift to a smaller depth. This will lead to the formation of smaller blisters, which indeed was observed in experiment.

CONCLUSION

Upon the investigation of hydrogen evolution from samples of austenitic steel 12Kh18N10T treated with a hydrogen plasma, anomalously large blisters with caps ~1 μm thick that contained hydrocarbons (methane, in particular) were found to be formed.

In the curve of thermal desorption of hydrogen from the samples containing blisters, three peaks were observed. The low-temperature peak (~500 K) was shown to correspond to the evolution of hydrogen redissolved from blisters, where it was present in the molecular form. The hydrogen-evolution peak located at ~700 K corresponds to the release of hydrogen from solid solution. The high-temperature peak corresponds to hydrogen release from blisters containing hydrocarbons which dissociate under certain conditions.

A mechanism of the formation of anomalous blisters is suggested that consists of the following. Upon the action of hydrogen plasma, thermal stresses arise in the surface layer of the sample, which may cause the initiation of microcracks. During cooling of the sample surface, at a certain depth under the surface significantly exceeding the range of hydrogen ions of a given energy, conditions arise (microvoids, temperature, presence of hydrogen and carbon) that are favorable for the formation of hydrocarbons (methane).

Since methane at temperatures below the temperature of its dissociation is insoluble in the metal, it will behave as an inert gas until the temperature of its dissociation T_{dis} is reached. It was shown that the blisters become broken if at temperatures below T_{dis} the pressure in the blisters exceeds the value necessary for their destruction. If at the dissociation temperature the pressure of methane in blisters is insufficient for them to be broken, the blisters will be retained upon further heating.

REFERENCES

1. A. G. Zholnin, A. G. Zaluzhnyĭ, B. A. Kalin, *et al.*, At. Énerg. **60** (5), 360 (1986).
2. V. L. Yakushin, B. A. Kalin, A. G. Zaluzhnyĭ, *et al.*, Izv. Ross. Akad. Nauk., Met., No. 5, 122 (1996).
3. A. G. Zaluzhnyi, V. P. Kopytin, and M. V. Tcherednichenko-Alchevskiy, Fusion Technol., 1815 (1997).
4. A. G. Zaluzhnyĭ, D. M. Skorov, and A. G. Zholnin, Fiz.-Khim. Mekh. Mater., No. 5, 85 (1982).
5. *Interaction of Radiation and Plasma and Electron Fluxes with Substance*, Ed. by D. M. Dykhane (Inst. Atomnoĭ Énergii, Moscow, 1990).
6. I. I. Chernov, B. A. Kalin, M. I. Guseva, *et al.*, Poverkhnost, No. 11, 75 (1983).
7. V. I. Pol'skiĭ, B. A. Kalin, P. I. Kartsev, *et al.*, At. Énerg. **56** (2), 83 (1984).
8. A. G. Zholnin and A. G. Zaluzhnyĭ, Poverkhnost, No. 10, 33 (1986).
9. A. G. Zaluzhnyĭ and A. L. Suvorov, in *Proceedings of the IX International Conference "Radiation Physics of Solids,"* Ed. by G. G. Bondarenko (Moscow, 1999), Vol. 1, p. 508.
10. A. G. Zholnin and A. G. Zaluzhnyĭ, Poverkhnost, No. 11, 27 (1986).
11. A. G. Zholnin, A. G. Zaluzhnyĭ, and S. E. Paremuzov, in *Proceedings of the VII All-Union Conference "Interaction of Atomic Particles with Solids"* (Minsk, 1984), Vol. 1, p. 94.
12. I. H. Evans, J. Nucl. Mater. **68**, 129 (1977).
13. T. I. Dolan and P. A. Anderi, Rep. Idaho Nat. Eng. Lab., 1994, pp. 21–33.
14. D. Keefer and A. Pard, J. Nucl. Mater. **47** (1), 97 (1973).
15. A. G. Zaluzhnyĭ, D. M. Skorov, A. G. Zholnin, *et al.*, *Radiation Defects in Metals* (Nauka, Alma-Ata, 1981), pp. 278–283.
16. *Chemist's Handbook* (Khimiya, Moscow, 1964), Vol. 3.
17. V. N. Chernikov, A. P. Zakharov, and A. A. Pisarev, Izv. Akad. Nauk SSSR, Ser. Fiz. **44**, 1210 (1980).
18. A. G. Zaluzhnyĭ, D. M. Skorov, A. G. Zholnin, *et al.*, At. Énerg. **47** (2), 113 (1979).
19. G. L. Saksaganskiĭ, Yu. N. Kotel'nikov, M. D. Maleev, *et al.*, *Ultrahigh Vacuum in Radiation-Physics Technology* (Atomizdat, Moscow, 1976), p. 137.
20. B. A. Kalin, D. M. Skorov, and V. T. Fedotov, *Interaction of Atomic Particles with Solids* (Kharkov, 1976), Part 1, pp. 120–123.
21. Yu. I. Archakov, *Hydrogen Stability of Steel* (Metallurgiya, Moscow, 1978).
22. S. Erents, C. Braganza, and G. McCracken, J. Nucl. Mater. **63**, 399 (1976).
23. R. Rioja, M. Yacaman, *et al.*, Scr. Metall. **16** (2), 129 (1982).
24. H. S. Carslaw and J. C. Jaeger, *Conduction of Heat in Solids* (Clarendon Press, Oxford, 1959; Nauka, Moscow, 1964).
25. Ya. B. Zel'dovich and Yu. P. Raizer, *Physics of Shock Waves and High-Temperature Hydrodynamic Phenomena* (Nauka, Moscow, 1966; Academic, New York, 1966).
26. B. I. Vasil'ev, A. Z. Grasyuk, A. P. Dyad'kin, *et al.*, Kvantovaya Élektron. (Moscow) **8** (11), 2390 (1981).

Translated by S. Gorin

Technical Physics, Vol. 46, No. 1, 2001, pp. 34–41. Translated from Zhurnal Tekhnicheskoĭ Fiziki, Vol. 71, No. 1, 2001, pp. 36–43.

SOLIDS

Self-localized Oscillations in High-Temperature Superconductors

A. G. Chirkov and V. G. Chudinov

Institute of Applied Mechanics, Ural Division, Russian Academy of Sciences, Izhevsk, 426001 Russia

e-mail: uufti@fti.udmurtia.su

Received January 10, 2000; in final form, May 12, 2000

Abstract—Molecular-dynamic characterization of high-temperature superconductors is discussed. Results obtained show strong anharmonicity of self-localized high-frequency oscillations of individual atoms. The localization of these oscillations near certain defects results in the spatial redistribution of the kinetic energy in the system. By the example of the La–Sr–Cu–O system, it was shown that the presence of the oscillations correlates with the superconductor transition temperature in this compound and causes fluctuations in the phonon and soliton subsystems. This may be a reason for the occurrence of high-temperature (high-T_c) superconductivity (HTSC). Calculations are compared with experimental data. © *2001 MAIK "Nauka/Interperiodica".*

INTRODUCTION

The properties of crystal lattices with nonlinear atomic interaction have been extensively studied in the past decade. It has been shown that self-localized modes with frequencies above the maximum frequency of a harmonic crystal may appear in these lattices [1, 2]. It has also been demonstrated [2] that, in a one-dimensional nonlinear system, the oscillations are localized near three atoms. The authors of [3] found that localization may occur at two atoms. In addition, they argue that, in a homogeneous system, localization may appear at any site of the lattice. The oscillations become spatially localized when an inhomogeneity is introduced [4]. All the results (both analytical and numerical) have been obtained largely for one-dimensional systems. In essence, the dimensionality of the systems does not have a noticeable effect on oscillation initiation; it only influences the initiation conditions. In three-dimensional (3D) systems, the conditions are much more severe and depend on the degree of nonlinearity (in LiF, for example, the oscillations are hardly possible even near the melting point) [5]. According to [2], such oscillations seem to exist in quantum crystals and alkaline halogenides.

In nonlinear 3D systems, the lattice dynamics is difficult to treat analytically. Appropriate analysis, however, can be performed with a computer experiment using the molecular dynamics method (MDM). Here, materials of practical value, first of all complex multicomponent systems, are most interesting. Among them are HTSCs. The HTSC mechanism is not yet understood. In particular, the formation of a superconductor current carrier, i.e., a Cooper pair, remains unclear. In conventional (low-temperature) superconductors, these pairs are produced by electron–lattice (electron–phonon) interaction. Their appearance shows up in the form of the isotope effect. Including anharmonicity in HTSC systems makes it possible to account for the anomalous isotope effect in them. Such an approach seems to be a promising way of tackling the problem of high-temperature superconductivity.

It has been shown [6–11] that nonlinearity in HTSC systems may initiate localized oscillations, which interact with lattice imperfections, redistributing the kinetic energy in the system. As a result, in the stationary state, the system becomes split into "hot" and "cold" subsystems. We assume that, at relatively high average temperatures, the superconductor current passes through the cold part.

COMPUTER EXPERIMENT

In this work, we used the MDM based on the numerical solution of the Newton equation for atom motion. In this case, we must specify a model crystalline grain and interatomic interaction potentials. The La–Sr–Cu–O [6–11] and Y–Ba–Cu–O [12] systems have been studied. Emphasis has been on the former because of its simpler structure. Therefore, we will consider this system in greater detail.

Once the crystallite and the potentials have been specified, the system is given a chance (within a time period of 10^{-12} s) to pass into the stationary state at a given temperature. If the lattice remains unchanged, calculations begin. The density of oscillatory states (OS) $G(\omega)$ was computed with the autocorrelation

1063-7842/01/4601-0034$21.00

function [13]:

$$G(\omega) = \int_0^\infty \gamma(\tau)\exp(-i\omega\tau)d\tau,$$

where $\gamma(\tau) = \sum_i \langle v_i(\tau)v_i(0)\rangle / v_i^2(0)$ is the autocorrelation function, $v_i(\tau)$ is the velocity vector of the ith atom at a time instant τ, and $\langle\ldots\rangle$ means averaging over different time intervals.

The model crystallite consisted of three layers: La(Sr)–O, Cu–O_2, and La(Sr)–O and contained about 2000 atoms. The atoms in the La(Sr)–O layer were rigidly fixed, imitating strong cross bonds, and the Cu–O_2 layer (responsible for HTSC) contained about 700 mobile atoms. Cyclic boundary conditions were set along the *a* and *b* axes. The interaction potentials were calculated with the combined technique that uses the theories of pseudopotential and density functional under the assumption that all current carriers are concentrated within the Cu–O_2 layer [14]. They confer metallic properties on it (the potential depth is ≈0.1 eV). In the transverse direction, the properties are close to ionic (≈1–10 eV). The Sr–O interaction potentials are especially deep, ≈25 eV, which is 30 times greater than the La–O potentials and ≈100 times greater than the Cu–O ones. Therefore, high nonuniformity appears in the system when Sr is substituted for La.

In the La–Sr–Cu–O systems, the basic peaks (their positions) of the phonon spectrum in the calculated OS densities agree well with those found experimentally. This shows the validity of the potentials and elastic constants used. The inequality of the kinetic, E_k, and potential, E_p, energies, i.e., $E_k = 2.3E_p$ both at 70 and 300 K, indicates that the interaction potentials are anharmonic.

The substitution of Sr impurity atoms for La atoms in the La_2CuO_4 lattice excites high-frequency oscillations (with the energy ≈0.4 eV) of four oxygen atoms in the Cu–O_2 layer near Sr atoms [6]. At Sr concentrations up to $x = 0.25$, the oscillations redistribute the kinetic energy of atoms in the system to produce "hot" centers (of size 10 Å) and a "cold" matrix. In the model system Sr_2CoO_4 (the La(Sr)–O plane is uniform), the oscillations are not localized and the space redistribution of the kinetic energy does not occur. Excitations appear equiprobably at any site on the Cu–O_2 plane. The localized high-frequency (LHF) oscillations originate from the specific Sr–O potential. In the model, a decrease in the depth of this potential shifts the peak toward lower energies and its increase causes the peak to move to higher energies.

The autocorrelation functions for La_2CuO_4 and $La_{2-x}Sr_xCuO_4$ decay incompletely, indicating the nonergodicity of the system [15] (Figs. 1, 2).

With Sr atoms introduced, the OS density (Fig. 3), together with its usual phonon part at low frequencies between 0 and 0.1 eV, exhibits high-frequency peaks (LHF oscillations) with an energy of ≈0.4 eV. The ratio S_P/S_{HF} of the areas under the phonon and LHF oscillation peaks was taken as the model parameter. At $x < 0.17$, this parameter is known to correlate with the superconductor transition temperature T_c, strontium concentration, and applied pressure [7]. Also, a decrease in S_P/S_{HF}

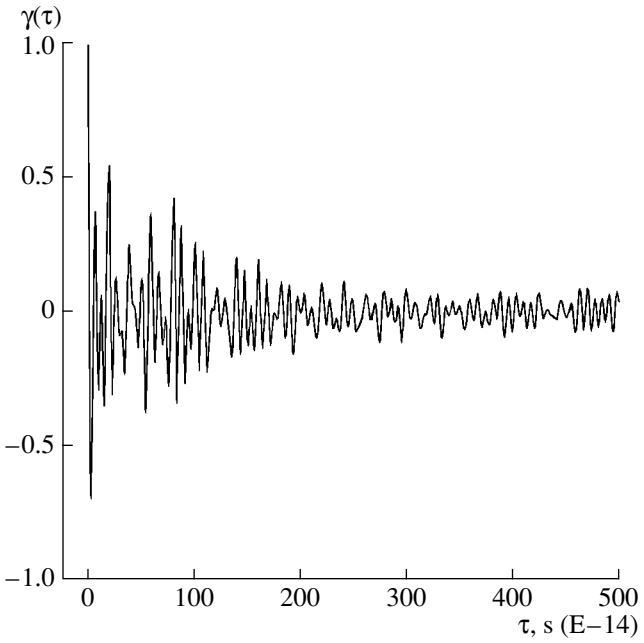

Fig. 1. Autocorrelation function of the La_2CuO_4 system (T = 70 K).

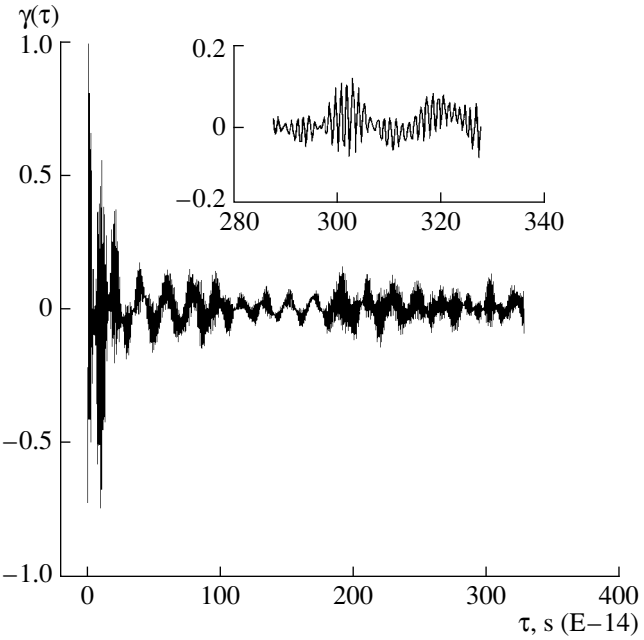

Fig. 2. Autocorrelation function of the $La_{1.88}Sr_{0.12}CuO_4$ system (T = 70 K).

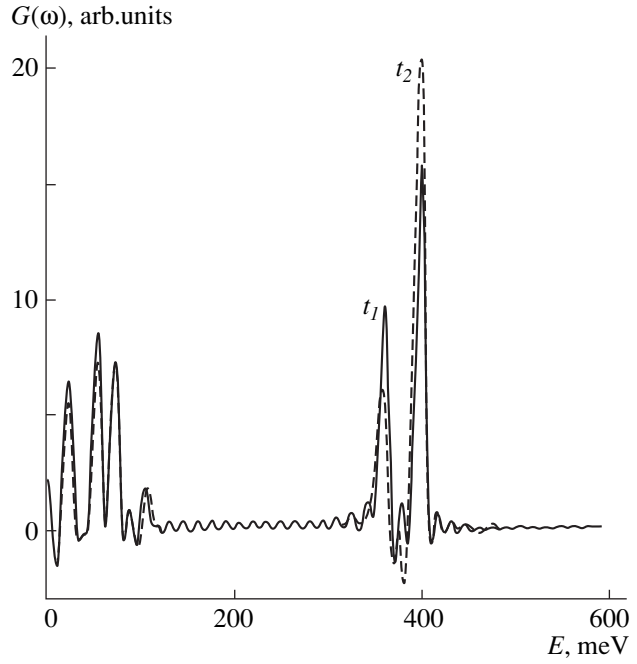

Fig. 3. OS density for the $Cu–O_2$ layer in the $La_{1.88}Sr_{0.12}CuO_4$ system at time instants t_1 and $t_2 = t_1 + 2\tau$.

when vacancies and/or interstitials (possible radiation-induced defects) are introduced into the $Cu–O_2$ layer correlates with a loss of the HTSC property upon irradiating HTSC systems [8]. The value of S_P/S_{HF} depends on the concentration of different vacancies. In the presence of copper vacancies with a concentration up to ≈1%, S_P/S_{HF} drops two- or threefold, while oxygen vacancies practically do not alter this parameter. Sr, La, Cu, and O interstitials in the $Cu–O_2$ layer affect the structure much more strongly. Quasi-morphic regions 10–15 Å in size appear. When the interstitial concentration rises to ≈0.15%, S_P/S_{HF} drops 30 times for Sr, ≈20 times for La, ≈20 times for Cu, and ≈15 times for O. When their concentration reaches ≈1%, the LHF oscillations are almost completely suppressed. It was found experimentally that the same irradiation dose has a stronger effect on higher T_c HTSCs. This fact correlates with a substantial decrease in S_P/S_{HF} at $x = 0.17$ (in experiments with $La_{2-x}Sr_xCuO_4$, to this concentration, there corresponds the highest T_c) compared with $x = 0.03$.

The calculation of the OS density at regular intervals ($\tau \approx 3 \times 10^{-13}$ s) without averaging the correlation function showed that, in all cases but $x = 0$, this parameter varies in time in the energy transfer regime; that is, S_P/S_{HF} varies periodically. This means that the number of eigenmodes of certain energies fluctuates with a characteristic transfer time of no more than 10^{-12} s (Fig. 3). Note that the transfer is observed only in the presence of the LHF oscillations.

The oxygen distributions over atom velocities at different concentrations of Sr deviate from the Maxwellian functions, with the greatest deviation at $x = 0.17$, which corresponds to the highest T_c in experiments [9, 11]. This fact reflects the emergence of hot centers in the cold matrix. For example, at $x = 0.17$ and $T = 70$ K, the "effective" temperature of the hot centers is 400–900 K (≈10%) and that of the matrix, ≈10 K (≈90%). The estimates were made by approximating the distribution functions by several Maxwellian distributions. For copper atoms, the deviation from the Maxwellian distribution is insignificant [11].

It has been shown [12] that local hot centers appear in the Y–Ba–Cu–O and La–Sr–Cu–O systems near Ba^{4+} charged defects in the $Cu–O_2$ and Cu–O planes, where the mean kinetic energy of oxygen atoms involved in the LHF oscillations reaches ≈0.5 eV. Qualitatively, the potentials of Ba^{4+} interaction with oxygen atoms and with copper atoms from the $Cu–O_2$ layer behave similarly to the Sr^{2+} interaction potentials in the lanthanum system. Here, the Sr–O potential had a deep minimum (≈25 eV), and oxygen atoms were involved in the LHF oscillation. In the yttrium system, the Ba^{4+} charged defect plays the same role. The potential of its interaction with oxygen is also very deep (≈36 eV). The effect of hot centers is observed when the velocity distribution function deviates from the Maxwellian distribution; in other words, the dynamics of the $Cu–O_2$ and Cu–O conductive layers in the yttrium system is akin to that of the $Cu–O_2$ layer in the lanthanum system. The appearance of Ba^{4+} correlates with an increase in the oxygen content in the chains, which, in turn, results in the superconducting composition and mid-IR absorption.

DISCUSSION

Our results suggest that, together with the usual phonon oscillations, high-frequency oscillations localized at four oxygen atoms in the $Cu–O_2$ layer are excited in the system being simulated. Essentially, they are similar to self-localized oscillations in nonlinear one-dimensional systems [1–4]. It should be emphasized that these oscillations are not phonon oscillations and are beyond the energy restrictions associated with the phonon wavelength in the crystal lattice. The energy scale is typical of intramolecular oscillations in molecular compounds. In two extreme cases, La_2CuO_4 and Sr_2CuO_4, the high-frequency oscillations do not appear and appear, respectively, although both systems are nonlinear. In the latter case, the oscillations behave similarly to self-localized oscillations in homogeneous one-dimensional nonlinear systems [2]. The latter case was analyzed solely for comparison with the former. Such an object is not found in nature. In the systems with intermediate Sr concentrations, $x = 0.03–0.25$, which introduce inhomogeneity in the La–O and $Cu–O_2$ planes, the oscillations were spatially localized

at the Sr impurity and caused kinetic energy redistribution in the system.

The validity of the potentials used is supported by the fact that they adequately describe the type of bonds in the La–Sr–Cu–O system: metallic along the layers and ionic in the cross direction. To date, as far as we know from the literature, the MDM investigations have used only ionic potentials calculated for the constituent HTSC oxides, which is incorrect in our opinion. When the potentials were calculated under the assumption that free carriers are uniformly distributed over the model crystallite, the potential wells for La–O and Sr–O were comparable to each other and the LHF oscillations were not excited. If, however, the carriers are concentrated in the $Cu–O_2$ plane (layer), these potentials differ considerably and the oscillations appear. The main validity test for the interaction potentials is obtaining proper values of the lattice constants, as well as of the upper phonon frequency limit and basic phonon peaks of the OS density. Those used in this work satisfy these conditions. The Sr–O potential wells are much deeper than for La–O, which may be a reason for a drastic decrease in the diffusion coefficient of oxygen atoms when Sr is substituted for La [16]. In addition to this, from a correlation between the onset of HTSC and the crystallochemical properties of HTSC materials, it was inferred that these materials must have a variable-valency atomic sublattice, an "oscillatory center" or a migrating point defect, and layers of different conductivity [17]. Our model fits these requirements.

Energy localization in a set of anharmonic oscillators is well known in theoretical mechanics [18]. Of interest is the practical application of this phenomenon and its consequences in real objects, specifically in HTSCs on the atomic level.

Our results reflect a situation that is quite possible in strongly anharmonic systems from the standpoint of statistical thermodynamics. In this case, the Gibbs canonic distribution may turn out to be inadequate, since this distribution, as well as the Maxwell–Boltzmann one, was deduced under the assumption that sets or particles are statistically independent to the maximum possible extent [19, 20]. For independent sets of particles, the equilibrium state, which is defined as the most probable or mean state, corresponds to the Maxwell–Boltzmann distribution. This statement is true for ergodic systems alone. However, the ergodicity of a specific dynamic system is difficult to prove. Ergodic systems coming to equilibrium are described by the Boltzmann kinetic equation, whose equilibrium solution is the Maxwellian distribution. However, the Boltzmann equation applies only to the case of "short-time" interaction forces (when atoms interact as absolutely rigid spheres or repulse as $\approx A/r^n$, where $n > 4$) [21] and also when space and time intervals are infinitesimal so as to loosen the correlations [22]. Boltzmann himself completely ignored correlations (the hypothesis of the number of collisions). In condensed matter, the problem comes down to considering a gas of quasi-particles, which meets the above conditions only in harmonic or quasi-harmonic approximations. In nonlinear systems, the ergodicity of a system is not obvious in general, since the assumptions underlying Gibbs statistical mechanics should be substantiated for each specific problem. In practice, the Gibbs canonical distribution is merely postulated, while being valid in the majority of cases [23]. Previously [9], we noted that anharmonicity due to the violation of statistical independence may disturb the Maxwellian distribution over velocities and the Gibbs canonical distribution. Correlation effects may yield the same result, since loosened correlations are necessary to deduce the Boltzmann kinetic equation [22].

Note that the MDM is the direct solution of a multiparticle problem and eventually takes into account correlations of all orders, unlike analytical calculations. Gibbs classical statistical mechanics is applicable only to ergodic systems for which the correlation coefficient equals zero. It covers systems having a single integral of motion, energy, which also is an approximation. When numerically solving dynamic systems, we may come to other integrals of motion (including nonanalytic), which violate the ergodicity. The general sign of system nonergodicity, irrespective of the reasons for its occurrence, is the nonzero autocorrelation function. Hence, HTSC materials are not ergodic, as follows from our results.

Unlike [9], we should say that correlation effects may disturb the Maxwellian distribution if the nonlinearity is weak. When a certain excitation threshold is exceeded (strong nonlinearity), stationary localized states arise [18], which is an additional reason for the non-Maxwellian distribution.

Of interest is the correlation of the model parameter indicating the presence of the LHF oscillations with T_c in the La–Sr–Cu–O systems. This correlation varies with applied pressure and concentration of point defects [7, 8]. This means that $T_c(S_P/S_{HF})$ is a function of the lattice parameter. Unlike the classical theory of superconductivity, here the Debye temperature is not the lattice parameter. It was found experimentally that the Hall constant R_H virtually does not depend on applied pressure, indicating that the carrier concentration remains the same. R_H also remains unchanged when the Sr content rises to $x \approx 0.17$, when local lattice distortions appear. This constant is also unchanged on neutron irradiation of $YBa_2Cu_3O_7$, especially at low temperatures, while T_c drops [24]. The exponential growth of the conductivity upon irradiation cannot be explained by a change in the hole concentration either [25]. Both irradiated and nonirradiated $YBa_2Cu_3O_7$ samples are single-phase [26]. According to [26], a drop of T_c is accompanied by changes in the crystal lattice, namely, by an increase in the lattice constant. As follows from neuron diffractometry data, irradiation

generates simple (similar to point) defects randomly distributed over the sample. Hence, T_c is affected largely by strains in the lattice subsystem. Our results imply that this is associated with the presence of the LHF oscillations in HTSCs; the oscillations depend on the character of atomic interaction. The basic reason for the occurrence of these oscillations is the drastic difference in the interaction potentials for La–O and Sr–O because of different ion sizes, which are well correlated with the adjusting parameters R_m (the model ion radius) in the pseudopotential system used [27]. Ba and Ca also have the same large R_m's, and, when they are replaced by La, HTSC is observed. The effect of the ion radius on the HTSC property was studied in [28, 29]. The larger the ion radius of the element *R*, the higher the T_c temperature in $R\mathrm{Ba_2Cu_3O_9}$ compounds (*R* = Yb, Er, Dy, Gd, Eu, or Nd) [28]. It was shown for $RE\text{–}\mathrm{Ba_2(Cu_{1-x}Me_x)_3O_{7-y}}$ systems (*RE* = Y, Gd, or Eu; *Me* = Ni or Fe) [29] that the superconducting properties of the system are controlled largely by the *RE* ion radius rather than by the presence or absence of the magnetic moment of this element.

Noteworthy also is the fact that the distance between Sr atoms in our model coincides with the superconducting coherence length in the $Cu–O_2$ plane. This length is known to be limited by the presence of defects and is close to the distance between holes introduced by Sr doping and also to the correlation length in antiferromagnetics [30].

That the obtained computer model is realistic follows also from low-frequency acoustic experiments [31], where low-frequency resonances appearing with the addition of Sr were related to solitons pinned by the lattice potential [31]. Similar resonances were discovered in the Y–Ba–Cu–O system [32]. These solitons are thought of as tunnel states that are also responsible for the linear term in the expression for heat capacity and the quadratic temperature dependence of heat conductivity (at $T < 10$ K) in HTSCs. The LHF oscillations may serve as these lattice-potential-pinned solitons.

It appears that the LHF oscillations may show up in experiments on IR absorption. HTSC systems have an intense absorption band in the mid-IR range (the peak at 0.5 eV), and their optical properties cannot unambiguously be described in terms of the simple Drude model of metallic conductivity [33]. Absorption bands in this part of the spectrum are typical only of superconductors, and the band intensities correlate with T_c. It is believed that low-frequency electron excitations or absorptions by polarons are responsible for these peaks (bands); however, this issue remains elusive. It was noted [34] that the reflection and absorption spectra cannot be calculated in terms of the band theory in the one-electron approximation, and the transition at 0.5 eV was assigned to the state in the $Cu–O_2$ cuprate planes. In $\mathrm{YBa_2Cu_3O_7}$, the broad IR absorption peak centered at 0.7 eV is likely to be due to localized states (presumably polarons) in the $Cu–O_2$ plane [35]. Direct observation of self-localized states in the mid-IR range for $\mathrm{La_{2-x}Sr_xCuO_4}$ was reported in [36]. These states are associated with the broad absorption peak centered at ≈0.5 eV at $x = 0.17$. The situation is the same for the reflection and absorption spectra of other HTSCs [37]. Note that broad IR absorption bands peaked near 0.4 eV, which are typical of vibratory spectra, have been found in molecular compounds (for example, the OH band in alcohols) [38].

The reciprocal of the optical relaxation time was found to linearly increase with energy to 0.4 eV in the lanthanum- and even up to 0.8 eV in bismuth-based compounds [37, 39]. It is generally accepted that the relaxation time is invariable at frequencies above the maximum phonon frequency. The upper phonon frequency limit in HTSCs corresponds to ≈0.1 eV, which is consistent with our calculations. Therefore, if electron relaxation is due to interaction with the lattice subsystem, the relaxation time behavior becomes unclear without considering the fact that oscillations with energies of 0.4–0.8 eV may be present in the lattice. As follows from our results, the LHF oscillations are the simplest explanation of these experiments. The situation could have been further clarified if neutron scattering studies had been carried out in this energy range. However, such investigations present a great technical challenge.

The presence of high-frequency atomic oscillations can also be judged from other experiments. The Debye temperature θ_D in the lanthanum-based compounds was estimated at ≈400 K [40]. In [41], the partial kinetic energies of the atoms in $\mathrm{La_2CuO_4}$ and $\mathrm{YBa_2Cu_3O_7}$ were measured by neutron scattering. It was shown that, in these compounds, oxygen atoms may have a kinetic energy of 1400 K (120 meV) and copper atoms, 1500 and 2000 K (130 and 170 meV). It was therefore suggested that latent (undetected) high-frequency oscillations of a nonphoton nature exist in these systems and that these oscillations are of considerable importance in the HTSC mechanism. The room-temperature heat capacity of $\mathrm{La_{1.85}Sr_{0.15}CuO_4}$ and $\mathrm{YBa_2Cu_3O_7}$ reaches only 85% of its maximum (the classical limit is $3Nk$), which also may be an indication of high-frequency oscillations in the lattice subsystem that do not contribute to the heat capacity at room temperature [42]. Raman scattering in $\mathrm{La_{1.85}Sr_{0.15}CuO_4}$ and $\mathrm{YBa_2Cu_3O_7}$ has revealed bands in the 100–150 meV range which are absent in $\mathrm{La_2CuO_4}$ [43]. They were associated with the crystal structure and phonon spectra of these compounds. The investigation into the electrical performance of point tunnel contacts has found phonon singularities in tunnel spectra at energies up to ≈180 meV [44].

The instability of the OS density is presumably a consequence of the system nonlinearity and is related to strong soliton interaction. It has been established that soliton interaction may significantly change the density of excited states in the system, specifically, the density

of phonon states [18]. On the one hand, the LHF oscillations tend to transform into delocalized low-frequency oscillations (phonons) [45]; on the other hand, the LHF oscillations, which are energetically favorable in a nonlinear system [2], tend to arise, since the resulting additional entropy reduces the free energy. Due to these discrepant tendencies, the number of elementary excitations, both coupled in solitons and delocalized, periodically varies; that is, a dynamic process of the decay and generation of localized states is set.

It was suggested [46] that nonlinear resonance in anharmonic systems (when the oscillator frequencies are multiples), which triggers energy transfer from an oscillator of one frequency to that of another frequency, the characteristic transfer time being other than the phonon time ($\approx 10^{-11}$ s), is responsible for the "central peak"—quasi-elastic neutron scattering near phase transitions in the structure. In systems exhibiting the central peak, one can distinguish fast (or phonon) and slow processes. The time scale of the latter corresponds to the central peak. Its origin still remains vague. A possible reason is phonon density fluctuations [47]. The central peak was also observed in $La_{2-x}Sr_xCuO_4$ [48]. Our results look as if nonlinear resonance is present in the system: a change in the area ratio for the peaks in the OS density means a change in the number of oscillators with one energy due to resonance interaction with oscillators of another energy. In the given case, one should consider resonant interactions not only between phonons but also between phonons and solitons (if any). The time-periodic variation of the OS density can explain the occurrence of the central peak through the above hypothesis of phonon density fluctuations and be a consequence of the presence of so-called "fluctuators" (time-fluctuating structure defects). In [49], from changes in the sound velocity and tempering experiments, it was concluded that fluctuators in HTSC systems are defects with inner degrees of freedom, i.e., quasi-molecules. A defect complex near the Sr atoms that causes the OS density to fluctuate in our work is nothing but a fluctuator. According to [49], the presence of these defects may result in local fluctuations of T_c, penetration depth of the magnetic field, and the density of superconducting current carriers. Some long-term relaxations and the memory effects in HTSCs are possibly related to these weakly relaxing fluctuators. That the autocorrelation decays incompletely in our work indicates that the system has "memory," i.e., is nonergodic. The possible relation between nonergodicity and high-temperature superconductivity was noted in [50]. The idea that the superconducting properties of HTSCs, particularly $YBa_2Cu_3O_7$, may be specified by coupled (i.e., correlated) oscillation of lattice atoms (as a result of ordered oscillations of oxygen atoms near oscillatory centers) has been put forward in [51]. In our opinion, hot centers, fluctuators, and oscillatory centers (which is essentially the same) just represent self-localized oscillations due to nonlinearity that are "captured" by various defects.

CONCLUSION

Thus, the MDM calculations indicate that self-localized oscillation of individual oxygen atoms appear in the superconducting $Cu–O_2$ layers of HTSCs that exhibit strong anharmonicity with respect to correlation effects. The strength of this phenomenon depends on the atomic interaction potentials. The situation may arise when part of the thermal oscillation energy is localized within small areas because of trapping of self-localized oscillations of oxygen atoms by defects of various types. Eventually, hot centers are produced: near the Sr impurity atoms (in the La–Sr–Cu–O system) or Ba^{4+} charge defects (in Y–Ba–Cu–O). The remaining part of the system is effectively "cooled," and the superconducting current can pass through it.

In thallium-based systems, Tl may have two valence states: Tl^{1+} and Tl^{3+}. In the bismuth-based HTSCs, Bi may be in the Bi^{3+} and Bi^{5+} charged states. Possibly, the difference in the Tl and Bi charges excites the self-localized oscillations in both the lanthanum- and yttrium-based systems. With regard for our results, the potentials of interaction of these defects with the oxygen atoms must differ drastically. These defects are similar to quasi-molecules, and the absorption behavior of the HTSCs in the mid-IR range resembles that of molecular compounds.

The degree of localization depends on the concentration of the defects. This can be best demonstrated with La–Sr–Cu–O. The greater the number of the Sr atoms, the stronger the matrix cools down and the higher the superconducting transition temperatures found experimentally. However, when the concentration of the Sr atoms exceeds some threshold, the hot areas begin to overlap, decreasing the experimentally found T_c.

The OS density in the crystal lattice exhibits nonlinear resonant effects, namely, periodic energy transfer between the phonon and soliton vibratory degrees of freedom with a characteristic time of no more than 10^{-12} s. The discovered oscillatory process can be related to a quasiparticle with an appropriate energy (several meV). Since the effective temperature of the superconducting transition for the matrix is much lower than that found experimentally, these quasiparticles may be involved in electron Cooper pairing. In other words, a possible mechanism underlying the HTSC phenomenon may include, together with charge and spin fluctuations, soliton and phonon fluctuations (or, in more exact terms, fluctuations of the OS density). A

comparison of our results with other theoretical and experimental investigations suggests that such a situation is a possibility in nonlinear systems with correlation effects.

ACKNOWLEDGMENTS

The authors are indebted to D.A. Indeĭtsev and E.L. Tonkov for much interest and valuable discussions.

Special thanks to O.Yu. Goncharov for technical assistance.

REFERENCES

1. A. M. Kosevich and A. S. Kovalev, Zh. Éksp. Teor. Fiz. **67** (5), 1793 (1974) [Sov. Phys. JETP **40**, 891 (1975)].
2. A. J. Sievers and S. Takeno, Phys. Rev. Lett. **61** (8), 970 (1988).
3. J. B. Page, Phys. Rev. B **41** (11), 7835 (1990).
4. R. F. Wallis, A. Franchini, and V. Bortolani, Phys. Rev. B **50** (14), 9851 (1994).
5. S. R. Bickham and A. J. Sievers, Phys. Rev. B **43** (3), 2339 (1991).
6. V. G. Chudinov, A. G. Chirkov, E. B. Dolgusheva, and V. M. Dyadin, Sverkhprovodimost: Fiz., Khim., Tekh. **6** (1), 204 (1993).
7. A. G. Chirkov and V. G. Chudinov, Sverkhprovodimost: Fiz., Khim., Tekh. **7** (5), 800 (1994).
8. V. G. Chudinov, A. G. Chirkov, and F. A. Sautin, Fiz. Tverd. Tela (St. Petersburg) **40** (6), 984 (1998) [Phys. Solid State **40**, 901 (1998)].
9. V. G. Chudinov, A. G. Chirkov, and R. R. Nurgayanov, Fiz. Nizk. Temp. **24** (1), 13 (1998) [Low Temp. Phys. **24**, 9 (1998)].
10. A. G. Chirkov and V. G. Chudinov, Fiz. Nizk. Temp. **25** (1), 94 (1999) [Low Temp. Phys. **25**, 71 (1999)].
11. A. G. Chirkov, Candidate's Dissertation (Izhevsk, 1996).
12. E. B. Dolgusheva, V. G. Chudinov, and A. G. Chirkov, Fiz. Tverd. Tela (St. Petersburg) **41** (10), 1729 (1999) [Phys. Solid State **41**, 1585 (1999)].
13. J. M. Dickey and A. Paskin, Phys. Rev. **188** (3), 1407 (1969).
14. V. G. Chudinov, E. B. Dolgusheva, and A. A. Yur'ev, Sverkhprovodimost: Fiz., Khim., Tekh. **4** (11), 2086 (1991).
15. V. I. Tikhonov, *Statistical Radio Engineering* (Sov. Radio, Moscow, 1966).
16. V. B. Vykhodets, M. A. Ivanov, V. Ya. Mitrofanov, *et al.*, Fiz. Met. Metalloved. **77** (3), 111 (1994).
17. L. M. Volkova, S. A. Polishchuk, and S. A. Magarill, Sverkhprovodimost: Fiz., Khim., Tekh. **6** (11-12), 2112 (1993).
18. A. M. Kosevich and A. S. Kovalev, *Introduction to the Nonlinear Physical Mechanics* (Naukova Dumka, Kiev, 1989).
19. L. D. Landau and E. M. Lifshitz, *Statistical Physics* (Nauka, Moscow, 1964; Pergamon, Oxford, 1980).
20. Yu. L. Klimontovich, *Statistical Physics* (Nauka, Moscow, 1982; Harwood, Chur, 1986).
21. *Nonequilibrium Phenomena. The Boltzmann Equation*, Ed. by J. Libovitz and E. Montroll (North-Holland, Amsterdam, 1983; Mir, Moscow, 1986).
22. N. N. Bogolyubov, *Problems of Dynamic Theory in Statistical Physics* (OGIZ GITTL, Moscow, 1946).
23. V. V. Kozlov, Dokl. Akad. Nauk **370** (3), 325 (2000).
24. B. N. Coshchitskii, S. A. Davydov, A. E. Karkin, and A. V. Mirmelstein, Physica C (Amsterdam) **162-164**, 997 (1989).
25. V. F. Elesin, I. A. Esin, A. A. Ivanov, *et al.*, Sverkhprovodimost: Fiz., Khim., Tekh. **3** (7), 108 (1990).
26. B. A. Aleksashin, V. I. Voronin, S. V. Verkhovskiĭ, *et al.*, Zh. Éksp. Teor. Fiz. **95** (2), 678 (1989) [Sov. Phys. JETP **68**, 382 (1989)].
27. *Interparticle Interaction in Liquid Metals*, Ed. by O. A. Esin (Nauka, Moscow, 1979).
28. G. V. M. Williams and J. L. Tallon, Physica C (Amsterdam) **258**, 41 (1996).
29. V. N. Narozhnyĭ, V. N. Kochetkov, E. P. Khlybov, *et al.*, in *Proceedings of the 30th Conference on Low Temperature Physics, Dubna, 1994*, Part 1, p. 187.
30. T. R. Thurston, R. J. Birgeneau, M. A. Kastner, *et al.*, Phys. Rev. B **40** (7), 4585 (1989); R. J. Birgeneau and G. Shirane, in *Physical Properties of High Temperature Superconductors*, Ed. by D. M. Ginzberg (World Scientific, Singapore, 1989; Mir, Moscow, 1990).
31. V. A. Melik-Shakhnazarov, L. L. Buishvili, N. L. Arabadzhyan, and V. M. Tavkhelidze, Sverkhprovodimost: Fiz., Khim., Tekh. **6** (2), 286 (1993).
32. V. A. Melik-Shakhnazarov, N. L. Arabadzhyan, and V. M. Tavkhelidze, Sverkhprovodimost: Fiz., Khim., Tekh. **3** (9), 2054 (1990).
33. T. Timusk and D. B. Tanner, in *Physical Properties of High Temperature Superconductors*, Ed. by D. M. Ginzberg (World Scientific, Singapore, 1989; Mir, Moscow, 1990).
34. N. V. Abrosimov, A. V. Bazhenov, A. V. Gorbunov, *et al.*, Sverkhprovodimost: Fiz., Khim., Tekh. **4** (11), 2165 (1991).
35. H. L. Dewing, E. K. H. Salje, K. Scott, and A. P. Mackenzie, J. Phys.: Condens. Matter **4**, L109 (1992).
36. Y. Yagil and E. K. H. Salje, Physica C (Amsterdam) **256**, 205 (1996).
37. A. El. Azrak, R. Nahoum, N. Bontemps, *et al.*, Phys. Rev. B **49** (14), 9846 (1994).
38. A. A. Mal'tsev, *Molecular Spectroscopy* (Mosk. Gos. Univ., Moscow, 1980).
39. L. D. Rotter, Z. Schlesinger, R. T. Collins, *et al.*, Phys. Rev. Lett. **67** (19), 2741 (1991).
40. B. N. Goshchitskiĭ, S. A. Davydov, M. G. Zemlyanov, *et al.*, in *Problems of High Temperature Superconductivity* (Ural. Otd. Akad. Nauk SSSR, Sverdlovsk, 1987), Part 1.
41. S. Ikeda, M. Misawa, S. Tomiyoshi, *et al.*, Phys. Lett. A **134** (3), 191 (1988).
42. J. A. Unod, A. Berzinge, D. Cattani, *et al.*, Jpn. J. Appl. Phys. **26**, 1119 (1987).
43. V. B. Preobrazhenskiĭ, V. D. Klimov, Sh. Sh. Nabiev, *et al.*, in *Problems of High Temperature Superconductiv-*

ity (Ural. Otd. Akad. Nauk SSSR, Sverdlovsk, 1987), Part 2.

44. M. Ohuchi, D. Shimada, and N. Tsuda, Jpn. J. Appl. Phys., Part 2 **32** (2B), L251 (1993).
45. B. A. Malomed, Phys. Rev. B **49** (9), 5962 (1994).
46. M. I. Katsnel'son and A. V. Trefilov, Fiz. Met. Metalloved. **64** (4), 629 (1987).
47. A. D. Bruce and R. A. Cowley, *Structural Phase Transitions* (Taylor and Francis, Philadelphia, 1981; Mir, Moscow, 1984).
48. P. Boni, J. D. Axe, G. Shirane, *et al.*, Phys. Rev. B **38** (1), 185 (1988).
49. V. I. Kozub, Phys. Rev. B **49** (10), 6895 (1994).
50. S. E. Krasavin and E. I. Kornilov, Sverkhprovodimost: Fiz., Khim., Tekh. **3** (9), 1 (1990).
51. L. M. Volkova, S. A. Polishchuk, S. A. Magarill, and S. V. Borisov, Sverkhprovodimost: Fiz., Khim., Tekh. **2** (8), 127 (1989).

Translated by V. Isaakyan

Technical Physics, Vol. 46, No. 1, 2001, pp. 42–46. Translated from Zhurnal Tekhnicheskoĭ Fiziki, Vol. 71, No. 1, 2001, pp. 44–48.

SOLIDS

A Study of the Synthesis Products of Fullerenes with Nickel and Cobalt

É. A. Petrakovskaya, N. V. Bulina, G. N. Churilov, and A. P. Puzyr'

Kirenskiĭ Institute of Physics, Siberian Branch, RAS, Krasnoyarsk, 660036 Russia

e-mail: churilov@post.krascience.rssi.ru

Received February 28, 2000

Abstract—Qualitative analysis of the products of plasmochemical synthesis of fullerenes with metallic nickel and cobalt has been carried out using electron paramagnetic resonance (EPR) and electron microscopy. These studies show that the synthesis products are mainly fullerenes, metallic nanoparticles coated with an insulating layer, and isolated atomic clusters. © *2001 MAIK "Nauka/Interperiodica".*

INTRODUCTION

In studies of fullerenes, great attention is now paid to their derivatives (heterofullerenes, endohedral complexes, metallofullerenes) [1, 2], because distortions of the symmetry of fullerenes produce new physical and chemical properties [1, 3, 4]. However, obtaining these unique materials in quantities sufficient for analysis is still a complicated task. We have undertaken an attempt to synthesize metallofullerenes containing nickel and cobalt.

MATERIALS AND METHODS

Earlier we described a plasmochemical reactor for the synthesis of fullerenes in a carbon plasma jet produced by an arc discharge between graphite electrodes at frequencies in the kilohertz range [5, 6].

In [7], a technique of synthesizing iron-containing fullerene complexes was described. The central electrode has an axial hole that was filled with carbonyl iron. In the present study, a similar technique was used, except that the hole in the central electrode was filled with nickel or cobalt. Carbon condensate was deposited on the chamber walls during synthesis, and the fullerenes extracted from this with benzol and the growth on the outer electrode (thermolysis residue [6]) were investigated by electron paramagnetic resonance using Se/X-2544 and RE1308 spectrometers in the temperature range 77 to 500 K and by electron microscopy in a JEM-100C electron microscope with an EM-ASID-4 scanning attachment and image processing equipment.

RESULTS AND DISCUSSION

1. In electron microscopic studies of the carbon condensate, particles of nickel coated with a non-conducting material (both groups of particles and isolated particles of sizes 10^3 to 10^4 nm) have been detected (Fig. 1). The fact that the particles were nonconducting has been established by an indirect method. The particles were placed under a microscope on a conducting (metallic) surface and irradiated with an electron beam. As a charge accumulated on the particles, a discharge via the substrate occurred. The discharge of the particles was accompanied by visually-detected radiation.

2. EPR spectroscopy detected a magnetic resonance of the metallic particles in the soot and the thermolysis residue (Fig. 2): ΔH^{Ni} = 80 mT, g^{Ni} = 2.20 and ΔH^{Co} = 150 mT, g^{Co} = 2.23. Similar results (ΔH^{Ni} = 100 mT, g^{Ni} = 2.22 and ΔH^{Co} = 90 mT, g^{Co} = 2.23) were obtained earlier by Bagguley [8] in experiments on the ferromagnetic resonance of metallic particles synthesized by the aerosol method in an RF arc discharge in a hydrogen atmosphere at 1 atm pressure with subsequent spinning in paraffin. The diameter of the particles was assumed to be 5–10 nm. It is known for single-domain particles of a monocrystalline metal in the absence of the skin effect that ΔH^{Co} = 11 mT and ΔH^{Ni} = 12 mT [9]. The large width of the electron paramagnetic resonance line in our experiments (Figs. 2a, 2b) is explained by the fact that the particles of nickel and cobalt in the soot have sizes amounting to a few millimeters. The *g*-factor values coincide with the data in [8].

Lines of EPR spectrum of the fullerene extract (Fig. 3) grouped by the types of their variation with temperature

Line No.	*g*	ΔH, mT
1	2.001	0.1
2	2.15	40
3′	2.6	15
3"	3.6	15
3"'	3.98	13
4	7.7	13

1063-7842/01/4601-0042$21.00

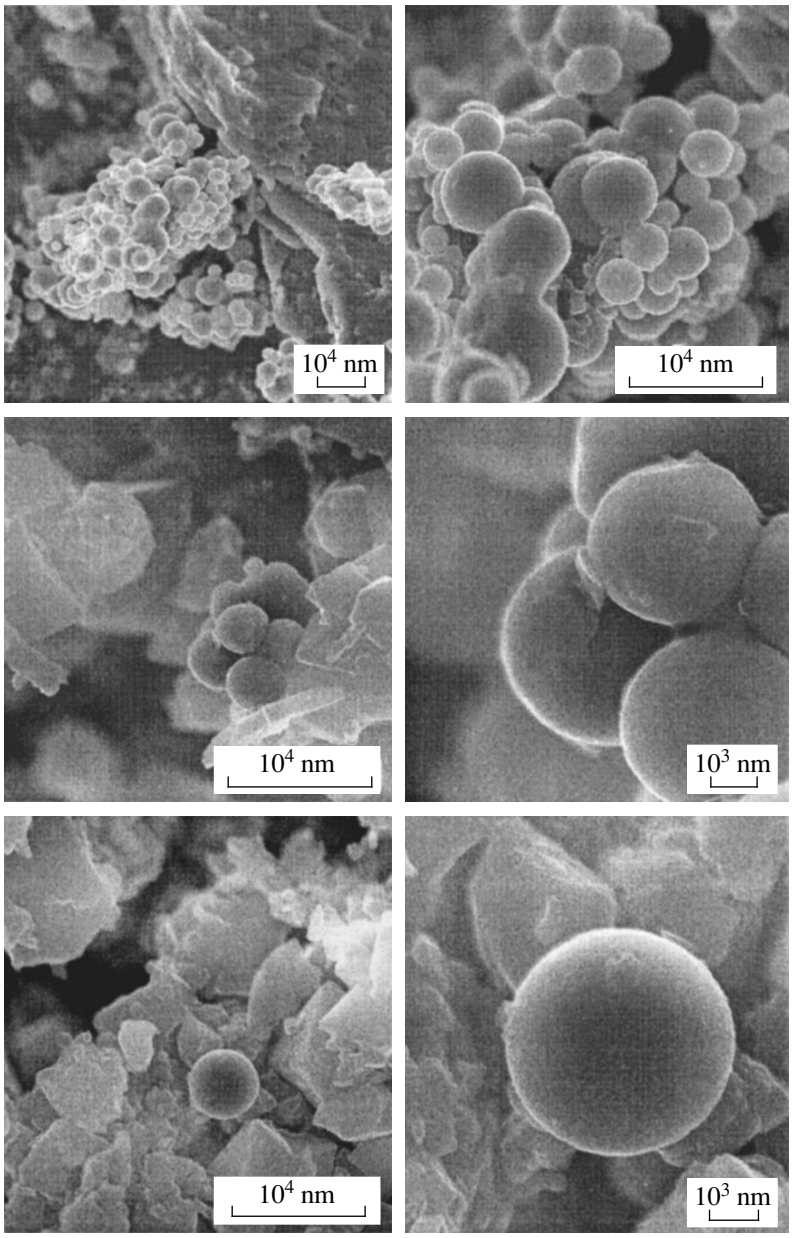

Fig. 1. Nickel particles in a fullerene-containing soot.

Line *1* for $g = 2.001$, as well as a narrower line *2* for $g \sim 2.15$ (Fig. 2), are observed not only in the spectrum of the nickel-containing soot but also in the thermolysis residue and in the fullerene extract, and are discussed below.

3. In the fullerene extract, the content of nickel according to the analysis of the X-ray luminescence data was 0.02%. Lines in the EPR spectra of the extract fall into four groups according to their temperature behavior (see table).

A narrow line *1* (Fig. 3a) for $g = 2.001$ usually observed in the spectra of solid fullerene mixtures [10] is due to a $C_{60(70)}$ radical. Its shift with temperature, typical of a paramagnetic center, can be seen in Fig. 4 (*1*).

At $T = 293$ K, parameters of line *2* are $g = 2.15$ and $\Delta H = 40$ mT (Fig. 3 (*2*)). Raising the temperature to 510 K causes gradual narrowing of this line down to 10 mT, an increase in its intensity and a shift to higher fields ($g = 2.08$). At temperatures below 293 K, the line first broadens to 70 mT (at $T = 250$ K) and then splits into two narrower components (at $T = 230$ K). At still lower temperatures, three lines are seen in the spectrum, having effective g-factor values of 2.06, 2.12, and 2.27, and the line width ~ 20 mT. At 77 K, the spectrum consists of a single asymmetric line *4* (Fig. 3b).

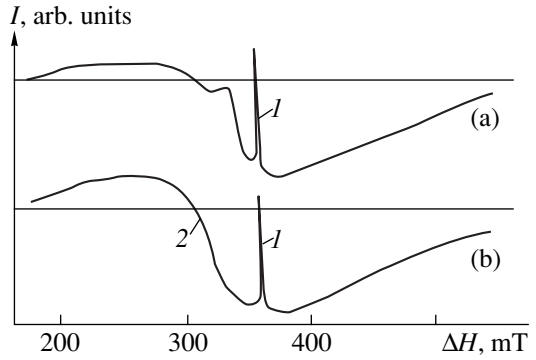

Fig. 2. Ferromagnetic resonance of Ni-containing soot (a) and Co-containing soot (b).

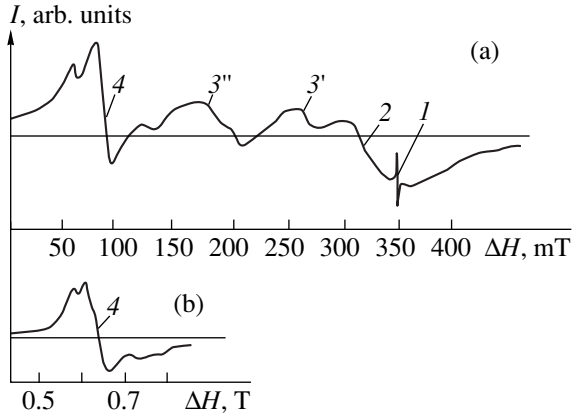

Fig. 3. Magnetic resonance spectra of Ni-containing fullerene extract at frequencies (a) 9 and (b) 35 GHz at 293 K; (a): g = 2.001 (*1*), 2.15 (*2*), 2.6 (*3*'), 3.6 (*3*''), and 7.7 (*4*).

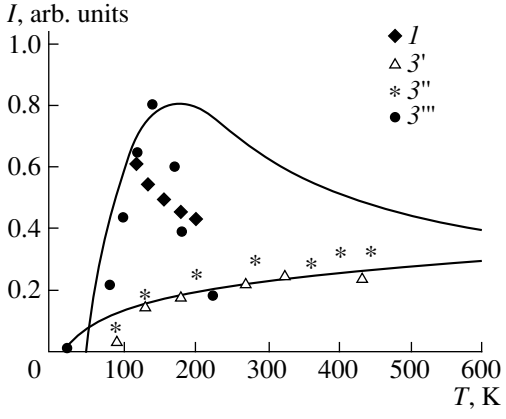

Fig. 4. Temperature variation of the EPR lines with g = 2.001 (*1*), 2.6 (*3*'), 3.6 (*3*''), and 3.98 (*3*'''). Solid line—calculation.

The observed spectrum is possibly associated with fine (~10 nm in diameter) crystalline particles of nickel that have anisotropic magnetic properties. Taking this into account, the temperature variation of the line width (which decreases with increasing temperature) can be explained by movement of the particles, which causes averaging of the anisotropy produced by internal fields. This mechanism was proposed by Kittel [11]. In this case, the width of the resonant line is calculated by the random walk method using the formula

$$\Delta H = \gamma^2[\Delta H(0)^2\tau(T)], \quad (1)$$

where $\tau(T)$ is a temperature-dependent mean time between two consecutive changes of the field direction and $\Delta H(0)$ is the line width at T = 0 K.

Substituting in (1) the values of $\Delta H(T)$ obtained in our experiment and $\Delta H(0)$ for the fine nickel particles [9, 12], we get $\tau(510\ \text{K}) = 0.9 \times 10^{-11}$ s, which is much less than the Larmor precession period of the magnetization vector in the field 0.3 T (1.05×10^{-10} s). Despite the approximate nature of the estimation, this mechanism can explain the narrowing of the line with increasing temperature by averaging of the magnetic anisotropy due to movement of the particles.

As the temperature is lowered from 286 to 77 K, the intensities of the EPR lines corresponding to g = 2.6 (curve *3*'), 3.6 (curve *3*''), and 3.98 (curve *3*''') vary as shown in Fig. 4. The line for g = 3.98 (*3*''') becomes noticeable at 230 K and reaches a maximum at 140 K, at which temperature the intensities of the other two lines decrease appreciably. This behavior is possible in dimer or tetramer clusters with antiferromagnetic exchange interaction between the atoms [13]. In Fig. 4, a temperature dependence is shown that has been obtained from a calculation in terms of a dimer cluster model in the Heisenberg–Dirac–van Vleck approximation for homonuclear systems. In this model, the energy levels of a system of two multielectron atoms are represented by a Heisenberg Hamiltonian for the exchange interaction ($\hat{H}$)

$$\hat{H} = -2J\hat{S}_1\hat{S}_2, \quad (2)$$

where S_1 and S_2 are total spins of the atoms.

Energy eigenvalues are determined by a semiempirical parameter of the exchange coupling of atoms (J) and the total spin of the system ($S = S_1 + S_2$), which is obtained from the usual rule for the summation of moments. For a pair of Ni^{+1} ions (s = 1), the total spin can take values of S = 0, 1, 2. The energy corresponding to each state is

$$E_S = J[S(S+1) - S_1(S_1+1) - S_2(S_2+1)]. \quad (3)$$

The rate of the resonant intralevel transitions for a level with spin S is given by the formula

$$I_S = \frac{\exp[-E_S/(KT)]}{\sum_S (2S+1)\exp[-E_S/(KT)]}, \quad (4)$$

where K is the Boltzmann constant and T is the temperature.

Proceeding from this, curves have been calculated for dimer clusters with spin $s_{1,2} = 1$. Coincidence of the calculated and experimental results suggests that the lines with the effective g-factor values 2.6, 3.6, and 3.98 correspond to dimer formations of nickel with exchange coupling constants on the order of 147 cm^{-1}. Positions of the lines are indicative of a splitting of the energy levels within the multiplets. The observed transitions with $g = 2.6$ and $g = 3.6$ take place within the total spin state with $S = 2$, which is the upper energy level of the cluster. The line $g = 3.98$ is due to transitions within state $S = 1$, which is lower in energy by $\Delta E = 2|J|$. In the low-temperature range, all transitions follow the same relationship. The decrease of the line intensity with increasing temperature for the lower transition cannot be described in terms of the Heisenberg–Dirac–van Vleck approximation; the complex couplings formed are outside the scope of this model.

Models of a dimer cluster containing a fullerene can be constructed using the data given in [14], where systems of C_{60} and C_{70} molecules and C_{70}^{4-} cations have been considered. Two Ni^{2+} ions attach to the fullerene molecule due to a donor-acceptor bond between electrons of the 4*S*-shell and the π system of the fullerene. This bond is activated by the electrostatic interaction between the charge of a C_{70}^{4-} anion and the total charge of the nickel pair $2Ni^{2+}$. Magnetic coupling between nickel ions arises as a result of polarization of the fullerene shell. Another possible candidate for the intermediate atom in this cluster model might be carbon.

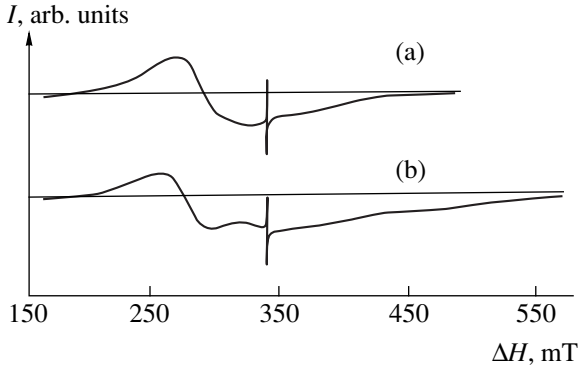

Fig. 5. Magnetic resonance spectra of the Co-containing fullerene extract from soot at (a) room temperature and (b) $T = 77$ K.

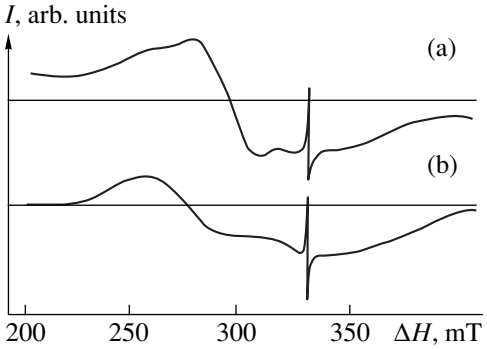

Fig. 6. Magnetic resonance spectra of the Ni-containing fullerene extract cooled in a magnetic field H = (a) 0 and (b) 0.5 T.

The low-field resonant transition ($g \sim 7.7$) is represented by a line characteristic of spectra from anisotropic powders. At 35 GHz, the line position shifts to higher fields ($g = 4$) and the line width increases to $\Delta H = 60$ mT. The intensity and width of the line does not change at temperatures down to 77 K. These observations indicate that this line can be related to atomic clusters of asymmetric type as well. A change taking place with an increase in the energy of ultrahigh frequency quanta [13] suggests that the exchange interaction in this cluster has both isotropic and anisotropic components. The isotropic exchange in this cluster is probably much less strong than in a dimer and the temperature dependence should be observable at temperatures below 77 K.

4. Spectra of the fullerenes extracted from soot and containing cobalt are an asymmetric line (Fig. 5a) with the following effective parameters: $g \sim 2.4$ and $\Delta H = 56$ mT. With decreasing temperature, the line width increases, but at 104 K, it shrinks to 36 mT and the effective g-factor drops to $g \sim 2.1$. At 77 K, the spectrum is a symmetric line (Fig. 5b). We attribute this spectrum to fine-grained cobalt particles isolated from one another by fullerene molecules. The spectrum at 77 K can be interpreted as due to modifications of the cobalt crystals with face-centered cubic and hexagonal close-packed lattices [12].

5. An interesting feature of the obtained materials is their behavior in a magnetic field at 77 K. Spectra of the samples containing cobalt, as well as of those with nickel cooled in a magnetic field of 500 mT differ by the shift of the resonant line to lower fields. The results for nickel are shown in Fig. 6b. Similar effects are observed in spin glasses [15]. In our case, this might be an indication of a coupling between separate magnetic particles.

CONCLUSION

As demonstrated by electron microscopy, in the synthesis of fullerenes with nickel, the latter is found in the form of particles coated with a layer of nonconducting substance. EPR analysis of the fullerene-containing soot with cobalt and nickel indicates the presence (apart from fullerenes) of large-sized particles (10^3 to 10^4 nm), which exhibit skin effect and a domain structure without magnetic anisotropy, and some finer particles (~10 nm). In the fullerene extract, the ratio of coarse and fine particles changes in favor of the latter. Clusters of several (from two to four) atoms can also be

observed via an intermediate nonmagnetic atom or molecule, possibly that of fullerene. The behavior of the fullerene extracts with cobalt and nickel in a magnetic field at 77 K bears resemblance to that of spin glasses.

This work has been performed in the framework of the State Scientific-Technical Program "Priority Directions in the Physics of Condensed Matter" (project no. 20004—Study of the Phase Transition Carbon Plasma—Condensed Phase of Carbon).

ACKNOWLEDGMENTS

The authors are grateful to G. Bondarenko for carrying out the X-ray luminescent analysis of the samples.

REFERENCES

1. A. V. Eletskiĭ and B. M. Smirnov, Usp. Fiz. Nauk **165** (9), 977 (1995) [Phys. Usp. **38**, 935 (1995)].
2. A. V. Eletskiĭ, Usp. Fiz. Nauk **164** (9), 1007 (1994) [Phys. Usp. **37**, 927 (1994)].
3. Ya. I. Pukhova, G. N. Churilov, V. G. Isakova, *et al.*, Dokl. Akad. Nauk **355** (2), 269 (1997).
4. L. B. Piotrovsky, in *Abstracts of 4th International Workshop, St. Petersburg, 1999*, p. 16.
5. G. N. Churilov, A. Ya. Korets, and Ya. N. Titarenko, Zh. Tekh. Fiz. **66** (1), 191 (1996) [Tech. Phys. **41**, 102 (1996)].
6. G. N. Churilov, L. A. Solovyov, Y. N. Churilova, *et al.*, Carbon **37** (3), 427 (1999).
7. G. N. Churilov, O. A. Bayukov, É. A. Petrakovskaya, *et al.*, Zh. Tekh. Fiz. **67** (9), 142 (1997) [Tech. Phys. **42**, 1111 (1997)].
8. D. M. S. Bagguley, Proc. Phys. Soc. London, Ser. A **66**, 765 (1953).
9. Z. Frait and B. Henrich, J. Appl. Phys. **35**, 904 (1964).
10. S. Kukolish and D. Huffman, Chem. Phys. Lett. **182**, 263 (1991).
11. C. Kittel, *Introduction to Solid State Physics* (Wiley, New York, 1976; Nauka, Moscow, 1978).
12. Yu. I. Petrov, *Physics of Small Particles* (Nauka, Moscow, 1982), p. 359.
13. B. S. Tsukerblat and M. I. Belinskiĭ, *Magnetochemistry and Radiospectroscopy of Stable Clusters* (Kishinev, 1983).
14. D. R. Lawson, D. L. Feldheim, C. A. Foss, *et al.*, J. Phys. Chem. **96**, 7175 (1992).
15. C. Y. Huang, Magn. Magn. Mater. **51**, 1 (1985).

Translated by B. Kalinin

Technical Physics, Vol. 46, No. 1, 2001, pp. 47–50. Translated from Zhurnal Tekhnicheskoĭ Fiziki, Vol. 71, No. 1, 2001, pp. 49–52.

SOLIDS

Space Charge and Thermal Depolarization Currents in PZT Thin Films

S. G. Gakh, E. D. Rogach, and E. V. Sviridov

Research Institute of Physics, Rostov State University, pr. Stachki 194, Rostov-on-Don, 344090 Russia

Received February 29, 2000

Abstract—Space-charge effects in PZT thin films obtained by rf cathode sputtering were studied. There is evidence that space charge forms in the ferroelectric phase during dielectric aging. Charge accumulation and disappearance were investigated by the method of thermally stimulated depolarization currents. Current peaks due to preliminary poling by a dc electric field and dielectric aging were determined. Effects that can be attributed to the rearrangement of point defects with the production of defect complexes, such as dimers, were observed for the first time. The activation energies for trap depletion (0.98 eV) and defect complex breakdown (1.20 eV) were found. © *2001 MAIK "Nauka/Interperiodica".*

INTRODUCTION

The internal bias fields of space charges considerably affect the performance of both bulk and film ferroelectrics [1–3]. In dielectrics, space charge is usually associated with the presence of defect-related traps. In thin ferroelectric films, the traps may be due to impurity ions, grain boundaries, vacancies, domain walls, and electrode–film and film–substrate interfaces.

In this work, we studied the occurrence and disappearance of space charge in thin PZT films. Space charge effects were revealed during the examination of polarization switching processes and temperature dependence of the permittivity. The presence of the space charge was directly detected by the method of thermally stimulated depolarization (TSD) currents [4, 5]. These methods provide information on traps responsible for space charge formation. Until recently, the method of TSD currents, as applied to studying thin ferroelectric films, has not been employed. In [6], TSD currents were determined only for temperatures between room temperature and 573 K in $(PbLa)TiO_3$ films.

SUBJECT OF INVESTIGATION AND EXPERIMENTAL TECHNIQUES

Thin PZT films of composition $Pb(Ti_{0.45}Zr_{0.53}W_{0.01}Cd_{0.01})O_3$ were obtained by rf sputtering on stainless steel and Pt substrates [7]. Pt electrodes of area 1.8 and 3.8 mm^2 were applied on the free surface of the film to produce sandwich structures. The thickness of the films was 1.5–2.0 μm. X-ray diffraction data indicate that the films were polycrystalline and had the perovskite structure. Charge loops $P(E)$ and current loops $i(E)$ were studied for the frequencies of polarization switching voltages between 0.001 and 100 Hz. The permittivity was measured with a bridge method (measuring voltage of 0.3 V with a frequency of 1 kHz). The TSD currents were determined in the short-circuited mode and were recorded by a potentiometer upon heating the film from room temperature to 870 K with a constant rate of 6 K/min.

RESULTS AND DISCUSSION

At a measuring voltage frequency of 50 Hz, as-prepared films on the platinum substrates had a coercive field $E_c = (3.0–3.5) \times 10^6$ V/cm, an orientational polarization of 0.25–0.28 C/m^2, and a remanent polarization of 0.19–0.24 C/m^2. As the films age (in the absence of electric fields and elevated temperatures), double, instead of single, peaks (Fig. 1) appear in the current loops $i(E)$, indicating the formation of the internal space-charge field. After aging for 100 days, the internal field of an unpolarized film was found to be (0.3–0.5) $\times$ 10^7 V/m and highly insensitive to external effects. Neither 10^5 polarization switching cycles in an external field of 3×10^7 V/m at 50 Hz nor short-term

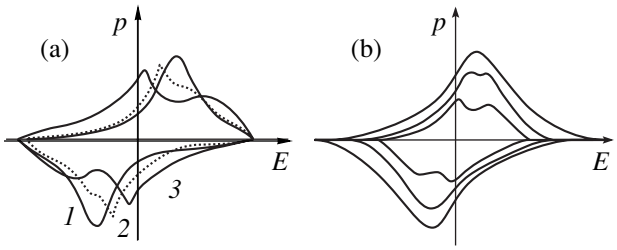

Fig. 1. Current loops $i(E)$ for PZT films on the platinum substrate: (a) (*1*) immediately after preparation, (*2*) after aging for 30 days, and (*3*) after aging for 100 days; polarization-reversing field 12×10^6 V/m; (b) after aging for 100 days at $f = 50$ Hz and polarization-reversing field amplitudes of 9×10^6, 12×10^6, and 17×10^6 V/m.

1063-7842/01/4601-0047$21.00

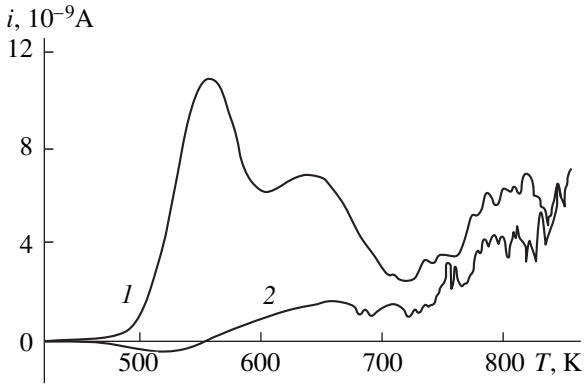

Fig. 2. TSD currents for (*1*) unpolarized aged film and (*2*) the same film after repeat heating. Substrate, stainless steel.

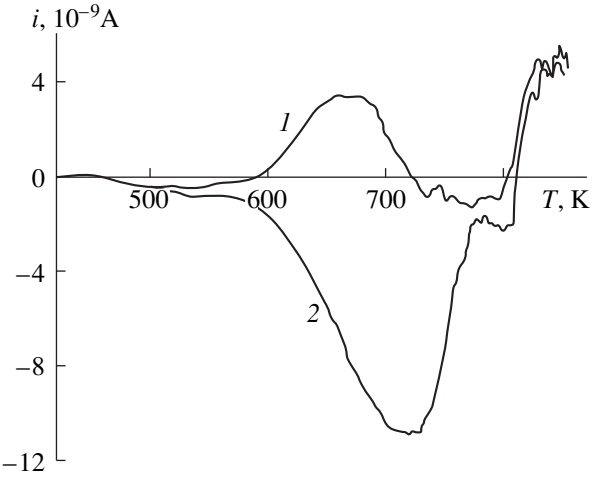

Fig. 3. TSD currents for the polarized film 1 day after poling.

heating up to 700 K break down the field. As the frequency of the switching field declined and the field amplitude grew, the internal field decreased but regained its value once the sample had been kept in an ac field with a frequency of 50 Hz. Aging effects were also observed in polarized films. Aged samples featured increased immunity to external effects. Aging proceeded faster at elevated temperatures: within 16–20 h at 350–390 K.

Energies of activation E_t and temperatures T_m for TSD current peaks (maxima)

Parameter	As-polarized film, peak χ	Aged film	
		lower temperature peak α	higher temperature peak β
Energy of activation E_t, eV	0.98	1.20	1.07
Peak temperature T_m, K	675	564	673

The internal field was also observed in the films deposited on the stainless steel substrates. However, we failed to determine its value because of the much wider spread in the coercive field over the film. In addition, the polarization did not saturate. The formation of the internal field was complete within 30–40 days at room temperature and within 7–9 h at 350 K. Double peaks in the current loops were also observed in [8], where polarization switching in thin solution-grown PZT films was studied.

The temperature curve of the permittivity showed, together with the well-known peak at the ferroelectric phase transition (the Curie temperature T_C = 660 K), a small additional peak between 520 and 570 K. This peak appeared upon heating, was absent upon cooling and repeat heating, and appeared again after dielectric aging for several days. Earlier, such an anomaly was observed in lead titanate crystals and lead titanate–based ceramics, as well as in PZT ceramics [9], and was associated with point defects, namely, lead vacancies.

The subsequent study of the formation and breakdown of the space charge was performed by the method of TSD currents in thin films on stainless steel substrates. Both unpolarized aged films and those aged and polarized by a direct current were investigated. Poling was carried out upon cooling the samples from 720 to 670 K, i.e., at temperatures above T_C for the bulk material. Further cooling to room temperature was carried out in the short-circuited mode. By choosing such poling conditions, we tried to preclude ferroelectric polarization from electret polarization and thereby to separate purely space-charge effects.

In the unpolarized aged films, two TSD current peaks were found (Fig. 2). For these films, the current in the outer circuit always passed from the platinum electrode to the substrate. After repeat heating, the peaks disappeared.

Figure 3 shows the TSD currents for the polarized samples. Curve *1* represents the case when the plus sign of the polarizing voltage is on the platinum electrode, and curve *2* is for the reverse polarity. As a rule, the temperature of the negative peak is several tens of degrees higher than that of the positive one. For the polarized film, the effect of aging time on the TSD current curve was discovered. Immediately after poling, a single peak was observed. As the time of room-temperature aging grows, an additional current peak at a lower temperature arises (Fig. 4). In the latter case, the main peak gradually shifts to lower temperatures and part of the charge responsible for the high-temperature peak "overflows" to the lower temperature one, with the total amount of the charge being conserved. The time of charge overflow was sample-dependent and varied from several days to several tens of days.

It seems likely that the difference in the TSD current peak heights, as well as the definiteness of the sign and shape of the initial current in the aged unpolarized film, stems from intrinsic asymmetry of the film and shows

up as natural self-polarization [10]. The TSD current peaks were considered under the assumption that the peaks come from the thermal depletion of the traps. The traps may be occupied either by injected carriers during poling or (in the absence of the external field) by free carriers redistributed in the internal field. Strong injection in the films considered was observed in [10]; this, in general, agrees with the literature data for thin films [3]. Cooling "freezes" trapped carriers, thus producing the space charge.

The table lists estimated activation energies of trap depletion E_t for one of the samples (current peaks from which the energies were calculated are shown in Fig. 4b). They were determined by the initial-rise and half-width methods [5, 12]. The activation energy $E_{t\alpha}$ corresponding to the low-temperature TSD current peak, appearing upon aging, is greater than those for the peaks resulting immediately after poling ($E_{t\chi}$). This is in conflict with the conventional idea that a higher temperature peak correlates with a higher energy of activation. With regard for the high spread in E_t (both from sample to sample and depending on the estimation technique), the estimates should be used with some caution and call for closer inspection. Yet, the obtained values of $E_{t\alpha}$ were always larger than or close to $E_{t\chi}$, with the temperature positions of the peaks differing by 100 or more degrees ($T_{m\chi} \gg T_{m\alpha}$). For all of the samples, dc prepoling was found to cause several specific TSD current peaks. Their number and temperature position, as well as the shape and direction of the current, depend on the polarizing field polarity and the duration of subsequent aging.

The density of the charge being released upon heating was estimated from the area under the TSD current peak. It was anomalously large (compared with the screening charge of ferroelectric polarization): as high as 5000 μC/cm^2 in several samples. Hence, assuming that the traps are uniformly distributed over the film volume, we obtain $N_t \cong 10^{20}$ cm^{-3}. This value is one or two orders of magnitude higher than that calculated from the space-charge-limited currents in perfect films [3].

The additional, lower temperature peak of the TSD currents (the specific feature of aging), accompanied by charge overflow, seems to have been observed for the first time. Usually, during aging of dielectrics, the TSD current peaks decreased and shifted toward higher temperatures, which was explained by charge capture by deeper traps.

Our results suggest that, upon dc poling, injected carriers are captured by vacancy-related traps, which, in the course of aging, take part in the formation of defect complexes, such as dimers, similar to those found in CdS [12]. In our case, these may be impurity ion–vacancy and lead vacancy–oxygen vacancy pairs. Then, the lower temperature peak in the aged film may be associated with the decomposition of the complex;

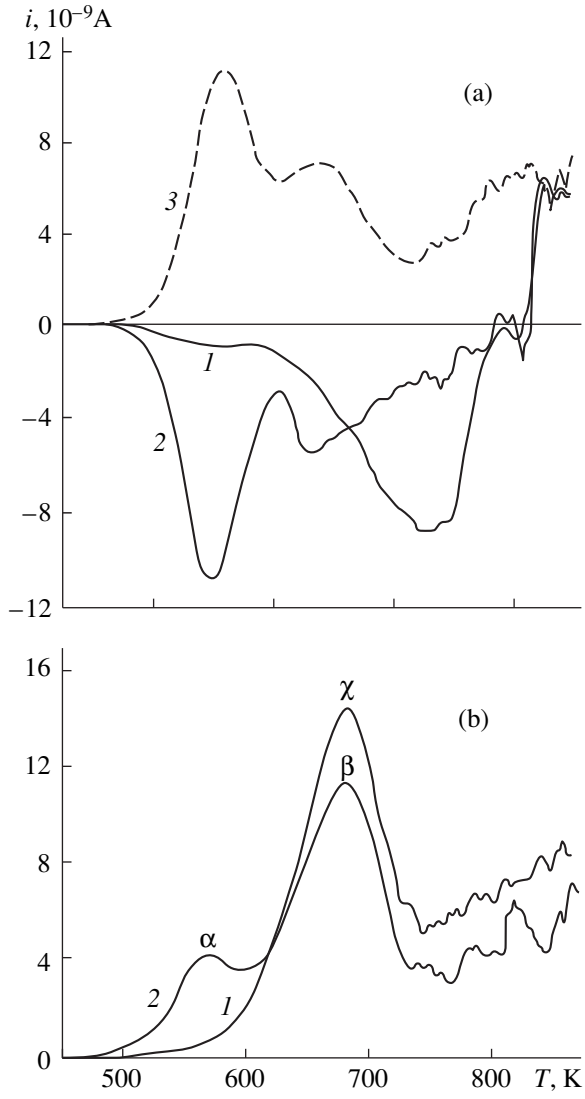

Fig. 4. TSD currents for two polarized films. (a) In (*1*) 3 and (*2*) 18 days after poling (the minus sign of the polarizing voltage on the Pt electrode, the same sample as in Fig. 2), (*3*) curve *1* in Fig. 2; (b) in (*1*) 2 h and (*2*) 6 days after poling (the plus sign of the polarizing voltage on the Pt electrode).

and the higher temperature one, with the depletion of resulting elementary traps. The activation energies of these processes are mutually independent; therefore, a peak with a higher E_t at a lower temperature may arise. Closer identification of defects responsible for the polarization and aging effects seems to be impossible at present, since the object considered is very complex (multicomponent) and calls for further investigation.

CONCLUSION

The ferroelectric phase of thin ferroelectric PZT films exhibits effects suggesting the presence of trapped space charge. They show up as the internal field upon polarization reversal and as an additional peak in

the temperature curve of the permittivity. The accumulation and disappearance of the space charge were studied by the method of TSD currents. The TSD current shape and direction, as well as the number of peaks and their temperature positions, were determined for polarized and unpolarized films, depending on dc prepoling conditions and aging time. The appearance of a lower temperature (additional) peak, the shift of the main peak toward lower temperatures, and charge overflow from the main peak to the additional one during aging were observed for the first time.

Our results can be explained under the assumption that, when applied, the dc electric field induces carrier injection and, subsequently, carrier trapping by defect (vacancy) centers. During aging, defect complexes, such as dimers, form owing to the presence of lead and oxygen vacancies, as well as impurity ions, in the PZT films.

The activation energies of trap depletion $E_{t\chi}$ and complex decomposition $E_{t\alpha}$ and also the concentration of occupied traps N_t were determined. For one of the films, they were estimated at $E_{t\chi}$ = 0.98 eV, $E_{t\alpha}$ = 1.20 eV, and $N_t = 10^{20}$ cm^{-3}.

ACKNOWLEDGMENTS

This work was supported by the Russian Foundation for Basic Research (project no. 98-02-18069).

REFERENCES

1. *Polarization of Piezoceramics*, Ed. by E. G. Fesenko (Rostov. Gos. Univ., Rostov-on-Don, 1968).
2. K. Okazaki, *Ceramic Engineering for Dielectrics* (Énergiya, Moscow, 1976), translated from Japanese.
3. J. F. Scott, Ferroelectr. Rev. **1** (1), 1 (1998).
4. *Electrets*, Ed. by G. M. Sessler (Springer-Verlag, Berlin, 1980; Mir, Moscow, 1983).
5. Yu. A. Gorokhovatskiĭ, *Foundations of Thermal Depolarization Analysis* (Nauka, Moscow, 1981).
6. Heung Jin Joo, Su Jae Lee, *et al.*, J. Korean Phys. Soc. **32**, S1411 (1998).
7. E. V. Sviridov, V. N. Mukhortov, V. P. Dudkevich, and E. G. Fesenko, Zh. Tekh. Fiz. **55** (5), 959 (1985) [Sov. Phys. Tech. Phys. **30**, 576 (1985)].
8. S. Seifert, K. Franker, *et al.*, in *Proceedings of the 5th International Conference on Electroceramics and Their Applications, Aveiro, Portugal, 1996*, Vol. 1, p. 483.
9. L. A. Barabanova, V. G. Gavrilyachenko, *et al.*, Neorg. Mater. **15** (9), 1612 (1979).
10. V. Sviridov, V. Alyoshin, *et al.*, Ferroelectrics **128**, 1 (1992).
11. E. D. Rogach, A. V. Zakharov, and E. V. Sviridov, in *Proceedings of the 8th International Workshop on the Physics of Ferroelectric Semiconductors, Rostov-on-Don, 1998*, Vol. 7, p. 163.
12. V. N. Vertoprakhov and E. G. Sal'man, *Thermostimulated Currents in Inorganic Matter* (Nauka, Novosibirsk, 1979).

Translated by V. Isaakyan

Technical Physics, Vol. 46, No. 1, 2001, pp. 51–54. Translated from Zhurnal Tekhnicheskoĭ Fiziki, Vol. 71, No. 1, 2001, pp. 53–56.

SOLIDS

The Effect of Impurity Atoms on the Multiplication of Edge Dislocations

N. M. Vlasov and V. A. Zaznoba

Received March 3, 2000

Abstract—The multiplication of edge dislocations in impurity atmospheres was studied. Impurities pin a dislocation line, so that additional stress must be applied to "drive" a multiplication mechanism. An expression for diffusion redistribution of impurity atoms along a dislocation segment due to the nonuniform chemical potential was derived. The early stage of moderate-temperature creep is qualitatively explained in terms of theoretical analysis. © *2001 MAIK "Nauka/Interperiodica".*

During plastic deformation of metals, the density of edge dislocations increases, as a rule, by several orders. This phenomenon is explained in terms of the Frank–Read or Bardeen–Herring models of dislocation multiplication [1]. The former mechanism is fairly illustrative. When exposed to shear stress, a linear segment of a dislocation line bends between the pinning points. Once the critical bend radius has been attained, the segment breaks down to form a closed dislocation loop. The same process is repeated for the remaining part of the dislocation. The latter mechanism, being essentially identical, differs in that here the multiplication mechanism is dislocation climb because of the nonuniform concentration of vacancies or interstitials.

The multiplication process is usually considered without taking into account the effect of impurity atoms. However, an impurity atmosphere around edge dislocations raises the critical shear stress necessary to form the loop. In this case, a multiplication source comes into effect at a higher applied stress. After the segment, together with the impurity atmosphere, has bent, the impurity atoms are redistributed along the segment by diffusion because of the chemical potential gradient. As a result, the segments become free of the impurity atoms and the shear multiplication stress decreases. The atoms migrate along the dislocation segment by the mechanism of pipe diffusion, for which the energy of activation is smaller than for volume diffusion, and sink to grain boundaries or pass to a solid solution.

In this work, we tried to give an in-depth analysis of how impurities influence the multiplication of edge dislocations. In the model adopted, we consider only the dimensional effect as applied to the dislocation–impurity binding energy. Theoretical findings are invoked to explain the early stage of moderate-temperature creep.

Let a linear segment of a dislocation line of length l be pinned at points A and B where dislocation lines intersect (Fig. 1a). The segment is surrounded by a homogeneous impurity atmosphere. The initial bend of the segment due to shear stress is limited by the volume diffusion of the impurity atoms. In an impurity-free material, the shear stress needed to trigger a multiplication mechanism is smaller. Impurity atmospheres pin a dislocation line, so that an additional shear stress must be applied to bend the segment to the critical value.

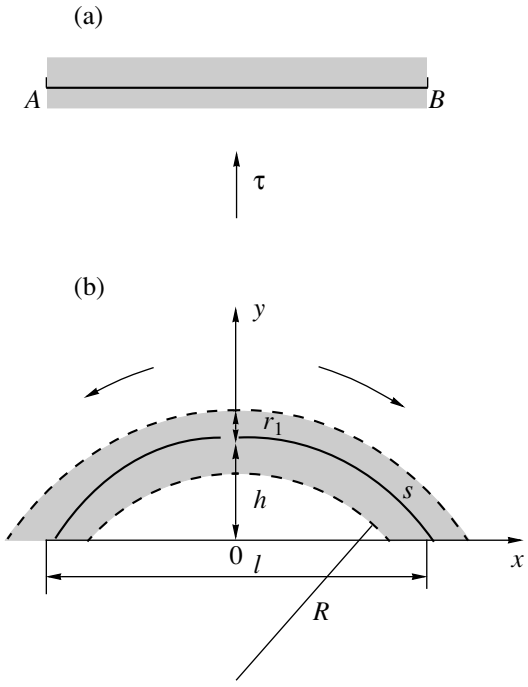

Fig. 1. (a) Linear and (b) bent dislocation segments surrounded by impurity atmosphere.

1063-7842/01/4601-0051$21.00 © 2001 MAIK "Nauka/Interperiodica"

Edge dislocation pinning by impurity atoms in the dilute and concentrated solid solution approximations has been studied extensively in [2]. Within these approximations, expressions for the force needed to break the dislocation–impurity bond were derived. As follows from estimates, the impurity hardening is comparable to the applied shear stress in order of magnitude. In fact, for the Fe–C system ($\delta v = 3 \times 10^{-30}$ m^3, $\nu = 0.28$, and $c_0 = 10^{26}$ m^{-3}), $F/L \simeq \beta c_0 = 0.6 \times 10^{-4}\,\mu b$. Here, $\beta = \mu b(1+\nu)[3\pi(1-\nu)]^{-1}\delta v$, μ is the shear modulus, b is the Burgers vector of a dislocation, δv is the impurity-induced change in the crystal volume, c_0 is the mean impurity concentration, and F/L is the force per unit length needed to detach a dislocation from the impurity atmosphere. If an edge dislocation is under a shear stress τ_0, the force acting on a unit length is $F_0/L = \tau_0 b$ and equals $10^{-4}\,\mu b$ at $\tau_0 = 10^{-4}\mu$. With the effect of impurities taken into account,

$$\frac{F_{\text{tot}}}{L} = \frac{F_0}{L} + \frac{F}{L} = 1.6 \times 10^{-4}\mu b.$$

It follows from the above that, in an impurity material, a multiplication source generates dislocation loops at much higher applied stresses.

If the applied stress is insufficient to make the segment free of impurity atoms, it bends together with the impurity atmosphere. The activation energy of this process is close to that of volume diffusion. As soon as a bend appears, the impurity atoms are redistributed by diffusion along the already convex segment of the dislocation (Fig. 1b), with decreased activation energy. The driving force of this process is the gradient of the chemical potential of an impurity atom along an arc s of the dislocation segment. The curvature K of the segment changes only its direction, remaining constant in magnitude. This favors diffusion migration of impurity atoms along the segment (arrows in the figure).

Under stress, a dislocation segment bends, and its curvature K is $K = 1/R \simeq \tau_0/(\mu b)$. For $\tau_0/\mu = 10^{-4}$, $b = 2.48 \times 10^{-10}$ m, and $l = 10^{-6}$ m, we obtain $R = 2.48 \times 10^{-6}$ m and $h = 0.05 \times 10^{-6}$ m (where h is the height of the segment).

The curvature of the segment causes diffusion redistribution of the impurity atoms along the dislocation line. They "slide down" from the top of the segment by pipe diffusion. This (enhanced) diffusion takes place in the narrow region (with a characteristic size of several Burgers vectors) around the dislocation core. In this region, the impurity concentration near the dislocation is the highest. To quantitatively characterize the process, we adopted the following model. Let an impurity atmosphere occupy a cylindrical region of radius $r_1 > r_0$ (r_0 is the dislocation core radius) where impurity atoms pin a dislocation most rigidly. The value of r_1 is determined from the condition

$$\frac{\beta \sin\theta}{r_1} = kT, \quad r_1 = \frac{\beta \sin\theta}{kT},$$

where k is the Boltzmann constant, T is temperature, and θ is an angle in polar coordinates.

For $kT = 10^{-20}$ J, $\sin\theta = 1$, and $\beta = 10^{-29}$ J m, we have $r_1 = 10^{-9}$ m. Physically, this means that, at $r > r_1$, the impurity atoms practically do not "sense" the dislocation because of the prevailing effect of thermal motion. In more rigorous terms, the potential field of the dislocation should be represented by a rectangular potential such that the total number of impurity atoms in the real and model potential wells are the same. Mathematically, this condition is written in terms of the number of excess impurity atoms per unit dislocation length:

$$\frac{N}{L} = c_0 \int_0^{2\pi} \int_{r_0}^{R} \left[\exp\left(-\frac{\beta \sin\theta}{rkT}\right) - 1 \right] r\,dr\,d\theta$$

$$= c_0 \int_0^{\pi} \int_{r_0}^{r_1} \left[1 - \exp\left(-\frac{U_1}{kT}\right) \right] r\,dr\,d\theta$$

$$+ c_0 \int_0^{2\pi} \int_{r_0}^{r_1} \left[\exp\left(\frac{U_1}{kT}\right) - 1 \right] r\,dr\,d\theta \simeq \frac{\pi c_0 \beta^2}{2(kT)^2} \sinh\left(\frac{U_1}{kT}\right).$$

Here, we made use of the fact that $\overline{\sin^2\theta} = 0.5$ and $r_1^2 \gg r_0^2$. To find the potential U_1 of the model rectangular well, we will take only the first even term in the expansion of the exponential (the even terms of the expansion are responsible for the accumulation of the impurity atoms around the dislocation line) and obtain

$$\frac{N}{L} = c_0 \int_0^{2\pi} \int_{r_0}^{R} \left[\exp\left(-\frac{\beta \sin\theta}{rkT}\right) - 1 \right] r\,dr\,d\theta$$

$$= \frac{\pi c_0 \beta^2}{2(kT)^2} \ln\left(\frac{R}{r_0}\right),$$

where $2R$ is the mean distance between the dislocation lines.

From the condition $\sinh[U_1/(kT)] = \ln(R/r_0)$, we find U_1. For $R = 10^4 b$, $r_0 = 2b$, and $\ln(R/r_0) = 8.5$, we obtain $U_1 \simeq 2.84kT$.

Now, the impurity atmosphere is concentrated within a cylinder of characteristic size r_1 and constant potential U_1; that is, the binding energy between an impurity atom and the dislocation is constant within the region $r_0 \le r < r_1$. This gives us a chance to simulate the migration of impurity atoms by diffusion along the segment and, thus, determine the decrease in the force of

dislocation pinning due to the impurity environment. As soon as the number of impurity atoms leaving the dislocation segment becomes sufficiently large, the applied stress will force the dislocation out of the impurity environment. The time during which the segment breaks free of the impurity environment can be considered as the preparatory (incubation) period of the multiplication source (mechanism) to generation of dislocation loops.

Pipe diffusion of impurities is associated with a nonuniform distribution of the chemical potential of the impurity along a dislocation line. Following [3], the chemical potential of an impurity atom on the dislocation pipe surface is written in the form

$$\mu_s = \mu_0 = \omega\gamma K,$$

where μ_0 is the chemical potential on the plane surface; ω is the volume of the atom; γ is the surface tension at the boundary between the impurity environment and the dislocation; and K is the curvature of the dislocation segment (Fig. 1b),

$$K = \frac{y''}{[1 + (y')^2]^{3/2}}.$$

The diffusion flux of impurity atoms along a dislocation is proportional to the chemical potential gradient:

$$I_s = \frac{D_s n}{kT}\frac{\partial \mu_s}{\partial s} = -\frac{D_s \gamma \omega n}{kT}\frac{\partial K}{\partial s},$$

where D_s is the pipe diffusion coefficient; s is the length of an arc of the bent segment; n is the number of impurity atoms per unit area of the impurity environment; and

$$\frac{\partial K}{\partial s} = \frac{1}{\sqrt{1 + (y')^2}}\frac{\partial K}{\partial x} = \frac{\partial K}{\partial x},$$

since

$$(y')^2 = \frac{x^2}{R^2 - x^2} \ll 1.$$

The last relationship is evident from the fact that $0 \le x \le 1/2$ and $l \ll R$; hence $K = y''$. Then, the rate of impurity migration by pipe diffusion is found by solving the equation

$$\frac{\partial y}{\partial t} = \omega \mathrm{div}(I_s) = -\frac{D_s \gamma \omega^2 n}{kT}\frac{\partial^4 y}{\partial x^4}.$$

The dislocation segment is surrounded by an impurity atmosphere of radius r_1, and the impurity concentration in this region is constant. The impurity atoms leave the bent surface of the segment, and, as this takes place, the radius of the atmosphere decreases. Mathematically, this is described as the rate of change of the coordinate y in time. It is assumed that the atom distribution inside the "impurity" pipe does not change, since the model potential U_1 is constant.

The mathematical statement of the problem can be simplified if the segment profile is approximated by the function $y = (h + r_1)\cos(\pi x/l)$, where h is the height of the segment. In this case, the solution of the equation changes but the general picture of impurity migration along the segment will remain qualitatively the same. In addition, one should take into account the evaluating character of the problem parameters, as well as the simplicity and physical clearness of the solution given below. Let us consider a periodic solution of the equation for $|x/l| \le 0.5$. If the profile of the segment is written as $y = h_1\cos(\pi x/l)$, $h_1(t)$ is found from the equation

$$\frac{\partial h_1}{\partial t} = -\frac{\pi^4 D_s \gamma \omega^2 n}{kTl^4} h_1(t), \quad h_1 = h + r_1 \quad \text{at} \quad t = 0.$$

Now, it is easy to obtain the time dependence of the impurity atmosphere profile:

$$y = (h + r_1)\exp(-t/\tau)\cos(\pi x/l),$$

where $\tau = kTl^4/(\pi^4 D_s \gamma \omega^2 n)$.

The relaxation time τ characterizes the departure of the impurity atoms from the environment of the segment; in other words, it is the preparatory time of the multiplication source to generation of the loops. Note that the characteristic size of the source base l can be expressed through the scalar dislocation density; then, we have

$$\tau = \frac{kT}{\pi^4 D_s \gamma \omega^2 n \rho^2}.$$

It is seen that the preparatory (incubation) time of the multiplication source in an impurity material is inversely proportional to the dislocation density squared. As the dislocation density grows, the source base shrinks and the segments break free of the impurity atmosphere faster. In the Fe–C system ($kT = 10^{-20}$ J, $\gamma = 1$ N/m, $\omega = 10^{-29}$ m^3, $n = 10^{20}$ m^{-2}, $D_s = 10^{-12}$ m^2/s, and $\rho = 10^{12}$ m^{-2}), $\tau = 10^4$ s. Now let us determine the time it takes for the segment to break free of the impurity atmosphere. It is assumed that all the impurity atoms leave the segment for the grain boundaries with the same rate. If $h = 0.05 \times 10^{-6}$ m and $r_1 = 10^{-9}$ m, we find $t \simeq 400$ s from the condition $h - 2r_1 = h\exp(-t/\tau)$. This means that, at $\tau = 10^4$ s, the height of the segment at its center ($\cos(\pi x/l) \simeq 1$) will decrease by $2r_1$, i.e., by the characteristic size of the impurity environment, for the time $t = 400$ s.

Let us discuss possible manifestations of the effect. It follows from the aforesaid that impurity atoms have a significant effect on the multiplication of edge dislocations. This shows up largely through the incubation time of the multiplication source. During this period,

the impurity atoms are redistributed along a dislocation segment by diffusion. The activation energy of this process is lower than that of volume diffusion. The experimentally found activation energy for pipe diffusion in fcc metals was found to be 0.4–0.7 of that for volume diffusion [4]. Therefore, the early stage of moderate-temperature creep or plastic deformation must be controlled by impurity atom redistribution along dislocation segments [5]. Only after the lapse of the incubation period, will the dislocation leave the remaining impurity environment and the multiplication source come into play.

REFERENCES

1. J. P. Hirth and J. Lothe, *Theory of Dislocations* (McGraw-Hill, New York, 1967; Atomizdat, Moscow, 1972).
2. N. M. Vlasov, Fiz. Met. Metalloved. **56** (3), 583 (1983).
3. N. M. Vlasov, Fiz. Met. Metalloved. **58** (5), 897 (1984).
4. R. Balluffi, in *Thermally Activated Processes in Crystals* (Mir, Moscow, 1973), pp. 42–74.
5. C. Bauer, in *Topical Problems of the Theory of Dislocations* (Mir, Moscow, 1968), pp. 98–114.

Translated by V. Isaakyan

Technical Physics, Vol. 46, No. 1, 2001, pp. 55–58. Translated from Zhurnal Tekhnicheskoĭ Fiziki, Vol. 71, No. 1, 2001, pp. 57–61.

SOLIDS

Mechanism of Acousto-Electromagnetic Conversion in Concrete

A. P. Surzhikov, T. V. Fursa, and N. N. Horsov

Tomsk Polytechnical Institute, Tomsk, 634034 Russia

Received March 27, 2000

Abstract—The electromagnetic response to impact acoustic excitation in concrete is studied theoretically and experimentally. It is revealed that the amplitude–frequency characteristic of the response depends on the dimensions and location of inclusions in the material. A physical model of acousto-electromagnetic conversion in concrete is suggested. The amplitude–frequency characteristic is computed on the basis of an equivalent circuit. It is found that the computed and measured data agree, which supports the physical model. © *2001 MAIK "Nauka/Interperiodica".*

It has been demonstrated that the electromagnetic (EM) response to impact acoustic excitation can be useful for the nondestructive strength testing of concrete, the response being evaluated from its amplitude–frequency characteristic (AFC) [1]. Furthermore, it has been found that the acousto-electromagnetic (AEM) conversion occurs in areas of adhesive contact between the aggregate and the binder [2]. However, this technique provides very inaccurate data in some cases. Presumably, this can be explained by the fact that the strength is evaluated from the frequency of the principal AFC maximum, although the response has a fairly wide spectrum. This study aims to assess the relationship between the AFC of the response and the parameters of internal EM sources.

Previous investigation has shown that the EM response is produced mainly by internal sources [3]. Nevertheless, it is yet to be understood what mechanism underlies AEM conversion in aggregate–binder materials. If the acoustic wave excited in the concrete changes the state of the double electric layer on an aggregate/binder interface, then the displacement current must be generating an electric signal in an external circuit. The AFC of the signal must depend on the location of the EM source in relation to the points of impact and detection, as well as on its size. In practice, we face the problem of interpreting the total response from many EM sources randomly distributed throughout the object. To simplify matters, we tested models made of sand–cement concrete with a few inclusions.

The measurements were carried out with an emission apparatus [4]. It produces impact excitation of acoustic waves in a tested object and digitizes the EM response.

Figure 1a shows a typical AFC for a model with a gravel grain serving as a single inclusion. Numerous peaks may be produced by inclusion faces, which differ in both their location relative to the faces of the model and the conditions under which acoustic waves are excited and pass through the inclusion faces. With a plate inclusion, the AFC has only a few clear-cut resonant peaks (Fig. 1b). The number of peaks rises with

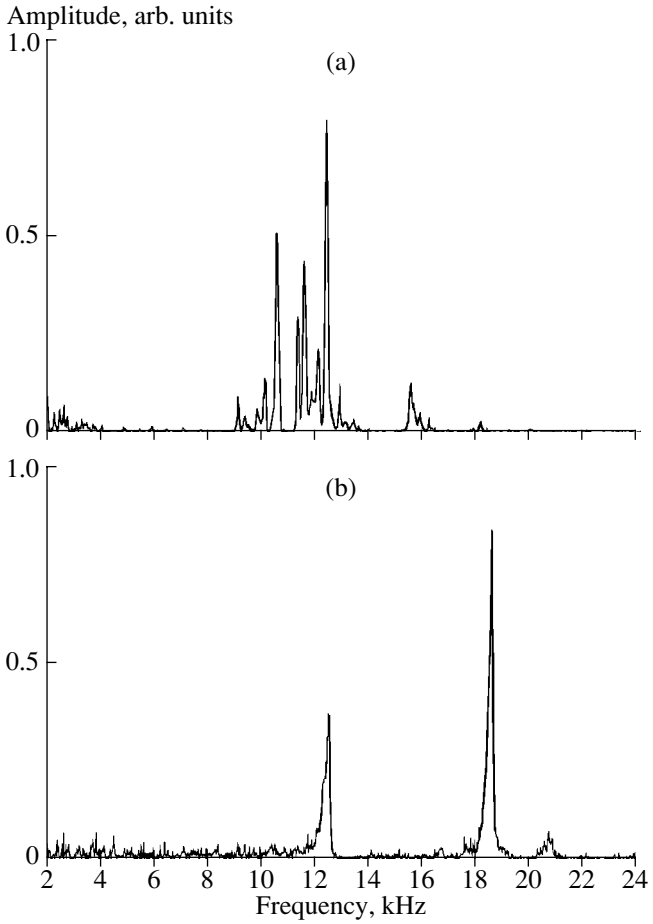

Fig. 1. Typical AFCs of concrete with a single inclusion in the form of (a) a grain of gravel or (b) a metallic plate.

1063-7842/01/4601-0055$21.00 © 2001 MAIK "Nauka/Interperiodica"

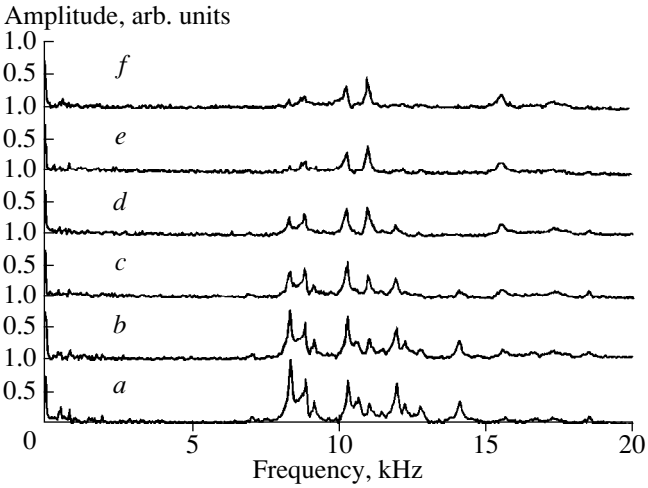

Fig. 2. AFCs measured for different rotation angles of the SEs: (*a*) 0° (vertical position), (*b*) 18°, (*c*) 36°, (*d*) 54°, (*e*) 72°, and (*f*) 90° (horizontal position).

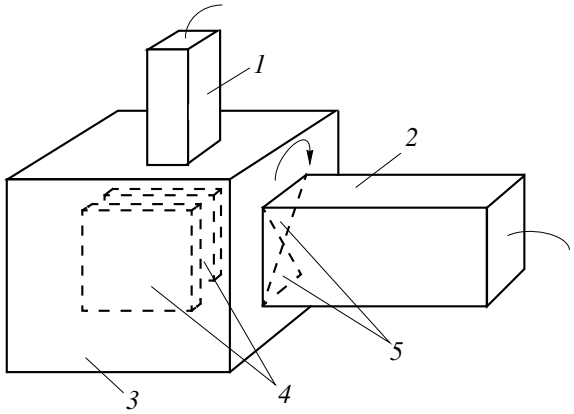

Fig. 3. Testing setup: (*1*) an impact exciter, (*2*) a differential electric transducer, (*3*) a model under test, (*4*) inclusions, and (*5*) SEs.

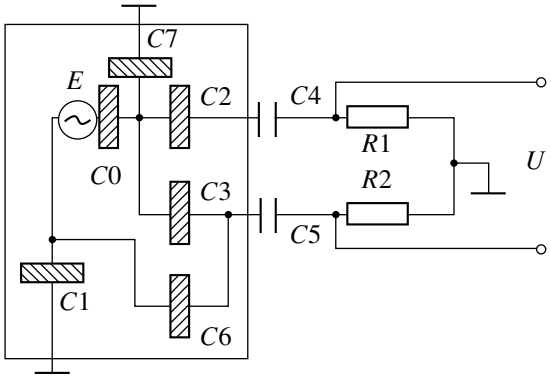

Fig. 4. Lumped-parameter equivalent circuit.

the number of inclusions. The case of two metallic plates is exemplified in Fig. 2.

Thus, even with a single inclusion, the response at the detection site is the superposition of the electric fields produced by elements of double electric layers on the surface of the inclusion, the elements differing in their orientation relative to both the direction of the acoustic wave and the sensing plane.

The EM response was detected with a differential capacitive transducer, which uses two metallic sensing elements (SEs) lying in a common plane to counter external interfering signals. The transducer has a figure-of-eight radiation pattern. If the dipole moment of a source is directed as the principal axis of the transducer pattern, the signal is maximum. If the dipole moment is perpendicular to the principal axis, the signal is insignificant. It is therefore conceivable that sources with differently oriented dipole moments can be distinguished by rotating the transducer about its axis, which passes through the center of the radiation pattern. To test this conjecture, we carried out an experiment on a cement model of dimensions $100 \times 100 \times 100$ mm with two parallel metallic inclusions ($40 \times 40 \times 1$ mm) situated around its center, as shown in Fig. 3. The transducer was rotated by steps of 18° from the vertical (0°) to the horizontal (90°) position of the SEs as indicated by the arrow, and the AFC was measured after each step. The results are shown in Fig. 2. It is seen that some of the spectral components progressively decrease, whereas others progressively increase. As a result, the spectrum of the response changes considerably. These findings support the view that AEM conversion in composite materials is connected with changes in the dipole moments of elements of double electric layers on the surface of an EM source, the elements differing in their orientation relative to both the direction of the acoustic wave and the sensing plane.

Being induced by changes in the dipole moment of the EM source, the voltage across the SEs corresponds to the distribution of electric current. Consequently, the relationship between the voltage and the EM response can be modeled with a distributed-parameter electric circuit, which in turn can be replaced with a lumped-parameter circuit. This approach enables us to qualitatively understand how the signal from the SEs depends on the size of the source and its location relative to the SEs. Figure 4 shows a lumped-parameter circuit representing the source and the SEs. Capacitors $C2$ and $C4$ model the capacitive coupling between an SE and a surface of the double electric layer ($C4$ refers to the gap), whereas capacitors $C3$ and $C5$ model that between the other SE and the same surface. Capacitor $C6$ represents the capacitive coupling between the latter SE and the layer surface of opposite charge. Resistors $R1$ and $R2$ ($R1 = R2 = R$) refer to input transducer resistances; capacitor $C0$, to the capacitance of the double electric layer; capacitors $C1$ and $C7$, to the capacitive coupling between the respective surfaces of the double electric layer and ground; and voltage source E, to the EM source. According to our views, the acoustic wave changes the thickness of the double electric layer, thus

producing an electric signal. Consequently,

$$E(\omega) = \frac{k\eta(\omega)\sigma d}{\varepsilon\varepsilon_0}, \quad (1)$$

where ω is the angular frequency of the oscillation, η is the normal strain of the double electric layer, σ is the surface charge density of the layer, d is the layer thickness, ε is the relative permittivity of the layer, ε_0 is the electric constant, and I_k is the misalignment between the dipole moment and the transducer principal axis.

The circuit in Fig. 4 suggests a simplified mathematical formalism of AEM conversion. Let us write equations for the mesh currents I_k:

$$\sum_{k=1}^{4} a_{i,k} I_k = b_i \quad (i = 1, 2, 3, 4). \quad (2)$$

In matrix form,

$$MI = b, \quad (3)$$

where

$$M = \begin{vmatrix} a_{11} & a_{12} & a_{13} & a_{14} \\ a_{21} & a_{22} & a_{23} & a_{24} \\ a_{31} & a_{32} & a_{33} & a_{34} \\ a_{41} & a_{42} & a_{43} & a_{44} \end{vmatrix}, \quad b = \begin{vmatrix} E \\ 0 \\ 0 \\ E \end{vmatrix}. \quad (4)$$

For the sake of simplicity, we neglect to indicate that the matrix entries, the currents, and the voltage are functions of ω. The matrix entries are expressed as follows:

$$a_{11} = z_0 + z_3 + z_6; \quad a_{12} = -z_3; \quad a_{13} = -z_6; \quad a_{14} = z_0;$$

$$a_{21} = -z_3; \quad a_{22} = z_2 + z_3 + z_4 + z_5 + 2R;$$

$$a_{23} = -(z_5 + R); \quad a_{24} = 0;$$

$$a_{31} = -z_6; \quad a_{32} = -(z_5 + R);$$

$$a_{33} = z_1 + z_5 + z_6; \quad a_{34} = z_1;$$

$$a_{41} = z_0; \quad a_{42} = 0; \quad a_{43} = z_1; \quad a_{44} = z_0 + z_1 + z_7.$$

Here, z_N is the impedance of C_N:

$$zN = \frac{1}{j\omega C_N}, \quad C_N = \frac{\varepsilon_0\varepsilon S_N}{d_N}, \quad (5), (6)$$

where ε is the relative permittivity of the concrete or air (the latter value being used with the capacitors representing the gap), S_N is the effective area of the Nth capacitance, and d_N is the separation between the surfaces that produce the Nth capacitance.

Although formula (5) ignores the fact that the electric field between the surfaces is nonuniform, it is adequate to roughly estimate the dependence of the displacement currents in the equivalent circuit on the distance of the double electric layer from the sensing face of the tested model and on the layer area. The solution of equation (3) is

$$I = M^{-1}b. \quad (7)$$

The output voltage of the circuit (Fig. 4) is expressed as

$$U(\bar{\omega}) = R[2I_2(\bar{\omega}) + I_3(\bar{\omega})]. \quad (8)$$

The above approach enables us to estimate the area of the double electric layer and its distance from the sensing face of the tested model. We measured the AFC of the electric signal for different values of the distance from the SEs to the model. The experiment was performed on concrete models containing a single plate. The models differed in the dimensions and the location of the plate. It follows from the above calculation that each model must offer a distinctive dependence of the AFC on the SE distance, which makes it possible to ascertain the relationship between the AFC and the parameters of the source (the distance from the surface, the dimensions, and the orientation relative to the direction of impact and to the SEs). This opens up new possibilities for more accurate algorithms to evaluate the strength and for novel techniques of flaw detection based on EM emission.

The testing was performed as follows. A model was placed on a metallic plate connected to a ground, and an acoustic wave was excited in it with the above-mentioned apparatus. The EM response was detected with a capacitive transducer situated in close proximity to the model. The transducer was fixed to a specially designed movable table, which was furnished with a micrometer screw to adjust the distance from the SEs to the model.

The AFC was measured at a given frequency. It has been found that a change in the area of the inclusion, its distance to the surface being the same, shifts the amplitude–SE distance characteristic, whereas a change in the distance from the inclusion to the surface alters the slope. It is possible to obtain intersecting characteristics by varying the two parameters of the inclusion. Figure 5a shows a measured characteristic for the frequency corresponding to the principal peak of the AFC (12 kHz). The data were obtained for two models of dimensions $100 \times 100 \times 100$ mm. In model 1, the inclusion has an area of 60 mm^2 and is situated at a distance of 96 mm (curve *1*). In model 2, the respective inclusion parameters are 120 mm^2 and 80 mm (curve *2*). With each point representing three amplitude measurements, the confidence intervals in Fig. 5a indicate that the changes in the behavior of the characteristic are statistically significant. Also notice that the change in the inclusion parameters both shifts the characteristic and affects its slope so that curves *1* and *2* intersect. Figure 5b presents a computed characteristic. The computation was based on formulas (5), (7), and (8). Formula (5) was used with values of the distances from the inclusion to the sensing face of the model and to the ground plate (allowing for SE spacing), the separation between the

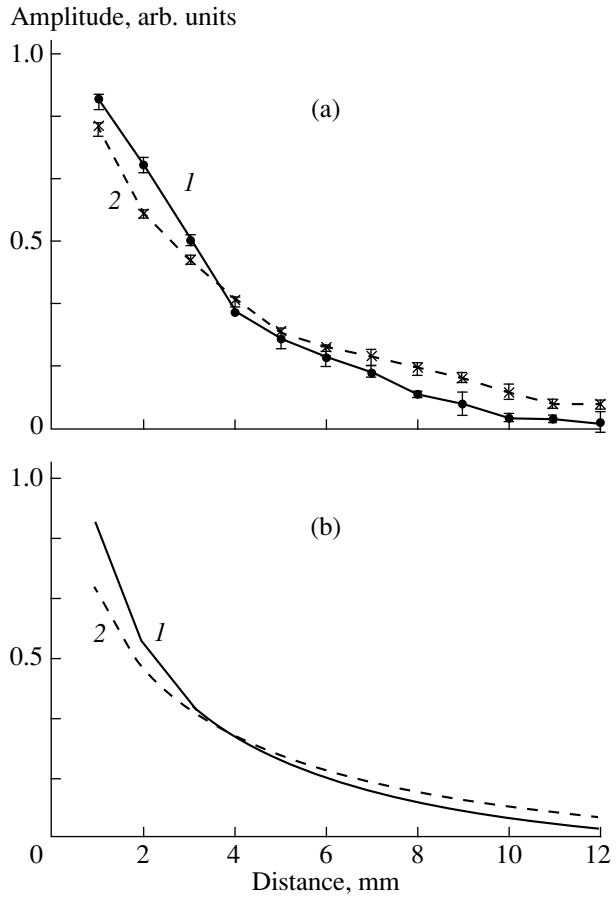

Fig. 5. Amplitude–SE-distance characteristics: (a) measured and (b) computed data. The frequency corresponds to the principal peak of the AFC.

SEs and the model, and the area of the double electric layer. The matrix entries were computed as well. It is seen that the computed characteristics agree with the measured ones in qualitative terms. This supports our approach to AEM conversion.

Yet another experiment was carried out with a metallic inclusion connected to a ground so that $C1$ and $C7$ are eliminated from the circuit. It provided further evidence for the AEM mechanism suggested here and for the above formalism to ascertain the dependence of the EM response on the inclusion parameters. It has been found that the amplitude–SE distance characteristic changes its height and slope (Fig. 6).

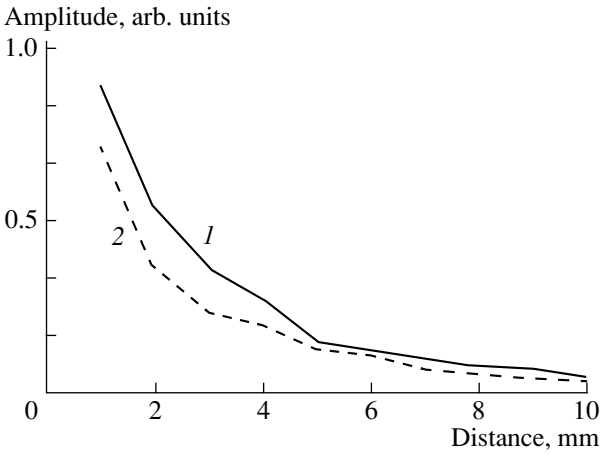

Fig. 6. Amplitude–SE-distance characteristics for a model with a single metallic inclusion, which is (*1*) disconnected from or (*2*) connected to ground.

In summary, the results of the experiments on models made of sand–cement concrete with an inclusion suggest that the AFC of the EM response to an impact depends on the location and dimensions of the inclusion. This supports the view that the AEM conversion results from the oscillation excited in the double electric layer on the interface between dissimilar materials.

In conclusion, it seems worthwhile to investigate the structure of different types of concrete that contain a large number of randomly distributed EM sources (grains of the aggregate). Such investigation should employ statistical methods. This line of research could yield more reliable techniques for the nondestructive strength testing of composite materials on the basis of AEM conversion.

REFERENCES

1. Yu. P. Malyshkov, V. F. Gordeev, T. V. Fursa, *et al.*, Izv. Vyssh. Uchebn. Zaved., Stroit., No. 5, 3 (1995).
2. T. V. Fursa, V. V. Lasukov, Yu. P. Malyshkov, *et al.*, Izv. Vyssh. Uchebn. Zaved., Stroit., No. 10, 127 (1997).
3. T. V. Fursa, N. N. Khorsov, and E. A. Baturin, Zh. Tekh. Fiz. **69** (10), 51 (1999) [Tech. Phys. **44**, 1175 (1999)].
4. V. F. Gordeev, V. P. Eliseev, Yu. P. Malyshkov, *et al.*, Defektoskopiya, No. 4, 48 (1994).

Translated by A. Sharshakov

Technical Physics, Vol. 46, No. 1, 2001, pp. 59–62. Translated from Zhurnal Tekhnicheskoĭ Fiziki, Vol. 71, No. 1, 2001, pp. 62–65.

SOLID-STATE ELECTRONICS

Simulation of Phase Transitions Induced in Gallium Arsenide by Combined Laser Radiation

S. P. Zhvavyĭ, G. D. Ivlev, and O. L. Sadovskaya

Institute of Electronics, Belarussian Academy of Sciences, Minsk, 220090 Belarus

Received January 17, 2000

Abstract—We performed a numerical simulation of phase transitions in gallium arsenide that are induced by the combined action of nanosecond laser pulses initiating melting and an additional neodymium-glass laser irradiation enabling the control of the interface velocity. In the case of counterpropagating laser beams, a strong temperature dependence of the absorption factor at 1.06 μm occurs. It causes a thermal wave, which separates from the melting front and, propagating towards the neodymium-glass laser beam, screens the melt. For copropagating laser beams, regimes with a nonmonotonic time dependence of the melt depth may exist. *© 2001 MAIK "Nauka/Interperiodica".*

One of the basic parameters that characterize the structure modification of thin semiconductor layers during heating and melting due to nanosecond laser pulses is the solid–liquid interface velocity V at the stage of epitaxial growth. For example, V specifies the nonequilibrium impurity distribution coefficient at the interface, ultimate concentration of electroactive impurity in the crystallized region [1], and concentration of point defects. Therefore, by varying the crystallization rate, one can control the properties of laser-modified semiconductors. Originally, V was controlled by varying the initial substrate temperature [2]. It was calculated [3] that the crystallization rate of Si melted by nanosecond laser pulses could be decreased more than ten times by preheating the substrate to 1000°C. However, high-temperature exposure of semiconductors is undesirable, specifically because of possible degradation of their electrical properties.

Another way to control the velocity V is combined laser heating [4–8]. In this case, a nanosecond laser pulse is used to melt a submicron layer, whereas its crystallization rate is defined by the intensity of additional radiation propagating either in the same direction as the melting pulse [4, 5] or opposite to it [6–8]. As applied to this situation, the Stefan problem was solved analytically for GaAs [7]. However, an analytical solution can hardly include temperature dependences of GaAs physical parameters, such as the absorption $\alpha(T)$ of additional radiation with a wavelength $\lambda = 1.06$ μm.

The aim of this work is numerical simulation of phase transitions induced in GaAs by the combined laser action. We studied the feasibility of controlling the interface velocity in gallium arsenide subjected to ruby laser pulses ($\tau = 70$ ns and $h\nu > E_g$, where E_g is the GaAs band gap), which are responsible for surface layer melting, and neodymium-glass laser radiation ($h\nu < E_g$), which has an effect on the velocity V through a change in the temperature distribution over the crystal.

The melting and crystallization processes were simulated by the finite difference method. In a one-dimensional approximation, the GaAs temperature is described by the heat conduction equation

$$\rho(T)[c(T) + L_m\delta(T - T_m)]\frac{\partial T}{\partial t} = \frac{\partial}{\partial x}\left[k(x)\frac{\partial T}{\partial x}\right] + S(x, t) \quad (1)$$

with the boundary and initial conditions

$$\left.\frac{\partial T}{\partial x}\right|_{x=0} = 0, \quad \left.\frac{\partial T}{\partial x}\right|_{x=h} = 0, \quad T(x, t=0) = T_0.$$

Here, ρ is the density, c is the specific heat, k is the heat conductivity coefficient, L_m is the heat of fusion, T_m is the fusion point, T_0 is the initial temperature, h is the layer thickness, and $\delta(x)$ is the delta function.

A heat source $S(x, t) = S_R(x, t) + S_N(x, t)$ takes into account heat release due to laser radiation. We have

$$S_R(x, t) = (1 - R)\alpha(x, t)\frac{W}{\tau_i}\exp\left(-\int_0^x \alpha(z, t)dz\right) \quad (2)$$

for the ruby laser pulses and

$$S_N(x, t) = (1 - R)\alpha(x, t)I_0\exp\left(-\int_0^x \alpha(z, t)dz\right) \quad (3')$$

for neodymium-glass laser radiation in the case of

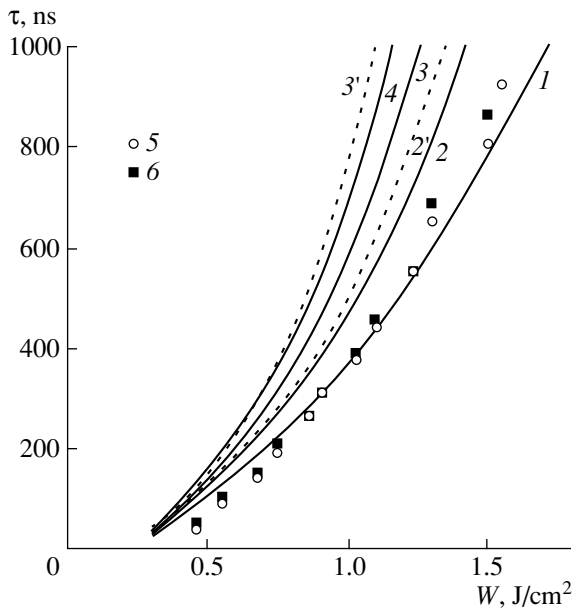

Fig. 1. Melt lifetime in gallium arsenide for counterpropagating (solid curves) and copropagating (dashed curves) laser beams versus the energy density of the ruby laser. The intensities I_0 of the Nd-glass laser radiation are (*1*) 0, (*2*) 300, (*3*) 500, and (*4*) 700 kW/cm^2; (*5*, *6*) experimental curves for $I_0 = 0$ and (100) and (111) orientations, respectively.

copropagating laser beams or

$$S_N(x,t) = (1-R)I_0\left\{\alpha(x,t)\exp\left(-\int_x^h \alpha(z,t)dz\right)\right.$$

$$+\alpha(x,t)R_{sl}\exp\left(-\int_d^h \alpha(z,t)dz - \int_x^d \alpha_l(z,t)dz\right) \quad (3'')$$

$$\left.+(1-R_{sl})\alpha_l(x,t)\exp\left(-\int_d^h \alpha(z,t)dz - \int_x^d \alpha_l(z,t)dz\right)\right\}$$

in the case of counterpropagating beams. The first two terms on the right side of (3") describe the absorption of the neodymium-glass laser pulses in the crystal, and the third term stands for absorption in the melt. Here, R and α are the reflection and absorption factors, respectively; R_{sl} is the reflection factor at the solid–liquid interface; $d = d(x, t)$ is the melting front position at a time t; W and τ_i are the energy density and the pulse duration of the ruby laser; I_0 is the intensity of neodymium-glass laser radiation; and subscript l denotes the melted (liquid) phase.

The set of Eqs. (1)–(3) was solved by the succession sweep method using iterations. The ruby laser pulse shape was defined by the function $\sin^2(\pi t/2\tau_i)$, where $\tau_i = 70$ ns. We assumed that the GaAs wafer thickness considerably exceeded the thermal diffusion length within the pulse duration (30 μm). Thermal and optical parameters used to solve the problem are listed in the table.

The dependences of the melt lifetime τ on the energy density of the ruby laser at different intensities of the Nd-glass laser radiation are presented in Fig. 1. The plot also shows the experimental curves $\tau(W)$ for

GaAs parameters used in solving the problem [9]

Parameter	Crystalline GaAs	Melted GaAs
ρ, g/cm^3	5.317	5.317
c, J/g K	$0.303 + 5.0\times10^{-5}T$	0.379
L_m, J/g	730 [10]	
k, W/cm K	$\frac{2271}{T^{1.463}}$	0.178 [10]
$E_g(T)$, eV	$1.575–5.0\times10^{-4}T$	
$\lambda = 1.06$ μm		
R	0.30	0.64
α, cm^{-1}	$10\exp[149(-0.36 + 0.5\times10^{-3}T)]$, $T < 812$ K $2.91\times10^4\exp[3.22(-0.77 + 0.5\times10^{-3}T)]$, $T < 812$ K	10^6
$\lambda = 0.69$ μm		
R	0.33	0.64
α, cm^{-1}	$2.91\times10^4\exp[3.22(-0.16 + 0.5\times10^{-3}T)]$, $T < 400$ K $3.48\times10^4\exp[1.71(-0.2 + 0.5\times10^{-3}T)]$, $T < 400$ K	10^6

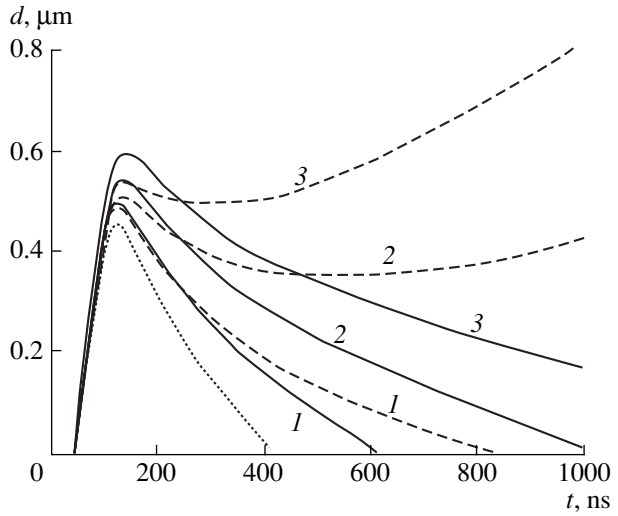

Fig. 2. Time dependences of the melt thickness at W = 1 J/cm^2 and I_0 = (*1*) 500, (*2*) 1000, and (*3*) 1500 kW/cm^2. Dotted line, I_0 = 0; counterpropagation and copropagation are indicated by solid and dashed curves, respectively.

the (100) and (111) crystallographic orientations of GaAs wafers. The curves were obtained without the additional irradiation (I_0 = 0). Obviously, the results of numerical simulation are in good agreement with experimental data [11]. It is also seen that additional heating by the neodymium-glass laser leads to a considerable increase in the melt lifetime. Note that, for copropagating beams, $\Delta\tau$ is considerably larger than in the case of counterpropagation. For example, at W = 1 J/cm^2 and I_0 = 300 kW/cm^2, $\Delta\tau$ is about 400 and 190 ns, respectively. Still more pronounced quantitative and qualitative differences between these two conditions of laser action are observed in the time dependences $d = d(t)$ (Fig. 2). Unlike [7], our calculations do not predict the "stretch-out" of the melting front in GaAs for beam counterpropagation. Due to the strong temperature dependence of the absorption factor at λ = 1.06 μm (at T > 600 K, α drastically increases and approaches ~10^4 cm^{-1} at $T \geq 800$ K), the heated layer in front of the crystal–melt interface begins to absorb the radiation. A thermal wave forms (Fig. 3a, curves *1*, *2*), which then separates from the melting front and, propagating towards the Nd-glass laser beam, screens the melt (curves *3*–*5*). Thus, the interface velocity drops, because additional heat release due to the absorption of the Nd-glass laser radiation smoothes out the temperature gradient.

In the case of copropagating laser beams, the interface movement can be nonmonotonic at a sufficiently high I_0 (Fig. 2; curves *2*, *3*). In the falling branch of the $d(t)$ curve (recrystallization), a temperature field with a quasi-stationary profile is produced (Fig. 3b, curves *1*–*3*). If the intensity of the additional radiation is sufficient to compensate for heat removal from the interface into the crystal volume, crystallization stops after a time and

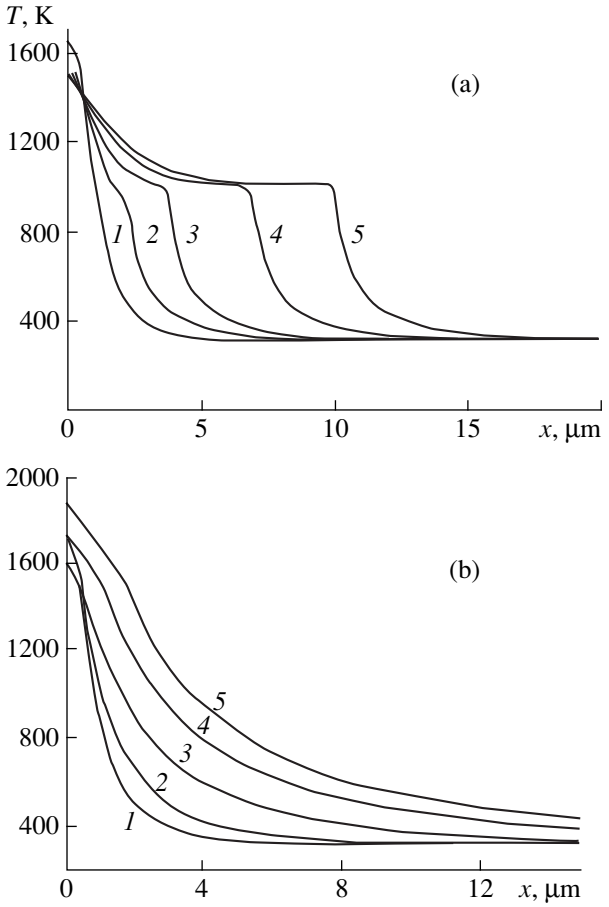

Fig. 3. Depth profiles of the temperature for (a) counterpropagation at t = (*1*) 140, (*2*) 290, (*3*) 430, (*4*) 730, and (*5*) 1015 ns and (b) copropagation at t = (*1*) 140, (*2*) 290, (*3*) 1000, (*4*) 2540, and (*5*) 4040 ns. W = 1 J/cm^2 and I_0 = 1000 kW/cm^2.

melting proceeds (Fig. 2, curves *2*, *3*). Under such conditions of laser heating, the melting front advances into the wafer and the surface temperature sharply grows (Fig. 3b, curves *4*, *5*).

In conclusion, in the case of counterpropagating laser beams, a strong temperature dependence of α at the fundamental absorption edge can give rise to a thermal wave that screens the phase transition region. For copropagating beams, the time dependence of the melt thickness may be nonmonotonic.

REFERENCES

1. *Surface Modification and Doping by Laser, Ion, and Electron Beams*, Ed. by J. M. Poate, G. Foti, and D. C. Jacobson (Plenum, New York, 1983; Mashinostroenie, Moscow, 1987).
2. A. G. Gullis, H. C. Webber, J. M. Poate, and A. L. Simons, Appl. Phys. Lett. **36**, 320 (1980).
3. S. P. Zhvavyĭ and G. D. Ivlev, Inzh.-Fiz. Zh. **69**, 790 (1996).

4. D. H. Auston, J. A. Golovchenko, and T. N. C. Venkatesan, Appl. Phys. Lett. **34**, 558 (1979).
5. G. G. Gromov, S. V. Zhuk, K. V. Rudenko, and V. B. Ufimtsev, Fiz. Tekh. Poluprovodn. (Leningrad) **21**, 688 (1987) [Sov. Phys. Semicond. **21**, 421 (1987)].
6. Yu. V. Koval'chuk, V. I. Kuchinskiĭ, V. E. Myachin, *et al.*, Pis'ma Zh. Tekh. Fiz. **10**, 220 (1984).
7. V. N. Abakumov, V. N. Guman, and V. S. Yuferev, Fiz. Tekh. Poluprovodn. (Leningrad) **20**, 2178 (1986) [Sov. Phys. Semicond. **20**, 1363 (1986)].
8. E. N. Arutyunov, L. V. Belyakov, A. N. Vasil'ev, *et al.*, Zh. Tekh. Fiz. **55**, 2144 (1985) [Sov. Phys. Tech. Phys. **30**, 1267 (1985)].
9. J. R. Meyer, M. R. Kruer, and F. T. Bartoli, J. Appl. Phys. **51**, 5513 (1980).
10. G. D. Ivlev and V. L. Malevich, Zh. Tekh. Fiz. **60**, 199 (1990) [Sov. Phys. Tech. Phys. **35**, 258 (1990)].
11. E. I. Gatskevich, G. D. Ivlev, and A. M. Chaplinov, Kvantovaya Élektron. (Moscow) **22**, 805 (1995).

Translated by A. Sidorova-Biryukova

Technical Physics, Vol. 46, No. 1, 2001, pp. 63–67. Translated from Zhurnal Tekhnicheskoĭ Fiziki, Vol. 71, No. 1, 2001, pp. 66–71.

OPTICS, QUANTUM ELECTRONICS

The Effect of UV Irradiation on Temperature Dependence of Photoluminescence and Photoacoustic Response in Porous Silicon

S. N. Bashchenko, I. V. Blonskiĭ, M. S. Brodyn, V. N. Kadan, and Yu. G. Skryshevskiĭ

Institute of Physics, National Academy of Sciences of Ukraine, pr. Nauki 144, Kiev, 252028 Ukraine

e-mail: kadan@iop.kiev.ua

Received January 14, 2000; in final form, April 13, 2000

Abstract—The influence of UV irradiation on temperature dependence of the integral intensity of luminescence $I_{lum}(T)$ in porous silicon was studied. It was found that, if luminescence decays with temperature nonmonotonically, the peak of $I_{lum}(T)$ shifts toward higher temperatures as the exciting radiation density increases. Under UV irradiation, the function $I_{lum}(T)$ becomes monotonically decreasing. If the function $I_{lum}(T)$ is initially monotonically decreasing, UV preirradiation changes the emission spectrum and accelerates temperature quenching of the red-orange emission band. The variation of the amplitude of the pulsed photoacoustic response with UV irradiation dose was studied. The dependence found is explained by the removal of foreign inclusions from the developed surface of porous silicon. An energy level diagram that makes it possible to explain the behavior of $I_{lum}(T)$ is suggested. It is noted that the shape of the function $I_{lum}(T)$ can be used as a test whereby the contributions from dissimilar oscillators to the red-orange emission band are estimated.

INTRODUCTION

Luminescence from porous silicon features a number of anomalies. The room-temperature red-orange emission band with a high quantum yield [1] is the most dramatic example. There are also some other features related to changes in the basic parameters of emission bands in response to external factors. Out of them, the nonmonotonic variation of the integral intensity of the red-orange band with temperature is the subject of investigation in this paper.

As follows from [2–5], when the temperature rises from the helium to the room value, the function $I_{lum}(T)$ first increases and then flattens out; at $T > 100$ K, temperature quenching of the band by a law other than the Arrhenius law is observed. There is no consensus of opinion among authors, for the most part, on the position of the $I_{lum}(T)$ peak. However, usual (exponential) temperature quenching of the band throughout the temperature range between 4 and 300 K was found in [6] and a continuous rise of the band intensity, in [7]. Analysis of works [2–7] and others suggests that there is a correlation between a porous silicon process and the shape of the $I_{lum}(T)$ curve.

In this paper, we studied the effect of pulsed UV irradiation on the shape of the $I_{lum}(T)$ function in porous silicon. The central idea was to elucidate the effect of a substance deposited on silicon fibers on the shape of the $I_{lum}(T)$ curve and gain new information on the nature of the basic emission band. The surface cleaning efficiency of the porous silicon films was judged from the pulsed photoacoustic (PA) response.

EXPERIMENTAL

Samples were irradiated by high-power UV pulses from a Xe–Cl excimer laser built around an oscillator and a three-pass amplifier [8]. The radiation wavelength was 308 nm; the pulse width, 25 ns; and the pulse energy, 20 mJ. Irradiation was carried out in a chamber where the gas composition can be varied.

The photoluminescence (PL) spectra were excited by a mercury-discharge lamp or a 337-nm pulsed nitrogen laser. The PL emission was detected by a grating spectrometer with a CCD chain (resolution 0.2 nm). The temperature was varied and kept accurate to 1 K.

During irradiation by nanosecond pulses of the Xe–Cl excimer laser, the pulsed PA response was detected by a wide-band oscilloscope provided with a high-sensitivity piezoelectric ceramic PA cell. (For more details, see [8].)

The porous silicon samples under study were prepared by the conventional technology [2] with anodizing current densities ranging from 5 to 80 mA/cm^2 and electrolytic etching times between 15 and 90 min. The aging time of the samples was between 1 h and 2 months. Ultimate cleaning techniques also differed. Initial *p*-type silicon wafers with a resistivity of 10 Ω/cm had the (111) orientation. In taking temperature dependences of the PL intensity and PA response,

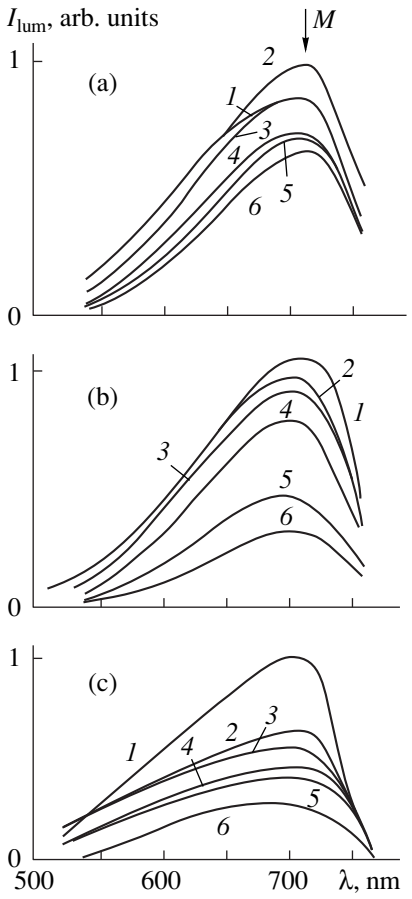

Fig. 1. Luminescence spectra from porous silicon samples of the first type: (a) initial sample, (b) after preirradiation by 50 pulses of the excimer laser, and (c) after preirradiation by 150 pulses of the excimer laser. T = (*1*) 5, (*2*) 70, (*3*) 150, (*4*) 200, (*5*) 250, and (*6*) 300 K.

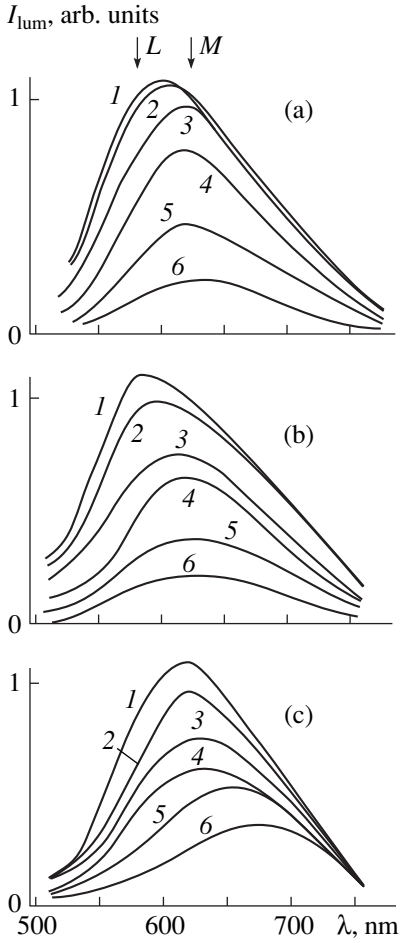

Fig. 2. The same as in Fig. 1 for the samples of the second type.

emphasis was on two types of samples differing in preparation conditions and in visual appearance. The samples of the first type had high mechanical strength and the metallic luster typical of single-crystal silicon. The technology of their preparation was described in [2]. For these samples, the emission band peaked at 720 nm. The samples of the second type were chestnut brown and had low mechanical strength, which implies that a thin weak porous silicon film can be separated from the single-crystal silicon substrate. The free porous silicon films were obtained as described in [9]. For them, the emission band peaked at a wavelength of 610 nm for T = 4.2 K.

THE INFLUENCE OF UV IRRADIATION ON THE PL PROPERTIES OF POROUS SILICON

Let us examine temperature dependences of $I_{lum}(T)$ for the red-orange emission band in samples of both types. Note that the exciting radiation density affects the shape of the $I_{lum}(T)$ curve [4]. This may be a reason for the discrepancy in the peak positions of the $I_{lum}(T)$ curve that were reported in [2–7]. Therefore, when considering the shape of the $I_{lum}(T)$ dependence, one should indicate the exciting radiation density at which the PL spectra have been obtained. The spectra excited by the mercury-discharge lamp with an excitation density of 10^{19} photon/(cm^2 s) are shown in Figs. 1 and 2 for the samples of the first and second types, respectively. The temperature dependences of the PL spectra (curves *1–6*) were obtained both for the as-prepared samples (Figs. 1a, 2a) and for those preirradiated by the excimer laser at various UV doses (Figs. 1b, 1c, 2b, 2c). In what follows, emphasis will be on (1) the nonmonotonic run of the $I_{lum}(T)$ curve for the samples of the first type, while the samples of the second type exhibit the usual (Arrhenius) temperature decay of the red-orange band; (2) the influence of UV irradiation, which changes the nonmonotonic $I_{lum}(T)$ curve to a monotonically decreasing one as the temperature of the type-2 samples grows and accelerates temperature quenching of luminescence in these samples; and (3) the tempera-

ture-related distortion of the emission band for the type-2 samples due to faster decay of its short-wave branch. The greater the irradiation dose, the more distinct the last feature. The difference in the rates of PL temperature quenching allows separation of the net band into two (*L* and *M*) bands. Note also that, because of faster decay of the *L* band, the shapes of the PL spectra at room temperature become nearly identical for samples of both types (Figs. 1, 2; curves *6*).

The PL integral intensity *I* vs. the excitation power density *P* (or lux–intensity characteristic) for the type-1 samples is shown in Fig. 3. For the type-2 samples, the *I–P* characteristics are the same. As is seen, the curves tend to saturation, which is typical of radiative recombination through impurity centers. Point *A* in the initial linear region of the characteristic corresponds to low excitation levels, at which the temperature dependences of the emission bands for the samples of both types (Figs. 1, 2) were taken. The same temperature dependences were also taken at greater excitation densities (point *B*). For the type-1 samples, the temperature dependences of the PL integral intensity at the excitation densities corresponding to points *A* and *B* are shown in Fig. 4. At the elevated excitation density, the peak of the $I_{lum}(T)$ curve tends to higher temperatures.

THE INFLUENCE OF UV IRRADIATION ON THE PULSED PA RESPONSE IN POROUS SILICON

The PA properties of the porous silicon samples of both types are similar in many respects. A typical oscillogram depicting the PA response of porous silicon irradiated by nanosecond pulses from the Xe–Cl laser is shown in the insert at the top of Fig. 5. Let us look more closely at the parameters of the PA response. It is bipolar and shows oscillation due to a photoexcited compression–dilatation wave. The PA response (pulse) amplitude varies as the electromagnetic–acoustic conversion efficiency; and the duration of a PA pulse, as the time of acoustic wave propagation through the region of photoexcitation. The response structure is of the "acoustic ringing" type. Such a train of pulses arises from multiple reflections of the acoustic wave when it propagates through the acoustic line between a photoexcitation region and the piezoelectric sensor [8, 10].

Consider mechanisms of sound generation in porous silicon. In discussing the nature of the experimentally observed phenomenon—photogeneration of sound with giant volume [10, 11]—we have already mentioned some with them: thermoelastic, pseudostriction, and pulsation (when individual fragments of the porous silicon framework are thermally isolated). However, at the exciting irradiation densities used in this work, other mechanisms may appear. The dependences of the PA response amplitude on the number of laser pulses n_{pulse} at various energy densities per pulse (Fig. 5) strengthen this supposition. A common property of the $u_{PA\ r}(n_{pulse})$ curves for the samples of both types is an

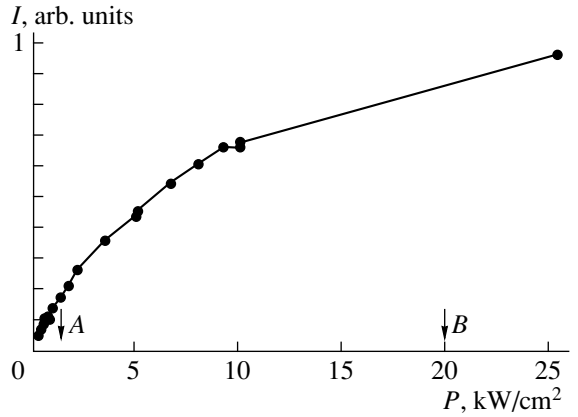

Fig. 3. Lux–intensity characteristic for the samples of the first type at $T = 300$ K.

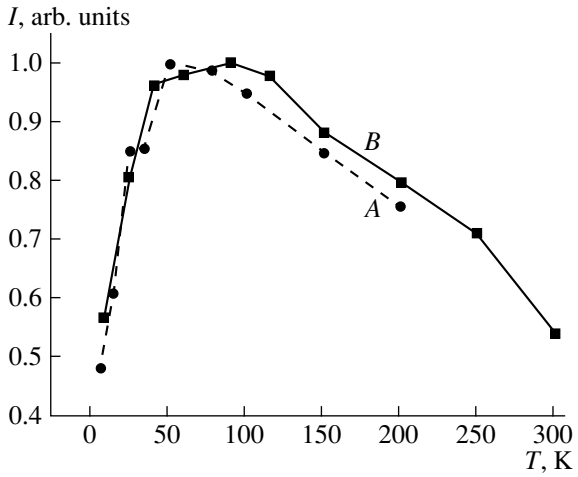

Fig. 4. PL integral intensity vs. temperature for the samples of the first type. The exciting radiation density per pulse of the nitrogen laser is (*A*) 1 and (*B*) 20 kW/cm^2.

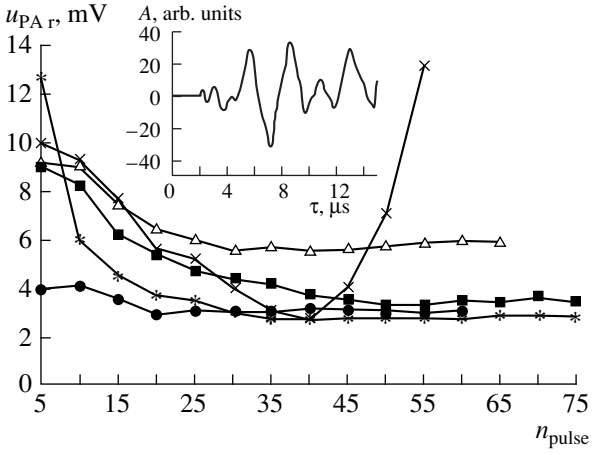

Fig. 5. PA response amplitude vs. the number of excimer laser pulses for the samples of the second type. The energy density per pulse is ◆ 156, ■ 210, △ 280, × 410, and ∗ 1950 mJ/cm^2. The insert shows a typical PA response from porous silicon irradiated by Xe–Cl laser pulses.

abrupt decrease in the PA response intensity, followed by a plateau at $n_{pulse} > 10$. However, for the type-2 samples, an increase in the power density (starting with 1950 mJ/cm^2) at $n_{pulse} > 40$ causes the value of $u_{PA\,r}$ to rise again.

The data in Fig. 5 can consistently be explained if we suppose that, when the samples are irradiated by high-power pulses of the Xe–Cl excimer laser, the ablation of foreign inclusions out of the surface of the silicon fibers forming the porous silicon framework makes the major contribution to sound generation. In this case, the decrease in $u_{PA\,r}(n_{pulse})$ reflects the degree of surface cleaning, which increases with the number of irradiation pulses. At power densities >1950 mJ/cm^2 and $n_{pulse} > 40$, a sound generation mechanism associated with the destruction of the porous silicon framework dominates. This explanation is independently supported by visual observations: the samples of the second type (chestnut brown) change in color and then show signs of destruction of their structure as n_{pulse} grows. With regard for such an explanation of the dependence $u_{PA\,r}(n_{pulse})$, it appears logical to assume that the *L* component of the red-orange band for these samples is closely related to foreign inclusions surrounding the silicon fibers. This is attested to by a correlation between a decrease in the *L* band intensity and a decrease in the PA response amplitude as the UV irradiation dose grows.

RESULTS AND DISCUSSION

The experimental results on the effect of UV irradiation on the shape of the $I_{lum}(T)$ curves for the type-1 and type-2 samples can consistently be explained within the following model. Let an element of the porous silicon structure have the form shown in the insert in Fig. 6; that is, nanometer silicon fiber *1* of variable thickness is covered first by SiO_2 layer *2* and then by composite layer *3* containing, among others, etching products. Assume that the difference in structure between the samples is that the thickness of layer *3* in the samples of the first type (with metallic luster) is significantly smaller than in the chestnut brown samples of the second type. We will proceed from the sensitized model of luminescence in porous silicon, which implies that light absorption and light emission occur in different substances; that is, the underlying mechanism of luminescence is spatial transfer of the excitation energy from one substance to another [12]. Assume that light is largely absorbed in layer *3*, covering silicon fiber *1* (Fig. 6, transition *0–1*). Then, the electrons pass into the conduction band of silicon nanostructures through nonradiative quantum transition *1–2* (the energy position of this band is renormalized with respect to the bulk silicon due to the quantum size effect). Bearing in mind that porous silicon has a developed surface, we must allow for the presence of a set of traps *3*. At helium temperature, the electrons are partly captured by these centers from the porous silicon conduction band (transition *2–3*). The rest of the conduction-band electrons radiatively recombine at positively charged defects (most likely at those localized near the porous silicon–silicon oxide interface), bringing about the *M* band of certain intensity (transition *2–4*). It is obvious that the electrons leave trap states *3* with an increase in the temperature. As a result, the population of the conduction band *2* and, hence, the *M*-band integral intensity grows. The peak integral intensity [the point where $I_{lum}(T)$ changes sign] corresponds to complete thermal delocalization of traps. Now, the fact that the position of the point where $I_{lum}(T)$ changes sign depends on the excitation intensity can easily be explained in terms of the proposed model: as the concentration of photoexcited electrons increases, so does the probability of deeper trap states being occupied. Subsequent temperature quenching of the *M* band at higher temperatures (above the sign reversal point) should be associated with thermal destruction of state *4*. Previous UF irradiation breaks down the centers responsible for the trap states. This is the reason why UV preirradiation changes the shape of the $I_{lum}(T)$ curve for the samples of the first type.

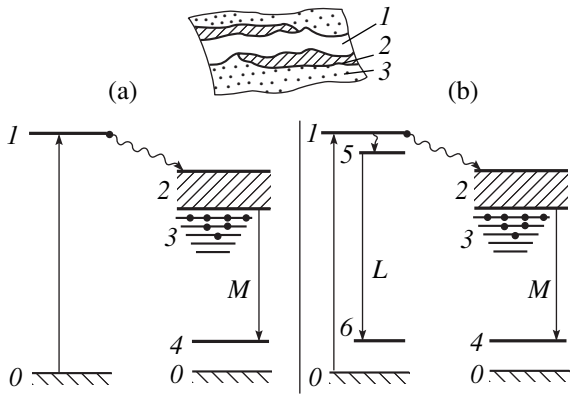

Fig. 6. Energy diagrams accounting for the luminescence spectra in porous silicon samples of (a) the first and (b) the second type. *0–1*, absorbing transition; *1–2*, nonradiative transition; *2–4*, transition giving rise to the *M* band; and *5–6*, transition giving rise to the *L* band.

Thus, we have outlined a model explaining the nonmonotonicity of the $I_{lum}(T)$ curve for the samples of the first type.

The same explanation is also valid when applied to the shape of the $I_{lum}(T)$ curve in the type-2 samples, but for the *M* component of the red-orange emission line alone. The more intense *L* component of the spectrum would be appropriately related to charge carrier recombination in outer envelope *3* covering the silicon fiber (transition *5–6*). This follows from the changes in the PL spectrum, the shape of the dependence $I_{lum}(T)$, and the PA response with the UV irradiation dose. A higher

rate of temperature decay of the *L* band as compared with the *M* band also supports this assumption.

Clearly, such an explanation for the shape of the $I_{lum}(T)$ curve is simplified. To gain a better understanding of processes responsible for the shape of $I_{lum}(T)$, we must have refined data for charge transfer through a partly disordered medium (in our case, through outer layer *3* covering silicon fiber *1*) and for the effect of UV irradiation on the composition of layers passivating porous silicon (by hydrogen transfer between oscillators, final oxidation of silicon, etc.).

The above issues are of importance, because the shape of $I_{lum}(T)$ may serve as a test that would make it possible to separate the emission of siloxens and other etching products from that closely associated with silicon fibers (see the energy diagrams in Fig. 6).

CONCLUSION

The effect of previous UV irradiation on the shape of the $I_{lum}(T)$ curve was studied for porous silicon irradiated under various conditions. In the case of samples with nonmonotonic temperature decay, the effect of the exciting irradiation intensity on the position of the point of sign reversal in the $I_{lum}(T)$ curve was also investigated. It was confirmed that, with a rise in the excitation density, the point of reversal is shifted to higher temperatures. UV preirradiation of the samples with a nonmonotonic function $I_{lum}(T)$ makes it monotonically decreasing. For type-2 samples, which initially show a monotonically decreasing $I_{lum}(T)$ curve, UV preirradiation changes the spectrum and accelerates temperature quenching of the red-orange band. The variation of the pulsed PA-response amplitude with the UV-irradiation dose was investigated. The analytical dependence deduced is explained in terms of cleaning the developed porous silicon surface from foreign inclusions covering the silicon fibers. The energy diagram that helps in explaining the behavior of $I_{lum}(T)$ for porous silicon samples obtained under different conditions is suggested. The shape of the $I_{lum}(T)$ curve can serve as a test whereby the contributions from dissimilar oscillators to the red-orange emission band can be separated.

REFERENCES

1. L. T. Canham, Appl. Phys. Lett. **57**, 1046 (1990).
2. A. G. Cullis, L. T. Canham, and P. D. Calcott, J. Appl. Phys. **82**, 909 (1997).
3. X. L. Zheng, W. Wang, and H. C. Chen, Appl. Phys. Lett. **60**, 986 (1992).
4. Y. Mochizuki, M. Mizuta, Y. Ochiai, *et al.*, Phys. Rev. B **46**, 12353 (1992).
5. P. K. Kashkarov, E. A. Konstantinova, S. A. Petrova, *et al.*, Fiz. Tekh. Poluprovodn. (St. Petersburg) **31**, 745 (1997) [Semiconductors **31**, 639 (1997)].
6. Z. Y. Xu, M. Gal, and M. Gross, Appl. Phys. Lett. **60**, 1375 (1992).
7. K. Murayama, S. Miyazaki, and M. Hirose, Jpn. J. Appl. Phys. A **33**, 3310 (1994).
8. S. N. Bashchenko, I. V. Blonskiy, and V. M. Puzikov, Proc. SPIE **3359**, 519 (1998).
9. S. V. Svechnikov, A. V. Sachenko, G. A. Sukach, *et al.*, Opt. Poluprovodn. Tekh. **27**, 3 (1994).
10. I. V. Blonskiy, M. S. Brodin, and V. A. Tkhoryk, Semicond. Sci. Technol. **12** (1), 11 (1997).
11. M. S. Brodyn, I. V. Blonskiĭ, and V. A. Tkhoryk, Pis'ma Zh. Tekh. Fiz. **20** (14), 41 (1994) [Tech. Phys. Lett. **20**, 580 (1994)].
12. I. A. Buyanova, I. Ya. Gorodetskiĭ, N. E. Korsunskaya, *et al.*, Fiz. Tekh. Poluprovodn. (St. Petersburg) **30**, 1516 (1996) [Semiconductors **30**, 797 (1996)].

Translated by B. Malyukov

Technical Physics, Vol. 46, No. 1, 2001, pp. 68–75. Translated from Zhurnal Tekhnicheskoĭ Fiziki, Vol. 71, No. 1, 2001, pp. 72–78.

Energy Deposition by Fission Fragments in Nuclear-Pumped Lasers: I. A General Method of Calculation

V. Yu. Mat'ev

Russian Federal Nuclear Center, All-Russia Research Institute of Experimental Physics, Sarov, Nizhegorodsk oblast, 607190 Russia

Received October 28, 1999; in final form, February 22, 2000

Abstract—A general method of calculating the energy deposition by fission fragments in nuclear-pumped lasers is presented. A specific case of a cylindrical cell is considered. © *2001 MAIK "Nauka/Interperiodica".*

INTRODUCTION

Direct conversion of nuclear energy into coherent light has been studied extensively in Russia and the United States [1–3]. The basic principle of nuclear pumping lies in producing the recombinating nonequilibrium plasma under bombardment of the gas by ions (fission fragments or light ions). These ions are the products of neutron-induced nuclear reactions either in the gas (internal pumping) or in a thin layer of the material (active layer) deposited onto a substrate inside a laser cell (external pumping). In practice, the use of fission fragments as bombarding ions is of particular interest.

The energy deposition by bombarding ions has a crucial role in forming optical and energy characteristics of the laser light. The methods for calculating the energy deposition were first devised within the framework of radiation chemistry [4–9] and then for nuclear-laser problems [10–14]. A complete solution to the problem was obtained for active layers of infinite plane geometry [8, 14]. For practical purposes [15], it is of interest to consider active layers of finite plane (rectangular) or cylindrical geometry. The Monte Carlo [9] and quadrature [12] methods were applied to cylindrical layers. However, reasonable results were obtained only for the integrated energy deposition, whereas the calculation of optical inhomogeneities requires knowledge of the spatial energy deposition distribution. For rectangular layers, the energy deposition was not calculated.

In this work, we proposed a general quadrature method for calculating the energy deposition [16, 17] in layers of arbitrary geometry for a nonuniform density of the media.

PHYSICAL PRINCIPLES OF THE PROPOSED METHOD

As a rule, the energy deposition is calculated under the following assumptions [4–14]: (i) isotropic separation of ions forming in an active layer, (ii) rectilinear ion trajectories, and (iii) instantaneous slowing down of ions. Let us suppose that the ion spectrum exhibits energy homogeneity. For fission fragments, this assumption ensures a sufficient calculation accuracy [5, 9]. The "moderation law"—the dependence of the ion energy E on the distance l—plays the key role in calculations of the energy deposition. This dependence is usually described by the empirical formula [4–14]

$$E(l) = E_0(1 - L)^n, \quad L = \sum_i \frac{l_i}{R_i}, \tag{1}$$

where E_0 is the initial ion energy, l_i are the ion path lengths in the sequentially crossed media, R_i is the ion path in the ith medium, and n is the parameter of the moderation law.

Formula (1) can be generalized to the case of media exhibiting nonuniform densities. To determine its applicability limits, let us consider the stopping power $S(E) = -dE/(Ndl)$, where N is the concentration of atoms in the medium. According to the experimental data [18, 19], the stopping power for a wide variety of media can be represented in multiplicative form with fair accuracy; that is,

$$S \approx \zeta s(E), \tag{2}$$

where the function $s(E)$ and the parameter ζ depend on the ion and the medium, respectively.

For a homogeneous medium, we can write

$$\eta(E_0) - \eta(E) = \zeta Nl, \quad \eta(E) = \int_0^E \frac{dE'}{s(E')},$$

$$R(E) = \frac{\eta(E_0)}{\zeta N}.$$

If an ion crosses several media of variable density

$N_i = N_i(l)$, then

$$\eta(E_0) - \eta(E) = \sum_i \zeta_i \int_{l_i} N_i(l)dl,$$

$$\eta(E) = \eta(E_0)(1-L), \quad L = \sum_i L_i,$$

$$L_i = \frac{\zeta_i \bar{N}_i}{\eta(E_0)} \int_{l_i} \frac{N_i(l)}{\bar{N}_i} dl = \frac{1}{\bar{R}_i} \int_{l_i} \frac{\rho_i(l)}{\bar{\rho}_i} dl = \int_{l_i} \frac{dl}{R_i(l)}, \tag{3}$$

$$\bar{R}_i = R_i(\bar{\rho}_i), \quad R_i(l) = \bar{R}_i \frac{\bar{\rho}_i}{\rho_i(l)},$$

where $\bar{N}_i$ is the mean concentration of atoms in the ith medium and $\rho_i(l)$ and $\bar{\rho}_i$ are the local and mean densities of the ith medium, respectively. The total ion energy loss ($E = 0$) corresponds to $L = 1$. Thus, the moderation law for the case of several inhomogeneous media can be represented as follows:

$$E(l) = E_0 u(L), \quad u(L) = E_0^{-1} \eta^{\#}[\eta(E_0)(1-L)], \quad L \le 1, \quad u(L=1) = 0, \tag{4}$$

where $\eta^{\#}$ is the inverse function with respect to η, so that $\eta^{\#}[\eta(E)] = E$.

For the dependence $S(E) = \zeta_i E^p$ and a uniform density, we obtain formula (1), so that $n = 1/(1-p)$ and $R = E_0^{1-p}[(1-p)\zeta_i N]^{-1}$. The linear moderation law ($n = 1$, $p = 0$, and $S = \text{const}$) can be applied to the light ions in the vicinity of the maximum stopping power. The exponents $n < 1$ ($p < 0$) have meaning only in the Bethe–Bloch velocity range. There are two traditions in characterizing fission fragments. One of them ("the law of 3/2" at $n = 3/2$, $p = 1/3$) [7, 12, 20] is based on the experimental energy dependence of the fission-fragment path [21]. The other tradition ("quadratic law" at $n = 2$, $p = 1/2$) [4, 9] is confirmed by measurements of the energy spectrum of the fragments radiated by uranium layers [5]. Note that the "path" in formula (1) is the parameter responsible for the exactness of the moderation law. The measurable fission-fragment path is primarily determined by the final stage of moderation at which the stopping power is minimum. Hence, the "law of 3/2" can be used to calculate the concentration of the moderated fragments. However, the energy deposition is predominantly determined by the initial stage of moderation at which the stopping power is maximum. Therefore, it is expedient to calculate the energy deposition according to the quadratic law, because it is more appropriate for "the initial part of the track" [4]. The parameters $p = 1/2$ ($n = 2$) agree well with both the moderation theory and the experiments with different ions [18, 19, 22].

MATHEMATICAL FORMULATION OF THE METHOD

Let us consider a cell (Fig. 1) in which the active layer occupies the volume V_A spatially bounded by the surfaces s_1 and s_2. The active layer is covered with a protective coating (a region between the surfaces s_0 and s_2). The irradiated volume of the gas V_0 is bounded by the surfaces s_0 and s_3 (s_3 contains the opposite wall and the cross sections of the side slots). We assume that a neutron flux is uniform in the active layer (or at least within the ion path). The number of nuclear reactions $N^*(\mathbf{r}_A)$ per unit volume of the active layer per unit time is proportional to the layer density $\rho_1(\mathbf{r}_A)$; that is,

$$N^*(\mathbf{r}_A) = \bar{N}^* \frac{\rho_1(\mathbf{r}_A)}{\bar{\rho}_1}, \tag{5}$$

where $\bar{N}^*$ and $\bar{\rho}_1$ are the $N^*(\mathbf{r}_A)$ and $\rho_1(\mathbf{r}_A)$ values averaged over the layer (within the ion path).

Within the initial approximations, we now consider isotropic monoenergetic ion sources with the initial ion energy E_0. Assume that the distribution of these sources over the active layer is given by Eq. (5). Then, the energy flux density produced by these sources at an arbitrary point C (Fig. 1) can be represented as

$$\Phi(\mathbf{r}_C) = \int_{V_A} \varphi_A(\mathbf{r}_C) E(l) dV_A,$$

$$\varphi_A(\mathbf{r}_C) = \frac{N^*(\mathbf{r}_A)}{4\pi l^2} \frac{\mathbf{l}}{l}, \quad l = l_{AC} = l_1 + l_2 + l_0. \tag{6}$$

Subscripts 0, 1, and 2 refer to the gas, the active layer, and the coating, respectively. The integration is performed within the path. Let dS_A be an element of the area of the surface s_A passing through the active layer and ϑ_A be an angle between the normal $\mathbf{n}_A$ to this surface and the vector $\mathbf{l}$. Then, $dV_A = (\mathbf{n}_A \cdot d\mathbf{l}_1)dS_A = \cos\vartheta_A dl_1 dS_A$. Let dS_C be an element of the area of the surface s_C passing through the point C and ϑ_C be an angle between the normal $\mathbf{n}_C$ to this surface and the

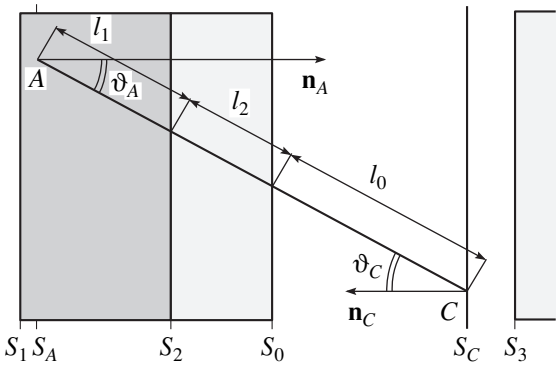

Fig. 1. A nuclear-pumped laser cell of arbitrary geometry.

vector **l**. The energy flux transferred by ions through the surface s_C is given by

$$\Psi(s_C) = \int_{s_C} (\mathbf{n}_C \Phi(\mathbf{r}_C)) dS_C$$

$$= \int_{s_C V_A} \frac{N^*(\mathbf{r}_A)}{4\pi l^3} E(l)(\mathbf{n}_C \mathbf{l})(\mathbf{n}_A d\mathbf{l}_1) dS_A dS_C \quad (7)$$

$$= \int_{s_C V_A} N^*(\mathbf{r}_A) E(l) \cos\vartheta_A dl_1 dS_A \frac{d\Omega_A}{4\pi}$$

$$= \int_{s_C V_A} N^*(\mathbf{r}_A) E(l) \cos\vartheta_C dl_1 dS_C \frac{d\Omega_C}{4\pi},$$

where $d\Omega_A = \cos\vartheta_C dS_C/l^2$ and $d\Omega_C = \cos\vartheta_A dS_A/l^2$ are the elements of the solid angle in the coordinate frames with the origins at points A and C, respectively. Both variants of formula (7) are equivalent.

The specific energy deposition (power absorbed by a unit volume) can be written as

$$F(\mathbf{r}_C) = -\mathrm{div}\Phi(\mathbf{r}_C) = \int_{V_A} N^*(\mathbf{r}_A)\left(-\frac{dE(l)}{dl}\right) dl_1 \frac{d\Omega_C}{4\pi}. \quad (8)$$

Formulas (7) and (8) (reported earlier in [16]) are applicable for any layer geometry and any moderation law. The stopping power defined by Eq. (2) suggests the moderation law (4) and allows integration over the layer thickness. With allowance made for Eqs. (3) and (5), we obtain

$$N^*(\mathbf{r}_A) dl_1 = \bar{N}^* \bar{R}_1 dL_1. \quad (9)$$

Substituting this expression into Eq. (8) gives

$$F(\mathbf{r}_C) = \bar{N}^* E_0 \frac{\bar{R}_1}{\bar{R}_0} \frac{\rho_0(\mathbf{r}_C)}{\bar{\rho}_0} j(\mathbf{r}_C), \quad (10)$$

$$j(\mathbf{r}_C) = w_C(s_2) - w_C(s_1),$$

$$w_C(s_A) = \int_{s_A} \hat{u}(L_{AC}) \frac{d\Omega_C}{4\pi}, \quad L_{AC} = L_0 + L_1 + L_2. \quad (11)$$

Here, we introduced the extended function to take into account the ion path length ($L \le 1$); that is,

$$\hat{f}(x) = \begin{cases} f(x), & x \le 1, \\ 0, & x > 1. \end{cases}$$

A similar formula for a uniform active layer and the moderation law (1) was given in [14] without derivation. The function $j(\mathbf{r}_C)$ contains all information regarding the active layer and the moderation law. This function reaches a maximum value (unity) in a hollow cavity surrounded by a thick (the thickness is greater than the ion path) active layer.

By substituting Eq. (9) into Eq. (7), we obtain the following expressions for the integrated energy deposition:

$$\Psi(s_C) = \bar{N}^* E_0 \bar{R}_1 [S_2 W(s_2, s_C) - S_1 W(s_1, s_C)], \quad (12)$$

$$W(s_A, s_C) = \int_{s_C s_A} \hat{U}(L_{AC}) \cos\vartheta_A \frac{dS_A}{S_A} \frac{d\Omega_A}{4\pi}$$

$$= \int_{s_A s_C} \hat{U}(L_{AC}) \cos\vartheta_C \frac{dS_C}{S_A} \frac{d\Omega_C}{4\pi}, \quad (13)$$

$$U(L) = \int_L^1 u(L')dL'.$$

The variable L_{AC} changes in such a way that the point A (C) is fixed when integrating over $d\Omega_A$ ($d\Omega_C$) and the point C (A) runs over the surface s_C (s_A). The function $U(L)$ represents a portion of the energy transferred from a thick (the thickness is greater than the path) active layer by the distance L. For the moderation law (1), we have $U(L) = (1 - L)^{n+1}/(n + 1)$. In order to characterize the layer as a whole, we can use the coefficient ε [9] equal to the ratio of the total power absorbed in the gas Q_0 to the power released in the bulk of the layer $Q_1 = \bar{N}^* E_0 V_A$. The active layer can be considered thin if its thickness d_1 is less than the longitudinal dimensions by several orders of magnitude. In this case, $S_0 = S_1 = S_2$ and $V_A = S_1 d_1$. Then,

$$Q_0 = \Psi(s_0) - \Psi(s_3) = \bar{N}^* E_0 \bar{R}_1 S_1 J(s_0, s_3),$$

$$J(s_0, s_3) = W(s_2, s_0) - W(s_1, s_0) - W(s_2, s_3) + W(s_1, s_3), \quad (14)$$

$$\varepsilon = \frac{Q_0}{Q_1} = \frac{\bar{R}_1 S_1}{V_A} J(s_0, s_3) = \frac{1}{D_1} J(s_0, s_3), \quad (15)$$

$$D_1 = \frac{d_1}{\bar{R}_1}.$$

Let us now assume that the surface of the energy inflow s_0 coincides with the surface of the energy outflow s_3 (as is the case in cylindrical active layers). Then, the separation of the inner surface of the laser cell into s_0 and s_3 means that $\Psi(s_0)$ and $\Psi(s_3)$ take into account the inflowing and outflowing energies, respectively. In a similar way, we calculate the energy deposition upon internal pumping when the gas contains a source of ions: He^3 [10] or UF^6 [11] (in the former case, the attenuation of the neutron flux should be taken into account). We also write expressions analogous to

Eqs. (5) and (9); that is, $N^*(\mathbf{r}) = \bar{N}^* \rho_0(\mathbf{r})/\bar{\rho}_0$ and $N^*(\mathbf{r})dl_1 = \bar{N}^* \bar{R}_0\, dL_0$. The specific energy deposition (8) is given by

$$F(\mathbf{r}_C) = \bar{N}^* E_0 \frac{\rho_0(\mathbf{r}_C)}{\bar{\rho}_0} j(\mathbf{r}_C), \quad j(\mathbf{r}_C) = 1 - w_C(s_0)$$

instead of Eqs. (10) and (11).

The function $w_C(s_0)$ is defined by Eq. (11), where $L_{AC} = L_0$ and the integration is performed over a closed surface s_0 bounding the gas volume. The absorbed power is given by $Q_0 = Q_1 - \Psi(s_0)$, where $Q_1 = \bar{N}^* E_0 V_0$ is the power released in the gas volume V_0 and $\Psi(s_0)$ is the energy carried away from the cell. From Eq. (7), we obtain expressions similar to Eqs. (12)–(15); that is,

$$\Psi(s_0) = \bar{N}^* E_0 \bar{R}_0 S_0 [W(s_0, s_0) - W(s_0, s_3)],$$

$$\varepsilon = \frac{Q_0}{Q_1} = 1 - \frac{\bar{R}_0 S_0}{V_0}[W(s_0, s_0) - W(s_0, s_3)],$$

$$W(s_0, s_0) = \int\limits_{s_C s_A} \int U(0) \cos\vartheta_A \frac{dS_A}{S_A} \frac{d\Omega_A}{4\pi}$$

$$= U_0 \int\limits_{s_C} \cos\vartheta_A \frac{d\Omega_A}{4\pi} = \frac{U_0}{4}, \quad U_0 = U(0).$$

For both internal and external pumping, the energy deposition is expressed via the same auxiliary functions $w_C(s_A)$ and $W(s_A, s_C)$, which are of crucial importance.

A CELL OF INFINITE PLANE GEOMETRY

For a cell of infinite plane geometry when all the media exhibit plane-laminated density distributions depending only on the transverse coordinate y, $d\Omega_C = d\Omega_A = 2\pi \sin\vartheta d\vartheta$, $L_{AC} = D_{AC}/\cos\vartheta$, and $\vartheta = \vartheta_A = \vartheta_C$ (angle between the vector $\mathbf{l}$ and the y axis). Then, functions (11) and (13) for the specific and integrated energy depositions have the form

$$w_C(s_A) = \frac{1}{2} \int\limits_{D_{AC}}^{1} \hat{u}\left(\frac{D_{AC}}{\cos\vartheta}\right) d(\cos\vartheta)$$

$$= \frac{D_{AC}}{2} \int\limits_{D_{AC}}^{1} \hat{u}(L) \frac{dL}{L^2}, \quad w(D_{AC} = 0) = \frac{1}{2}, \tag{16}$$

$$W(s_A, s_C) = \frac{1}{2} \int\limits_{D_{AC}}^{1} \hat{U}\left(\frac{D_{AC}}{\cos\vartheta}\right) \cos\vartheta\, d(\cos\vartheta)$$

$$= \frac{D_{AC}^2}{2} \int\limits_{D_{AC}}^{1} \hat{U}(L) \frac{dL}{L^3} = \frac{\hat{U}(D_{AC})}{4} - \frac{D_{AC}}{2} \hat{w}(D_{AC}), \tag{17}$$

$$W(D_{AC} = 0) = \frac{U(0)}{4}.$$

For details of the infinite plane geometry of homogeneous media, see [4–9, 13] and especially [8], in which the integrated and specific energy depositions are represented in the quadratures consistent with Eqs. (16) and (17). The integral $\psi_k(a, b)$ taken from [8] is related to Eq. (16) by the expressions $w(D) = (1/2)D\psi_k(1, D)$, $k = 1/n - 1$, where n is the parameter of the moderation law (1). The extension to the case of an inhomogeneous gas was performed in [14].

A CELL OF LONGITUDINALLY UNIFORM GEOMETRY

Let us consider a cell of longitudinally uniform geometry (Fig. 2). The active layer is applied on the surface of the plates with a length much larger than R_0. The plates are either plane or bent around the optical z axis so that the cross section of the cell is uniform along the z axis. Such a configuration of the cell allows free passage of the laser beam and is generally accepted [16]. The density distribution of media is assumed to be longitudinally uniform.

Now, we consider a coordinate frame $(\lambda, \varphi, \theta)_C$ with the origin at point C (Fig. 2). The λ axis is directed along the projection of vector $\mathbf{l}$ onto the cross section of the cell, φ is the angle between the λ axis and the normal $\mathbf{n}_C$ to the surface s_C (the normal belongs to the same cross section), and θ is the angle between the λ axis and vector $\mathbf{l}$. A similar coordinate frame is constructed at point A, so that $\theta_A = \theta_C$, $\cos\vartheta_C = \cos\theta\cos\varphi_C$, $\cos\vartheta_A = \cos\theta\cos\varphi_A$, $d\Omega_C = \cos\theta d\theta d\varphi_C$, and $d\Omega_A = \cos\theta d\theta d\varphi_A$.

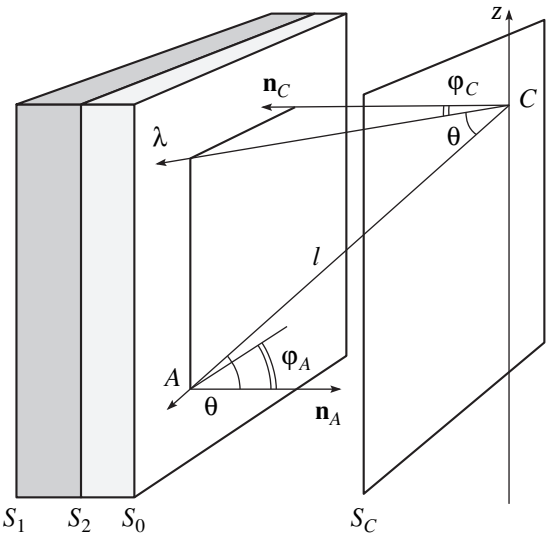

Fig. 2. A nuclear-pumped laser cell of longitudinally uniform geometry.

Then,

$$L_i = \frac{\Lambda_i}{\cos\theta}, \quad \Lambda_i = \frac{1}{\bar{\rho}_i \bar{R}_i}\int_{\lambda_i} \rho_i(\lambda, \varphi)d\lambda, \qquad \lambda_i = l_i\cos\theta, \tag{18}$$

and the energy deposition functions (11) and (13) have the form [16]

$$w_C(s_A) = \frac{1}{2\pi}\int_{\varphi} \hat{v}(\Lambda_{AC})d\varphi_C, \qquad v(\Lambda) = \int_0^{\arccos\Lambda} \hat{u}\left(\frac{\Lambda}{\cos\theta}\right)\cos\theta d\theta, \tag{19}$$

$$W(s_A, s_C) = \frac{1}{2\pi\sigma_A}\int_{\sigma}\int_{\varphi} \hat{V}(\Lambda_{AC})\cos\varphi d\varphi d\sigma, \qquad V(\Lambda) = \int_0^{\arccos\Lambda} \hat{U}\left(\frac{\Lambda}{\cos\theta}\right)\cos^2\theta d\theta. \tag{20}$$

Here, for the near (s_2) and far (s_1) surfaces of the active layer, we have $\Lambda_{AC} = \Lambda_0 + \Lambda_2$ and $(s_1) - \Lambda_{AC} = \Lambda_0 + \Lambda_1 + \Lambda_2$, respectively. The integration over dS_C (dS_A) implies the change in the variable σ along the cross section of the surface s_C (s_A). The quantity σ_A represents the length of the active layer in the cross section of the surface s_A (measured along the arc σ). The functions $v(\Lambda)$ and $V(\Lambda)$ are independent of the cross section and the density profile. In particular, for the linear moderation law $u(L) = 1 - L$, we obtain

$$v(\Lambda) = \sqrt{1-\Lambda^2} - \Lambda\arccos\Lambda,$$

$$V(\Lambda) = \frac{1}{4}[(1+2\Lambda^2)\arccos\Lambda - 3\Lambda\sqrt{1-\Lambda^2}].$$

For the quadratic moderation law $u(L) = (1-L)^2$, we have

$$v(L) = \sqrt{1-\Lambda^2} - 2\Lambda\arccos\Lambda + \Lambda^2\mathrm{Arth}(\sqrt{1-\Lambda^2}), \tag{21}$$

$$V(\Lambda) = \frac{1}{6}[(1+6\Lambda^2)\arccos\Lambda - 5\Lambda\sqrt{1-\Lambda^2} - 2\Lambda^3\mathrm{Arth}(\sqrt{1-\Lambda^2})]. \tag{22}$$

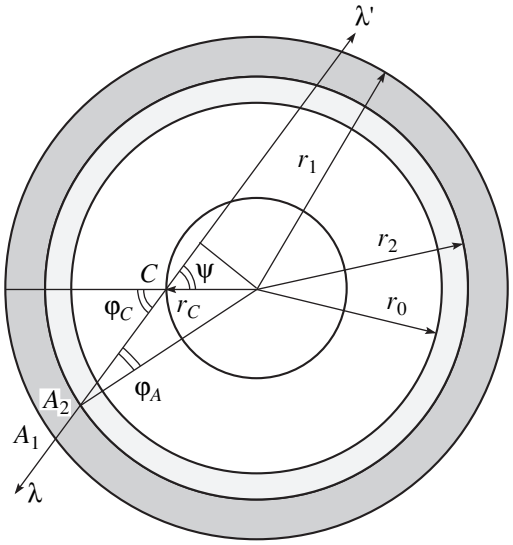

Fig. 3. A nuclear-pumped laser cell of cylindrical geometry.

A CYLINDRICAL CELL

Let us consider a cylindrical layer bounded by the coaxial cylindrical surfaces of radii r_1 and r_2 (Fig. 3). The thickness of the layer is $d_1 = r_1 - r_2 \ll r_2$. The gas is bounded by the cylindrical surface of radius r_0. Such a configuration represents a particular case of the longitudinally uniform geometry. To calculate specific energy deposition, we can use formulas (10), (19), and (21) and the quantities Λ_i determined by expressions (18). For homogeneous media, we can write

$$\Lambda_1 = \frac{\sqrt{r_1^2 - r_C^2\sin^2\varphi} - \sqrt{r_2^2 - r_C^2\sin^2\varphi}}{R_1},$$

$$\Lambda_2 = \frac{\sqrt{r_2^2 - r_C^2\sin^2\varphi} - \sqrt{r_0^2 - r_C^2\sin^2\varphi}}{R_2},$$

$$\Lambda_0 = \frac{D_0}{2}(\sqrt{1-\Delta_C^2\sin^2\varphi} - \Delta_C\cos\varphi),$$

$$D_0 = \frac{2r_0}{R_0}, \quad \Delta_C = \frac{r_C}{r_0}.$$

Here, $\varphi \equiv \varphi_C$. For $\pi/2 < |\varphi| \le \pi$, it is more convenient to use the angle $\psi = \pi - \varphi$, $\cos\psi = -\cos\varphi$. We restrict our consideration to uncoated layers, so that $r_2 = r_0$ and $\Lambda_2 = 0$. In this case,

$$\Lambda_1 = 2D_1\frac{1 + c/2}{Z},$$

$$Z = \sqrt{(1+c)^2 - \Delta_C^2\sin^2\varphi} + \sqrt{1-\Delta_C^2\sin^2\varphi},$$

$$D_1 = \frac{d_1}{R_1}, \quad c = \frac{d_1}{r_0}.$$

The function $j(\Delta_C)$ is determined by three parameters D_0, D_1, and $c \ll 1$. In practice, $c \sim 10^{-4}$, and, there-

fore, we can neglect the dependence on this parameter because of its smallness. Then,

$$\Lambda_1 \approx D_1(1 - \Delta_C^2 \sin^2\varphi)^{-1/2}. \quad (23)$$

Specifically, at the axis ($\Delta_C = 0$), $\Lambda_1 = D_1$ and $\Lambda_0 = D_0/2$; at the wall ($\Delta_C = 1$), $\Lambda_1 \approx D_1/|\cos\varphi|$ (as in the case of the infinite plane geometry); and $\Lambda_0 = 0$ at $|\varphi| \le \pi/2$ and $\Lambda_0 = D_0\cos\psi$ at $\pi/2 < |\varphi| \le \pi$. For the quadratic moderation law and $D_0 = 1$, the energy deposition at the wall is $j(\Delta_C = 1) = (2.5 + G)/\pi - 1/2 \approx 0.587$, where $G = 0.916\ldots$ is the Catalan constant.

The integrated energy deposition is determined from formulas (12), (20), and (22). Similarly to Eq. (14), the power absorbed in the bulk of the gas bounded by the cylindrical surface s_C of radius r_C (coaxial to the active layer) is given by

$$\begin{aligned} Q_C &= \bar{N}^* E_0 \bar{R}_1 S_1 J(r_C), \\ J(r_C) &= W(s_2, s_C) - W(s_1, s_C) \\ &\quad - W(s_2, s_C') + W(s_1, s_C'), \\ W(s_A, s_C) &= W(r_A, r_C) = \int_0^{\pi/2} \hat{V}(\lambda_{AC}) \cos\varphi_A \frac{d\varphi_A}{\pi}. \end{aligned} \quad (24)$$

Here, we used a coordinate frame centered at point A, for which we can write (Fig. 3)

$$\Lambda_1 = \frac{r_1\cos\varphi_A - \sqrt{r_2^2 - r_1^2\sin^2\varphi_A}}{R_1},$$

$$\Lambda_2 = \frac{\sqrt{r_2^2 - r_A^2\sin^2\varphi_A} - \sqrt{r_0^2 - r_A^2\sin^2\varphi_A}}{R_2},$$

$$\Lambda_0 = \frac{\sqrt{r_0^2 - r_A^2\sin^2\varphi_A} \mp \sqrt{r_C^2 - r_A^2\sin^2\varphi_A}}{R_0}.$$

Here, $r_A = r_1$ (r_2) at the surface s_1 (s_2); the minus and plus signs in the expression for Λ_0 correspond to the functions $W(s_i, s_C)$ and $W(s_i, s_C')$ that characterize the inward and outward energy flows, respectively. To determine the efficiency ε, we assume that $r_C = r_0$. Then, similarly to Eqs. (15), we obtain

$$\varepsilon = \frac{J(r_0)}{D_1}, \quad (25)$$

$$J(r_0) = W(r_2, r_0) - W(r_1, r_0) - W(r_2, r_0') + W(r_1, r_0').$$

Here, for uncoated layers ($r_2 = r_0$), we have $\Lambda_0 = D_0\cos\varphi_A$ and $\Lambda_1 \approx D_1/\cos\varphi_A$ similarly to relationship (23). For the quadratic moderation law, $W(r_0, r_0) = 1/12$. If $D_1 \ge 1$ and $D_0 = 1$, we obtain $J(r_0) = (77 + 18G)/(72\pi) - 1/3 \approx 0.07997$, where G is the Catalan constant.

Let us compare the proposed method with the currently available techniques. Kazazyan *et al.* [9] were the first to calculate the efficiency of the cylindrical active layers by the Monte Carlo method. These authors used the quadratic moderation law in the calculations. Their data (taken from the plots in [9]) and the results of our calculations by formulas (24) and (25) are presented in the table. The insignificant discrepancies between our results and the data obtained in [9] are within the accuracy of digitizing the graphical data from [9].

In [9], the authors made the first attempt to calculate the distribution of the energy deposition from a cylindrical layer with respect to the radius by dividing the gas volume into cylindrical layers and calculating the integrated energy deposition for each layer by the same method. However, one can hardly obtain a continuous profile of the energy deposition (which is necessary for calculating the optical inhomogeneities) from these histograms.

Chung and Prelas [12] applied the quadrature method to calculate the energy deposition for cylindrical layers. They calculated the energy flux density and then approximated it by a polynomial of the sixth order. The specific energy deposition was determined by differentiating this polynomial. However, the high accuracy of the approximation does not ensure acceptable accuracy of the derivative of the approximated function. Note that the energy flux density was calculated in [12] by using the triple quadrature, even though the problem can be reduced to the double quadrature [see the transformation of Eqs. (7) and (8) into Eqs. (10)–(13) with the use of Eq. (9)].

Figure 4 compares the results obtained in [12] for a cell with CO_2 irradiated by an UO_2 layer and the results of calculations by the proposed method using the parameters taken from [12]. Unfortunately, the numerical value of the uranium enrichment factor is not given in [12] (although this factor enters into formulas used in [12]). In our calculations, its value is taken equal to

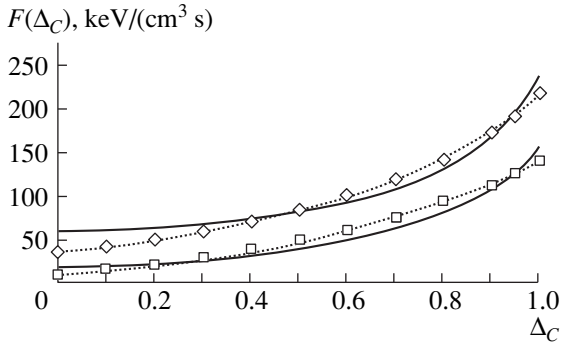

Fig. 4. Specific energy deposition in a cylindrical cell at a unit neutron flux density: (solid lines) calculations by Eqs. (10), (19), and (21); (dashed lines) the data taken from [12]; (squares) heavy fragments ($D_1 = 0.35$, $D_0 = 1.3$); and (rhombs) light fragments ($D_1 = 0.25$, $D_0 = 1.0$).

Efficiency ε (in %) for uncoated cylindrical layers

D_0	$D_1 = 0.3$		$D_1 = 0.5$		$D_1 = 1.0$	
	Data taken from [9]	Calculation by Eqs. (24) and (25)	Data taken from [9]	Calculation by Eqs. (24) and (25)	Data taken from [9]	Calculation by Eqs. (24) and (25)
0.1	5.36	5.34	4.14	4.03	2.14	2.20
0.2	10.0	9.64	7.29	7.20	3.61	3.88
0.3	13.4	13.06	10.0	9.66	5.00	5.15
0.4	15.7	15.75	11.4	11.51	6.21	6.09
0.5	17.5	17.80	12.9	12.87	6.60	6.76
0.6	19.3	19.30	13.9	13.81	7.14	7.24
0.7	20.0	20.36	14.3	14.46	7.60	7.56
0.8	21.0	21.07	14.8	14.88	7.86	7.77
0.9	21.5	21.52	15.1	15.15	7.93	7.91
1.0	22.0	21.82	15.5	15.33	8.00	8.00
1.2	22.5	22.18	15.7	15.55	8.07	8.11
1.4	22.8	22.39	15.8	15.68	8.14	8.17
1.6	22.9	22.52	16.0	15.75	8.14	8.21
1.8	22.9	22.61	16.1	15.81	8.21	8.24
2.0	22.9	22.68	16.1	15.85	8.21	8.25

90%. The calculations in [12] were performed with the moderation law (1) at $n = 1.45$. However, this is not the main reason for the discrepancies in the results of the calculations. The use of the method proposed in [12] involves difficulties in calculating the energy deposition in the vicinity of the wall (the authors of [12] did not take into account sharp bending of the energy deposition profile) and near the axis (where the energy flux is small and differentiating with respect to radius can present problems). Note also that the derivative of the profile given in [12] is not equal to zero at the axis.

CONCLUSION

We proposed a general quadrature method for calculating the energy deposition in nuclear-pumped lasers. This method can be used (in contrast with the existing techniques) for both external and internal pumping for any moderation law in inhomogeneous media. For a cell of longitudinally uniform geometry (the universally accepted laser configuration) and a uniform density of the media, the method makes it possible to express the specific and integrated energy depositions in the double and triple quadratures, respectively. In the case of the quadratic moderation law, these quadratures are reduced to the single and double ones, respectively. For a cylindrical cell, both integrated and specific energy depositions are reduced to the double quadratures (and to single quadratures for the quadratic moderation law). Earlier, the specific energy deposition for cylindrical geometry of the layer was calculated by numerical differentiation of the energy flux density expressed in triple quadratures.

REFERENCES

1. *Proceedings of the Conference "Physics of Nuclear-Excited Plasma and Problems of Nuclear-Pumped Lasers"* (Fiz. Énerg. Inst., Obninsk, 1992–1993), Vols. 1–3.
2. *Proceedings of the Second Conference "Physics of Nuclear-Excited Plasma and Problems of Nuclear-Pumped Lasers"* (Vseross. Nauchno-Issled. Inst. Éksp. Fiz., Arzamas-16, 1995), Vols. 1, 2.
3. R. T. Schneider and F. Hohl, in *Advances in Nuclear Science and Technology* (Plenum, New York, 1984), Vol. 16, pp. 123–287.
4. G. Long, *The Production of Chemicals from Reactors: Part II. Deposition of Energy by Fission Fragments in Two-Phase Systems* (Atomic Energy Research Establishment, Harwell, 1958), AERE-C/M-345.
5. S. Kahn, R. Harman, and V. Forgue, Nucl. Sci. Eng. **23** (1), 8 (1965).
6. C. B. Leffert, D. B. Rees, and F. E. Jamerson, J. Appl. Phys. **37** (1), 133 (1966).
7. D. H. Nguyen and L. M. Grossman, Nucl. Sci. Eng. **30** (2), 233 (1967).
8. G. H. Miley and P. E. Thiess, Nucl. Appl. **6** (5), 434 (1969).
9. V. T. Kazazyan, B. A. Litvinenko, L. P. Roginets, and I. A. Savushkin, *Physical Principles of Utilizing Kinetic Energy of Fission Fragments in Radiation Chemistry* (Nauka i Tekhnika, Minsk, 1972).
10. J. W. Wilson and R. J. DeYoung, J. Appl. Phys. **49** (3), 980 (1978).

11. J. W. Wilson and R. J. DeYoung, J. Appl. Phys. **49** (3), 989 (1978).
12. A. K. Chung and M. A. Prelas, Nucl. Sci. Eng. **86**, 267 (1984).
13. A. V. Karelin, O. V. Sereda, V. V. Kharitonov, *et al.*, At. Énerg. **61** (1), 44 (1986).
14. J. R. Torczynski, J. Fluid Mech. **201**, 167 (1989).
15. V. V. Borovkov, B. V. Lazhintsev, S. P. Mel'nikov, *et al.*, Izv. Akad. Nauk SSSR, Ser. Fiz. **54** (10), 2009 (1990).
16. V. Yu. Mat'ev, in *Proceedings of the Conference "Physics of Nuclear-Excited Plasma and Problems of Nuclear-Pumped Lasers"* (Fiz. Énerg. Inst., Obninsk, 1992–1993), Vol. 2, p. 79.
17. V. Yu. Mat'ev and A. N. Sizov, in *Proceedings of the Conference "Physics of Nuclear-Excited Plasma and Problems of Nuclear-Pumped Lasers"* (Fiz. Énerg. Inst., Obninsk, 1992–1993), Vol. 2, p. 209.
18. Ya. A. Teplova, V. S. Nikolaev, I. S. Dmitriev, *et al.*, Zh. Éksp. Teor. Fiz. **34** (3), 559 (1958) [Sov. Phys. JETP **7**, 387 (1958)].
19. Ya. A. Teplova, V. S. Nikolaev, I. S. Dmitriev, *et al.*, Zh. Éksp. Teor. Fiz. **42** (1), 44 (1962).
20. P. W. Frank, *Recoil Range of Fission Fragments. WAPD-BT-30* (Bettis Atomic Power Lab., 1964).
21. J. M. Alexander and M. F. Gazdik, Phys. Rev. **120** (3), 874 (1960).
22. M. A. Kumakhov and F. F. Komarov, *Energy Loss and Paths of Ions in Solids* (Belarus. Gos. Univ., Minsk, 1979).

Translated by A. Chikishev

Technical Physics, Vol. 46, No. 1, 2001, pp. 7–13. Translated from Zhurnal Tekhnicheskoĭ Fiziki, Vol. 71, No. 1, 2001, pp. 9–15.

Simple Estimation of the Switching Wave Velocities in a Superconducting Composite

I. B. Krasnyk and Yu. V. Medvedev

Galkin Physicotechnical Institute, National Academy of Sciences of Ukraine, Donetsk, 83114 Ukraine

e-mail: Kras@host.dipt.donetsk.ua

Received March 13, 2000

Abstract—Consequences derived from the results of the theory of systems of parabolic equations were used in the analysis of the behavior of thermal switching waves and their propagation velocity in a cooled composite superconductor at different coverages by a nonconductive coating. The value of the minimum normal zone propagation current was also studied, taking into account the local nonlinearity of the specific resistance of the composite. © *2001 MAIK "Nauka/Interperiodica".*

INTRODUCTION

Evaluation of the velocity v of a switching wave (*NS*-boundary) which breaks the superconducting properties of a current-carrying unit is the central problem of applied superconductivity [1]. This problem is of particular significance for composite superconductors (superconductors with a normal matrix) with a nonconducting coating. As shown in [2], the presence of even minor coverages can result in an essential change of the character of the thermal processes in a composite superconductor. When evaluating v in [2], the electrical and physical parameters of the matrix were assumed to be temperature-independent and, therefore, the one-dimensional non-steady-state heat conductivity equation with a heat source $Q(T)$ and heat sink $W(T)$ could be made dimensionless and the problem was reduced to the known problem [3]. However, the general nonlinear heat transfer equation allows no global dimensionless complexes.

The present study is devoted to the evaluation of the range of propagation velocities of the thermal switching waves, taking into account local nonlinearity of the specific resistance $\rho_0(T)$ of the normal conductive matrix in the vicinity of the temperature of the transition of the superconducting core. In evaluating the velocities of the switching waves, the consequences deduced from fundamental results of the theory of wave propagation for the systems of parabolic equations were utilized [4]. According to [4], the character of the thermal waves (or the systems of waves) and of their propagation velocities can be qualitatively and quantitatively analyzed if a source-sink function $F = Q - W$ is specified. The qualitative agreement of the results with those obtained for the case $\rho_0(T) \equiv \text{const}$ [2] clearly demonstrates the validity of the approach used.

Consider an infinite cooled superconductor in a normally conducting matrix, whose surface is covered with a nonconductive coat. Suppose that the boundary surfaces of the sample are planar and the contact heat resistance between the coating and the composite is zero [2, 3]. Then, the temperature variation in the longitudinal direction can be described by an equation in dimensionless variables [2]:

$$\left(1 + c\frac{\Delta_i}{\Delta_k}\right)\frac{\partial\Theta}{\partial\tau} = \left(1 + \lambda\frac{\Delta_i}{\Delta_k}\right)\frac{\partial^2\Theta}{\partial x^2} - \frac{\Theta}{\alpha + \beta} + i^2 r(\Theta), \quad (1)$$

where $c = c_i/c_k$, $\lambda = \lambda_i/\lambda_k$, $\Delta_{i,k} = d_{i,k}/L_k$, $\alpha = I_c^2\rho_0/hpS(T_{cb} - T_0)$, $\beta = \Delta_i\Delta_k/\lambda$, and I_c and T_{cb} are the critical parameters of the superconductor [2]; ρ_0 is the specific resistance of the normally conducting matrix; h is the heat dissipation coefficient; p is the perimeter cooled; S is the cross-sectional area; $i = I/I_c$ (I is the transport current); c_k, c_i are the heat capacities of the composite and the coating; λ_k, λ_i are the heat conductivity coefficients; and d_k, d_i are transversal dimensions of the composite and the coating.

Further,

$$\Theta = (T - T_0)/(T_{cb} - T_0),$$

where T_0 is the reservoir temperature, $\tau = \lambda_k t/(c_k L_k^2)$, t is time, $x = s/L_k$, and $L_k = [\lambda_k S^2(T_{cb} - T_0)/I_c^3\rho_0]^{1/2}$.

For the function $r(\Theta)$, we adopt the conventional model of stepwise heat release [1–3]

$$r(\Theta) = \left\{\begin{array}{cc} 1, & \Theta > 1 \\ (\Theta - 1 + i)/i, & 1 - i \le \Theta \le 1 \\ 0, & \Theta < 1 - i \end{array}\right\}. \quad (2)$$

1063-7842/01/4601-0007$21.00

DETERMINATION OF *N*-ZONE PROPAGATION VELOCITIES AT CONSTANT SPECIFIC RESISTANCE OF THE MATRIX USING THE STEPWISE HEAT RELEASE MODEL

Let us denote

$$F(\Theta, \alpha, \beta, i) = -\frac{\Theta}{\alpha + \beta} + i^2 r(\Theta) \qquad (3)$$

and determine zeros of this function, since it is known [4] that, according to the character of the considered wave systems and the behavior of the solutions at infinite time, all sources $F(\Theta, \cdot)$ can be grouped into three types depending on the behavior of the function $F(\Theta)$ in the vicinity of zeros $F(\Theta) = 0$. The roots of this equation represent steady states (stable and unstable) of the dynamic system. Thus, a new feature here is the dependence of steady states (points) not only on the current density i (in the fixed current regime), but also on additional parameters α and β (see definition). This certainly makes the dynamics of the system more diverse. Using Eq. (2) and the definition for $F(\Theta)$, it is not difficult to identify the following steady states: the point $\Theta_1 = 0$ is a steady state at $0 < \Theta < 1 - i$; at $1 - i < \Theta \le 1$, we have

$$\Theta_2 = (\alpha i - 1)/(\alpha i(1 - i)).$$

In particular, at $\alpha \gg 1$ and/or $i \gg 1$, $\Theta_2 = (1 - i)^{-1}$. So, at $i \longrightarrow +0$ due to inequality $\Theta < 1 - i$, the composite switches to the superconducting state $r(\Theta) \equiv 0$ [1]; at $\Theta > 1$, we obtain

$$\theta_3 = (\alpha + \beta) i^2,$$

particularly, $\Theta_3 = \alpha i^2$ at $\alpha \gg \beta$, which agrees with the known result [1] for the uncoated superconductors.

Consider the case when the function $F(\Theta)$ at some values of the parameters α, β, and i takes the form shown in Fig. 1. It is obvious that $F(\Theta) < 0$ at $\Theta \in (0, a)$ and $F(\Theta) > 0$ at $\Theta \in (0, 1)$, where

$$a = \frac{1 - i}{1 - [i(\alpha + \beta)]},$$

and hence, in the presence of the parameters, the transition point of the superconductor to the *N*-state is formally shifted towards higher temperatures.

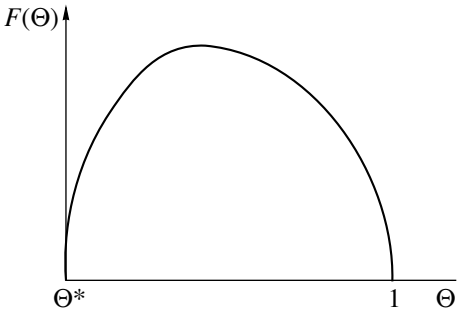

Fig. 1. Kolmogorov's graphical solution (1937), in which evolution of the temperature profile (in the normal phase) tends to a simple wave at infinite time.

For the sources in Fig. 1, the considered problem has a unique solution, which is a wave propagating with a velocity $v > 0$, if the inequality

$$\int_{\Theta}^{1} F(\Theta) d\Theta > 0$$

holds [3] for all $\Theta \in (0, 1)$. Simple calculation shows that this is possible if

$$\Theta > \frac{2(i - 1)}{1 - [(\alpha + \beta) i]} = \Theta^*,$$

i.e., at $i > 1$, a traveling wave characterizing the *N*-zone propagation appears, which is an obvious occurrence.

In the range $(\Theta^*, 1)$, the function F has the form shown in Fig. 2 and meets the following conditions:

$$F(0) = F(1),$$

$$F'(0) > 0 \quad \text{at} \quad 0 < u < 1,$$

$$F'(0) = \kappa > 0,$$

$$F'(u) < \kappa \quad \text{at} \quad 0 < u \le 1,$$

where $u \longrightarrow (\Theta - \Theta^*)(1 - \Theta^*)$; i.e., we normalized the temperature range (by substituting $\Theta \longrightarrow \Theta - \Theta^*$ to shift the left boundary to zero and stretch the range by a factor $1 - \Theta^*$).

In such a temperature range, a unique normal zone propagation velocity exists [3]:

$$\lambda_0 = 2\sqrt{\frac{k\kappa}{C^2}},$$

where C denotes the general coefficient in Eq. (1).

To simplify the mathematics, we suppose that the following inequalities are satisfied:

$$c\frac{\Delta_i}{\Delta_k} \ll 1 \quad \text{and} \quad \lambda\frac{\Delta_i}{\Delta_k} \ll 1;$$

i.e., the influence of the coating on the temperature field is assumed to be negligible. In particular, at a minimum current of the normal zone propagation i_p, the velocity is equal to zero [1, 3] and the inequality [1, 4]

$$2\sqrt{F'(0, \alpha, \beta, i)} \le v \ll 1.$$

at currents far in excess of i_p can be interpreted as a necessary, but not a sufficient, condition for the superconductivity break-up. Let us write this inequality in the form

$$-(\alpha + \beta)^{-1} + i \ll 1$$

and, assuming the right side to be equal to zero, determine the minimum current density for normal zone

propagation

$$i_p = \frac{I_c^2 \rho_0}{h_p S(T_{cb} - T_0)} + \frac{\Delta_i \Delta_k}{\lambda}.$$

This formula can be used for approximate calculations of the current densities $i > i_p$ at sufficiently large (and fixed) values of $\beta > 0$. The general necessary condition has the form

$$F'(0, \alpha, \beta, 1) \ll 1.$$

In specific calculations, we can use a curve of allowed parameters for the superconductivity break-up

$$F'(0, \alpha, \beta, i) = 0,$$

which in the most trivial case is reduced to the determination of the emergence of the normal phase due to heat release (see definition of $r(\Theta)$).

Returning to the general case, for $F(u)$, the point $\Theta = \Theta^*$ is stable, while the point $\Theta = 1$ is unstable. Then, there should be a constant v_* such that the (0,1)-wave exists only if $v > v_*$, where the quantity v_* (minimum velocity) satisfies inequalities [3]

$$2\sqrt{\kappa} \le v_* \le 2\sqrt{\gamma},$$

$$\gamma = \sup \frac{F(u)}{u}, \quad 0 < u < 1,$$

where sup denotes an exact upper limit of the maximum value of the function in the specified range, whose maximum is in general not necessarily attained.

In particular, if the condition $F'(u) < \kappa$, $0 < u < 1$ is satisfied, we obtain $\kappa = \gamma$, which is a unique traveling wave propagating at a velocity of $2\sqrt{F'(0, \alpha, \beta, i)}$ (see the substitution above of the unknown functions). Note that this scenario occurs in the range $(\Theta^*, 1)$.

For the range (0, 1), following [3], we assume that $F(u) \le 0$ at a sufficiently small u, which is in the vicinity of the point $i = 1$ and $F(u) \ge 0$ at u close enough to unity. If waves $(0, \Theta^*)$ and $[\Theta^*, 1]$ (S and N waves, respectively) are propagating at velocities $v_s < v_n$, then a [switching] wave (0, 1) exists that propagates with a velocity $v_s < v < v_n^2$.

In particular, for bistable superconductors (for which there is typically no S wave, although it could be induced under a special heat removal regime), a unique velocity exists (at $t \longrightarrow \infty$) that coincides with the minimum velocity, while it is known that a multistable superconductor (for example, because of the coolant boiling crisis) can be found in one of three stable states with different temperatures $T_1 < T_3 < T_5$ (see, for example, [4]). Then, from the formal results of [3, 5], it immediately follows that in the temperature range $T_2 < T < T_4$, the end points of which are unstable steady-state points while the point T_3 is stable, three switching waves exist: one in the range $T_2 < T < T_3$, which at $t \longrightarrow \infty$ transforms into a wave of constant amplitude [4]; and a wave in the range $T_3 < T < T_4$, which (after some time has elapsed) acquires the temperature T_3, and the steady-state solution $T = T_3$ is stable (therefore, these waves collapse). A similar case has been considered in [1, 4], except that there is no filmlike boiling of the coolant at point $T = T_5$ [4] in our case. Thus, using the terminology of [4], there are two hot (normal) phases and, since the superconductor cools at $T = T_3$ in the bubble boiling regime [3], these phases naturally assume this temperature value at $t \longrightarrow \infty$.

Each of the hot phases moves with its own velocity $v_{N_1} < v_{N_2}$, where v_N is the velocity of the normal wave in the multistable state [3]. In this case, according to the theorem in [3, theorem 3, p. 338], there exists a wave that propagates with a velocity of $v_{N_1} < v_N < v_{N_2}$ and is, in fact, a (T_2, T_4)-wave. Such a wave can exist only if $v > v_*$, where the quantity v_* (minimum velocity of the (T_2, T_3)-wave) satisfies inequalities

$$2\sqrt{F'(T_2)} \le v_* \le \sqrt{\gamma(T)},$$

and the maximum value of the function $\gamma(T)$ (see above) is chosen in the range $T_2 < T < T_4$. It will be shown below (in a rather rough approximation) that this maximum is attained at a point $\Theta = \Theta_3$. Hereafter, it will be assumed that the upper bound of the velocity is reached only in multistable conductors. All this, including the terminology, follows from the results obtained in [3, p. 338].

To simplify the mathematics we consider the particular case of $\Delta_i \ll 1$. Then, the minimum wave propagation velocity is

$$v_{\min} = 2\sqrt{-\frac{1}{\alpha + \beta} + i}.$$

In particular, with dimensional variables it will be

$$v_{\dim} = 2\frac{\lambda_k}{c_l L_k}\sqrt{-\frac{1}{\alpha + \beta} + i}.$$

By way of comparison, for $\Delta_k = 1$and $\Delta_i \sim 5 \times 10^{-2}$, and $\lambda = 10^{-3}$, simple calculations show that $v \simeq 0.5$ (this is in exact correspondence with the plot presented in

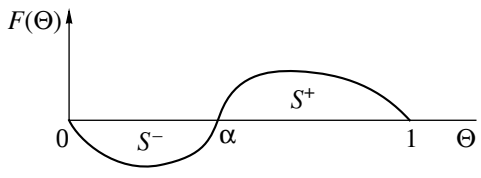

Fig. 2. The steady-state points of the bistable system of a composite superconductor occurring as a result of thermal isolation of the normal matrix with strong temperature dependence $\rho_n(T)$. (S^- is the region of enhanced heat removal.)

[2, Fig. 2] for $i = 0.85$); for other parameters the comparison results are similar (here, calculations have been made for the dimensionless velocity). Also, at $\alpha \longrightarrow \infty$ an expected coincidence with the results of [2] is obtained, as well at the velocity values $0 < v < 1$ and in the range $10^{-1} < \Delta_i < 10^{-3}$. Finally,

$$\frac{F(\Theta)}{\Theta} = -\frac{1}{\alpha+\beta} + i + \left[\frac{i(i-1)}{\Theta}\right],$$

with the maximum at a point $\Theta_*^2 = \alpha i(i-1)$, which can be easily calculated:

$$v_{\max}^2 = 2 - \frac{1}{\alpha+\beta} + i - \frac{i(i-1)}{\Theta}\Big|_{\Theta=\Theta_*}$$

$$= 2 - \frac{1}{\alpha+\beta} + i - \frac{1}{\sqrt{\alpha}}\sqrt{i(i-1)}.$$

So, a rough calculation shows that at $i \gg 1$ (actually, $i > 1$ is sufficient), the maximum is reached at a point $\Theta = \alpha i^2 - \alpha i = \alpha i^2 = \Theta^3$. Then,

$$v_{\max} = 2\sqrt{-\frac{1}{\alpha+\beta} + i - \frac{i-1}{\alpha+\beta}}$$

$$= 2\sqrt{i[1-(\alpha+\beta)^{-1}]}.$$

It is easily seen that $\alpha + \beta > 1$; so at $\beta = 0$, we have $v_{\max} = 0$ and the resistive state, in which the heat release does not break superconductivity, does not exist, which agrees with the result of [2, p. 13]:

$$v_{\max} = 2\sqrt{-\frac{1}{\alpha+\beta} + i + \frac{i-1}{\alpha i}} \quad \text{at} \quad \Theta = \Theta_*.$$

So, at $\alpha \longrightarrow \infty$, the maximum and minimum velocities coincide. Using the notations of [1], this formula can be written in the form

$$v_{\max} = 2\sqrt{-\frac{1}{\alpha_e} + i - \frac{i-1}{\alpha i}}. \tag{4}$$

It is to be recalled that in [2], the following relationship has been obtained:

$$V = \frac{\sqrt{1+\Lambda\Delta_i/\Delta_k}}{1+C\Delta_i/\Delta_k}\left[\frac{\alpha_e i^2 + i - 2}{\alpha_e(\alpha_e i^2 - 1)}\right.$$

$$\left. + \sqrt{\frac{\alpha_e - 1}{\alpha_e}}\left(2 - 2\sqrt{\frac{1-i}{1-i_s}} - \frac{i-i_s}{1-i_s}\right)\right], \tag{5}$$

where $\alpha_e = \alpha + \beta$, $i_s = (\sqrt{1+8\alpha_e} - 1)/2\alpha_e$.

So, at $\alpha_e \longrightarrow \infty$, the first terms of formulas (4) and (5) are close by an order of magnitude, the second term is of the same order as (i), and the third is on the order of ($i - 1$). Therefore, a qualitative agreement of representations (4) and (5), respectively, can be assumed in an asymptotic limit; that is, for the parameters α and/or $\beta \gg 1$.

N-ZONE PROPAGATION VELOCITY DETERMINATION

It should be noted that the above mentioned results are valid under an assumption that the specific resistance $\rho_0(\cdot)$ is constant. If this is not the case, then it is necessary to use the relationship

$$\rho(T) = \rho_0(T)$$

$$\times\left\{\begin{array}{cc} 1, & T > T_{cb}, \\ (T-T_c)/(T_{cb}-T_c), & T_c \le T \le T_{cb}, \\ 0, & T < T_c = T_{cb} - (T_{cb}-T_0)I/I_c, \end{array}\right\}$$

and, correspondingly, consider the equation

$$C_e\frac{\partial T}{\partial t} = \lambda_e\frac{\partial^2 T}{\partial x^2} - \frac{h_e p}{S}(T-T_0) + \frac{I^2}{S^2}\rho(T),$$

the coefficients in which we determine below after [2]. Unfortunately, the general nonlinear equation does not allow the use of global dimensionless complexes. However, it can be made dimensionless in the same manner as the previous equation, in the vicinity of the each fixed point of the image

$$f(T) = -\frac{h_e p}{S}(T-T_0) + \frac{I^2}{S^2}\rho(T),$$

so that in the vicinity, fixed points in a system of dimensionless spatial-temporal variables will exist, which in the vicinity of the set is invariant with respect to the (T_{fix})-zeros of the function $f(T)$.

Since the averaged C_e values are constant [1], then without restricting the generality, we can assume $C_e = 1$ without qualitatively affecting the results stated below, and make the substitution $\hat{T} \longrightarrow T + T_0$ (the upper angle will be omitted in what follows).

Let us begin with the case $h_e p/S \ll 1$, where it will suffice to have only the source $f(T) = \dfrac{I^2}{S^2}\rho(T)$. It is convenient to assume formally that $\rho_0(T_{cb}) = 0$, so as not to introduce a new function $\rho(T) = \rho(T) - \rho_0(T_{cb})$. This will make the result obtained accurate to within a constant. It is also evident (not formally) that $\rho(T_c) = 0$. Then, the source $f(T)$ will obviously satisfy the following conditions:

$$f(T_c) = f(T_{cb}) = 0;$$

$$f(T) > 0 \quad \text{at} \quad T_c < T \ll T_{cb};$$

$$f'(T_c) = \frac{I^2}{S^2}\rho'(T_c) = \alpha > 0.$$

Finally, assume that $f'(T) < \alpha$ for all $T_c \le T \le T_{cb}$ and introduce the notation $T = T_c + \Theta(T_{cb} - T_c)$. Then, the

last constraint can be written in more detail in the form of the inequality

$$\rho_0'(T)\frac{T-T_c}{T_{cb}-T_c}+\frac{\rho_0(T)}{T_{cb}-T_c}<\alpha = \frac{I^2}{S^2}\rho_0'(T_c),$$

which up to a constant (this constant can be easily determined as the solution of the differential equation, i.e., as the largest of the possible constants evaluating the solution of the differential inequality) can be represented as

$$\frac{d\rho(T(\Theta))}{d\Theta} = \frac{d\rho}{dT}\frac{dT}{d\Theta}\le\frac{dT}{d\Theta}\frac{\rho(T)}{T-T_c}$$
$$= \frac{T_{cb}-T_c}{T-T_c}\rho(T) = \frac{1}{\Theta}\rho(T(\Theta)).$$

Denoting $\rho(T(\Theta)) = \tilde{\rho}(\Theta)$ and integrating the differential inequality

$$\frac{d\tilde{\rho}}{\tilde{\rho}}<\frac{d\Theta}{\Theta}$$

in a range from Θ_c to Θ, where Θ_c is a dimensionless critical temperature, we obtain that the above requirement $f'(T) < \alpha$ is merely a restriction on the growth rate of the function

$$\tilde{\rho}_0(\Theta)<\frac{\tilde{\rho}_0(\Theta_c)}{\Theta_c}\Theta = \text{const}\Theta,$$

i.e., the rate of growth with temperature of the nonlinear specific resistance of the matrix should be not higher than the linear.

Note that since (formally) $\Theta_c = 0$ at $T = T_c$ (see above) and the function considered, $\rho_0(T)$, is not the same as the function $\rho(T)$ (see above representation for $\rho(T)$) possessing the property $\rho(T_c) = 0$, in contrast to the quantity $\rho_0(T_c)$, which in general is not necessarily equal to zero, then the obtained inequality in the vicinity of the critical temperature appears to be fine. To evaluate the growth rate of the function $\rho_0(T_c)$, we need to calculate the limit

$$\lim_{T\to T_c}\frac{\rho_0(T_c)}{T_c},$$

which can exist only if $\rho_0(T_c) \longrightarrow 0$ at $T \longrightarrow T_c$. Then, if the conditions of applicability of the L'Hospital theorem are satisfied, this limit is equal to $\rho_0'(T_c)$ and the estimation obtained above acquires a clear qualitative sense. Then, according to [3], the unique limiting velocity of the normal zone propagation is

$$v_p = 2\sqrt{\lambda_e(I^2/S^2)\rho_0'(T_c)} = 2\frac{I}{S}\sqrt{\lambda_e\rho_0'(T_c)}.$$

Taking into account that $\lambda_e = \lambda_k d_k/d + \lambda_i d_i/d$, where $d = d_k + d_i$, and the quantities C_e and ρ_e are defined as in [1], we obtain a qualitative agreement with the plot in [2] of the normal zone propagation velocity versus the coating thickness Δ_i. However, the slope of the plots should be corrected by the factor $\rho_0(T_c)$ (compare with the results of [2]).

Thus, the *N*-zone propagation velocity decreases with the increase of the composite cross-sectional area *S* and is the smaller variation of the resistance of the superconducting composite.

HEAT RELEASE IN A COMPOSITE WITH A LOCALLY NONLINEAR SPECIFIC RESISTANCE NEAR THE CRITICAL TEMPERATURE

Finally, to account for the influence of the heat dissipation coefficient, it is necessary to carry out the procedure considered in the beginning. It is obvious that at $T < T_c$, because of $T > T_0$, the inequality $f(\Theta) \ll 0$ is satisfied at fairly small $T > 0$. The function $f(T)$ for the chosen $\rho(T)$ by definition (see above) has three fixed points, which can be determined from the equations

$$-\frac{h_e p}{S}(T-T_0)+\frac{I^2}{S^2}\rho(t) = 0 \quad \text{at} \quad T>T_{cb},$$

$$\frac{h_e p}{S}(T-T_0) = 0 \quad \text{at} \quad T<T_{cb},$$

these being the basic points. Lastly,

$$-\frac{h_e p}{S}(T)+\frac{I^2}{S^2}\rho_0(T)\frac{T-T_c}{T_{cb}-T_c} = 0 \quad \text{at} \quad T_c\le T\le T_{cb}.$$

This point determines the position of the normal zone front. Then, the minimum propagation velocity of the *N*-zone is

$$v_{\min} = 2\sqrt{-\frac{h_e p}{S}+2\frac{I^2}{S^2}\rho_e'(T_c)},$$

and the maximum velocity is

$$v_{\max} = 2\sqrt{\sup_{0<T<T_3}\frac{f(T)}{T}}$$
$$= 2\sqrt{\sup_{0<T<T_3}\left\{-\frac{h_e p}{S}+\frac{I^2}{S^2}\frac{\rho_e(T)}{T}\right\}},$$

provided that the upper limit sup is attained. A simple analysis shows that the derivative

$$\left(\frac{f(T)}{T}\right)' = \left(\frac{I^2}{S^2}\frac{\rho_e(T)}{T}\right)'-\frac{h_e p}{S}\left(1-\frac{T_0}{T}\right)'$$

is equal to zero if the function $\rho_e(T)$ represents a solution of the differential equation

$$\frac{I^2}{S^2}\rho'(T)-\frac{I^2}{S^2}\rho(T)-\frac{hpT_0}{S} = 0, \qquad (6)$$

which it is convenient to write in the form

$$\frac{I^2\rho'(T)}{hpST_0} - \alpha(T) - 1 = 0,$$

where by definition

$$\alpha(T) = \frac{I^2\rho(T)}{hpST_0}.$$

Then, it is readily seen that this equation takes the form

$$\alpha'(T) - \alpha(T) - 1 = 0.$$

Note that at $\rho_0(T)$ = const, the quantity α is a dimensionless Stakly parameter [2]; however, in such a general form, we do not even have a representation of $\rho(T)$ through the function $\rho_0(T)$. Therefore, we will proceed in the same way as above and introduce the formally dimensionless temperature using the a priori parameters T_c and T_{cb}, so that it is not necessary to single out the quantity $\rho_0(T)$ as was done in [2] (see above). As a result, we obtain a chain of inequalities

$$\frac{d\alpha(T(\Theta))}{d\Theta} = \frac{d\alpha}{dT}\frac{dT}{d\Theta} \le \frac{dT}{d\Theta}\frac{\alpha(T)}{T - T_c} = \frac{1}{\Theta}\alpha(T(\Theta))$$

(to be solved to within unity) and, therefore,

$$\frac{\tilde{\alpha}}{\tilde{\alpha}_c} < e^{\Theta} - e^{\Theta_c} = e^{\Theta} - 1.$$

In distinction from the previous estimation obtained by solving the differential inequality under the condition that $h_c p(T - T_0)/S \ll 1$, here this restriction is removed. Therefore, the rate of growth of the function $\rho(T)$ can be exponential instead of linear.

If the function $\tilde{\alpha}(\Theta)$ is specified (and, hence, the function $\rho(T)$ as well), the points at which the quantity $f(\Theta)/\Theta$ is extremal are determined in a given range as solutions of the functional equation

$$\tilde{\alpha}(\Theta) = \tilde{\alpha}_c(\Theta)(e^{\Theta} - 1),$$

where $\tilde{\alpha}_c(\Theta) = \tilde{\alpha}(\Theta_c)$, $\Theta_c = (T_c - T_0)/(T_{cb} - T_0)$. In the general case, there can be several such points $\Theta = \Theta_*$, and if Θ is one of them, then a maximum of $f(\Theta)/\Theta$ will be attained if the inequality $\alpha''(\Theta) < 0$ is satisfied. It is evident that a minimum of three terms is required in a series expansion of the function e^{Θ}. Then

$$\alpha(\Theta) = \Theta + \frac{\Theta^2}{2} + \frac{\Theta^3}{3}.$$

Hence, $\alpha'' = 1 + \Theta$ and the maximum is attained if the inequality $1 + \Theta < 0$ is satisfied. Taking into account (see the introduction) that $1 - i \le \Theta \le 1$ (that is, $2 - i \le 1 + \Theta \le 2$ and, therefore, $2 - i \le 1 + \Theta < 0$), we find that $i \ge 2$ or (using notation of [2]) $I > 2I_c$.

Thus, the allowed range of the normal zone propagation velocities is determined by the inequalities

$$v_{\min} < v < \frac{f(\Theta_*)}{\Theta_*}.$$

The approximation $\rho_0(T)$ = const leads to a value of Θ_* that is given (to within unity) by the equation $e^{\Theta} - 1 = \Theta$. It is also easy to see that the following inequality should be true (see above):

$$\rho_0(T) > = \frac{h_e}{\lambda_e}\frac{pS}{I^2},$$

that is, the N-zone propagation in the composite begins starting from current densities

$$i^2 > \frac{1}{\rho_0'(T_c)}\frac{pS}{I_c^2}\frac{h_e}{\lambda_e},$$

or at $i^2 > \lambda_e/\alpha$, where

$$\alpha = 1/[\alpha + \rho_0'(T_c)]T_c^2/h_e pS(T_c - T_0),$$

where it is assumed that $T_c = T_{cb}$; at $\alpha \le 1$, we obtain $i = i_p = 1/\alpha$. At the same time, the last formula takes into account a finer mechanism of the superconductivity break-up.

This formula gives approximately the same [qualitative] dependence of the N-zone velocity on current density as in [2, Fig. 1], except that in this case, the term $h_e pS$ characterizing heat removal through the cross-sectional area S takes into account (and determines) variation with the transport current of the slope of curve $V = V(I)$. Note that the maximal velocity no longer depends on the heat conductivity coefficient λ_e. Finally, since the model problem is primordial, these simple estimates are adequate in a qualitative study.

Note that formally, the estimation of the normal zone propagation velocity is a trivial consequence of the fundamental results obtained in [4], which provide the lower bound, and of the well-known results of the theory of wave propagation for systems of parabolic equations (Wolpert *et al.*), which give the upper bound of the velocity.

The outlined results have been motivated by study [2], in which the influence of a nonconductive coating on the velocity of irreversible propagation of the normal zone along a cooled composite superconductor has been established. In comparison with the known results, the results obtained in this study take into account heat transfer in the classic model of stepwise heat release. It has been shown that the heat transfer coefficient depends on the transversal dimensions of the composite and the coating and an estimate has been made of the allowed range of the normal zone propagation velocities.

Obviously, at $\Theta < 1 - i$ (see formula (2)), the function $F(\Theta) = -\Theta/(\alpha + \beta) + i^2 r(\Theta)$ is negative and since

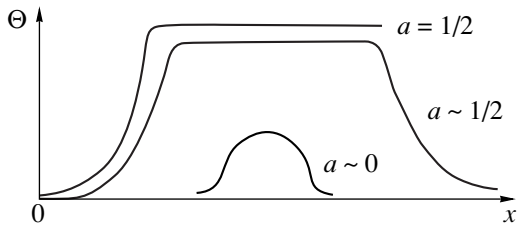

Fig. 3. Initial excitation of the heat domain at $a \sim 0$; evolution of the heat domain in the vicinity of the resistive transition temperature at $a \sim 1/2$; the shape of the heat domain at $a = \Theta_2/\Theta_3 \sim 0$, where $\Theta_2 = (\lambda_i - 1)/(\lambda_i(a - i))$ and $\Theta_3 = (\lambda \in \beta)i^2$.

the equation $F(\Theta) = 0$ has three roots $\Theta_1 = 0$, Θ_2, and Θ_3, it can be readily seen that the continuity of this function should have the form as in Fig. 1 and, therefore, can be approximated by $f(e) = e(1 - e)(e - a)$, where $0 < a < 1$ and $e = \Theta/\Theta_3$ (this is simply normalization for the range (0, 1)). Here, $e = \Theta_2/\Theta_3$.

It is known (see, for example, [6, 7]) that in his study of wave solutions of the heat conductivity equation, Hauksley constructed a solution of the type

$$e(x) = [1 + \exp(-x/\sqrt{2})]^{-1},$$

which is shown in Fig. 3. In particular, at $a = 1/2$ and $v = 0$ (that is, at $\Theta_2 = \Theta_3/2$), a reflected solution of the form $(1 - e)$ appears simultaneously with the family of periodic solutions, which can be presented as elliptic functions [6, 7]. Hauksley's solution propagates with a velocity of $v = \sqrt{2}(1/2 - a)$. McKean [7, p. 146] gave a detailed picture of the behavior of the solutions at $0 < a < 1/2$. Hauksley's solution exits point (0, 0) and approaches point (1,0) in the phase plane $e = T$ and $e' = T'$, and, in essence, represents a classical heat domain, whose dynamics in superconductors was investigated in detail in a number of studies [1, 4, 8].

REFERENCES

1. A. V. Gurevich and R. G. Mints, *Heat-Autowaves in Normal Metals and Semiconductors* (Inst. Vys. Temp. Akad. Nauk SSSR, Moscow, 1987).
2. V. K. Ozhogina and V. R. Romanovskiĭ, Zh. Tekh. Fiz. **68** (12), 95 (1998) [Tech. Phys. **43**, 1487 (1998)].
3. A. N. Vol'pert, *Differential Equations. Probability Theory* (Nauka, Moscow, 1988), pp. 333–358.
4. A. A. Pukhov, Sverkhprovodimost: Fiz., Khim., Tekh. **6** (2), 235 (1993).
5. V. P. Maslov, V. G. Danilov, and K. A. Volosov, *Mathematical Modeling of Heat and Mass Transfer Processes* (Nauka, Moscow, 1987).
6. H. P. McKean, Jr., Adv. Math. **4** (3), 209 (1970).
7. O. Henry, *Geometric Theory of Semilinear Parabolic Equations* (Springer-Verlag, Berlin, 1981; Nauka, Moscow, 1985).
8. R. G. Mints and A. L. Rakhmanov, *Instabilities in Superconductors* (Nauka, Moscow, 1984).

Translated by M. Lebedev

Technical Physics, Vol. 46, No. 1, 2001, pp. 76–83. Translated from Zhurnal Tekhnicheskoĭ Fiziki, Vol. 71, No. 1, 2001, pp. 79–85.

Optical Nonuniformities in Nuclear-Pumped Lasers with Plane Uranium Layers

V. Yu. Mat'ev, V. V. Borovkov, and S. P. Mel'nikov

Russian Federal Nuclear Center, All-Russia Research Institute of Experimental Physics, Sarov, Nizhni Novgorod oblast, 607190 Russia

Received October 28, 1999; in final form, February 22, 2000

Abstract—Optical nonuniformities in the nuclear-pumped gas lasers are calculated. The nonuniformities are formed due to inhomogeneous energy deposition by the fission fragments from thin plane uranium layers that irradiate the laser active gas. The results of calculations agree with experimental data. © *2001 MAIK "Nauka/Interperiodica".*

INTRODUCTION

Direct conversion of nuclear energy into coherent light is being actively studied in Russia and the United States [1–3]. The basic principle of the nuclear pumping is based on creating a nonuniform recombination plasma by irradiating the working gas by ions produced in nuclear reactions. The nonuniform energy deposition by ions lead to gas nonuniformities, which worsen the optical quality of laser light, transverse (with respect to the optical axis) nonuniformities being the most dangerous. Experimental studies of the optical nonuniformities in laser cells irradiated by fission fragments from thin uranium layers (plane or cylindrical) were reported in [4]. The transverse profile of the gas density in cylindrical cells was numerically calculated in [5, 6]. A series of one-dimensional analytical models [7–11] of the gas dynamics in nuclear-pumped lasers have been developed either neglecting [7–10] or incorporating [11] the heat flux onto the wall. However, the calculation of optical nonuniformities in experiments using cells with plane layers [4] is rather difficult because of the gas leakage from the laser active region to a large buffer volume. The results of the phenomenological calculations of the gas density in such cells [12] have not been compared yet with the experimental data [4]. This study is aimed at calculating (based on the model of [11] generalized to the case of a cell with a buffer volume) optical nonuniformities in the experiments using cells with plane layers [4].

EXPERIMENTAL

In experiment [4], a laser cell (Fig. 1) was a tube with a length of $l_1 = 230$ cm and a diameter of $\phi_1 = 8$ cm. Uranium layers were deposited on two plane plates (with the length $l_0 = 200$ cm and width $b = 6$ cm) placed inside the tube at a distance of $d_0 = 2$ cm from each other. The laser active volume (the gas volume between the plates) was $V_0 = bl_0d_0 = 2.4 \times 10^3$ cm^3. The ratio of the active volume to the total gas volume V_G was $\beta = V_0/V_G = 0.24$. The cell was filled with inert gas (He or Ar) at various initial pressures P_0 (see table).

The average (over the plate area) thickness of the uranium layer (90%-enriched oxide–protoxide mixture) was $d_1 \approx 4.1$ μm (or 3.2 mg/cm^2). The reduced thickness of the layer was $D_1 = d_1/R_1 \approx 0.43$, where $R_1 \approx 9.6$ μm was the range of fission fragments inside the layer. The mean fluence of thermal neutrons in the layer attained 0.7×10^{13} cm^{-2} per pulse. The table shows the mean number N^* of fissions in a unit volume of the layer per pulse.

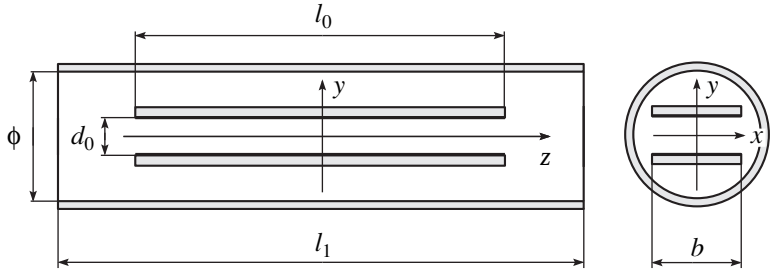

Fig. 1. Schematic of a plane cell of a nuclear-pumped laser.

1063-7842/01/4601-0076$21.00 © 2001 MAIK "Nauka/Interperiodica"

Calculation parameters ($D_1 = 0.43$, $d_0 = 2$ cm, $\beta = 0.24$)

Gas	P_0, atm	N^*, 10^{14} cm^{-3}	R_0, cm	D_0	$\bar{f}_0$	$f(0, 0, 0)$	f_1	$\Theta \times 0.9$	χ, cm^2/s	C, 10^{-5}
He	2.0(∥)	0.66	5.5	0.36	0.34	0.94	1.50	0.31	0.86	6.37
He	2.0(⊥)	0.70	5.5	0.36	0.34	0.94	1.50	0.33	0.86	6.37
He	5.0	0.69	2.2	0.91	0.164	0.47	2.79	0.157	0.34	15.9
Ar	0.25	0.66	10.4	0.192	0.45	1.04	1.26	1.75	0.8	6.5
Ar	0.5	0.67	5.2	0.38	0.33	0.93	1.53	1.29	0.4	12.9

Note: For He at 2 atm, the measurements were carried out for two cases. In the first case (∥), the longitudinal density profile (density distribution along the plate) was measured. In the second case (⊥), the transverse (with respect to the plates) density profile and the parabolic coefficient of the refractive index were measured.

The time profile of the neutron pulse was approximated by the function [13]

$$\psi(t) = A\psi_0(t), \quad \psi_0(t) = \cosh^{-2}\left[\frac{a(t-t_1)}{\tau^*}\right], \qquad \tau^* = \begin{cases}\tau_0, & t < t_1,\\ \tau_1, & t > t_1,\end{cases} \quad A = \frac{a}{\tau_0 + \tau_1}, \tag{1}$$

where $t_1 = 7.6$ ms corresponds to the pulse maximum, $\tau_0 = 3.30$ ms, $\tau_1 = 2.45$ ms, and $a = 2\mathrm{Arch}\sqrt{2} = 1.763$.

In this case, we have

$$\Psi(t) = \int_{-\infty}^{t} \psi(t')dt' = \left\{\tau_0 + \tau^* \tanh\left[\frac{a(t-t_1)}{\tau^*}\right]\right\}(\tau_0 + \tau_1)^{-1}. \tag{2}$$

Formally, we can assume that the pulse starts at $t = -\infty$ ($\Psi(0) \approx 3 \times 10^{-4} \ll \Psi(\infty) = 1$). Figure 2 compares the $\psi_0(t)$ function with the exact profile.

Optical nonuniformities were measured with a Mach–Zehnder interferometer at the He–Ne laser wavelength (633 nm) with a resolution of 50 μs. In the measurements, the optical nonuniformities were averaged over the cell length. Therefore, below, all the quantities in the active region are assumed to be averaged over the cell length. Special consideration will be given to the nonirradiated end regions.

ENERGY DEPOSITION BY FISSION FRAGMENTS

A method for calculating energy deposition by the fission fragments in nuclear-pumped lasers with rectangular uranium layers was proposed in [14, 15]. The method is based on the following commonly accepted approximations [16, 17]: the neutron flux is uniform, separation of fission fragments is isotropic, the fragment trajectories are straight, and the spectrum of fragments is monoenergetic. The calculations employ the quadratic stopping law [16, 17]: the fragment energy E depends on the path length l as $E = E_0(1 - l/R)^2$, where E_0 is the initial energy of the fragment and R is the range of fission fragments. According to [14], the energy δE^* absorbed in a unit volume δV per unit time δt is equal to

$$\frac{\delta E^*}{\delta V \delta t} = \frac{\rho(\mathbf{r}, t)}{\rho_0} Q(\mathbf{r}, t), \qquad Q(\mathbf{r}, t) = \frac{\Theta P_0}{\gamma - 1}\psi(t) f(\mathbf{r}, t), \quad f(\mathbf{r}, t) = \frac{j(\mathbf{r}, t)}{\bar{j}_0}, \tag{3}$$

$$\Theta = (\gamma - 1)\frac{2E_0}{P_0}\frac{R_1}{R_0}N^*\bar{j}_0, \quad \gamma = \frac{c_p}{c_p} = \frac{5}{3}, \tag{4}$$

where $\rho(\mathbf{r}, t)$ is the gas density; ρ_0 is the initial gas density; P_0 is the initial pressure; c_p and c_v are the heat capacities at constant pressure and constant volume, respectively; R_1 and R_0 are the fragment ranges in the layer and in the unperturbed gas, respectively; $j(\mathbf{r}, t)$ is the energy deposition function, which depends on the configuration of the layers and the gas density; and $\bar{j}_0$ is the energy deposition function averaged over the volume V_0 for the unperturbed gas.

The parameter Θ is the ratio of the energy absorbed in the volume V_0 per pulse (calculated for the unperturbed gas) to the gas internal energy. In [11], this parameter was introduced to characterize the thermodynamics of energy deposition. This parameter is approximately equal to the relative increase in the mean temperature of the gas. Since the range of fission fragments and the pressure contribute to Θ as the product P_0R_0 and $R_0 \propto 1/P_0$, we can use the ratio R_1/R_0 taken at a pressure of 1 atm. In this case, the value of the expression $(\gamma - 1)E_0/P_0$ (also taken at a pressure of 1 atm) is equal to 1.77×10^{-10} cm^3 at $E_0 = 168$ MeV.

For a long plane plate ($l_0 \gg R_0$) and uniform gas density, we have

$$j_1(x, y) = \omega(H_0, \varphi_L) + \omega(H_0, \varphi_R) - \omega(H_0 + D_1, \varphi_L) - \omega(H_0 + D_1, \varphi_R), \quad (5)$$

$$\omega(D, \varphi) = \int_0^{\varphi} \hat{\nu}\left(\frac{D}{\cos\varphi}\right)\frac{d\varphi}{2\pi},$$

$$\nu(\Lambda) = \sqrt{1-\Lambda^2} - 2\Lambda\arccos\Lambda + \Lambda^2\mathrm{Arth}(\sqrt{1-\Lambda^2}),$$

$$\hat{\nu}(\Lambda) = \begin{cases} \nu(\Lambda), & \Lambda \le 1 \\ 0, & \Lambda > 1 \end{cases}, \quad (6)$$

$$\varphi_L = \arctan\frac{b/2 + x}{h_0}, \quad \varphi_R = \arctan\frac{b/2 - x}{h_0},$$

$$H_0 = \frac{h_0}{R_0} = \frac{D_0}{2} + Y, \quad h_0 = \frac{d_0}{2} + y,$$

$$D_0 = \frac{d_0}{R_0}, \quad Y = \frac{y}{R_0}, \quad D_1 = \frac{d_1}{R_1}.$$

Here, h_0 is the distance from the bottom plate and the origin of the x and y coordinates are counted from the cell axis (Fig. 1). The energy deposition function for the upper plate can be obtained by substituting h_0 with $d_0 - h_0$ in expression (5). Then, both functions must be summed up. For a wide plate with $b \gg R_0$, which corresponds to infinite plane geometry, we have $\omega(D, \arccos D) = \omega_\infty(D) \equiv (1 - D^2 + 2D\ln D)/4$ [15].

The parabolic approximation of the energy deposition in the vicinity of the medial plane ($y = 0$) is of special interest for optical applications

$$j(x, y) = j(x, 0) + \frac{1}{2}Y^2 j''(x, 0), \quad y \ll \frac{d_0}{2},$$

$$j''(x, 0) = 2\omega''(D_0/2, \varphi_L) + 2\omega''(D_0/2, \varphi_R) - 2\omega''(D_0/2 + D_1, \varphi_L) - 2\omega''(D_0/2 + D_1, \varphi_R), \quad (7)$$

$$\omega''(D, \varphi) = \int_0^{\varphi} \hat{\nu}''\left(\frac{D}{\cos\varphi}\right)\frac{d\varphi}{2\pi\cos^2\varphi},$$

$$\nu''(\Lambda) = 2\mathrm{Arth}(\sqrt{1-\Lambda^2}).$$

For infinite plane geometry, we have $2\omega''_\infty(D) = 1/D - 1$.

FORMATION OF OPTICAL NONUNIFORMITIES

It is typical of the gas dynamics in nuclear-pumped lasers that the gas pressure is almost uniform across the cell [4–11] and heat conduction plays a significant role only in a narrow wall region where the beam refraction is large [4, 5]. Indeed, for the cell width $d_0 \sim 2$ cm, the relaxation time of the transverse pressure gradients $\tau_P \sim d_0/u_s \sim 0.01$ ms (where $u_s \sim 10^5$ cm/s is the speed of sound) is much less than the pulse duration $\tau^* \sim 1$ ms. The characteristic length of heat diffusion can be estimated as

$$\lambda \cong \sqrt{\chi\tau}, \quad (8)$$

where $\chi \sim 1$ cm^2/s is the thermal diffusivity [18]. For the time equal to the pulse duration τ^*, this length is $\lambda \sim 0.03$ cm $\ll d_0$.

The heat conduction manifests itself only in the vicinity of the cell wall (which is cooler than the gas) where a thermal boundary layer develops [5]. The transverse Reynolds number is $\mathrm{Re} = d_0 u/\eta \sim 10^3 \gg 1$ (where $u \sim d_0/\tau^*$ is the transverse gas velocity and $\eta \sim 1$ cm^2/s is the kinematic viscosity). In the vicinity of the wall, the transverse velocity vanishes regardless of the viscosity force. Therefore, the effect of viscosity on the transverse motion is negligible.

Thus, for the main part of the cell, the gas is assumed to be ideal, non-heat-conducting, and nonviscous, and the pressure is assumed to be uniform ($P = P(t)$). Then the problem is reduced to thermodynamics [11]: the energy ΔE^* absorbed by a small gas volume V is spent on the increase in its internal energy $E_T = PV(\gamma - 1)$ and the expansion work $P\Delta V$. Therefore, we have

$$(\gamma - 1)\Delta E^* = \gamma P\Delta V + V\Delta P.$$

With allowance for mass conservation ($\rho V = \rho_0 V_0$), we arrive at the basic equation [11]

$$(\gamma - 1)\frac{\delta E^*}{\delta V \delta t} = \frac{dP}{dt} - \frac{\gamma P}{\rho}\frac{d\rho}{dt}, \quad \frac{\delta E^*}{\delta V \sigma t} = \frac{\rho(\mathbf{r}, t)}{\rho_0}Q(\mathbf{r}, t). \quad (9)$$

This equation can also be derived in the zero-order approximation by expanding the gas dynamics equations for an ideal, non-heat-conducting, and nonviscous gas in powers in the Mach number [7]. At the energy deposition given by expression (3) (nonadiabat equation) and for arbitrary motion, a formal solution to Eq. (9) has the form [11]

$$\frac{\rho_0}{\rho(\mathbf{r}, t)} = \left(\frac{P_0}{P(t)}\right)^{1/\gamma}\left\{1 + \frac{\Gamma}{P_0}\int_{t_0}^{t}\left(\frac{P_0}{P(t')}\right)^{\Gamma} Q(\mathbf{r}(t'), t')dt'\right\}, \quad (10)$$

$$\Gamma = \frac{\gamma - 1}{\gamma}.$$

The gas pressure is determined by the energy deposition averaged over the cell volume (minus the heat

flux onto the cell wall) [8, 19]

$$P(t) = P^*(t) - p(t), \quad \frac{dP^*}{dt} = (\gamma - 1)\left\langle \frac{\delta E^*}{\delta V \delta t} \right\rangle_V, \qquad \frac{dp}{dt} = \frac{\gamma - 1}{V_G} \oint_{S_V} \mathbf{q} d\mathbf{S}, \tag{11}$$

where $\mathbf{q} = -k\nabla T$ is the heat flux onto the wall, k is the thermal conductivity, and T is the gas temperature. As the heat removal region is small, we can assume that $p \ll P^*$.

The changes in the gas density are determined by the energy deposition, which, in turn, depends on the density profile. For the case of infinite plane geometry and transverse gas motion, the energy deposition function at a given Lagrangian coordinate does not depend on the density redistribution [7, 15]. In the general case (especially, in the presence of gas leakage into the buffer volume), the change in the density implies the recalculation of the energy deposition. In this study, the gas dynamics is calculated in two stages. In the first approximation, the gas inside the laser active volume V_0 (including the effluent gas elements) is characterized by the energy deposition function for the unperturbed gas $f(x(t), y(t), t) = f_0(x_0, y_0)$, $x_0 = x(0)$, $y_0 = y(0)$. The energy deposition outside the volume V_0 is negligibly small. With neglect of the heat flux onto the wall ($p = 0$), from Eqs. (3), (10), and (11), we obtain

$$P(t) \approx P^*(t) \equiv P_0(1 + \beta\Theta\Psi(t)), \quad \beta = V_0/V_G, \tag{12}$$

$$\frac{\rho_0}{\rho(x, y, t)} = \left(\frac{P_0}{P^*(t)}\right)^{1/\gamma} \left\{1 + \left[\left(\frac{P^*(t)}{P_0}\right)^{1/\gamma} - 1\right] \frac{f_0(x_0, y_0)}{\beta}\right\}, \tag{13}$$

$$\frac{T(x, y, t)}{T_0} = \left(\frac{P^*(t)}{P_0}\right)^{\Gamma} \left\{1 + \left[\left(\frac{P^*(t)}{P_0}\right)^{1/\gamma} - 1\right] \frac{f_0(x_0, y_0)}{\beta}\right\}, \tag{14}$$

where $T(x, y, t)$ is the gas temperature and $T_0 = T(x, y, 0)$.

At low energy depositions ($\Theta \ll 1$), we have

$$\frac{\rho(x, y, t)}{\rho_0} \approx 1 - \frac{\Theta}{\gamma}[f_0(x_0, y_0) - \beta]\Psi(t), \qquad \frac{T(x, y, t)}{T_0} \approx 1 + \frac{\Theta}{\gamma}[f_0(x_0, y_0) + (\gamma - 1)\beta]\Psi(t). \tag{15}$$

Since the gas mass is conserved within a two-dimensional problem, we can write

$$\rho_0 dv_0 = \rho(x, y, t) dv(x, y, t), \tag{16}$$

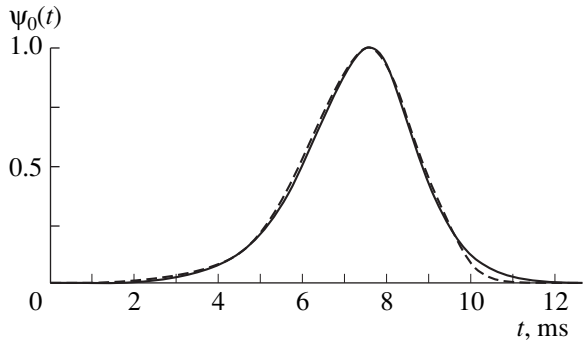

Fig. 2. Calculated (solid line) and measured (dashed line) time profiles of the neutron pulse.

where dv_0 and dv are the initial and current values of the gas element volume.

According to Eqs. (13) and (16), the total volume of the irradiated gas $V_A(t)$ is given by

$$V_A(t) = \int_{V_0} \frac{\rho_0}{\rho(x, y, t)} dv_0 = \frac{V_0}{\Sigma(t)}, \qquad \frac{1}{\Sigma(t)} = \left(\frac{P_0}{P^*(t)}\right)^{1/\gamma} \left\{1 + \frac{1}{\beta}\left[\left(\frac{P^*(t)}{P_0}\right)^{1/\gamma} - 1\right]\right\}, \tag{17}$$

where $V_A(0) \equiv V_0$. In the nonirradiated region, where $f(x, y) = 0$, the gas volume changes adiabatically ($V_B(t) = V_B(0)(P_0/P^*(t))^{1/\gamma}$), whereas the total gas volume remains constant ($V_A(t) + V_B(t) = V_G$). Therefore, the mean gas density in the bulk of the active volume is given by

$$\langle \rho \rangle_A(t) = \rho_0 \frac{V_0}{V_A(t)} = \rho_0 \Sigma(t). \tag{18}$$

Figure 3 demonstrates the time evolution of $\Sigma(t)$. The calculation parameters are shown in the table. A correction factor of 0.9 for the quantity Θ is related to the nonuniformity of the layers [19].

In the second-order approximation, the energy deposition function is still related to the initial coordinates ($f(x(t), y(t)) = f(x_0, y_0, t)$; however, the gas density is taken from Eq. (18). This means that in relationships (6), the range R_0 is divided (and the quantities Y, D_0, and H_0 are multiplied) by $\Sigma(t)$. Thus, the redistribution of the gas density is taken into account only on the average.

Let us estimate the heat flux on to the wall considering it as a perturbation. According to estimate (8), the increase in the gas temperature near the wall by $\delta T(t')$ leads to an increase in the heat flux onto the wall (the temperature of the wall is assumed to be constant

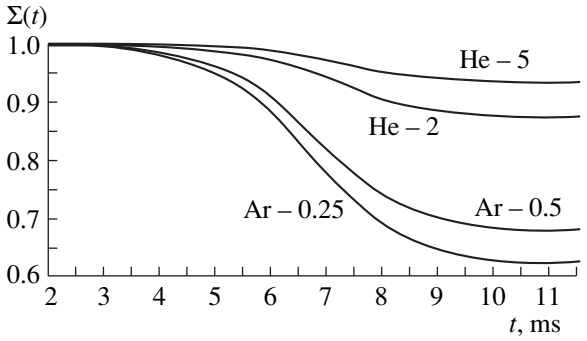

Fig. 3. Mean gas density in the active volume versus time. Numerals indicate the gas pressure (in atm).

and equal to T_0)

$$\delta q(t) \cong k\frac{\delta T(t')}{\lambda(t,t')}, \quad \lambda(t,t') = \sqrt{\chi(t-t')}, \quad \chi = \frac{k}{\rho_0 c_P}.$$

Integration over the pulse yields the intensity of the heat flux onto the wall

$$q(t) \cong k\int_{t_0}^{t}\frac{dT_1}{dt}\bigg|_{t'}\frac{dt'}{\sqrt{\chi(t-t')}} = \frac{\gamma P_0}{\gamma-1}\int_{t_0}^{t}\frac{d}{dt}\left(\frac{T_1}{T_0}\right)_{t'}\sqrt{\frac{\chi}{t-t'}}dt', \tag{19}$$

where $T_1(t)$ is the gas temperature near the wall neglecting the heat flux [see Eq. (14)]. Since the thickness of the boundary layer is small, the energy deposition function in the layer $f_0(x_0, y_0)$ can be replaced by its value on the wall $f_1 = \langle f_0(x_0, d_0/2)\rangle$ averaged over the surface of the active layer (in the buffer volume, we have $f_1 = 0$). The quantities k and χ are assumed to be constant.

Then, we have

$$\frac{dT_{1A}}{dt} = T_0\left[f_1 + \Gamma(\beta - f_1)\left(\frac{P_0}{P^*(t)}\right)^{1/\gamma}\right]\Theta\psi(t),$$

$$\frac{dT_{1B}}{dt} = T_0\left(\frac{P_0}{P^*(t)}\right)^{1/\gamma}\beta\Gamma\Theta\psi(t)$$

in the active and buffer volumes, respectively. With neglect of the heat flux onto the cell ends and mounting rings, the total heat flux onto the wall is equal to

$$\oint_{S_V}\mathbf{q}d\mathbf{S} \approx q_A S_A + q_B(S_A + S_B), \tag{20}$$

$$\frac{S_A}{V_G} = \beta\frac{S_A}{V_0} = \frac{2\beta}{d_0}, \quad \frac{S_B}{V_G} = \beta\frac{S_B}{V_0} = \beta\frac{\pi\phi}{bd_0}\frac{l_1}{l_0},$$

where $S_A = 2bl_0$ is the area of the active layer surface (and the outer substrate surface) and $S_B \approx \pi\phi l_1$ is the area of the buffer volume surface.

From Eqs. (11), (19), and (20) we have

$$\frac{dp}{dt} \approx \frac{2\beta\gamma P_0}{d_0}\int_{t_0}^{t}\left\{\frac{d}{dt}\left(\frac{T_{1A}}{T_0}\right)_{t'} + \left(1 + \frac{\pi\phi}{2b}\frac{l_1}{l_0}\right)\frac{d}{dt}\left(\frac{T_{1B}}{T_0}\right)_{t'}\right\} \times\sqrt{\frac{\chi}{t-t'}}dt' = \beta\xi\Theta P_0\int_{t_0}^{t}G(t')\frac{\psi(t')dt}{\sqrt{t-t'}},$$

$$\xi = \frac{2\gamma}{d_0}\sqrt{x}, \tag{21}$$

$$G(T) = f_1 + \Gamma\left(\frac{P_0}{P^*(t)}\right)^{1/\gamma}\left[\beta - f_1 + \beta\left(1 + \frac{\pi\phi}{2b}\frac{l_1}{l_0}\right)\right],$$

$$p(t) = 2\beta\xi\Theta P_0\int_{t_0}^{t}G(t')\sqrt{t-t'}\psi(t')dt'.$$

Substituting the varying energy deposition $f(x_0, y_0, t)$ and pressure into Eq. (10), we arrive at

$$\frac{\rho_A(x,y,t)}{\rho_0} = \left(\frac{P(t)}{P_0}\right)^{1/\gamma}\left\{1 + \frac{\Theta}{\gamma}\int_{t_0}^{t}\left(\frac{P_0}{P(t')}\right)^{\Gamma} \times\frac{j(x_0,y_0,t')}{j_0}\psi(t')dt'\right\}^{-1}, \quad \frac{\rho_B(t)}{\rho_0} = \left(\frac{P(t)}{P_0}\right)^{1/\gamma}$$

in the active and buffer volumes, respectively. Note that the dependences $x = x(x_0, y_0, t)$ and $y = y(x_0, y_0, t)$ need to be additionally specified. The density averaged over the entire cell length is given by

$$\left\langle\frac{\rho(x,y,t)}{\rho_0}\right\rangle = \frac{l_0}{l_1}\frac{\rho_A(x,y,t)}{\rho_0} + \frac{l_1 - l_0}{l_1}\frac{\rho_B(t)}{\rho_0}. \tag{22}$$

Figure 4 compares the results of calculations of the relative density determined by Eq. (22) at the cell axis ($x = x_0 = 0$, $y = y_0 = 0$) with the experimental data. The calculations were performed both with allowance for the heat flux onto the wall and neglecting the heat flux ($P(t) = P^*(t) - p(t)$ or $P(t) = P^*(t)$, respectively). It is seen that there is reasonable agreement between the results of calculations and the experimental data. Since the buffer volume is relatively large, the pressure variations are rather small (the maximum variation is one-third for the case of argon at a pressure of 0.25 atm) and the correction related to the heat flux onto the wall appears to be insignificant. Figure 5 shows the longitudinal profiles of the relative density at the medial plane ($y = 0$) at different instants for helium at a pressure of 2 atm. In the calculations, two models of the longitudinal gas motion were employed: the model of the gas at rest ($x = x_0$) and the model of the uniform longitudinal

expansion $x(x_0, t) = x_0/\Sigma(t)$. The second model describes the shape of the density profile well. The disagreement in the absolute values is rather large, although the results of the other experiment (Fig. 4) with helium at a pressure of 2 atm correlate well with the results of the calculations.

Let us briefly consider alternative gas-dynamic models. One-dimensional models [7–11] can not be used to analyze the experimental data [4]. In these models, the gas density is maximum at the axis (where the energy deposition is minimum) and monotonously increases with time, whereas the experimental data [4] show a decrease in the gas density at the axis (Fig. 4). This can be easily explained using Eq. (15). If $f(0, 0, 0) < \beta < 1$, the gas density at the axis increases, whereas if $\beta < f(0, 0, 0)$ (large buffer volumes), the gas density at the axis decreases. If $\beta = 1$, Eqs. (12)–(15) can be reduced to the models presented in [7, 11].

To overcome the limitations of the models [7, 8] Torczynski and Neal [20] introduced rapidly cooled regions (narrow slits) in the bulk of the cell volume. These regions were described phenomenologically and the equations of the gas dynamics were solved numerically. However, one can hardly assume that the large buffer volumes exhibit large heat fluxes onto the wall. Prikhod'ko and Sizov [12] proposed a calculation scheme in which (in our notations)

$$\frac{T(x, y, t)}{T_0} = 1 + \Xi(t)\frac{\rho(x, y, t)}{\rho_0} f_0(x, y),$$
$$x = x_0, \quad y = y_0,$$

the coefficient $\Xi(t)$ was determined by the condition of gas mass conservation in the cell, and the heat flux onto the wall was not taken into account.

At small energy depositions and with allowance for Eq. (12), we obtain

$$\frac{\rho(x, y, t)}{\rho_0} = 1 - [\Xi(t) f_0(x, y) - \beta\Theta\Psi(t)],$$
$$\Xi(t) = \Theta\Psi(t), \quad \Xi(t) \ll 1.$$

Being similar to Eq. (15), this expression overestimates the relative increase in the gas density by the factor $\gamma \approx 1.7$.

PARABOLIC COEFFICIENT OF THE REFRACTIVE INDEX

Experiments [4] show that in the major part of the cell (except for the wall region), the refractive index is given by

$$n(y, t) = n(y, t) - \alpha(t)y^2. \qquad (23)$$

The parabolic coefficient $\alpha(t)$ is important for practical calculations of the beam trajectories and the stability of the laser cavity. The density dependence of the gas refractive index is given by $n = 1 + C(\rho/\rho_0)$ (the values of the constant C are given in the table). Taking into account Eqs. (22) and (23) and the expansion of the energy deposition function (7), we can represent the length-averaged parabolic coefficient at the cell axis as

$$\langle\alpha(t)\rangle = -\left\langle\frac{\partial^2 n(x, y, t)}{2\partial y^2}\right\rangle = -\frac{C}{2}\frac{\partial^2}{\partial y^2}\left\langle\frac{\rho(x, y, t)}{\rho_0}\right\rangle$$
$$= -\frac{l_0}{2l_1}C\frac{\partial^2}{\partial y^2}\left(\frac{\rho_A(x, y, t)}{\rho_0}\right), \qquad (24)$$

$$\frac{\partial^2}{\partial y^2}\left(\frac{\rho_A(x, y, t)}{\rho_0}\right)_{y=0} = g^2(x, 0, t)\frac{\partial^2}{\partial y_0^2}\left(\frac{\rho_A(x, y, t)}{\rho_0}\right)_{y_0=0},$$
$$g(x, y, t) = \frac{\partial y_0}{\partial y}, \qquad (25)$$

$$\frac{\partial^2}{\partial y_0^2}\left(\frac{\rho_A(x, y, t)}{\rho_0}\right)_{y=0} = -\left(\frac{P(t)}{P_0}\right)^{1/\gamma}$$
$$\times\left\{1 + \frac{\Theta}{\gamma}\int_{t_0}^{t}\left(\frac{P_0}{P(t')}\right)^{\Gamma}\frac{j(x_0, y_0, t')}{\bar{j}_0}\psi(t')dt'\right\}^{-2} \qquad (26)$$
$$\times\frac{\Theta}{\gamma}\int_{t_0}^{t}\left(\frac{P_0}{P(t')}\right)^{\Gamma}\left[\frac{\Sigma(t')}{R_0}\right]^2\frac{j''(x_0, 0, t')}{\bar{j}_0}\psi(t')dt'.$$

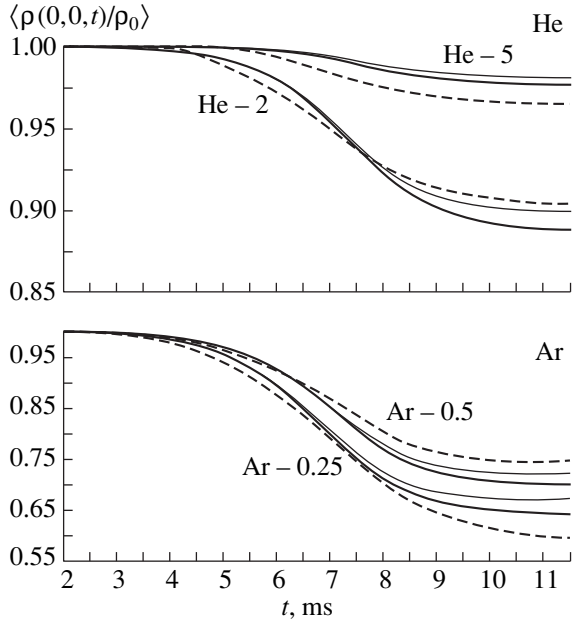

Fig. 4. Relative density at the cell axis versus time: experimental data [4] (dotted line) and results of calculations neglecting the heat flux onto the wall (light line) and with allowance for the heat flux (heavy line). Numerals indicate the gas pressure (in atm).

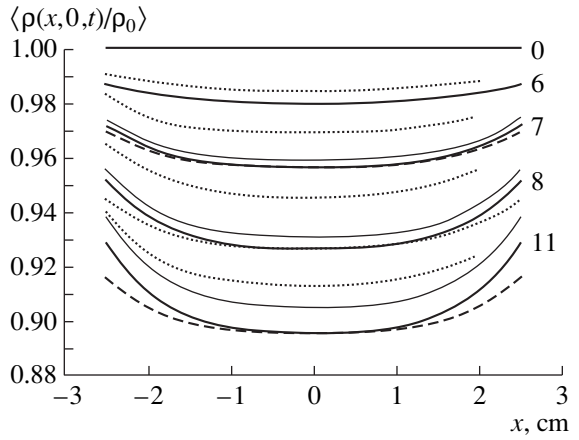

Fig. 5. Relative density at the medial plane ($y = 0$) versus x for He at 2 atm: experimental data [4] (dotted line) and the results of calculations neglecting the heat flux onto the wall for the gas at rest (light line), with allowance for the heat flux for the gas at rest (heavy line), and with allowance for the heat flux in the model of a uniform longitudinal expansion (dashed line). Numerals indicate time in milliseconds.

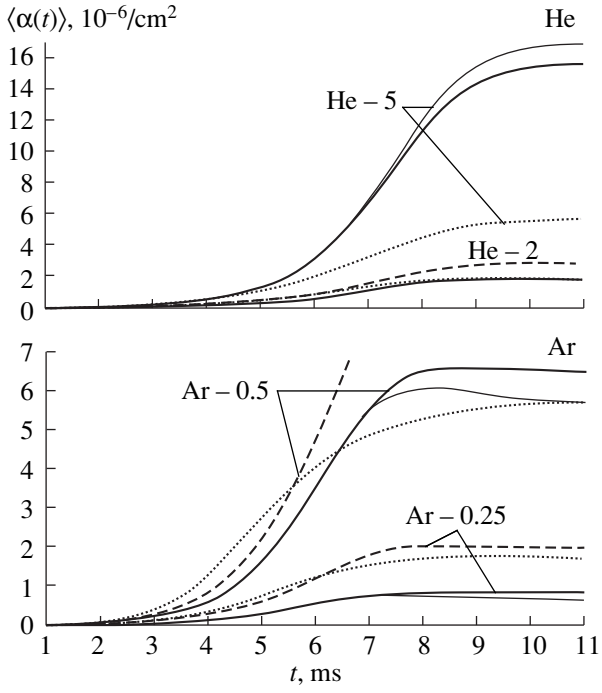

Fig. 6. Parabolic coefficient of the refractive index at the cell axis versus time: experimental data [4] (dotted line) and results of calculations for the gas at rest (heavy line), the model of uniform longitudinal expansion (light line), and the gas at rest with the energy deposition for infinite plane geometry neglecting the heat flux onto the wall (dashed line). Numerals indicate the gas pressure (in atm).

It is necessary to define the relationship between the coordinates $y = y(x_0, y_0, t)$. Let us consider three versions of this relationship. If the gas is at rest, we have $y = y_0$ and $g(x, y, t) = g_0 = 1$. In the case of only transverse motion, we have $\rho_0 dy_0 = \rho_A(x, y, t)dy$ and $g(x, y, t) = g_1(x, y, t) = \rho_A(x, y, t)/\rho_0$. Neglecting changes in the energy deposition and the heat flux onto the wall and based on Eqs. (13) and (25), we obtain

$$\frac{\partial^2}{\partial y^2}\left(\frac{\rho_A(x, y, t)}{\rho_0}\right)_{y=0} = \frac{1 - (P_0/P^*(t))^{1/\gamma}}{\{f(x, 0, 0)/\beta + (P_0/P^*(t))^{1/\gamma}[1 - f(x, 0, 0)/\beta]\}^4} \times \frac{j''(x, 0, 0)}{\bar{j}_0 R_0^2 \beta}.$$

For infinite plane geometry and $\beta = 1$, this result reduces to the known result of [8].

In the approximation of the uniform longitudinal expansion, we substitute $dV = dxdy$, $dV_0 = dx_0 dy_0$, and $dx = dx_0/\Sigma(t)$ in Eq. (16) to obtain $g(x, y, t) = g_2(x, y, t) = \rho_A(x, y, t)/(\rho_0\Sigma(t))$.

For low energy depositions and neglecting the heat flux onto the wall, we have

$$\frac{\partial^2}{\partial y^2}\left(\frac{\rho_A(x, y, t)}{\rho_0}\right)_{y=0} \approx -\frac{\Theta}{\gamma}\Psi(t)\frac{j''(x, 0, 0)}{\bar{j}_0 R_0^2}, \quad (27)$$

$$g(x, y, t) = 1, \quad \Theta \ll 1.$$

Figure 6 compares the results of calculations of the parabolic coefficient with the experimental data [4]. The calculations for the gas at rest and uniform longitudinal expansion yield close results (almost coinciding for He at 2 atm), which means that the longitudinal expansion and transverse compression balance each other. The calculations carried out in the approximation of the transverse gas motion and the calculations by formula (27) yield only qualitative agreement with the experimental data for He, for which ($\Theta \ll 1$), but not for Ar, for which $\Theta > 1$ (the results of calculations for argon are not shown). The results of calculations with neglect of the heat flux onto the wall differ from the presented curves to the same extent as in Fig. 4. Figure 6 also shows the results of calculations employing the energy deposition function for infinite plane geometry (with neglect of the heat flux). The effect of the finite width of the plates with uranium layers is rather small for He (almost undetectable for He at 5 atm), whereas for Ar it is more important than the heat flux onto the wall and two-dimensional gas motion.

The agreement with the experimental data is good in the most important cases (He at 2 atm and Ar at 0.5 atm), bad in the case of Ar at 0.25 atm, and very bad for He at 5 atm. Note that we did not take into account the gas motion along the optical axis; this may play a specific role in the latter case, which differs from the others only by the small range. It is also possible that the quadratic stopping law (a good model for calculating the energy deposition [16, 17]) employed in the cal-

culations of the energy deposition at large D_0 does not allow for accurate calculations of the parabolic coefficient. The latter is determined by the second derivative of the energy deposition distribution, which makes it very sensitive to the character of the stopping law.

ACKNOWLEDGMENTS

We are grateful to A.A. Sinyanskiĭ for supporting this work.

REFERENCES

1. *Proceedings of the Conference "Physics of Nuclear-Exited Plasma and the Problems of Nuclear-Pumped Lasers"* (Fiz. Énerg. Inst., Obninsk, 1992–1993).
2. *Proceedings of the 2nd Conference "Physics of Nuclear-Exited Plasma and the Problems of Nuclear-Pumped Lasers"* (Vseross. Nauchno-Issled. Inst. Éksp. Fiz., Arzamas-16, 1995), Vols. 1, 2.
3. R. T. Schneider and F. Hohl, in *Advances in Nuclear Science and Technology* (Plenum, New York, 1984), Vol. 16, p. 123.
4. V. V. Borovkov, B. V. Lazhintsev, S. P. Mel'nikov, *et al.*, Izv. Akad. Nauk SSSR, Ser. Fiz. **54**, 2009 (1990).
5. A. N. Sizov and Yu. N. Deryugin, Zh. Tekh. Fiz. **62** (6), 107 (1992) [Sov. Phys. Tech. Phys. **37**, 734 (1992)].
6. B. V. Kachanov and A. V. Gulevich, in *Proceedings of the 2nd Conference "Physics of Nuclear-Exited Plasma and the Problems of Nuclear-Pumped Lasers"* (Vseross. Nauchno-Issled. Inst. Éksp. Fiz., Arzamas-16, 1995), Vol. 1, p. 358.
7. J. R. Torczynski, J. Fluid Mech. **201**, 167 (1989).
8. J. R. Torczynski, J. Thermophys. Heat Transfer **5**, 318 (1991).
9. M. G. Anuchin, K. F. Grebenkin, Ya. Z. Kandiev, *et al.*, Zh. Tekh. Fiz. **61** (1), 3 (1991) [Sov. Phys. Tech. Phys. **36**, 1 (1991)].
10. A. V. Gulevich, V. A. Dubovskaya, A. V. Zrodnikov, *et al.*, in *Proceedings of the 2nd Conference "Physics of Nuclear-Exited Plasma and the Problems of Nuclear-Pumped Lasers"* (Vseross. Nauchno-Issled. Inst. Éksp. Fiz., Arzamas-16, 1995), Vol. 3, p. 77.
11. V. Yu. Mat'ev, in *Proceedings of the 2nd Conference "Physics of Nuclear-Exited Plasma and the Problems of Nuclear-Pumped Lasers"* (Vseross. Nauchno-Issled. Inst. Éksp. Fiz., Arzamas-16, 1995), Vol. 1, p. 410.
12. E. V. Prikhod'ko and A. N. Sizov, Kvantovaya Élektron. (Moscow) **22**, 613 (1995).
13. K. R. Chikin and V. V. Kharitovov, At. Énerg. **65**, 435 (1988).
14. V. Yu. Mat'ev, in *Proceedings of the 2nd Conference "Physics of Nuclear-Exited Plasma and the Problems of Nuclear-Pumped Lasers"* (Vseross. Nauchno-Issled. Inst. Éksp. Fiz., Arzamas-16, 1995), Vol. 2, p. 79.
15. V. Yu. Mat'ev and A. N. Sizov, in *Proceedings of the 2nd Conference "Physics of Nuclear-Exited Plasma and the Problems of Nuclear-Pumped Lasers"* (Vseross. Nauchno-Issled. Inst. Éksp. Fiz., Arzamas-16, 1995), Vol. 2, p. 209.
16. S. Kahn, R. Harman, and V. Forgue, Nucl. Sci. Eng. **23** (1), 8 (1965).
17. V. T. Kazazyan, B. A. Litvinenko, L. P. Roginets, and I. A. Savushkin, *Physical Foundations of Using Kinetic Energy of Fission Fragments in Radiation Chemistry* (Nauka i Tekhnika, Minsk, 1972).
18. V. S. Chirkin, *Thermophysical Properties of Materials* (Fizmatgiz, Moscow, 1959).
19. V. V. Borovkov, G. V. Vlokh, B. V. Lazhintsev, *et al.*, Kvantovaya Élektron. (Moscow) **22**, 219 (1995).
20. J. R. Torczynski and D. R. Neal, Nucl. Sci. Eng. **113** (3), 189 (1993).

Translated by A. Chikishev

Technical Physics, Vol. 46, No. 1, 2001, pp. 84–88. Translated from Zhurnal Tekhnicheskoĭ Fiziki, Vol. 71, No. 1, 2001, pp. 86–91.

RADIOPHYSICS

Nonlinear Response of a Bistable Ferromagnetic Resonator to a Microwave Pulse

Y. K. Fetisov and A. V. Makovkin

Moscow State Institute of Radio Engineering, Electronics, and Automation (Technical University), Moscow, 117454 Russia

e-mail: fetisov@orc.ru

Received February 7, 2000

Abstract—The reflection frequency response and bistability characteristic of a ferromagnetic resonator are studied experimentally and theoretically. The resonator is a 25-μm-thick rectangular yttrium-iron-garnet film with perpendicular magnetization. A technique to construct the bistability characteristic of the resonator from its measured response to a pulsed signal is suggested. It is demonstrated that the microwave bistability results from the intrinsic nonlinearity of ferromagnetic resonance. It is found that the bistability characteristic can adequately be described on the basis of a dispersive-bistability model. © *2001 MAIK "Nauka/Interperiodica"*.

INTRODUCTION

Intense electromagnetic radiation applied to a passive resonant system produces a variety of nonlinear phenomena. Among them is bistability [1]. A bistable system has two stable states differing in the level of absorption (reflection). As a rule, bistability stems from the fact that the resonant frequency or absorption coefficient depends on radiation power.

At microwave frequencies, bistability may attend nonlinear ferromagnetic resonance (FMR) in ferrites experiencing an external magnetic field. It was first detected in the form of a foldover in ferrite resonators; with a high radiation power, the line shape of FMR absorption becomes distorted so that the resonator offers two different levels of absorption for the same field [2]. Ferrite resonators also exhibit conventional bistability, i.e., a double-valued characteristic of reflected versus incident power for a given radiation frequency in the presence of a magnetostatic field [3]. Careful investigations into the nonlinear characteristics of ferrite-film resonators [4] confirmed that both effects have the same nature and may result from either the intrinsic nonlinearity of FMR [5, 6] or the heating of the sample by absorbed radiation [7, 8].

The bistability of ferrite resonators has been explored under quasistationary conditions only: in all measurements, the magnetic field or radiation power was varied slowly compared with the typical values of magnetic relaxation time with a continuous or pulsed microwave signal being applied to the sample. It seems interesting to examine the response of a bistable resonator to a short microwave pulse. This line of research would enable one to directly measure typical values of the switching time and to ascertain the mechanism of the nonlinearity underlying the bistable behavior. Such an investigation seems to be important to possible applications as well.

Accordingly, this study addresses the nonlinear response of a bistable ferrite resonator to a short, high-power microwave pulse.

RESONATOR CONFIGURATION AND EXPERIMENTAL SETUP

The ferromagnetic resonator was a 25-μm-thick yttrium-iron-garnet (YIG) film covering an area of 1×4 mm^2, with a saturation magnetization of $4\pi M_0 = 1750$ Gs and a uniform FMR linewidth of $\Delta H \approx 0.6$ Oe. The film was grown on a 0.6-mm gadolinium-gallium-garnet substrate by liquid-phase epitaxy. The signal was coupled into the resonator via a microstrip line 100 μm wide and 4 mm long on a polycor substrate. The microstrip was placed near the center of the resonator and was parallel to the longer resonator side. An 80-μm teflon interlayer was inserted between the microstrip and the YIG film so as to limit the coupling coefficient. The structure was situated in a uniform magnetostatic field of strength $H_0 = 3200$ Oe perpendicular to the film. The field was produced by a permanent magnet. The microwave signal was transmitted to the microstrip via a ferrite circulator, and the signal reflected from the resonator was measured. Under continuous-wave conditions, the reflection frequency response was recorded in the range of 4–5 GHz for different fixed levels of incident power by an R2-78 network analyzer, and the sweep time was 60 s. Under pulsed conditions, the resonator received microwave pulses with smooth envelopes, a fixed center frequency in the range of 4–5 GHz, a maximum peak power of 300 mW, a half-height width of about 27 μs, and a pulse spacing of 50 ms. Reflected microwave pulses were

1063-7842/01/4601-0084$21.00

detected with a calibrated diode. Their envelopes were recorded with a Wiltron digital oscilloscope and were stored in 512-point data files.

REFLECTION FREQUENCY RESPONSE

Figure 1a shows the reflection frequency response of the resonator as the reflection loss $L = 10 \log(P_{ref}/P)$ versus the signal frequency f, where P is the incident power and P_{ref} is the reflected power. Obtained at a low incident power, the curve has a single dip indicating strong absorption. Centered at $f_0 = 4400$ MHz, the dip has a depth of about 12 dB and a width of $2\Delta f = 4.4$ MHz for a 3-dB level of reflected power. The frequency response retains its shape if the incident power is varied from –60 to –10 dBm. This indicates that the system is linear at low powers. Note that all of the figures are drawn with regard for nonresonant loss in the connectors and the circulator and that the values of P and P_{ref} refer to the resonator input. In Fig. 1a, the circles depict a computed resonator line (see below).

As P is increased from –10 to +20 dBm, the response first develops asymmetric distortion and then becomes hysteretic (Fig. 1b). Concurrently, the resonant frequency f_r goes up and the absorption coefficient at f_r goes down. The resonant frequency corresponds to the maximum absorption when the input frequency is raised.

Based on measured data similar to those presented in Fig. 1b, we computed the resonant-frequency shift $f_r - f_0$ and the absorption coefficient $A = P_a/P$ at this frequency versus the absorbed power P_a. Figure 2 demonstrates that, if P_a is raised from 0 to 13 mW, the dependence is virtually linear and the proportionality coefficient is $B = 1.18$ MHz/mW. The maximum shift in f_r was 30 MHz measured at $P_a = 40$ mW. With P_a raised from 0 to 40 mW, the absorption coefficient monotonically decreases from $A_0 = 0.95$ to 0.72.

PULSED CONDITIONS

Quasi-monochromatic microwave pulses were applied to the resonator under pulsed conditions. Their peak power was high enough to produce appreciable nonlinear effects. The pulse shape is shown by the dashed line curve in Fig. 3. If the pulse carrier frequency f is less than the low-power resonator frequency f_0, reflected pulses have the same shape as incident ones. Otherwise, reflected pulses are distorted with distinctive dips, which affect both edges and occur at different levels. This is shown by the solid curve in Fig. 3. If the frequency detuning $\delta f = f - f_0$ is small, the dips arise at low powers. Their positions go toward the top of the pulse with increasing δf.

The bistability characteristic (the P_{ref}–P relationship) can easily be constructed from the recorded envelopes of incident and reflected pulses. Figure 4 shows

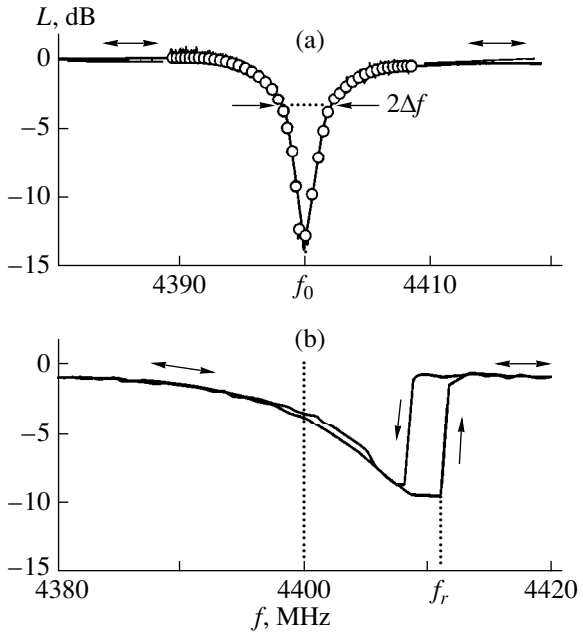

Fig. 1. Reflection frequency response of the resonator for an incident power of (a) –20 or (b) +10 dBm. The solid curves refer to the experiment and the circles refer to the computation. The arrows indicate the directions in which the signal frequency is varied.

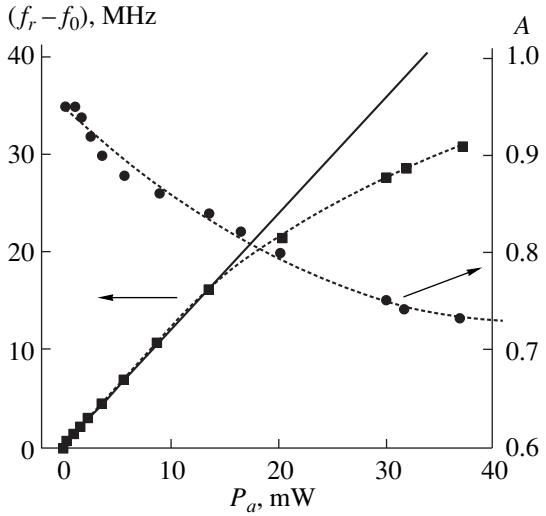

Fig. 2. Resonant-frequency shift and the absorption coefficient at f_r vs. absorbed power. The marks refer to the experiment and the solid curve refers to a linear approximation of the experimental data.

the instantaneous reflected power P_{ref} against the instantaneous incident power P for different input carrier frequencies. The curves are plotted from data similar to those in Fig. 3.

With P increased from zero (which corresponds to the leading edge of the incident pulse), the reflected power first grows linearly, then falls abruptly at $P = P_1$, and finally grows again. With P decreased from the

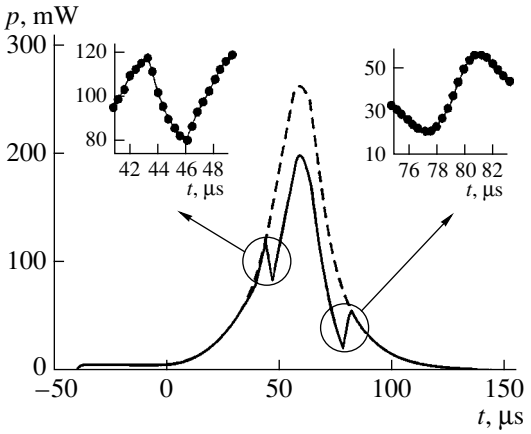

Fig. 3. Envelopes of incident (broken curve) and reflected (solid curve) pulses for δf = 18 MHz. The insets show magnified dips, which indicate switching.

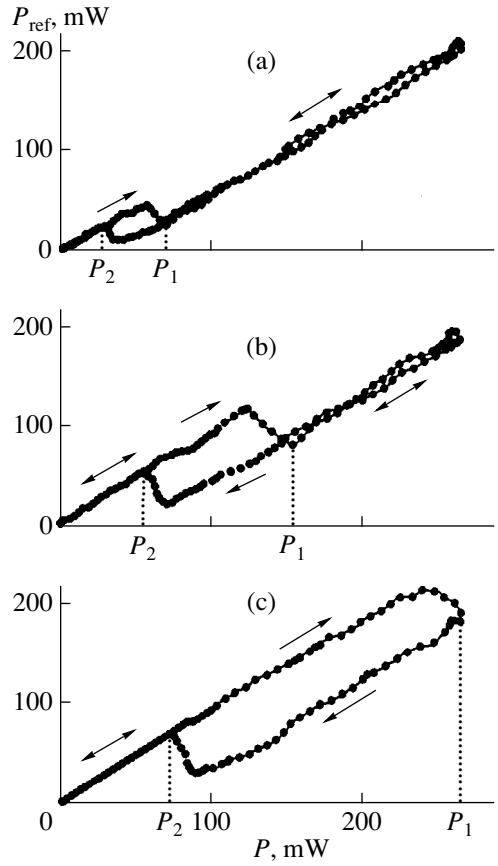

Fig. 4. Bistability characteristic for δf = (a) 15, (b) 20, or (c) 23 MHz. The arrows indicate the directions in which the input power is varied.

maximum value to zero (which corresponds to the trailing edge of the incident pulse), the reflected power first decreases smoothly, then rises abruptly at $P = P_2$, and finally decreases again in a linear fashion following the curve of growing input power. With $P_2 < P < P_1$, bistability occurs and two values of reflected power are possible with the same input power, with the actual one determined by the previous conditions. With increasing initial detuning of the signal frequency, the bistability loop widens and moves toward higher input powers (Fig. 4). The maximum loop width is $10\log(P_1/P_2)_{max}$ = 12 dB, and the maximum loop height is 10 dB. These values correspond to the depth of the dip in the reflection frequency response at low powers.

The time to switch between stable states can be directly measured from the response of the bistable resonator to a driving pulse. The insets in Fig. 3 demonstrate that the switch-on time (at P_1) is almost the same as the switch-off time (at P_2), which is equal to $\tau \approx 3$ μs. The switching times monotonically decrease by a factor of about 2 with increasing the absolute value of frequency detuning and the incident power for the moment of switching. The measured switching times are the same order of magnitude as the YIG magnetic-relaxation time $\tau = 1/(\gamma\Delta H) \approx 0.5$ μs (γ = 2.8 MHz/Oe). On the other hand, they are much less than typical values of thermal-relaxation time for ferrite-film structures, which may be tens or hundreds of milliseconds [9]. These findings indicate that the bistability of the resonator results from the intrinsic nonlinearity of FMR, not from the heating of the YIG film by absorbed microwave power.

DISCUSSION

To describe the bistable behavior of the resonator, we adapted a model of dispersive optical bistability [10]. Its FMR version is based on the resonator characteristics for linear conditions (low incident powers) and on the f_0–P_a relationship.

The frequency response of the resonator is determined by nonuniform magnetostatic oscillations excited in the ferrite. For a rectangular ferrite film of width a, length b, and thickness d, the frequency of the fundamental mode is approximately expressed as

$$f_0 = \gamma(H_0 - 4\pi M_z) + \gamma 4\pi M_z\left(\frac{d}{a} + \frac{d}{b}\right) + \gamma 4\pi M_z \frac{\pi d}{4}\sqrt{\left(\frac{1}{a}\right)^2 + \left(\frac{1}{b}\right)^2}. \quad (1)$$

Here, the first term equals the frequency of uniform FMR in an infinite ferrite film and the magnetization is perpendicular to the film. Also, H_0 is the strength of an external magnetostatic field; M_z is the time-independent magnetization component, which is parallel to the field and perpendicular to the film; and γ is the absolute value of the gyromagnetic ratio. If the power is so low that the magnetization precesses at a small angle with the z-axis, then M_z equals the saturation magnetization M_0 of the ferrite. The second term in (1) is a first-order correction due to demagnetization. The third term allows for the sinusoidal amplitude distribution of the

high-frequency magnetization along the sides of the film. With measured parameter values, formula (1) yields $f_0 = 4312$ MHz, which differs from the measured value by as little as 2%. The difference results from the crystalline anisotropy of the ferrite and the nonuniformity of its magnetic field. We ignored these factors, because they are unimportant in the context of this study.

With low powers, the absorption line shape of an FMR resonator is described by the well-known Lorentzian expression

$$P_a(f) = P\frac{A_0}{1 + \{(f - f_0)/\Delta f\}^2}. \quad (2)$$

Accordingly, reflection loss as a function of frequency is $L(f) = 10\log\{P_{\text{ref}}(f)/P\}$, where $P_{\text{ref}}(f) = P - P_a(f)$, with $P_a(f)$ given by (2). In Fig. 1a, the circles refer to the absorption line computed for $f_0 = 4400$ MHz, the resonance linewidth $\Delta f = 2.2$ MHz, and the absorption coefficient $A_0 = 0.95$. In what follows, we use the parameter values that provide the best agreement between the computed and measured data for low powers.

Now, let us take a close look at Fig. 2. As already mentioned, the shift in f_r with increasing signal power results from the intrinsic nonlinearity of FMR. We will show that this also follows from formula (1). Since the first term dominates in (1), we infer that the resonant frequency must be rising if M_z decreases. The conservation of the magnetization magnitude M_0 implies $M_z = M_0 - 2m^2/M_0$ to a first approximation. With the squared magnitude m_2 of the high-frequency magnetization proportional to P_a, we see that formula (1) implies the linear growth of f_r with P_a. Let us express the dependence of f_r on P_a as

$$f_r = f_0 + BP_a, \quad (3)$$

where $B = 1.18$ MHz/mW, according to the experiment.

Inserting (3) into (2), we obtain a cubic equation that relates the incident power P to the absorbed power P_a:

$$P = \frac{P_a}{A_0}\left[1 + \left(\frac{\delta f - BP_a}{\Delta f}\right)^2\right], \quad (4)$$

where $\delta f = f - f_0$ is the initial detuning of the signal frequency.

Using (4), we can draw P_a–P curves for a given signal frequency f. Figure 5 presents typical examples of such curves, which are computed by the above approach with measured parameter values. Broken line *1* represents the linear relationship $P_a = A_0P$ for linear resonator conditions ($B = 0$) and $\delta f = 0$ ($f = f_0$). Curve *2* refers to nonlinear resonator conditions and $\delta f = 10$ MHz. Notice the unstable segment between points *b* and *c*, where P_a decreases with increasing P. As

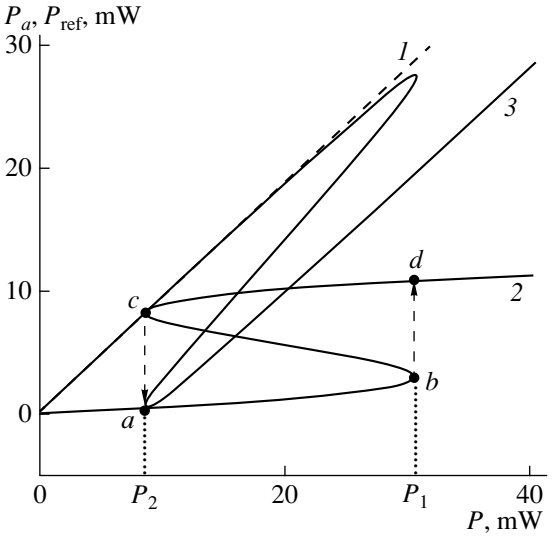

Fig. 5. Computed graphs of absorbed (*1*, *2*) and reflected (*3*) power vs. incident power.

P is raised from zero, P_a first rises smoothly until point *b* is reached (at $P = P_1$), then jumps to point *d*, and finally continues to rise in a smooth manner. As P is lowered from its maximum value, P_a first smoothly decreases until point *c* is reached (at $P = P_2$), then drops to point *a*, and finally continues to decrease in a smooth manner. Thus, the resonator behaves in a bistable fashion if P is varied between P_2 and P_1. With the same P, it may offer higher or lower absorption depending on the previous conditions.

Curve *3* in Fig. 5 depicts the dependence of P_{ref} on P. It is seen that P_{ref} drops at $P = P_1$ and jumps at $P = P_2$, which totally agrees with the experiment in qualitative terms (Fig. 4).

The model enables one to compute the powers at which the resonator switches from one stable state to the other. It follows from Fig. 5 that $\partial P/\partial P_a = 0$ at switching points *b* and *c*. Differentiating the right-hand side of (4) and setting the result equal to zero, we obtain two values of absorbed power at the switching points:

$$P_a^{1,2} = \frac{2\delta f \pm \sqrt{\delta f^2 - 3\Delta f^2}}{3B}. \quad (5)$$

Inserting them into (4), we find P_1 and P_2.

Expression (5), the zero-loop condition $P_{a1} = P_{a2}$, and equation (4) suggest the following analytic conditions for bistability

$$\delta f > \delta f_{\text{th}} = \sqrt{3}\Delta f, \quad P > P_{\text{th}} = \frac{8}{3\sqrt{3}}\frac{\Delta f}{A_0 B}. \quad (6)$$

Thus, we arrive at two conclusions: (1) an FMR resonator with the Lorentzian line shape becomes bistable only if the signal-frequency detuning exceeds a certain threshold. (2) For the threshold power P_{th} to be low, the

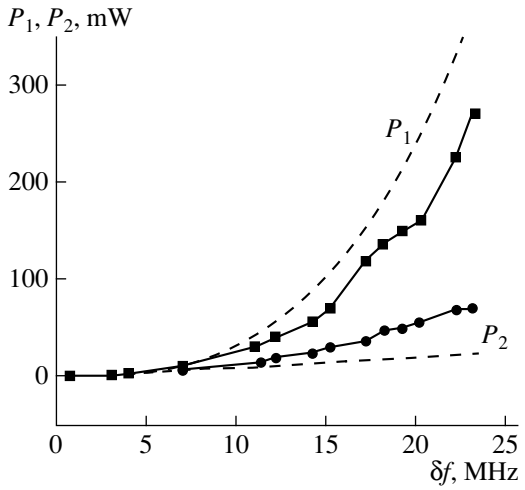

Fig. 6. The upper (P_1) and the lower (P_2) bistability limit vs. δf. The marks refer to the experiment and the broken curve refers to the computation.

resonator must have a small linewidth, an absorption coefficient approaching unity, and considerable nonlinearity.

In our experiment, the minimum values of δf and P, at which bistability arises, were about 7 MHz and 5 mW, respectively. They are fairly close to the computed values δf_{th} = 3.8 MHz and P_{th} = 3.02 mW, which are obtained from (6) with parameter values corresponding to the experimental data.

Figure 6 depicts the dependences of P_1 and P_2 on the initial frequency detuning δf. The solid lines refer to the measurements, whereas the dashed ones refer to the computation by the above approach. It is seen that the latter agree with the former in qualitative terms. Specifically, the observed bistability loop is between the computed values of P_2 and P_1 for any δf, although its width is smaller than the predicted one.

Presumably, the discrepancies between the computed and the measured data stem from the parametric excitation of spin waves in the ferrite. As is known, if the amplitude of magnetization precession exceeds a certain threshold, transfer from uniform precession to exchange spin waves results [11]. This causes the saturation of FMR absorption and resonance line broadening. In our experiment, FMR saturation manifested itself in a considerable decrease in the absorption coefficient with increasing power (Fig. 2). Furthermore, the maximum frequency shift observed, by 30 MHz, implies $\theta = \arccos(M_z/M) \approx 5.5°$. The latter value is well above the limit angle at which the parametric excitation of spin waves arises in the ferrite, $\theta_c \approx 1°$.

CONCLUSIONS

We conducted an experimental investigation into the microwave bistability of a ferromagnetic resonator. The resonator was a 25-μm-thick rectangular YIG film with a perpendicular magnetic field. Measuring the response to a pulsed signal, we obtained resonator bistability characteristics for low powers and different detunings of the driving frequency from the resonant one. The time of switching between the stable states was a few microseconds. It has been found that the bistability results from the intrinsic nonlinearity of FMR, the latter being caused by an increase in the angle at which the magnetization precesses. A comparative review of the measured and the computed characteristics has demonstrated that the performance of the resonator at high signal powers can be described in general terms by a phenomenological model of dispersive bistability. To provide a detailed description, the theory should allow for the parametric excitation of spin waves in the ferrite at high signal powers.

In practical terms, bistable resonators constructed in FMR films could find application in microwave solid-state devices for signal forming and processing, such as limiters or amplitude modulators. They could also be part of microwave logic with microwave control.

ACKNOWLEDGMENTS

This study was funded in part by grants from the Ministry of Education (Russia) and DAAD (Germany).

We are grateful to Prof. C.E. Patton and Prof. J. Pelzl for discussions and caring attitudes.

REFERENCES

1. H. Gibbs, *Optical Bistability: Controlling Light with Light* (Academic, New York, 1985; Mir, Moscow, 1988).
2. M. T. Weiss, Phys. Rev. Lett. **1** (2), 239 (1958).
3. Y. K. Fetisov and K. E. Petton, in *Proceedings of the XVI International School-Workshop "Novel Magnetic Materials of Microelectronics"* (Moscow, 1998), Part 1, p. 276.
4. Y. K. Fetisov, V. T. Synogach, and C. E. Patton, IEEE Trans. Magn. **35** (6), 4511 (1999).
5. P. V. Anderson and H. Suhl, Phys. Rev. **100** (2), 1788 (1955).
6. Y. K. Fetisov and C. E. Patton, in *Abstracts of the 1998 MMM Conference, Miami, 1998*, p. 103.
7. Y. T. Zhang, C. E. Patton, and M. V. Kogekar, IEEE Trans. Magn. **22** (2), 993 (1986).
8. Y. K. Fetisov and C. E. Patton, in *Abstracts of the 44th MMM Conference, San Jose, 1999*, p. 371.
9. A. N. Myasoedov, Y. K. Fetisov, A. V. Maryakhin, *et al.*, Zh. Tekh. Fiz. **61** (1), 118 (1991) [Sov. Phys. Tech. Phys. **36**, 71 (1991)].
10. F. S. Felberg and J. H. Magburger, Appl. Phys. Lett. **28** (12), 731 (1976).
11. A. G. Gurevich and G. A. Melkov, *Magnetic Oscillations and Waves* (Nauka, Moscow, 1994).

Translated by A. Sharshakov

Technical Physics, Vol. 46, No. 1, 2001, pp. 89–100. Translated from Zhurnal Tekhnicheskoĭ Fiziki, Vol. 71, No. 1, 2001, pp. 92–105.

RADIOPHYSICS

Ultrasensitivity in a Chain of Oscillating Dipoles with Variable Moments

E. G. Fateev

Institute of Applied Mechanics, Ural Division, Russian Academy of Sciences, Izhevsk, 426001 Russia
e-mail: fateev@ipm.uni.udm.ru; e@fateev.udm.ru

Received June 1, 1999

Abstract—A chain of closely spaced oscillators is studied theoretically. The oscillators are interrelated electric dipoles whose moments may vary within a wide range. An expression for the oscillator interaction potential is suggested. On the basis of this potential, a one-dimensional nonlinear equation of motion is derived with allowance made for dissipation and external driving. A numerical investigation is carried out and various nonlinear phenomena are revealed in the chain. Among them are the size effect and ultrasensitivity, i.e., a giant response of the chain to extremely weak periodic perturbations. The findings are compared with previously obtained experimental results on naturally occurring objects with similar structure. It is inferred that the model is realistic. © *2001 MAIK "Nauka/Interperiodica".*

INTRODUCTION

This paper deals with a system of closely spaced oscillating electric dipoles with variable and interrelated dipole moments in the presence of dissipation and perturbation. It is a challenging problem to ascertain the behavior of the system even in a one-dimensional case. In practical terms, this model may provide valuable insight into remarkable phenomena in some types of heterogeneous condensed media that has been exposed to an electromagnetic field of an ultralow frequency (ULF) below 10^3 Hz. The medium consists of a nonconducting or semiconducting continuous phase and inclusions with liquid or quasi-liquid conducting sheaths. Such structures are usually formed in almost any insulator during a phase transition. They permanently exist in powders and water-saturated rock. They are also basically similar to certain systems of cells in organisms. A realistic model of such media should take into account the close spacing of the oscillators and the variation in their dipole moments. Otherwise, many interesting phenomena may be overlooked.

Among these phenomena is the ultrasensitivity of crystalline hydrates to ULF under strong compression. This recently detected effect manifests itself in the giant mechanical response to an extremely weak electric field in a very narrow ULF range where the field strength is lower than the electric breakdown threshold by a factor of about 10^3 [1]. Furthermore, the frequency range shifts if the medium is heated [2]. The effect is preceded by giant bursts of dielectric susceptibility at ULFs, which apparently result from the formation of short-lived heterogeneous structures, including nonconducting microinclusions with thin liquid sheaths containing mobile ions. Susceptibility bursts in such media experiencing ULF fields have been reported by many researchers (see the references in [3]). The phenomenon stems mainly from the accumulation of extremely large amounts of polarization charges (free anions or cations) at the poles of the microinclusions so that the dipole moments of the oscillators change considerably. However, in contrast to dielectric-loss spectra, the reported shapes of ULF permittivity have no narrow or wide peaks at any moment of growth. They are smooth curves obeying the Debye-spectrum dispersion relation. The point is that the dipole–dipole interaction in the chain has been neglected when dealing with inhomogeneous media in ULF fields because of computational difficulties. Accordingly, attempts to relate the giant susceptibility bursts at ULFs to the giant mechanical response resulted in rather academic models of gas breakdown in microcracks of crystalline-hydrate plates under compression. The models imply that a ULF peak may arise in the input-power spectral density, which leads to a singularity in the ultrasensitivity spectrum [3]. The peak would be noticeable if the charge relaxation time τ of the sheaths was about 10^{-2} s and the particle size was in the micrometer range. In reality, $\tau = 1/\Omega \sim 10^{-5}$ s, where $\Omega \sim 5 \times 10^4$ Hz is the frequency corresponding to the maximum in dielectric loss. Furthermore, the models state that a ULF peak arises only if each physical property of the gas in microcracks is within a very narrow range. The above considerations have led us to the conclusion that a chain of closely spaced oscillating dipoles with variable moments should be used as a physical model of ultrasensitivity. In particular, this approach could help one understand why the phenomenon is confined to a narrow ULF range, at least at the onset of excitation.

It is interesting to note that the model examined here can also be applied to the recently detected excitation

1063-7842/01/4601-0089$21.00

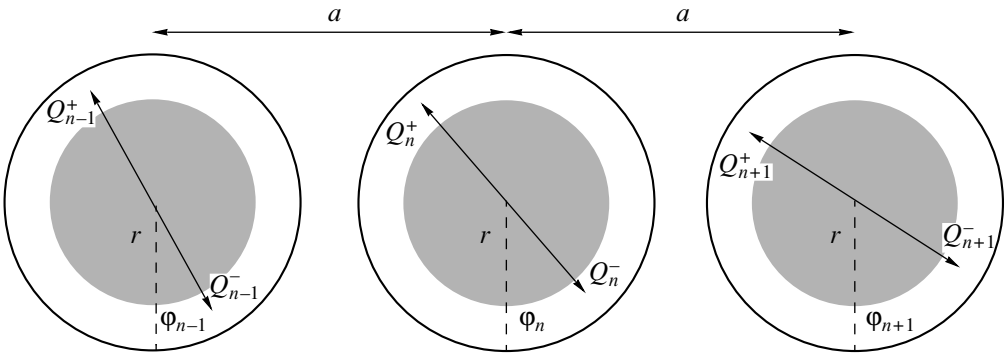

Fig. 1. Configuration of the dipole-oscillator chain with spacing a. Each oscillator represents a particle of diameter $2r$ with a sheath containing oscillating charges. The sheath thickness may be ~30–300 Å.

and synchronization of short-term ULF electric oscillations, predominantly at 25–45 Hz, in many macroscopic biological systems when two similar objects approach each other very closely [4–6]. These unusual effects were interpreted in terms of olfactory phenomena [4–6]. By contrast, we associate them with the excitation of electric oscillators in cells. The level of excitation must depend on the effective oscillator sizes, which increase as the objects approach each other.

To explain the above phenomena, a one-dimensional chain of closely spaced oscillating electric dipoles is considered, with a and $2r$ standing for the average dipole spacing and the charge spacing of a dipole, respectively (Fig. 1). Based on this model, the total potential of the interaction between the oscillators should be determined and the system behavior under the action of an ULF electric field should be investigated. Recall that well-known models based on oscillator chains with nonlinear coupling typically imply that the dipole moments are constant and $a \gg 2r$ [7, 8]. Although this approach works well with certain quasi-one-dimensional chains, it fails when applied to various systems where dipole charges vary by one to four orders of magnitude, depending on the oscillator spacing, oscillator natural frequencies, etc. Accordingly, this study follows the course outlined in this section. Also, we compare the computed behavior of the chain with experimental data.

MODEL DESCRIPTION

The model is illustrated in Fig. 1. The potential energy will be calculated for the case of $a \gg 2r$, where a is the average oscillator spacing and r is the oscillator radius with variable dipole moments. Thus, neighboring oscillators may be in contact. Furthermore, we assume that the polarization level may be very sensitive to both the frequencies and the strengths of local and external fields. Dipole–dipole interaction will be treated in the Coulomb approximation. For the respective oscillators, let φ_{n-1}, φ_n, and φ_{n+1} denote the deflection angles of the dipole axes from the unstable-equilibrium positions (Fig. 1). Then, the potential energy of the oscillator system has the general form

$$U_{\text{int}} = \frac{1}{4\pi\varepsilon\varepsilon_0}\sum_n\left\{\left(\frac{Q^+_{n-1}Q^+_n\mathbf{R}^{++}_{n-1,n}}{(R^{++}_{n-1,n})^2} + \frac{Q^-_{n-1}Q^-_n\mathbf{R}^{--}_{n-1,n}}{(R^{--}_{n-1,n})^2}\right.\right.$$
$$\left. - \frac{Q^-_{n-1}Q^+_n\mathbf{R}^{-+}_{n-1,n}}{(R^{-+}_{n-1,n})^2} - \frac{Q^+_{n-1}Q^-_n\mathbf{R}^{+-}_{n-1,n}}{(R^{+-}_{n-1,n})^2}\right)$$
$$+\left(\frac{Q^+_nQ^+_{n+1}\mathbf{R}^{++}_{n,n+1}}{(R^{++}_{n,n+1})^2} + \frac{Q^-_nQ^-_{n+1}\mathbf{R}^{--}_{n,n+1}}{(R^{--}_{n,n+1})^2}\right. \quad (1)$$
$$\left.\left. - \frac{Q^-_nQ^+_{n+1}\mathbf{R}^{-+}_{n,n+1}}{(R^{-+}_{n,n+1})^2} - \frac{Q^+_nQ^-_{n+1}\mathbf{R}^{+-}_{n,n+1}}{(R^{+-}_{n,n+1})^2}\right)\right\}.$$

Here, the distances between the charges of the $(n-1)$th dipole and those of the nth dipole are expressed as

$$R^{++}_{n-1,n} = [(a - r(\sin\varphi_{n-1} - \sin\varphi_n))^2$$
$$+ (r(\cos\varphi_{n-1} - \cos\varphi_n))^2]^{1/2}$$
$$= \left[a^2 + 4r\sin\left(\frac{\varphi_n - \varphi_{n-1}}{2}\right)\right. \quad (2)$$
$$\left.\times\left(r\sin\left(\frac{\varphi_n - \varphi_{n-1}}{2}\right) + a\cos\left(\frac{\varphi_n + \varphi_{n-1}}{2}\right)\right)\right]^{1/2},$$

$$R^{--}_{n-1,n} = [(a + r(\sin\varphi_{n-1} - \sin\varphi_n))^2$$
$$+ (r(\cos\varphi_{n-1} - \cos\varphi_n))^2]^{1/2}$$
$$= \left[a^2 + 4r\sin\left(\frac{\varphi_n - \varphi_{n-1}}{2}\right)\right. \quad (3)$$
$$\left.\times\left(r\sin\left(\frac{\varphi_n - \varphi_{n-1}}{2}\right) - a\cos\left(\frac{\varphi_n + \varphi_{n-1}}{2}\right)\right)\right]^{1/2},$$

$$R^{-+}_{n-1,n} = [(a + r(\sin\varphi_{n-1} + \sin\varphi_n))^2 + (r(\cos\varphi_{n-1} + \cos\varphi_n))^2]^{1/2} = \left[a^2 + 4r\cos\left(\frac{\varphi_n - \varphi_{n-1}}{2}\right) \times \left(r\cos\left(\frac{\varphi_n - \varphi_{n-1}}{2}\right) + a\sin\left(\frac{\varphi_n + \varphi_{n-1}}{2}\right)\right)\right]^{1/2}, \quad (4)$$

$$R^{+-}_{n-1,n} = [(a - r(\sin\varphi_{n-1} + \sin\varphi_n))^2 + (r(\cos\varphi_{n-1} + \cos\varphi_n))^2]^{1/2} = \left[a^2 + 4r\cos\left(\frac{\varphi_n - \varphi_{n-1}}{2}\right) \times \left(r\cos\left(\frac{\varphi_n - \varphi_{n-1}}{2}\right) - a\sin\left(\frac{\varphi_n + \varphi_{n-1}}{2}\right)\right)\right]^{1/2}. \quad (5)$$

In (1), $\mathbf{R}^{++}_{n-1,n}$; $\mathbf{R}^{--}_{n-1,n}$; $\mathbf{R}^{-+}_{n-1,n}$; $\mathbf{R}^{+-}_{n-1,n}$; $\mathbf{R}^{++}_{n,n+1}$; $\mathbf{R}^{--}_{n,n+1}$; $\mathbf{R}^{-+}_{n,n+1}$; and $\mathbf{R}^{+-}_{n,n+1}$ denote the radius vectors between the respective charges in the chain. The respective distances $R^{++}_{n,n+1}$; $R^{--}_{n,n+1}$; $R^{-+}_{n,n+1}$; and $R^{+-}_{n,n+1}$ between the charges Q^+_n, Q^-_n, Q^+_{n+1}, and Q^-_{n+1} in dipoles $n+1$ and n obey formulas that can be derived from (2)–(5) by replacing n with $n+1$ and $n-1$ with n. Finally, ε is the relative permittivity of the medium and ε_0 is the permittivity of free space. It is convenient to recast (1) as

$$U_{\text{int}} = \frac{1}{4\pi\varepsilon\varepsilon_0}\sum_n \left\{ Q^+_n\left(\frac{Q^+_{n-1}\mathbf{R}^{++}_{n-1,n}}{(R^{++}_{n-1,n})^2} + \frac{Q^+_{n+1}\mathbf{R}^{++}_{n,n+1}}{(R^{++}_{n,n+1})^2}\right) + Q^-_n\left(\frac{Q^-_{n-1}\mathbf{R}^{--}_{n-1,n}}{(R^{--}_{n-1,n})^2} + \frac{Q^-_{n+1}\mathbf{R}^{--}_{n,n+1}}{(R^{--}_{n,n+1})^2}\right) - Q^+_n\left(\frac{Q^-_{n+1}\mathbf{R}^{-+}_{n,n+1}}{(R^{-+}_{n,n+1})^2} + \frac{Q^-_{n-1}\mathbf{R}^{-+}_{n-1,n}}{(R^{-+}_{n-1,n})^2}\right) - Q^-_n\left(\frac{Q^+_{n+1}\mathbf{R}^{+-}_{n,n+1}}{(R^{+-}_{n,n+1})^2} - \frac{Q^+_{n-1}\mathbf{R}^{+-}_{n,n+1}}{(R^{+-}_{n,n+1})^2}\right)\right\}. \quad (6)$$

Now, let us take into account that the charge of dipole n depends on external and local electric fields, the latter being produced by the moving charges of dipoles $n-1$ and $n+1$. Assume that the other dipoles act on dipole n only indirectly via the chain as a result of shielding. We neglect other physical and chemical processes in the oscillators and around them that may affect polarization (for details, see [9–11]). The contribution of external and local fields to the polarization of any of the charges Q^+_n, Q^-_n, Q^+_{n-1}, and Q^-_{n-1} is assumed to obey the superposition principle, allowing for the frequency dependence. For any oscillator, the frequencies of the positive and the negative charges are considered to be the same. For each oscillator, let the dependence of the polarization on the frequencies of the local and the external field, ω_n and Ω, respectively, obey the Debye dispersion law [9, 10]. Since $|Q^+_n| = |Q^-_n|$, the respective dipole charges of the $(n-1)$th, nth, and $(n+1)$th oscillators are expressed as

$$Q^+_n = \beta\left(\frac{c_0 e(\varepsilon_s - \varepsilon_\infty)\mathbf{R}^{++}_{n,n-1}}{4\pi\varepsilon\varepsilon_0(1 + (\tau\omega_{n-1})^2)(R^{++}_{n,n-1})^3} + \frac{c_0 e(\varepsilon_s - \varepsilon_\infty)\mathbf{R}^{++}_{n,n+1}}{4\pi\varepsilon\varepsilon_0(1 + (\tau\omega_{n+1})^2)(R^{++}_{n,n+1})^3} - \frac{c_0 e(\varepsilon_s - \varepsilon_\infty)\mathbf{R}^{+-}_{n,n-1}}{4\pi\varepsilon\varepsilon_0(1 + (\tau\omega_{n-1})^2)(R^{+-}_{n,n-1})^3} - \frac{c_0 e(\varepsilon_s - \varepsilon_\infty)\mathbf{R}^{+-}_{n,n+1}}{4\pi\varepsilon\varepsilon_0(1 + (\tau\omega_{n+1})^2)(R^{+-}_{n,n+1})^3} + \frac{E^{\text{ext}}_n}{1 + (\tau\Omega)^2}\right), \quad (7)$$

$$Q^+_{n-1} = \beta\left(\frac{c_0 e(\varepsilon_s - \varepsilon_\infty)\mathbf{R}^{++}_{n-1,n-2}}{4\pi\varepsilon\varepsilon_0(1 + (\tau\omega_{n-2})^2)(R^{++}_{n-1,n-2})^3} + \frac{c_0 e(\varepsilon_s - \varepsilon_\infty)\mathbf{R}^{++}_{n-1,n}}{4\pi\varepsilon\varepsilon_0(1 + (\tau\omega_n)^2)(R^{++}_{n-1,n})^3} - \frac{c_0 e(\varepsilon_s - \varepsilon_\infty)\mathbf{R}^{+-}_{n-1,n-2}}{4\pi\varepsilon\varepsilon_0(1 + (\tau\omega_{n-2})^2)(R^{+-}_{n-1,n-2})^3} - \frac{c_0 e(\varepsilon_s - \varepsilon_\infty)\mathbf{R}^{+-}_{n-1,n}}{4\pi\varepsilon\varepsilon_0(1 + (\tau\omega_n)^2)(R^{+-}_{n-1,n})^3} + \frac{E^{\text{ext}}_{n-1}}{1 + (\tau\Omega)^2}\right), \quad (8)$$

$$Q^+_{n+1} = \beta\left(\frac{c_0 e(\varepsilon_s - \varepsilon_\infty)\mathbf{R}^{++}_{n+1,n}}{4\pi\varepsilon\varepsilon_0(1 + (\tau\omega_n)^2)(R^{++}_{n+1,n})^3} + \frac{c_0 e(\varepsilon_s - \varepsilon_\infty)\mathbf{R}^{++}_{n+1,n+2}}{4\pi\varepsilon\varepsilon_0(1 + (\tau\omega_{n+2})^2)(R^{++}_{n+1,n+2})^3} - \frac{c_0 e(\varepsilon_s - \varepsilon_\infty)\mathbf{R}^{+-}_{n+1,n}}{4\pi\varepsilon\varepsilon_0(1 + (\tau\omega_n)^2)(R^{+-}_{n+1,n})^3} - \frac{c_0 e(\varepsilon_s - \varepsilon_\infty)\mathbf{R}^{+-}_{n+1,n+2}}{4\pi\varepsilon\varepsilon_0(1 + (\tau\omega_{n+2})^2)(R^{+-}_{n+1,n+2})^3} + \frac{E^{\text{ext}}_{n+1}}{1 + (\tau\Omega)^2}\right), \quad (9)$$

where τ is the relaxation time of bound charges in sheaths and ε_s and ε_∞ are the maximum SLF (static) and the minimum high-frequency (optical) values of the permittivity, respectively.

The coefficient c_0 is the number of elementary dipole charges e that change the permittivity of the system by unity during polarization. Let the chain be subjected to a uniform harmonic external field directed along the chain axis. In the vicinity of an nth oscillator, the field is expressed as

$$E_n^{\text{ext}} = 2\varepsilon^{-1}E\sin(2\pi\Omega t)\cos(\varphi_n). \tag{10}$$

Similar expressions describe the field near oscillators $n-1$ and $n+1$. To evaluate E_n, E_{n-1}, and E_{n+1} we assume that the charge of dipole n or $n-1$ tends to $Q_\infty = c_0 e\varepsilon_\infty$ for $\omega_n \longrightarrow \infty$ and to $Q_0 = c_0 e(\varepsilon_s - \varepsilon_\infty)$ for $\omega_n \longrightarrow 0$. Also, we assume that c_0 = const for each oscillator in the chain. The coefficient β corresponds to the dipole charge that is induced in a field of unit strength. In other words, β specifies the polarization susceptibility of an oscillator. It is similar to the dielectric susceptibility, which represents the relationship between the polarization and the field strength in a macroscopic dielectric body. To a first approximation, we regard β as a constant here. In reality, it may depend on many other parameters.

Let us assume that the variables φ_n are nearly identical for neighboring dipoles at the same point in time. Accordingly, if we perform the change $na \longrightarrow x$ and $\varphi_n(t) \longrightarrow \varphi(x, t)$ in the continuum approximation $\varphi_n - \varphi_{n-1} \sim \delta$, then U_{int} can be expanded in terms of a small parameter as

$$\varphi_{n-1} - \varphi_n \sim \varphi_n - \varphi_{n+1} \sim a\frac{\partial\varphi}{\partial x}. \tag{11}$$

In view of (1)–(11) and the accompanying comments, we obtain an expression for U_{int} by passing to the limit for $a \longrightarrow 2r + \Delta$ in the expansion to second-order terms. In the continuum approximation, it can be written as

$$U_{\text{int}} = \frac{1}{4\pi\varepsilon\varepsilon_0}\int\frac{dx}{a}\beta^2 V_1(x,t)V_2(x,t)$$

$$\times\left\{-[P(t)\cos(\varphi) + B(x,t)V_3(x,t)]\right.$$

$$-B(x,t)[P(t)\cos(\varphi)V_4(x,t) + V_3(x,t)V_5(x,t)]\frac{\partial\varphi}{\partial x} \tag{12}$$

$$-B(x,t)[5P(t)\cos(\varphi)\{V_6(x,t) + V_7(x,t)\}$$

$$\left.+ 9V_3(x,t)V_7(x,t)]\frac{\partial^2\varphi}{\partial x^2}\right\}$$

with

$$P(t) = \frac{2E\sin(2\pi\Omega t)}{\varepsilon(1 + (\tau\Omega)^2)}, \tag{13}$$

$$B(x,t) = \frac{c_0 e(\varepsilon_s - \varepsilon_\infty)}{4\pi\varepsilon\varepsilon_0(1 + (\tau\varphi_t)^2)}, \tag{14}$$

$$S_1(x,t) = a^2 + 4r^2 - 4ra\sin(\varphi), \tag{15}$$

$$S_2(x,t) = a^2 + 4r^2 + 4ra\sin(\varphi), \tag{16}$$

$$V_1(x,t) = P(t)\cos(\varphi) + B(x,t)[S_1^{-1}(x,t) - S_2^{-1}(x,t)], \tag{17}$$

$$V_2(x,t) = S_1^{-1/2}(x,t) + S_2^{-1/2}(x,t), \tag{18}$$

$$V_3(x,t) = S_1^{-1}(x,t) + S_2^{-1}(x,t), \tag{19}$$

$$V_4(x,t) = 4ra^2\cos(\varphi)[S_1^{-2}(x,t) + S_2^{-2}(x,t)], \tag{20}$$

$$V_5(x,t) = -ra^2\cos(\varphi)B(x,t)S_1^{-1}(x,t), \tag{21}$$

$$V_6(x,t) = 2ra^3\sin(\varphi)S_2^{-2}(x,t) + 4r^2a^4\cos^2(\varphi)S_2^{-3}(x,t), \tag{22}$$

$$V_7(x,t) = -2ra^3\sin(\varphi)S_1^{-2}(x,t) + 4r^2a^4\cos^2(\varphi)S_1^{-3}(x,t). \tag{23}$$

When deriving (12), formula (6) was used, because in the limit of $a \longrightarrow 2r + \Delta$, the first two summands in parentheses become negligible compared to the remainder. For the same reason, each of the formulas (7)–(9) was used without the first two summands that account for the interaction between like charges of neighboring dipoles. Obviously, this simplification is justified by the existence of potential wells at $\varphi_n = \pi/2 + n\pi$, which become deeper as opposite charges of neighboring dipoles grow owing to polarization.

Let c_n denote the number of uncompensated charged particles (such as cations or anions) in the sheath of an nth oscillator so that the total mass of the charged particles at the ends of the nth dipole is $M_n = c_n m$, each particle having mass m. Then the kinetic energy of the chain is given by

$$T_k = \frac{1}{2}\sum_n J_n\dot{\varphi}_n^2. \tag{24}$$

Here, $J_n = c_n m r^2$ is the moment of inertia. Furthermore, in view of (7)

$$c_n = Q_n^+/e. \tag{25}$$

In the continuum approximation, expansion to the

second-order terms yields

$$T_k = \beta\frac{mr^2}{e}\int\frac{dx}{a}\Big\{V_1(x,t) + B(t)V_8(x,t)\frac{\partial\varphi}{\partial x} + B(t)V_9(x,t)\frac{\partial^2\varphi}{\partial x^2}\Big\}\Big(\frac{\partial\varphi}{\partial t}\Big)^2 \quad (26)$$

with

$$V_8(x,t) = 6ra^2\cos(\varphi)S_1^{-2}(x,t), \quad (27)$$

$$V_9(x,t) = -5ra^3\sin(\varphi)S_1^{-2}(x,t) + 36r^2a^4\cos^2(\varphi)S_1^{-3}(x,t). \quad (28)$$

Now, we assume that the dissipative forces are linear functions of charge angular velocities. Then, with ξ_n denoting the dissipation parameter, the dissipation function has the form

$$D = \frac{1}{2}\sum_n c_n\xi_n r^2\dot{\varphi}_n^2. \quad (29)$$

The above reasoning for the kinetic energy, including formulas (25) and (7), can be also applied to the dissipation function. In the continuum approximation, expansion to the second-order terms yields

$$D = \beta\frac{\xi r^2}{e}\int\frac{dx}{a}\Big\{V_1(x,t) + B(t)V_8(x,t)\frac{\partial\varphi}{\partial x} + B(t)V_9(x,t)\frac{\partial^2\varphi}{\partial x^2}\Big\}\Big(\frac{\partial\varphi}{\partial t}\Big)^2. \quad (30)$$

The force with which the external field acts on the chain can be expressed as

$$F_n = 2\varepsilon^{-1}E\sin(2\pi\Omega t)\sum_n Q_n\cos(\varphi_n), \quad (31)$$

where Q_n additively depends on local and external fields, according to (7). Let us expand F into a series. By analogy with (26) and (30), the continuum approximation yields

$$F(x,t) = 2\varepsilon^{-1}E\sin(2\pi\Omega t)\int\frac{dx}{a}\cos(\varphi)\Big\{V_1(x,t) + B(x,t)\frac{\partial\varphi}{\partial x}\Big(V_8(x,t) + V_9(x,t)\Big(\frac{\partial\varphi}{\partial x}\Big)\Big)\Big\}. \quad (32)$$

It follows from expressions (11) and (30) that the effective force applied to the chain is proportional to the squared amplitude of the external ac field. Now, let us write the Euler–Lagrange equation with regards for dissipation (30) and pertubation

$$\frac{\partial}{\partial t}\Big(\frac{\partial L}{\partial\varphi_t}\Big) + \frac{\partial}{\partial x}\Big(\frac{\partial L}{\partial\varphi_x}\Big) - \frac{\partial L}{\partial\varphi} = -\frac{\partial D}{\partial\varphi_t} + F(x,t). \quad (33)$$

Here, the Lagrangian

$$L = T_k - U_{\text{int}} \quad (34)$$

involves formulas (26) and (12) for the potential and kinetic energies, respectively. In the continuum approximation, Eq. (33) can be transformed into the following nonlinear motion equation written in natural units:

$$W_1\frac{\partial^2\varphi}{\partial t^2} + W_2 + X_1\frac{\partial^2\varphi}{\partial x^2} + X_2 - \Gamma_1\sin(\varphi) + \text{Dis}\frac{\partial\varphi}{\partial t} = F. \quad (35)$$

When deriving equation (35), for each differentiation, we neglected the terms with $1/a$ raised to the minimum power. This simplification is based on the assumption that $a \ll 1$ in natural units. Introducing the notation

$$\varphi_t = \frac{\partial\varphi}{\partial t}, \quad \varphi_x = \frac{\partial\varphi}{\partial x}, \quad \varphi_{x,t} = \frac{\partial^2\varphi}{\partial x\partial t}, \quad \varphi_{x,x} = \frac{\partial^2\varphi}{\partial x^2},$$

we write expressions for the functions appearing in (35) as

$$W_1(x,t) = 2MV_1(x,t) + 2V_2(x,t)V_{11}(x,t) \times\Big[V_1(x,t)V_3(x,t) + V_{10}(x,t)\Big(\frac{\partial\varphi}{\partial x}\Big)^2\Big], \quad (36)$$

$$W_2(x,t) = 2M\frac{\partial}{\partial t}V_1(x,t)\frac{\partial\varphi}{\partial t} + 2\beta^2V_2(x,t)\frac{\partial}{\partial t}B(x,t) \times\Big\{V_3(x,t)\frac{\partial}{\partial t}V_1(x,t) + V_1(x,t)\frac{\partial}{\partial t}V_3(x,t) + \frac{\partial}{\partial t}V_{10}(x,t)\Big(\frac{\partial\varphi}{\partial x}\Big)^2 + 2V_{10}(x,t)\Big(\frac{\partial\varphi}{\partial x}\Big)\frac{\partial^2\varphi}{\partial t\partial x}\Big\}, \quad (37)$$

where

$$V_{10}(x,t) = 5P(t)\cos(\varphi)[V_6(x,t) + V_7(x,t)] + 9V_3(x,t)V_7(x,t), \quad (38)$$

$$V_{11}(x,t) = \frac{2AC\tau^2}{(1+\tau^2\varphi_t^2)^2}\Big\{\frac{4\tau^2\varphi_t^2}{1+\tau^2\varphi_t^2} - 1\Big\}, \quad (39)$$

$$A = c_0e(\varepsilon_s - \varepsilon_\infty), \quad M = \frac{mr^2}{2e}, \quad C = \frac{1}{4\pi\varepsilon\varepsilon_0}. \quad (40)$$

Also, we have

$$\Gamma_1(x,t) = M\sin^{-1}(\varphi)[V_{13}(x,t) + 48r^2a^3MB(x,t)\cos^2(\varphi)S_1^{-3}(x,t)\varphi_x]\left(\frac{\partial\varphi}{\partial t}\right)^2 + 12\sin^{-1}(\varphi)\beta^2V_1(x,t)V_{12}(x,t)[P(t)\cos(\varphi) + B(x,t)V_3(x,t)], \quad \Gamma_2(x,t) = 0, \tag{41}$$

where

$$V_{12}(x,t) = 2ra\cos(\varphi)[S_1^{-3/2}(x,t) - S_2^{-3/2}(x,t)], \tag{42}$$

$$V_{13}(x,t) = -P(t)\sin(\varphi) + 4raAC\cos(\varphi)[S_1^{-2}(x,t) - S_2^{-2}(x,t)]. \tag{43}$$

In addition,

$$X_1(x,t) = 2MB(x,t)V_9(x,t)\varphi_t^2 + 2\beta^2P(t)V_2(x,t)\{5\cos(\varphi)[V_6(x,t) + V_7(x,t)] + 9V_3(x,t)V_7(x,t)\}, \tag{44}$$

$$X_2(x,t) = MB(x,t)\frac{\partial}{\partial x}V_8(x,t)\varphi_t^2 + 2MB(x,t)\frac{\partial}{\partial x}V_9(x,t)\varphi_t^2\varphi_x + A\beta^2V_2(x,t) \times\left\{2V_5(x,t)\frac{\partial}{\partial x}V_3(x,t) + 2V_3(x,t)\frac{\partial}{\partial x}V_5(x,t) - P(t)\sin(\varphi)V_4(x,t)\varphi_x\right\} + 18A\beta^2V_2(x,t) \times\left\{V_7(x,t)\frac{\partial}{\partial x}V_3(x,t) + V_3(x,t)\frac{\partial}{\partial x}V_7(x,t)\right\}\varphi_x. \tag{45}$$

Finally,

$$\mathrm{Dis}(x,t) = 2\beta\Psi\{V_1(x,t) + B(x,t)[V_8(x,t)\varphi_x + V_9(x,t)\varphi_x^2] - B(x,t)(1+\tau^2\varphi_t^2)^{-1}V_8(x,t)\tau^2\varphi_x\varphi_t^2\} \tag{46}$$

with

$$\Psi = \frac{\xi r^2}{2e} \tag{47}$$

and

$$F(x,t) = 2\varepsilon^{-1}E\beta\sin(2\pi\Omega t)\cos(\varphi)[V_1(x,t) + B(x,t)V_8(x,t)\varphi_x + B(x,t)V_9(x,t)\varphi_x^2]. \tag{48}$$

It is convenient to recast equation (35) in a form similar to the sine-Gordon (SG) equation:

$$\frac{\partial^2\varphi}{\partial t^2} + v_0^2\frac{\partial^2\varphi}{\partial x^2} - \Theta_0^2\sin(\varphi) - \eta\frac{\partial\varphi}{\partial t} = \gamma(x,t). \tag{49}$$

Here,

$$v_0 = \sqrt{X_1(x,t)/W_1(x,t)} \tag{50}$$

is an analog of the maximum velocity at which a perturbation propagates into the chain. Also,

$$\Theta_0 = \sqrt{\Gamma_1(x,t)/W_1(x,t)} \tag{51}$$

is an analog of the plasma frequency. In Eq. (49), the level of dissipation is represented by

$$\eta = \mathrm{Dis}(x,t)/W_1(x,t) \tag{52}$$

and the perturbation, by

$$\gamma(x,t) = [F(x,t) - W_2(x,t) - X_2(x,t)]/W_1(x,t). \tag{53}$$

With l denoting the length of the chain, we introduce the boundary condition

$$\varphi(0,t) = \varphi(l,t) = 0. \tag{54}$$

Physically, condition (54) may correspond to an interphase boundary which is impermeable to the perturbations under consideration.

ESTIMATIONS FOR THE COEFFICIENTS IN EQUATION (49)

Let us find the values for the coefficients in Eq. (49) so that the chain can most closely simulate the behavior of naturally occurring objects, such as disperse systems or long chains of living cells. To this end, let us estimate the number of uncompensated elementary charges in the thin liquid sheaths which determine the spherical shape of each oscillator (Fig. 1). We assume that a particle of the majority carrier has a charge $e \sim 1.6 \times 10^{-19}$ C and a mass $m \sim 1.6 \times 10^{-27}$ kg (its effective mass may be much larger). For example, such a carrier may be an H^+ ion, since its mobility is much higher than that of OH^- or other anions and cations. Let $r \sim 10^{-6}$–10^{-3} m and $a \sim 3 \times 10^{-6}$–3×10^{-3} m. The sheath thickness d may be set at about 10^{-9}–10^{-8} m [11]. We assume that at least $\chi_1 \sim 1\%$ of water in the sheaths is dissociated and that $\chi_2 \sim 1\%$ of the anions and cations constitute the uncompensated charges. Then, the density of elementary charges that may be involved in polarization is estimated at

$$c_1 = \chi_1\chi_2 4\pi[\{r+d\}^3 - r^3]\rho_{H_2O}(3m)^{-1} \sim 10^{11}\text{–}10^{14}\ \text{charge/mm}^3, \tag{55}$$

where $\rho \sim 10^3$ kg/m^3 is the water density and $m_{H_2O} \approx 3 \times 10^{-27}$ kg is the mass of a water molecule.

Thus, we see that the above estimate of c_1 agrees with the well-known value of ~10^{11} charge/mm^3 [11]. Correspondingly, $Q^+ = c_1 e$ is ~10^{-12}–10^{-9} C ($Q^+ = c_1 e$). Strictly speaking, the parameters should depend on the thermodynamic and local properties of the medium.

We select the value of c_1 such that the uncompensated charge Q is no larger than 10^{-12}–10^{-9} C when the polarization is at its maximum. The relaxation time is defined as $\tau_1 = r^2/2D$, where D is the volume diffusion coefficient of charges in the sheaths. The relaxation time is evaluated from the frequency $\omega = 1/\tau_1$, which corresponds to the highest dielectric loss. In the context of this study, $\omega \approx 6.29 \times 10^4$ rad/s, so that $\tau_1 \approx 1.6 \times 10^{-5}$ s.

Finally, consider the case of a disperse system. For the nth dipole, the fraction of its kinetic energy (apart from thermal fluctuations) that is converted into heat is proportional to the dielectric-loss tangent $\tan\delta_n \approx \omega_n \tau$, where ω_n is the natural frequency of the dipole [11]. Accordingly, all other things being the same, formulas (26) and (30) imply that

$$\frac{1}{2}\omega_n \tau m r^2 \left(\frac{\partial \varphi}{\partial t}\right)^2 \approx \frac{1}{2}\xi_n r^2 \left(\frac{\partial \varphi}{\partial t}\right)^2. \qquad (56)$$

Hence, we obtain the estimate

$$\xi \sim \omega \tau m \sim 10^{-33}.$$

RESULTS

As is known, the disturbed SG equation has been solved analytically only in certain special cases [7, 12]. Nevertheless, we will demonstrate that the motion equation (49), which describes the transmission of signals in disperse systems with double electrical layers, allows resonance-like excitation at ULFs despite very stringent restrictions that were imposed on the equation. This section deals with the numerical analysis of Eq. (49) with a constraint on the length of the chain (the computational scheme is outlined in the appendix). The analysis aims at ascertaining the nature of the excitation and to explore the possibilities for other effects.

As one would expect, the chain exhibits ULF ultrasensitivity in a wide range of relaxation times: $\tau_1 \sim 10^{-5}$–10^{-0} s. Figure 2 depicts the evolution of the polarization-level spectrum when the chain is subjected to an extremely weak harmonic electric field with a chain length l of 1 m and a field strength E of 10^{-8} V/m. Numerical analysis was performed with the following realistic values of the parameters: $r = 10^{-6}$ m, $a = 2.1 \times 10^{-6}$ m, $\tau_1 = 1.6 \times 10^{-5}$ s, $c_0 = 10^5$, $\varepsilon_\infty = 8$, $\varepsilon_s = 650$, $\beta = 1$, $\xi = 10^{-33}$, and $m = 1.6 \times 10^{-27}$ kg. Moreover, the values of ε_∞, ε_s, and τ_1 are typical of disperse systems where manifestations of ULF ultrasensitivity were first observed [1–6] according to our interpretation. The values of r and a are selected on the basis of [1–6]. In this study, unless otherwise stated, the term *polarization level* means the number of elementary charges involved

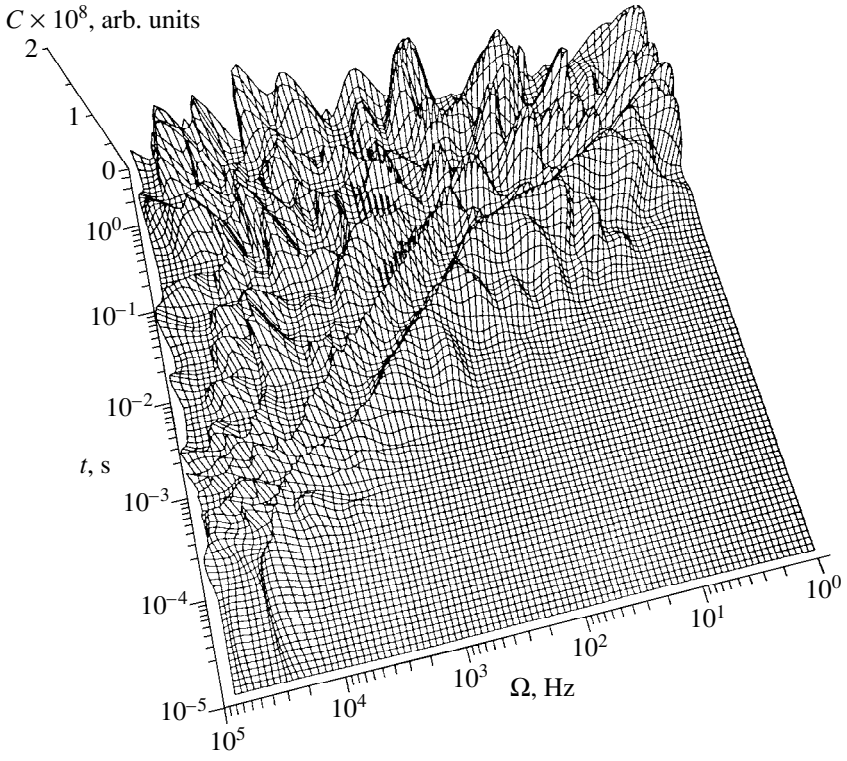

Fig. 2. Evolution of polarization-level spectrum under the action of an extremely weak harmonic ULF electric field.

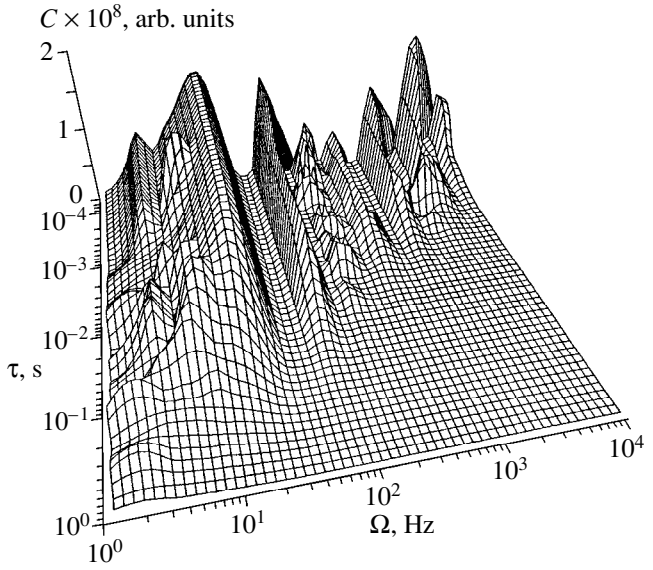

Fig. 3. Polarization level vs. drive frequency and relaxation time.

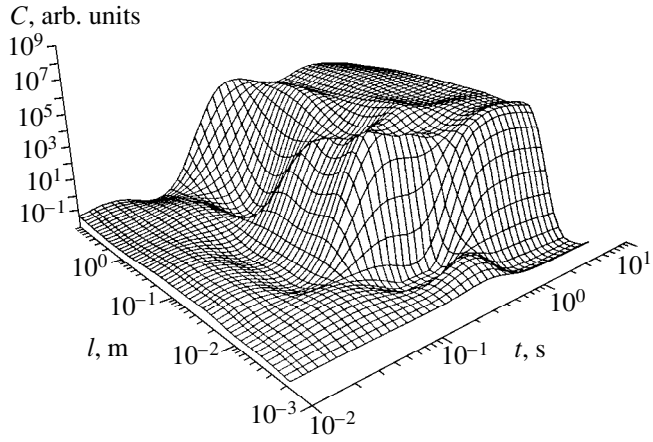

Fig. 4. Polarization level vs. time and chain length for an extremely small drive amplitude.

in polarization. This number is determined from a continuum version of formula (7), namely,

$$Q(x,t) = \beta\left\{V_1(x,t) + B(x,t)V_8(x,t)\frac{\partial\varphi}{\partial x} + B(x,t)V_9(x,t)\frac{\partial^2\varphi}{\partial x^2}\right\} \quad (57)$$

after the spectrum $\varphi_t(\Omega, t)$ has been computed.

Let us examine the behavior of the chain under the action of a ULF field. It can be seen that the polarization-level spectrum has a resonance–excitation portion if $t < 1$ s. For $t > 1$s, this portion gradually changes into that of the dispersion law Debye characteristic. In the first stage, we observe main-resonance peaks and satellite resonances for $t > 10^{-3}$ s. With $r \longrightarrow 1$ s, they all shift to the region of $\Omega < 10$ Hz. Such frequencies are called ultralow frequencies (ULFs). The dispersion properties of the chain at ULFs become apparent if the Z-axis is transformed to a logarithmic scale. In the final stage, the characteristic does not follow the Debye law in the strict sense. Instead, we can see a plateau disturbed at certain harmonics and occasionally disrupted by subharmonic bursts. Indeed, the evolution of the polarization-level spectrum depends on the parameters related to the driving, the oscillators, etc. Nevertheless, the pattern retains the distinctive features of Fig. 2 even when computed for other values of l and τ_1. Figure 3 shows this phenomenon in relation to the polarization level as a function of Ω and τ_1. We note that a decrease in τ_1 corresponds to an increase in the temperature of the chain. It can be seen that the frequencies of both the main and the satellite resonances are virtually fixed when τ_1 is varied within a wide range: $\tau_1 \approx 10^{-5}$–10^{-2} s. A slight frequency shift occurs only when the chain is cooled in the region of $\tau > 10^{-2}$ s. On the other hand, the region occupied by the satellite resonances extends to higher frequencies as the temperature is raised.

Remarkably, in the realistic model under consideration, the chain exhibits the dependence of the polarization level on the chain length. Figure 4 illustrates how this size effect changes with time for $\Omega \sim 31$ Hz and E as low as 10^{-8} V/cm. In particular, the effect indicates that the chain may possess an ultrasensitivity to ULF. On the other hand, ultrasensitivity arises only if the chain length exceeds a certain threshold. Specifically, ultrasensitivity is impossible if l is smaller than 1 cm but is appreciable for $l \sim 5$–10 cm, with $r \sim 10^{-6}$ m and $a \sim 2.1 \times 10^{-6}$ m (Fig. 4). In the latter case, the polarization level increases by a factor of 10^9. Furthermore, it was found that the polarization level of a long chain exposed to an extremely weak field may be as large as that of a short chain ($l < 10^{-3}$ m) subjected to a strong field (Fig. 5). However, it takes a certain time for the response to develop after a harmonic field is applied with the delay increasing with η. The above behavior can be detected in spite of the considerable changes in the pattern when any of the parameters are varied.

The nonlinear nature of the above effects is demonstrated in Figs. 6a and 7a. They show the polarization level (Fig. 6a) and phase velocity (Fig. 7a) as functions of the coordinate and time. Figure 6b clearly shows that soliton-like excitations develop at both ends of the chain, with $l = 1$ m and $t > 0.2$ s. If $t < 0.1$ s when the chain responds resonantly, then the polarization level oscillates fairly regularly throughout the chain exposed to an external field with $\Omega \sim 31$ Hz (Fig. 6a). Afterward, these oscillations become more and more chaotic, starting from the chain ends. If $t > 0.2$ s, the chaos gives way to distinct periodic positive bursts. This obviously suggests that soliton-like standing waves develop synchronously in the chain. Arising at the ends, they gradually

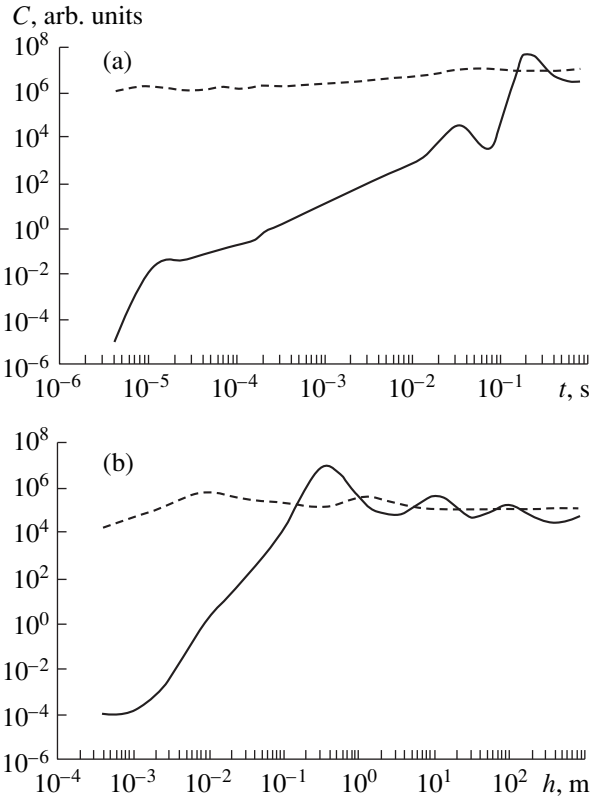

Fig. 5. Polarization level vs. (a) time and (b) length for $\Omega \sim 31$ Hz. The solid and the dashed lines refer to $E = 10^{-6}$ and 10^{-5} V/m, respectively.

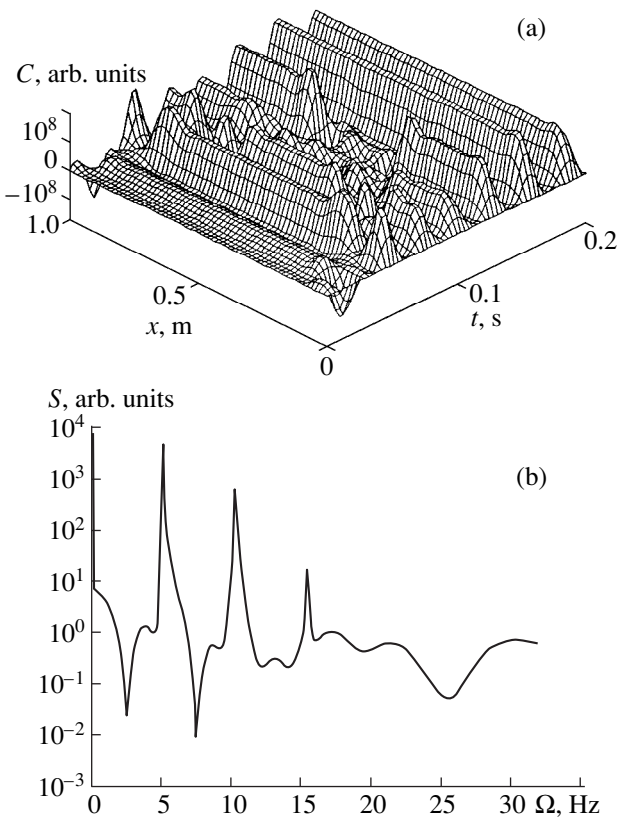

Fig. 6. (a) Polarization level vs. time and the coordinate, and (b) the corresponding power spectrum after averaging over the chain. The data were obtained for an extremely small drive amplitude and $\Omega \sim 31$ Hz.

extend to the entire chain. Clearly, any two neighboring dipoles occupied by any of the solitons oscillate in antiphase (since opposite charges of the dipoles prefer a positive-to-negative oscillation pattern). This growing oscillation seems to end in the rotation of the dipoles in opposite directions. The chain thus acquires a special type of dynamics whereby the charges of a dipole move throughout the sheath. Specifically, the rate of polarization bursts is lower than the pump frequency by a factor of about 6 (Fig. 6a). This is also confirmed by the power spectra in Figs. 6b and 7b, which correspond to the spatial–temporal distributions in Figs. 6a and 7a, respectively. For example, if the chain is subjected to an extremely weak harmonic field with $\Omega = 31$ Hz, it exhibits polarization bursts at the fundamental frequency $f \sim 5$ Hz and its subharmonics $2f$ and $3f$. It was found that subharmonics at other frequencies may also appear and disappear as a result of bifurcations with respect to certain parameters. Figure 7a demonstrates that with $c_0 > 10^1$ and $\Omega = 31$ Hz, the power spectrum corresponding to the phase velocity as a function of time is continuous if averaged over the entire chain. It can be seen that the spectral curve has an oscillatory shape only if $c_0 < 10^0$ (Fig. 7c).

DISCUSSION

It follows from the above results that a resonance response to a harmonic perturbation at any ULF develops during three to five periods. Afterward, the chain is in a chaotic state for three to seven periods (depending on parameters). Finally, its behavior changes to correspond to the Debye dispersion law. By this moment, the chain develops soliton-like wave packets, which are confined to its ends or occupy the entire chain. These features testify to the nonlinearity of the system dynamics, which obeys an SG-like equation. In simulating the oscillator coupling, the complicated and evidently nonlinear fashion in which the polarization level of any oscillator depends on those of its neighbors was taken into account, as well as the frequencies with which concentrated charges oscillate in them. The interaction between the oscillators was treated in the Coulomb approximation, allowing for the fact that the intercharge spacings vary with time. Indeed, if the parameters of the basic equations were varied, we could find many more trajectories, main and satellite resonances, and chaotic-region widths. Furthermore, we could observe domains in the distributions of the polarization level and sign throughout the chain. A deeper insight into the phenomena described by the

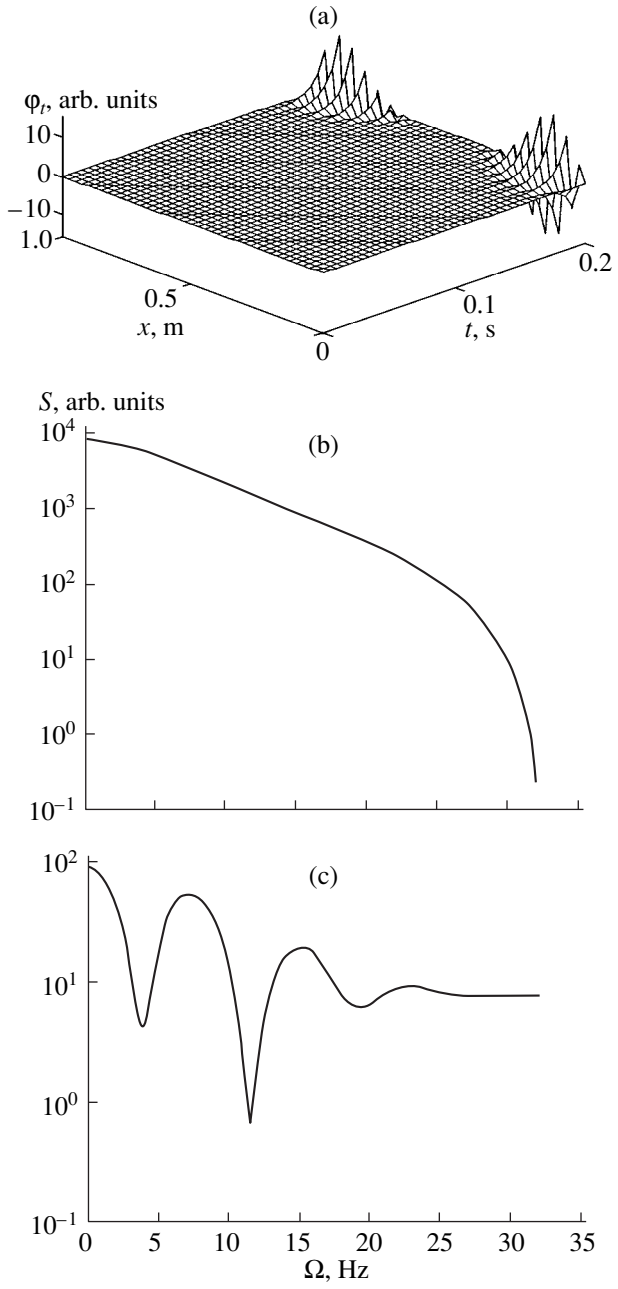

Fig. 7. (a) Phase velocity vs. time and the coordinate and (b, c) the corresponding power spectra after averaging over the chain. The curves in panels (b) and (c) were computed for $c_0 > 10^1$ or $c_0 < 10^0$, respectively. The chain is driven at an extremely small field amplitude and $\Omega \sim 31$ Hz. The other parameter values are specified in the text.

model could be gained from its two- or three-dimensional versions. Also, quite a different pattern may be obtained if we allowed for the magnetic field of the oscillating dipoles. At higher driving frequencies, the magnetic field must scatter a fraction of the concentrated charges in the region where solitons are formed. This factor may reduce the polarization level at medium frequencies.

The size effect and ultrasensitivity in the chain are direct consequences of the strongly nonlinear coupling between the dipoles. Their moments change considerably, primarily due to the fact that c_1 varies from 0 to about $c_1 \approx c_0(\varepsilon_s - \varepsilon_\infty)$. In the context of this study, the maximum value of c_1 may be on the order of 10^{11}. It is worth noting that if a storm wave on a sea had the same number of water molecules in its crest, then the height of the wave, $h \approx c_1 \times d_{mol}$ (with $d_{mol} \approx 3 \times 10^{-10}$ m), would be as large as 30 m. Since the depth and size of a basin govern the amplitude of waves in it [13], it is tempting to view the problem from the standpoint of the theory of deep-water waves [14]. Accordingly, the number of elementary polarization charges concentrated at the dipole ends corresponds to the height of the water column involved in wave motion and the standing solitons resulting from ultrasensitivity correspond to storm waves. However, there is an important difference between the two patterns. It consists of the condition of specular reflection imposed on the chain boundaries. Consequently, there is no dissipation at the boundaries, so storm electromagnetic waves may arise even at a chain length of about 1 cm. With increasing oscillator spacing and diameter, the threshold length may reach 1 m. Nevertheless, it is likely to equal several tens of centimeters at most for actual objects.

As indirect experimental evidence for our theoretical results, we cite the giant response of strongly compressed crystalline hydrates to an extremely weak electric field in the frequency range of 20–40 Hz [1–3]. This effect seems to cause the pronounced loss of mechanical strength (by a factor of 1.5–2) observed in some compressed crystal hydrates. Clearly, the ultrasensitivity spectrum of a substance can be determined from the dip in the ULF spectrum of the threshold of mechanical strength. The beauty of using this approach to design high-sensitivity ULF transducers consists of the following. We believe that ultrasensitivity is possible when crystalline hydrates experience short-term phase transitions involving partial dehydration produced by considerably nonuniform compression at a high pressure (over 5 kbar) or temperature [1–3]. Under such conditions, crystalline hydrates are basically heterogeneous media that can be regarded as one-dimensional seas of nonlinear electromagnetic oscillators (ideally, the oscillators can be regarded as grains with double electric layers.) On the one hand, the short duration of the phase transitions allows one to ascertain the ultrasensitivity spectrum in the initial stage of excitation. On the other hand, we believe that the model furnished with realistic parameter values, such as those used above, can provide an estimate of the average dehydration time under highly nonuniform compression. The phase transition is sufficiently long for resonance electromagnetic excitation to develop with threshold parameter values allowing efficient detection of ULF ultrasensitivity from the mechanical response (impaired mechanical stability). If the threshold condi-

tions of a pronounced response are aroused only by the moment when the state of the excited system entered the dispersion portion of the polarization characteristic, then supersensitivity would occur in the entire ULF region. Since the latter was never observed, we can infer that the oscillation ceased growing as early as the resonance stage. For systems with a narrow resonance-like peak, ULF ultrasensitivity is most likely to occur at $20 < \Omega < 40$ Hz, according to experiments [1–3]. Figure 2 demonstrates that this frequency range corresponds to an excitation time of about 0.1–0.2 s. Thus, we see that the attempts to attribute the ULF ultrasensitivity of the heterogeneous media (in the above-mentioned frequency range) to the Debye frequency dispersion only [1–3] were based on the highly overstated relaxation times for disperse systems ($\tau \sim 10^{-2}$–10^{-1} s). The reason is that the early models relying on these values predict that ultrasensitivity peaks will lie fairly close to the ULFs at which the excitation threshold of the Bridgman effect decreases. In reality, experiments with certain model objects yield $\tau \sim 10^{-5}$ s at normal temperature [3]. Furthermore, the early models seem to be unable to adequately explain the shift of the ultrasensitivity spectral peak in the ULF region for crystalline hydrates under strong nonuniform compression, the effect of which was first reported in [2]. By contrast, the model suggested in this study attributes the slight shift of the peaks to higher frequencies as the temperature of crystalline hydrates is raised to the fact that the delay is decreased below the threshold of electromagnetic storm as early as in the resonance stage. The numerical analysis showed that the decrease results neither from an increase in the number of elementary charges in the oscillators under heating nor from changes in the dissipation of oscillation energy, oscillator diameter or spacing, etc. We believe that a shorter time of phase transitions in the crystalline hydrates under strong compression and heating leads to a shorter resonance-excitation time, which in turn produces the shift to higher frequencies.

It is worth noting that ultrasensitivity was also theoretically discovered in an overdamped Kramers oscillator subjected to a weak time-dependent signals with parametric noise [15]. Furthermore, high sensitivity to weak constant perturbation and noise was studied in the context of a chiral selective chemical reaction [16]. By contrast, the ultrasensitivity examined here is induced by a weak alternating signal and the response level depends on chain length, excitation time, and other parameters. However, the effect does not result from a radical change in the asymptotic behavior of the system (the crossover) in response to a noise-induced perturbation of a parameter appearing in the model equations. Instead, it is caused by nonlinear effects producing giant narrow peaks of charge density in the chain. Consequently, no crossover boundary conditions are required to test our model in experiments.

Perhaps the ULF ultrasensitivity due to the size effect can explain, to some extent, the synchronous electromagnetic oscillations at frequencies from 25 to 35 Hz that were recently discovered in biological systems ranging from neurons to macroscopic organisms [4–6]. For example, ULF oscillations were observed in such objects as apples or mushrooms when they are situated very closely apart or are in contact [4–6]. In my opinion, this increases the effective size of cellular-oscillator chains. Admittedly, this is arguable, since the ultrasensitivity may well be triggered by chemical reactions involved in sensory or reflex olfactory processes [4–6]. Nevertheless, it should be pointed out that the resonance during the excitation in living objects occurs in the range of 25–35 Hz and lasts only a few milliseconds, after which the system passes to a state that has some features of a dispersion plateau. Such behavior is in accord with our numerical results for the model presented here.

Finally, let us estimate the local electric field E_{int} between the sheaths of two neighboring oscillators. Existing for a limited period, the field arises when the dipoles intensely oscillate under local focusing during an electromagnetic storm. The formula $E = Q^2(4\varepsilon\varepsilon_0\pi r^2 q_0)^{-1}$ yields $E_{\text{int}} \sim 10^7$–10^{11} V/cm, with the dipole charge Q set to its maximum value for the stated conditions, $Q \sim 10^{-12}$–10^{-9} C. Such charge storms can cause microscopic breakdown at numerous sites together with shock waves and explosion-like phenomena. This effect is possible in various materials subjected to relatively weak ULF electric fields [1–3].

CONCLUSION

We examined the behavior of a chain of closely spaced dipole oscillators ($a \geq 2r + \Delta$) with interrelated and variable dipole moments. To this end, a potential was determined for the dipoles. On the basis of this potential, the Euler–Lagrange equation was solved and a corresponding one-dimensional nonlinear-motion equation was derived. The latter was then transformed to a modified SG equation with dissipation.

The numerical analysis of the above equations suggests that the chain may feature strongly nonlinear dynamics. It was demonstrated that if an SLF harmonic field is applied to the chain, the latter first experiences a resonance type of excitation, then passes to chaos, and finally enters a state with the Debye dispersion. During the first stage, the resonance frequency shifts to still lower frequencies and may reach a fraction of a hertz. We also found some other interesting features typical of many systems with nonlinear coupling, such as the emergence of resonance frequencies by heating in the first stage and the formation of soliton-like objects in the third one.

Remarkably, the computation has revealed the size effect in the chain. This implies that the model may possess ultrasensitivity to extremely weak periodic sig-

nals. We believe that such phenomena were observed in experiments with disperse substances exposed to a ULF electric field [1–6]. Apparently, the first experimental evidence for the size effect was the ultrasensitivity of crystalline hydrates in an appropriate disperse phase, with the particle size lying in the millimeter range [1–3]. With those media, ultrasensitivity arises if the amplitude of the perturbing signal is smaller than the electric-breakdown value by a factor of 1000.

Admittedly, we had to neglect many features of naturally occurring oscillator systems with variable dipole moments. Nevertheless, the model has demonstrated some effects that were previously observed in physical experiments. We therefore believe that our approach can be used to predict some new phenomena.

ACKNOWLEDGMENTS

The author is grateful to T.V. Bakitskaya for her helpful participation in discussions.

APPENDIX

To numerically solve Eq. (49), we use an appropriate finite-difference method (see, e.g., [17, 18]). Using the mesh function $\varphi_{n,i} = \varphi(ih, nk)$ for $\varphi(x, t)$, we obtain the following approximate formulas:

$$\varphi_t = (\varphi_{n+1,i} - \varphi_{n-1,i})/2k + O(k^2), \quad \text{(A1)}$$

$$\varphi_{tt} = (\varphi_{n+1,i} - 2\varphi_{n,i} + \varphi_{n-1,i})/k^2 + O(k^2), \quad \text{(A2)}$$

$$\varphi_{xx} = (\varphi_{n+1,i+1} - 2\varphi_{n+1,i} + \varphi_{n+1,i-1} + \varphi_{n-1,i+1} - 2\varphi_{n-1,i} + \varphi_{n-1,i-1})/2h^2 + O(h^2 + k^2). \quad \text{(A3)}$$

Inserting (A1)–(A3) into Eq. (49) and neglecting the $O(k^2)$ and $O(h^2)$ terms, we arrive at

$$a_1(\varphi_{n+1,i+1} + \varphi_{n+1,i-1} + \varphi_{n-1,i+1} + \varphi_{n-1,i-1}) + a_3\varphi_{n+1,i} + a_2\varphi_{n-1,i} + a_4\varphi_{n,i} = \Theta_0^2\sin(\varphi_{n,i}) - \gamma; \quad \text{(A4)}$$
$$i = 1, 2, \ldots, I; \quad n = 0, 1, \ldots, N,$$

where

$$a_1 = v_0^2/2h^2; \quad a_3 = (v_0^2/h^2 + 1/k^2 + \eta/2k); \quad a_2 = (\eta/2k - v_0^2/h^2 + 1/k^2); \quad a_4 = -2/k^2. \quad \text{(A5)}$$

Here, the parameters v_0, Θ_0, η, and γ are determined from (50)–(53), respectively, with $x = ih$ and $t = nk$. The computational procedure for Eq. (A4) with $k = h$ is robust only if the step h is less than 0.1 [12]. If, e.g., $I \sim 1000$ and $N \sim 1000$ with $h \sim 0.001$ m and $k = 0.001$ s, then $l = Ih = 1$ m and $t = Nk = 1$ s, where l is the chain length and t is the observation time.

REFERENCES

1. E. G. Fateev, Dokl. Akad. Nauk **354** (2), 252 (1997).
2. E. G. Fateev, Pis'ma Zh. Éksp. Teor. Fiz. **65** (12), 876 (1997) [JETP Lett. **65**, 919 (1997)].
3. E. G. Fateev, Zh. Tekh. Fiz. **66** (6), 93 (1996) [Tech. Phys. **41**, 571 (1996)].
4. M. Stopfer, S. Bhagavan, B. Smith, and G. Laurent, Nature **390**, 70 (1997).
5. V. N. Murthy and E. E. Fetz, Proc. Natl. Acad. Sci. USA **89**, 5670 (1992).
6. K. MacLeod and G. Laurent, Science **274**, 976 (1996).
7. *Solitons in Action*, Ed. by K. Lonngren and A. Scott (Academic, New York, 1978; Mir, Moscow, 1981).
8. A. S. Davydov, *Solitons in Molecular Systems* (Naukova Dumka, Kiev, 1988; Kluwer, Dordrecht, 1991).
9. P. J. W. Debye, *Polar Molecules* (Chemical Catalog, New York, 1929; Gostekhizdat, Moscow, 1931).
10. R. Hagedorn, in *Prelude in Theoretical Physics in Honour of V.F. Weĭskopf* (North-Holland, Amsterdam, 1966).
11. T. L. Chelidze, A. I. Derevyanko, and O. D. Kurilenko, *Electric Spectroscopy of Heterogeneous Systems* (Naukova Dumka, Kiev, 1977).
12. R. K. Dodd, J. C. Eilbeck, J. Gibbon, and H. C. Morris, *Solitons and Nonlinear Wave Equations* (Academic, New York, 1982; Mir, Moscow, 1988).
13. O. M. Phillips, *Dynamics of the Upper Ocean* (Cambridge Univ. Press, Cambridge, 1966; Mir, Moscow, 1969).
14. M. J. Lighthill, *Waves in Fluids* (Cambridge Univ. Press, Cambridge, 1978; Mir, Moscow, 1981).
15. S. L. Ginzburg and M. A. Pustovoĭt, Pis'ma Zh. Éksp. Teor. Fiz. **67**, 592 (1998) [JETP Lett. **67**, 627 (1998)].
16. D. K. Kondepudi, I. Prigogine, and G. W. Nelson, Phys. Lett. A **111A**, 29 (1985).
17. W. F. Ames, *Numerical Methods for Partial Differential Equations* (Academic, New York, 1977).
18. G. I. Marchuk, *Methods of Numerical Mathematics* (Nauka, Moscow, 1989; Springer-Verlag, New York, 1975).

Translated by A. Sharshakov